Title

Zero and Ultra-Low-Field Nuclear Magnetic Resonance Spectroscopy Via Optical Magnetometry

Author

Blanchard, John Woodland

Publication Date

2014

Zero and Ultra-Low-Field Nuclear Magnetic Resonance Spectroscopy Via Optical Magnetometry

by

John Woodland Blanchard

A dissertation submitted in partial satisfaction of the
requirements for the degree of
Doctor of Philosophy

in

Chemistry

in the

GRADUATE DIVISION
of the
UNIVERSITY OF CALIFORNIA, BERKELEY

Committee in charge:
Professor Alexander Pines, Chair
Professor David Wemmer
Professor Dmitry Budker

Fall 2014

Abstract

Zero and Ultra-Low-Field Nuclear Magnetic Resonance Spectroscopy Via Optical Magnetometry

by

John Woodland Blanchard

Doctor of Philosophy in Chemistry

University of California, Berkeley

Professor Alexander Pines, Chair

Nuclear magnetic resonance (NMR) is among the most powerful analytical tools available to the chemical and biological sciences for chemical detection, characterization, and structure elucidation. NMR experiments are usually performed in large magnetic fields in order to maximize sensitivity and increase chemical shift resolution. However, the high magnetic fields required for conventional NMR necessitate large, immobile, and expensive superconducting magnets, limiting the use of the technique. New hyperpolarization and non-inductive detection methods have recently allowed for NMR measurements in the inverse regime of extremely low magnetic fields. Whereas a substantial body of research has been conducted in the high-field regime, taking advantage of the efficient coherent control afforded by a spectroscopy dominated by coupling to the spectrometer, the zero- and ultra-low-field (ZULF) regime has remained mostly unexplored. In this dissertation, we investigate the applicability of ZULF-NMR as a novel spectroscopic technique complimentary to high-field NMR.

In particular, we consider various aspects of the ZULF-NMR experiment and the dynamics of nuclear spins under various local spin coupling Hamiltonians. We first survey zero-field NMR experiments on systems dominated by the electron-mediated indirect spin-spin coupling (J-coupling). The resulting J-spectra permit precision measurement of chemically relevant information due to the exquisite sensitivity of J-couplings to subtle changes in molecular geometry and electronic structure. We also consider the effects of weak magnetic fields and residual dipolar couplings in anisotropic media, which encode information about nuclear magnetic moments and geometry, and further resolve topological ambiguities by lifting degeneracies. By extending the understanding of the interactions that contribute to ZULF-NMR spectra, this work represents a significant advancement towards a complete description of zero- and ultra-low-field nuclear magnetic resonance spectroscopy.

For my parents, and all my other teachers.

Contents

List of Figures

List of Tables

Acknowledgments

I am extremely grateful for all of the opportunities and assistance given to me, leading to this dissertation as a culmination of my adventures in science thus far. Without every one of my teachers, colleagues, friends, and mentors, it is impossible that I would be where I am now. So while I will try to acknowledge as many of the major contributors to my life and research as possible, I will almost certainly forget something or someone. As a result, to anyone reading this who doesn't see their name anywhere else:

Thank you – I couldn't have done it without you.

First of all, I would like to thank my Ph.D. committee: Alexander Pines, David Wemmer, and Dmitry Budker, who provided guidance throughout the Ph.D. program.

I am particularly indebted to my Ph.D. advisor Alex Pines, whose brilliance made everything possible. Who else could manage to find funding for something as ridiculous as nuclear magnetic resonance at *zero magnetic field*? Even more importantly, without his decades of seminal work, I wouldn't have had any idea where to start. Alex has been constantly positive and is an invaluable source of new ideas, and deeper intuitive explanations of ideas that it turns out I only thought I understood. Perhaps even more importantly, Alex has helped me to grow as a teacher, a speaker, a leader, and as a scotch enthusiast (more on that later).

Dima Budker effectively served as both a mentor and a secondary advisor, helping with theory, writing, collaboration, and instrumentation. Dima's confidence in me was frequently a source of reassurance, even when nothing seemed to be working. If nothing else, I hope that I have repaid some of his kindness by teaching him a bit of chemistry – maybe someday we'll find a problem that moves us beyond hydroxyl exchange and the structures of formic acid and acetonitrile ... I look forward to continued adventures with axions and shooting antiprotons at parahydrogen-polarized nuclear targets.

I also have to thank all of the people who were directly involved in my research and contributed to various aspects of this thesis. First and foremost, Micah Ledbetter was a fantastic mentor at the beginning of my time as a graduate student, teaching me how all of the instrumentation worked, and providing insight into the physics of ZULF-NMR. To this day, I doubt that any of this work would have gotten done if it weren't for Micah, which is further evidenced by how long it took to get everything working again once he finished his postdoc and left to work in the real world. From the beginning of my time in the Pines Lab, Thomas Theis provided guidance and an introduction to the zero-field project. Mark Butler was always available to explain complicated physical and mathematical principles in great depth and with great patience. While we only overlapped briefly, Gwendal Kervern was a source of significant theoretical insight at the beginning of my graduate career, especially in terms of understanding parahydrogen experiments. Despite the fact that we were always working on different aspects of ZULF-NMR, Paul Ganssle was a very helpful source of instrument design advice, and interesting discussions of relaxometry and diffusometry. Tobias

"F." Sjölander is not only my favorite Scandinavian ice creature, but also an excellent scientist who should be very successful carrying ZULF-NMR spectroscopy into the future. Tobias is an exceptional theorist who always forced me to provide *real* explanations, and who has a particular talent for finding holes in my half-formed ideas, as well as for forming good fully-formed ones. Even though he's in principle more of a diamond nitrogen-vacancy person than a ZULF-NMR with alkali magnetometer person, Jonathan King's involvement has been very useful to recent ZULF-NMR ideas, especially in terms of his command of symmetry and group theory. And of course, he's a valuable source of many of the crazier ideas about chirality and antisymmetric J-couplings that might someday come to fruition.

I am also thankful for the work performed by undergraduates who I have had the pleasure to mentor: Nick Malecek, Will Yashar, Emma Levine, Arne Kentner, Jörg Ackermann, Marcin Konowalczyk, and James Eills.

Though they may not have directly contributed to the work presented here, I would also like to thank the whole of Alex's research group, the Pinenuts (current, former, and scattered around the globe), who made the work environment so enjoyable. Scott Seltzer was always extremely useful as our resident magnetometry expert. I must also thank my good friend and conference/-travel buddy, Claudia Avalos, who for some reason was always willing to not only listen to me ramble on about whatever nonsense I was thinking about, but would frequently join me down the mathematical and/or fundamental physics rabbit hole. Dan Kennedy was a crucial ingredient for various shenanigans, scientific and otherwise (does it count as science when we discovered that it is indeed possible for the sun to come up while one is still drinking at a club in Hersonissos?). Though he generally did his best to avoid getting sucked into the sometimes less-than-applicable world of ZULF-NMR, Vik Bajaj was always willing to share a drink and talk about science/career-s/politics/etc. Vik was also kind enough to introduce me to the finer things in the Bay Area life, like sailing, fine cigars, and high-quality spirits.

Speaking of alcohol, I'd also like to thank alcohol. *To alcohol!* This thesis would be a decidedly different document without it. I would particularly like to thank St. George Spirits in Alameda, CA – without their incredible line of artisan gins, I very much doubt that any of this research would have been possible.

I am acutely aware that anything I have accomplished at this point in my life is wholly dependent on the teachers who laid the foundation in my earlier years. Perhaps the most outstanding example is my third-grade teacher Holly Omlin-Ruback, who established a *deep* appreciation for mathematics that persists to this day. I still have no idea how she did it, but she managed to teach third-grade students so much about mathematics that every math class for the following 7 years seemed trivial – even now I occasionally encounter a problem in tiling or fractal structures that reminds me of something from that class. Also at Stafford Primary in West Linn, Donna Kenny was an excellent teacher who understood how to keep advanced students interested without separating them from their peers. I also had the privilege to learn from talented and devoted science teachers at West Linn High School, of which Tana Dearborn, Jon Isensee, and Jeff Bilyeu are particularly notable examples. My career as a physical chemist was then cemented by undergraduate work at Arizona State University with Prof. Jeff Yarger and Prof. C. Austen Angell. Prof. George Wolf was an extraordinary lecturer on both quantum chemistry and statistical mechanics, and Prof. Richard Lebed brought such a thoroughness and excitement to his quantum mechanics lectures that he probably deserves a great deal of credit for any quantum understanding that I now possess. I also owe a debt of gratitude to Professor Frank Wilczek, whose matter-of-fact answer to my naive question "but what is spin *really*?" while he was visiting ASU reignited my interest in the mathematical foundations of fundamental physics. He deserves credit for inspiring any of the good abstract portions of Chapter 2, while I will assume all of the blame for the bad parts ...

Finally, I am of course indebted to my family – my mother Sally, my father Dale, my sister Brianna, my grandmother Ann (the list goes on and on) – who have done all they can to support me throughout my entire life. My parents were, furthermore, the first of my many teachers. Without the opportunity to play with those "Measure Up! Cups" in the bath as a kid, who knows if I would have ever been able to learn math or appreciate science?

Symbols and Physical Constants

Symbols

$\rightarrow$	Relates source and target sets of a map, e.g. $\phi : A \rightarrow B$
$\mapsto$	Relates a typical source element and its target element, e.g. $f : x \mapsto x^2$
$\exists$	"There exists"
$\forall$	"For all"
$\times$	Product; rarely, the vector cross product
$\otimes$	Tensor product
$\wedge$	Exterior product
$\circ$	Interior product
$\in$	Relates an element to its set, such as $x \in \mathbb{R}$
$\subset$	Set inclusion, such as $A \subset B$
V, V^*	A vector space, and its dual
$\boldsymbol{e}_i$	Basis vectors
$\boldsymbol{f}^i$	Dual basis vectors
y'	Differentiation of a function with respect to its argument
$\dot{y}$	Differentiation of a function with respect to time
$\Vert\quad\Vert$	Norm on a vector space
A^{T}	Transpose of the matrix A
$\mathbb{R}$	The set of real numbers
$\mathbb{C}$	The set of complex numbers
$\mathbb{H}$	The set of quaternions
$(\quad\cdot\quad)$	Metric inner product
$\boldsymbol{g}$ or $\eta_{\mu\nu}$	Metric tensor
S^n	Surface of an $(n + 1)$-dimensional sphere
$[A, B]$	Commutator of operators A and B; rarely, the Lie bracket of two vector fields
$\{A, B\}$	Anti-commutator of operators A and B
∇	3-vector differential operator "del"
$\delta^{\alpha\beta}_{\mu\nu}$	Kronecker delta - may contain any number of upper indices, with an equal number of lower indices
ϵ_{ijk}	Levi-Civita permutation symbol
$\langle j_i j_2 m_1 m_2 \vert JM \rangle$	Clebsch-Gordan coefficients

$C^{jm}_{j_1m_1j_2m_2}$	Clebsch-Gordan coefficients, alternative form
$\begin{Bmatrix} j_1 & j_2 & j_3 \\ j_4 & j_5 & j_6 \end{Bmatrix}$	Wigner 6-j symbols
$\begin{Bmatrix} j_1 & j_2 & j_3 \\ j_4 & j_5 & j_6 \\ j_7 & j_8 & j_9 \end{Bmatrix}$	Wigner 9-j symbols
$D^j_{m'm}(\alpha,\beta,\gamma)$	Wigner D-matrix
$d^j_{m'm}(\beta)$	Reduced (Wigner) rotation matrix
$\lvert\psi\rangle$	A “ket” vector in a quantum mechanical Hilbert space
$\langle\psi\rvert$	A “bra” dual vector in a quantum mechanical Hilbert space
$\rho_{nm} = c_n c_m^* \lvert n\rangle\langle m\rvert$	A “density matrix” describing an ensemble quantum state; note the assumed summation over repeated indices
$\lvert\uparrow\uparrow\rangle$	A vector in a 2-spin uncoupled basis, may be generalized to any number of spins with additional arrows
$\lvert S_0\rangle$	A vector in a 2-spin coupled basis with zero total spin angular momentum
$\lvert T_{0,\pm1}\rangle$	Vectors in a 2-spin coupled basis with total spin angular momentum 1
$R(\Omega)$	A 3D Euler rotation
θ	Polar angle, with respect to the z-axis
ϕ	Azimuthal angle, with respect to the x-axis
$\mathcal{H}$	Hamiltonian or total energy operator of a system
$\mathcal{H}_D$	Direct dipolar coupling Hamiltonian
$\mathcal{H}_{RDC}$	Residual dipolar coupling Hamiltonian remaining in a partially ordered medium
$\mathcal{H}_J$	Indirect spin-spin coupling Hamiltonian
$\mathcal{H}_{CSA}$	Chemical shift anisotropy Hamiltonian
$\mathcal{H}_Q$	Quadrupolar Hamiltonian
$\mathbf{B}$	Magnetic field vector
B_0	Amplitude of a static magnetic field
$\mathbf{I}_i$	Spin operators
γ_i	Gyromagnetic ratio of spin $\mathbf{I}_i$
$\mathbf{J}_{ij}$	J-coupling tensor between spins $\mathbf{I}_i$ and $\mathbf{I}_j$
$J_{\alpha\beta,(ij)}$	Components of the J-coupling tensor between spins $\mathbf{I}_i$ and $\mathbf{I}_j$, covariant form
J^{iso}_{ij}	Isotropic J coupling between spins $\mathbf{I}_i$ and $\mathbf{I}_j$

D_{jk}	Residual dipolar coupling between spins $\mathbf{I}_i$ and $\mathbf{I}_j$
$T^{(k)}_{q,q'}$	Rank-k spherical tensor
$\mathbf{r}$	Spatial vector, typically the one joining two nuclei
T_1	Spin-lattice relaxation rate constant
T_2	Spin-spin relaxation rate constant
t_1	Evolution time in the indirect dimension of 2D experiment
t_2	Evolution time in the direct dimension of 2D experiment
ω_1	Indirect dimension in 2D experiment
ω_2	Direct dimension in 2D experiment

Physical Constants

h	Planck constant (quantum of action), $6.626\,176 \times 10^{-34}$ J $\cdot$ s
$\hbar$	Reduced Planck constant $\hbar = h/2\pi$
k_B	Boltzmann constant, $1.380\,662 \times 10^{-23}$ J/K
e	Electron charge, $1.602\,177 \times 10^{-19}$ C
m_e	Electron rest mass, $1.672\,622 \times 10^{-27}$ kg
m_p	Proton rest mass, $9.109\,383 \times 10^{-31}$ kg
μ_0	Vacuum permeability, $4\pi \times 10^{-7}$ V $\cdot$ s/(A $\cdot$ m)
ϵ_0	Vacuum permittivity, $8.854\,187 \times 10^{-12}$ $\mathrm{C}^2 \cdot \mathrm{N}^{-1} \cdot \mathrm{m}^{-2}$
g_s	Electron g-factor = $-2.002\,319\,304\,361\,53 \pm 2.6 \times 10^{-13}$
μ_B	Bohr magneton, $(e\hbar)/(2m_e) = 9.274 \times 10^{-24}$ J/T
μ_N	Nuclear magneton, $(e\hbar)/(2m_p) = 5.051 \times 10^{-27}$ J/T
G_F	Fermi coupling constant, $4.5437 \times 10^{14}\ \mathrm{J}^{-2} = 1.1664 \times 10^{-5}\ \mathrm{GeV}^{-2}$

Chapter 1

Introduction

Nuclear magnetic resonance (NMR) experiments are conventionally performed in large magnetic fields in order to increase chemical shift resolution and to maximize signal via higher nuclear spin polarization and improved inductive detection sensitivity. Zero-field NMR is an alternative magnetic resonance modality where measurements are performed in the absence of an applied magnetic field. Unlike conventional NMR, in which "external" spin interactions - couplings to fields originating from the experimental apparatus - are dominant, zero-field NMR presents a regime dominated by "internal" spin interactions - couplings to fields originating from the sample itself.

Specifically, in zero- and ultra-low-field nuclear magnetic resonance (ZULF-NMR) the Zeeman interaction is negligible or small enough that it can be treated as a perturbation on the "local" J-coupling and dipole-dipole interactions. In this regime, the internal spin-spin coupling Hamiltonians are not truncated by the imposed symmetry of a large magnetic field, so all chemical and structural information encoded in the interaction tensors is preserved. Whereas the high-field weak-coupling regime is optimal for chemical shift measurements, the "inverse weak coupling" regime of zero-field is the natural environment for the observation of spin-spin couplings. These local interactions are exquisitely sensitive to subtle changes in geometry, conformation, and electronic structure, thus serving as a valuable source of chemical and structural information.

This dissertation describes the current state of the art in zero- to ultra-low-field nuclear magnetic resonance (ZULF-NMR). Chapter 2 provides a theoretical background covering topics from the fundamental nature of spin to specific Hamiltonians involved in ZULF-NMR. Chapter 3 serves as an introduction to the operational principles and instrumentation involved in the optical detection of low-frequency magnetic resonance signals. Chapter 4 describes the means by which observable signals are generated in terms of non-equilibrium spin polarizations and magnetic field pulses. Chapter 5 discusses the interpretation of zero-field J-spectroscopy in terms of perturbation theory. Chapter 6 details the effects of small magnetic fields on ultra-low-field NMR spectra in terms of a Zeeman perturbation on the J-coupling Hamiltonian. Chapter 7 considers the effect of anisotropy via the introduction of residual dipolar couplings as perturbations on the J-coupling Hamiltonian. Chapter 8 further emphasizes consequences of working in the ZULF regime by describing the formation of long-lived heteronuclear spin states. Finally, Chapter 9 summarizes current results, describes ongoing experiments, and proposes future directions for ZULF-NMR.

Chapter 2

Theoretical Preliminaries

So I guess this is where we begin –
As we ponder the nature of spin:
Those Pauli matrices
Provide relative ease,
But what symmetry added them in?

This chapter will provide essential (and at times, perhaps non-essential) background to facilitate understanding of later chapters. We will begin with a discussion of relevant symmetries and their effect on physical phenomena. This will be followed by a brief introduction to quantum mechanics, which is then applied to examples in nuclear magnetic resonance (NMR). The chapter will finish with an elucidation of definitions and conventions necessary for the discussion of zero- and ultra-low-field NMR.

Please note that while Sections 2.1 and 2.2 provide a deeper understanding of spin as a consequence of symmetry, the only *essential* result for the rest of the thesis will be that protons and neutrons are spin-$\frac{1}{2}$ particles. While I hope that the road to this result may be an entertaining diversion, many readers may prefer to instead begin their journey with Section 2.3, which presents a summary of quantum mechanics in terms relevant to nuclear magnetic resonance. Section 2.4 includes definitions and naming conventions that will be important going forward.

2.1 Axioms, Conventions, and Other Assumptions

For convenience, we will avoid much in the way of metamathematics. That is, we will make a number of assumptions that are rarely, if ever, questioned outside of courses on set theory along the lines of

Postulate 2.1.1 $\exists x(x = x)$

or

Postulate 2.1.2 $\exists x(x \text{ is reading this thesis})$

both of which seem to be readily acceptable assumptions, even if they can't be proven by anything other than life experience. The reader who may now otherwise feel abandoned in an abyss of abstract absurdity is referred to Zermelo–Fraenkel set theory [1, 2] (for a finitely axiomatizable theory, see von Neumann–Bernays–Gödel set theory [3]) and/or the works of Camus [4] and Sartre [5], as appropriate.

One assumption worth considering is the existence of the Universe, which we can define as the place where experimental measurements are made. One might complain that this is another trivial abstract assumption, but beyond defining a domain of discourse, this assumption and definition of the Universe allows us to avoid further distractions by avoiding what cannot or has not been observed. Specifically, we will only consider Lorentz-invariant systems governed by the symmetries described in the next section. Furthermore, we will *generally* consider only systems in flat space-time for which the Standard Model provides a satisfactory description. We will not concern ourselves with questions of why the fine structure constant or gravitational constant are what they are, or why the apparent consequence of nothing nothing-ing is the existence of everything.

Additional postulates are defined as follows, beginning with five that are necessary for a proof of the spin-statistics theorem [6, 7]:

Postulate 2.1.3 *Lorentz Covariance: All physical quantities transform under some representation of the Lorentz group.*

Furthermore, the Lagrangian of any field theory is a Lorentz scalar, and is thus a Lorentz invariant (i.e. we are working with gauge theories). That is, the laws of physics remain the same, regardless of the given rest frame. The continuous symmetries are those of temporal translation, spatial translation, spatial rotation, and Lorentz boosts. More specifically, these are all space-time transformations that are isometries of Minkowski space-time. The requirement of Lorentz covariance (and the slightly stronger requirement of Poincaré covariance) will have a variety of additional uses in this section.

Postulate 2.1.4 *Locality: An object can only be affected by interactions with its immediate surroundings.*

Postulate 2.1.5 *Causality: A given event can only be affected by those events that occur in the past light-cone of the given event. Similarly, space-like separated field operators must either commute or anticommute.*

Postulate 2.1.6 *Finite mass: All particles have finite mass, and thus propagate.*

This is important because infinitely massive particles are totally non-relativistic, which as we will see would cause problems in describing the spin of such particles.

Postulate 2.1.7 *Positive Definite: Particles are real objects, and thus the states describing such particles possess a positive definite norm.*

This last assumption is further tied to the postulates of quantum mechanics, which largely serve to define a means by which linear algebra can be used to study quantum mechanics. The remaining crucial postulates are as follows:

Postulate 2.1.8 *A physical system is associated with a complex Hilbert space, H.*

A Hilbert space is a special type of vector space, which will be defined in the next section.

Postulate 2.1.9 *The space of a complex system is the tensor product of component Hilbert spaces.*

For example, if the space of one particle is H_1 and the space of another is H_2, the space of a system consisting of the two particles is $H_{12} = H_1 \otimes H_2$.

Postulate 2.1.10 *The physical state of a quantum system is associated with one-dimensional subspaces (rays) within H.*

Equivalently, the state is designated by a vector in a projective Hilbert space, $\mathbf{P}H$.

Postulate 2.1.11 *Observables are represented by Hermitian matrices on H.*

This is essentially equivalent to the requirement that measurements must yield positive definite eigenvalues.

Theorem 2.1.12 *Wigner's Theorem: transformations via physical symmetries act on H as either unitary or antiunitary operators. [8]*

Conjecture 2.1.13 *Gell-Mann's Totalitarian Principle: "Anything not forbidden is compulsory" [9, 10].*

Specifically, as Gell-Mann wrote it, "any process which is not forbidden by a conservation law actually does take place with appreciable probability." He continues to note that relying on "this principle is somewhat dangerous, since it may be that while the laws proposed in this communication are correct, there are others, yet to be discussed, which forbid some of the processes that we suppose to be allowed." [9]. This may be reformulated to say that any particle, state, or transition that is not forbidden by symmetry does exist or will occur and the absence of any apparently allowed particle, state, or transition is then evidence that there exist additional symmetries that have not been considered.

We also point out that covariant and contravariant tensor indices are denoted with subscripts and superscripts, respectively. For notational convenience, we will sometimes follow the Einstein summation convention, omitting explicit summation symbols for the case of repeated indices. This is primarily for Section 2.2, after which we will try to be more explicit to avoid confusion for readers who may have less experience with tensor analysis.

2.2 Physics → Symmetry: Symmetry → Physics

At a fundamental level, physics is based on geometry. The basic building blocks of the Universe – particles and fields – may be understood as geometric objects, and the properties of these objects are directly related to how they transform under symmetry operations.

2.2.1 Group Theory Basics

In order to effectively discuss the symmetries involved in physics, we now introduce the mathematical tools of group theory. The first natural first step is to define what a group *is*.

Definition A *group* G is a set of elements $\{a, b, c, \dots\}$ which includes a composition rule and is *closed* such that if $a \in G$ and $b \in G$, then the product $ab \in G$.

Furthermore, the composition rule must be associative, i.e. $(ab)c = a(bc)$, and the group must contain a unique identity element e such that $ae = ea = a$. In order for the group to be closed, there must also exist an inverse a^{-1} for each element $a \in G$ such that $aa^{-1} = a^{-1}a = e$. If a group is commutative, i.e. $ab = ba$, then the group is said to be *abelian*.

There exists a prodigious literature on the fundamentals of group theory, so we will not attempt to expound too thoroughly on the topic. We will instead simply define a few terms that will be useful going forward.

Definition A *homomorphism* is a structure-preserving map between two groups (or more generally, between any two algebraic structures). Given two groups $(G, *)$ and $(H, \cdot)$ a group homomorphism from $(G, *)$ to $(H, \cdot)$ is a function $h : G \to H$ such that for all $a, b \in G$, $h(a * b) = h(a) \cdot h(b)$.

Definition An *isomorphism* is a bijective homomorphism.

Definition An *endomorphism* is a homomorphism from a mathematical structure onto itself. So a group endomorphism would be $f : G \to G$, an endomorphism of a factor space is a linear map $f : V \to V$, etc.

Definition An *automorphism* is an isomorphism from a mathematical structure onto itself. Because an automorphism is a bijective mapping of a structure onto itself while preserving its structure, automorphisms correspond to symmetries of mathematical structures. The automorphism group is the set of all automorphisms of a mathematical structure. In the case of a topological space endowed with a metric, an *isometry* is an automorphism between metric spaces that preserves distance.

Definition The *general linear group* of degree n over a field F is the set of $n \times n$ invertible matrices, together with the group operation of matrix multiplication, denoted $\mathrm{GL}_n(F)$. More generally, the general linear group of a vector space V is the automorphism group of V. For n dimensional V over F, $\mathrm{GL}(V)$ is isomorphic to $\mathrm{GL}_n(F)$. The *special linear group* is the subgroup of the general linear group consisting of matrices with unit determinant.

Definition A *Lie group* is a group that is also a differentiable manifold, in which the group operations of multiplication and inversion are smooth maps. Lie groups are deeply connected to physics and symmetry, but before we can describe this connection further, we need to first focus on a few other basic geometric concepts.

2.2.2 Vectors, Forms, Tensors, etc.

The careful (or, perhaps, confused) reader may notice that many of the postulates that were introduced earlier made mention of things called vector spaces, without providing any explanation of what these mysterious mathematical entities actually *are*. Having moved past the somewhat philosophical overview, we will now remedy this situation.

Definition A *vector space* over a field F is a set, V, that includes the operations of vector addition (which maps two elements of V into a third element of V) and scalar multiplication (which multiplies an element of F by an element of V to yield another element of V). Furthermore, the vector addition must be associative and commutative, and there must exist an inverse (and thus an identity element). The scalar multiplication must also be distributive with respect to both vector and field addition.

Definition A *vector*, $\boldsymbol{v}$, v^i, or $|a\rangle$ is an element of a vector space V.

Definition A *scalar* is an element of the field, F, over which V is defined.

It should be noted that these are "mathematical" definitions, and are thus very general. The definitions used in classical physics are somewhat more specific, referring to geometric vectors. In order to we will need to define a few more concepts.

Definition A *dual space* V^* is a set of linear functionals that map the elements of V into elements of F, $(\phi : V \to F)$.

Definition A *covector* or *1-form*, $\boldsymbol{\alpha}$, α_j, or $\langle b|$ is an element of a dual space V^*. When using the bold-face symbol representation, we will try to use Greek letters to distinguish 1-forms from vectors.

If the vector space V is endowed with an *inner product* operation, $(\quad\cdot\quad) : V \times V \to F$ that maps two vectors into a scalar, then that vector space is referred to as a *Hilbert space*. As a consequence of this property of the space, there is then a bijective correspondence between vectors in V and the 1-forms in V^*. Because we can define an *orthonormal basis* of vectors such that $(|a'\rangle \cdot |a\rangle) = 1$ if $|a'\rangle = |a\rangle$ and $(|a'\rangle \cdot |a\rangle) = 0$ otherwise, we can then identify a 1-form $\langle a|$ that operates the exact same way on vectors as $(|a'\rangle \cdot \quad)$ does. Then we can rewrite the inner product $(|a'\rangle \cdot |a\rangle) = \langle a'|a\rangle$ with the same properties.

If the vector space is also endowed with a metric, $\eta_{\mu,\nu}$, the inner product between a^μ and b^ν may also be written as $a^\mu \eta_{\mu,\nu} b^\nu$, implying a metric-dependent correspondence between 1-forms a_μ and b^ν such that $a_\mu b^\nu = a^\mu \eta_{\mu,\nu} b^\nu$. In the case of Euclidean space, the metric is simply the 3×3 identity matrix, so we may then write $a_\mu b^\nu = \delta^\mu_\nu$

Definition A *tensor* is a multilinear map, $T : V^* \times \cdots \times V^* \times V \times \cdots \times V \to F$, that transforms under rotations as $T^{i_1 \cdots i_n}_{i_n+1 \cdots i_m} \mapsto (R^{-1})^{i_1}_{j_1} \cdots (R^{-1})^{i_n}_{j_n} R^{j_{n+1}}_{i_{n+1}} \cdots R^{j_m}_{i_m} T^{j_1 \cdots j_n}_{j_n+1 \cdots j_m}$, where summation over repeated indices is assumed. An order-m tensor of type $(n, m-n)$, having n contravariant indices and $m-n$ covariant indices maps n copies of V^* and m copies of V onto F.

Here we point out that geometric vectors, covectors, and scalars are actually all examples of geometric tensors, differing only by their rank. A vector is a type $(1, 0)$ tensor, a covector is a type $(0, 1)$ tensor, and a scalar can be thought of as a type $(0, 0)$ tensor. It is also immediately apparent that a scalar is invariant under rotations, as the definition above becomes $T^0_0 \mapsto T^0_0$ for a type $(0, 0)$ tensor. We also see that the product of a covector with a vector is a scalar, as expected from the definition of a covector, because $T^0_i T^i_0 \mapsto (R^{-1})^i_j R^j_i T^0_j T^j_0 = T^0_j T^j_0$.

Reducible Cartesian Tensors

This (Cartesian) approach to tensor analysis does, however, have certain limitations, as some potentially intuitive aspects of the geometric interpretation become muddled. For example, the identity matrix (of any rank, in any number of dimensions) is by definition a tensor, but it is also invariant under rotations, which makes it seem rather more like a scalar. Another common example is that of a "dyadic," an easily constructed tensor of the form $a^i b^j$. In Euclidean 3-space, this may be written as

$$a^i b^j = \begin{pmatrix} a^1 b^1 & a^1 b^2 & a^1 b^3 \\ a^2 b^1 & a^2 b^2 & a^2 b^3 \\ a^3 b^1 & a^3 b^2 & a^3 b^3 \end{pmatrix}. \tag{2.1}$$

Clearly $a^i b^j$ is a rank-2 tensor. However, while the entire tensor transforms as a rank-2 tensor should, it can be rewritten as

$$a^i b^j = \frac{a^i b^j + a^j b^i}{2} + \frac{a^i b^j - a^j b^i}{2}, \tag{2.2}$$

where the first term is symmetric under exchange of indices, and the second is antisymmetric. This may be extended further to write

$$a^i b^j = \frac{a^i b^j \delta^j_i}{3} + \frac{a^i b^j - a^j b^i}{2} + \left(\frac{a^i b^j + a^j b^i}{2} - \frac{a^i b^j \delta^j_i}{3} \right), \tag{2.3}$$

where the first term transforms as a scalar, the second term transforms as an antisymmetric rank-1 tensor, and the third term transforms as a symmetric and traceless rank-2 tensor. The first term has only one independent component, the second has three independent components, and the third has five independent components. Our dyadic tensor is therefore reducible to three different tensors that transform differently under rotations! The idea of tensors that may also be referred to as scalars is somewhat disconcerting, and furthermore, easily leads to major confusion (particularly for those of us who are not mathematicians). While this may not necessarily be a common issue in quantum mechanical practice, it still seems that a resolution of this increasingly opaque problem is needed.

More on Tensors

As we attempt to clarify our definitions, we will adapt some of the language from Misner, Thorne, and Wheeler's seminal book on differential geometry (and, of course, general relativity) [11], where tensors are defined as "machines" that take a certain set of inputs to produce a certain kind of output. Vectors can then be treated as any kind of object satisfying earlier definitions, including arrows pointing between two points in Euclidean space (or two events in space-time), a tangent vector, basis states of a quantum system, etc.. A 1-form is then a machine that takes a vector as its input and outputs a number (specifically, an element of the field over which the vector space is defined). Conveniently, we can also define vectors and 1-forms in a coordinate-free fashion such that a vector $\boldsymbol{v} = v^i \boldsymbol{e}_i$ or a 1-form $\boldsymbol{\alpha} = \alpha_i \boldsymbol{f}_i$, where $\boldsymbol{e}_i$ are the basis vectors (which, potentially confusingly, are 1-forms) and $\boldsymbol{f}^i$ are the basis 1-forms (again, note that they are vectors) for a given rest frame. A tensor of type (n, m) is a linear machine with "slots" for n 1-forms and m vectors. In a specific rest frame, we can define basis vectors and 1-forms such that the components of the tensor $\boldsymbol{S}$ are

$$S^{\alpha\beta}_{\gamma} \equiv \boldsymbol{S}(\boldsymbol{f}^{\alpha}, \boldsymbol{f}^{\beta}, \boldsymbol{e}_{\gamma}), \tag{2.4}$$

where $\boldsymbol{S}$ is a type $(2, 1)$ tensor. Then the output for actual 1-forms and vectors is

$$\boldsymbol{S}(\boldsymbol{\phi}, \boldsymbol{\psi}, \boldsymbol{v}) = \boldsymbol{S}(\phi_{\alpha}\boldsymbol{f}^{\alpha}, \psi_{\beta}\boldsymbol{f}^{\beta}, v^{\gamma}\boldsymbol{e}_{\gamma}) = \phi_{\alpha}\psi_{\beta}v^{\gamma}\boldsymbol{S}(\boldsymbol{f}^{\alpha}, \boldsymbol{f}^{\beta}, \boldsymbol{e}_{\gamma}) = S^{\alpha\beta}_{\gamma}\phi_{\alpha}\psi_{\beta}v^{\gamma}. \tag{2.5}$$

That the output of Eq. (2.5) is a scalar reinforces a fact about tensors that may have been missed previously: a tensor of any rank other than zero may be *contracted* to a tensor of lower rank by summing over repeated indices. For example the type $(3, 1)$ tensor $\boldsymbol{R}$ with components R^{ijk}_{i} is by definition equivalent to the type $(2, 0)$ tensor with components R^{jk}.

There are several other ways to produce tensors from other tensors – we will only discuss a few relevant ones, while others are listed in Ref. [11]. One method that we have already used implicitly is the *tensor product*, defined for two vectors as $\boldsymbol{T} = \boldsymbol{u} \otimes \boldsymbol{v}$, which produces a tensor with components $T^{ij} = u^i v^j$. As with the dyadic example, this can be written in terms of a symmetric product and an antisymmetric product: $\boldsymbol{T} = \frac{1}{2}(\boldsymbol{u} \otimes \boldsymbol{v} + \boldsymbol{v} \otimes \boldsymbol{u}) + \frac{1}{2}(\boldsymbol{u} \otimes \boldsymbol{v} - \boldsymbol{v} \otimes \boldsymbol{u})$.

The antisymmetric term of the tensor product is also referred to as the *exterior product* and may be written as $\boldsymbol{u} \wedge \boldsymbol{v} = \boldsymbol{u} \otimes \boldsymbol{v} - \boldsymbol{v} \otimes \boldsymbol{u}$. When the exterior product acts on two vectors, it produces a *bivector*, which may be visualized as an oriented two-dimensional surface. The orientation is dependent on the ordering of the terms, so $\boldsymbol{u} \wedge \boldsymbol{v} = -\boldsymbol{v} \wedge \boldsymbol{u}$. Because orientation implies a sense of rotation, bivectors are related to rotations in that bivectors generate rotations through an exponential map (more specifically, they generate rotations in three-dimensions and Lorentz transformations in four-dimensional Minkowski space-time). Furthermore, the bivector algebra is isomorphic to the quaternion algebra, which is unsurprising considering the connection to rotations. Bivectors are also associated with *axial vectors* (or *pseudovectors*) by way of an isomorphism provided by the Hodge dual. That is to say that both bivectors and pseudo vectors transform like rotations under proper rotations, but change sign relative to vectors under improper rotations, such as reflections.

The exterior product of two 1-forms is a 2-form given by $\boldsymbol{\alpha} \wedge \boldsymbol{\beta} = \boldsymbol{\alpha} \otimes \boldsymbol{\beta} - \boldsymbol{\beta} \otimes \boldsymbol{\alpha}$. 2-forms are somewhat more difficult to visualize, but may be thought of as a machine that takes a surface (consider the connection to bivectors) as an input and outputs a scalar. While we will not make significant use of such objects in this thesis, two-forms are of immense value in the relativistic theory of the electromagnetic force. For example, the electromagnetic field tensor is defined as $\boldsymbol{F} = \frac{1}{2} F_{\alpha\beta}\, \boldsymbol{d}x^\alpha \wedge \boldsymbol{d}x^\beta$ (where $\boldsymbol{d}x^\alpha$ are basis 1-forms in the language of the exterior calculus of differential forms), allowing the electromagnetic field equations to be written succinctly as $\boldsymbol{dF} = 0$ and $\boldsymbol{d}{}^*\boldsymbol{F} = 4\pi\, {}^*\boldsymbol{J}$ where ${}^*\boldsymbol{F}$ is the dual of $\boldsymbol{F}$, and ${}^*\boldsymbol{J} = \frac{1}{6} J^\alpha \epsilon_{\alpha\beta\gamma\sigma} \boldsymbol{d}x^\beta \wedge \boldsymbol{d}x^\gamma \wedge \boldsymbol{d}x^\sigma$ is the current 3-form.

The symmetric *interior product* of two vectors is given as $\boldsymbol{u} \circ \boldsymbol{v} = \boldsymbol{u} \otimes \boldsymbol{v} + \boldsymbol{v} \otimes \boldsymbol{u}$. The symbol $\circ$ is used to differentiate the interior product, which produces a rank-2 tensor that transforms like a scalar, from the inner product, which produces an actual scalar. The tensor produced by the interior product may be transformed into the scalar produced by the inner product by contraction with the metric.

Irreducible Spherical Tensors

Having now established some of the tools of tensor analysis, we return to the problem of our reducible tensors that seem confusingly to sometimes also be vectors or scalars. The answer, perhaps unsurprisingly, lies in the awareness that the Cartesian basis is not generally well-suited for describing rotational symmetry – describing tensors in the spherical basis is far more appropriate! We will denote contravariant spherical tensors of rank (k) and index q as $\boldsymbol{T}_q^{(k)}$. A vector $\boldsymbol{v}$, which in three-dimensional Euclidean space can be expressed as

$$\boldsymbol{v} = v^x \boldsymbol{e}_x + v^y \boldsymbol{e}_y + v^z \boldsymbol{e}_z \tag{2.6}$$

can be expressed in the spherical basis as

$$\boldsymbol{v} = v^+ \boldsymbol{e}_+ + v^- \boldsymbol{e}_- + v^0 \boldsymbol{e}_0, \tag{2.7}$$

where the spherical basis vectors may be written in terms of the Cartesian basis vectors as

$$\begin{aligned} \boldsymbol{e}_0 &= \boldsymbol{e}_z, \\ \boldsymbol{e}_\pm &= \mp \frac{1}{\sqrt{2}} \left(\boldsymbol{e}_x \pm i \boldsymbol{e}_y \right). \end{aligned} \tag{2.8}$$

A spherical tensor $\boldsymbol{T}_q^{(k)}$ may then be written by simply constructing it out of spherical vectors (a similar procedure may be used to produce covariant or mixed-type spherical tensors by including spherical 1-forms). For the dyadic tensor $a^i b^i$ we can then write the irreducible tensor components as

$$\begin{aligned}
T_0^{(0)} &= \frac{(a^+b^- + a^-b^+ - a^0b^0)}{3}, \\
T_0^{(1)} &= \frac{(a^+b^- - a^-b^+)}{2}, \\
T_{\pm1}^{(1)} &= \frac{(a^\pm b^0 - a^0b^\pm)}{2}, \\
T_0^{(2)} &= \frac{(a^+b^- + 2a^0b^0 + a^-b^+)}{\sqrt{6}}, \\
T_{\pm1}^{(2)} &= \frac{(a^\pm b^0 + a^0b^\pm)}{\sqrt{2}}, \\
T_{\pm2}^{(2)} &= a^\pm b^\pm.
\end{aligned} \tag{2.9}$$

We will consider additional details of spherical tensors, in terms of quantum mechanical spherical tensor operators in Section 2.3.7.

2.2.3 Representation Theory Basics

In order to connect the abstract notions of group theory to more concrete physical systems, we consider *representations* of group elements as linear transformations of vector spaces. This effectively transforms group theory into linear algebra, which is generally more cognitively comfortable. Formally, a representation ρ of a group G on a vector space V is a group homomorphism from G to the general linear group on V, i.e.

$$\rho : G \to \mathrm{GL}(V)$$

such that

$$\rho(g_1g_2) = \rho(g_1)\rho(g_2), \quad \forall g_1g_2 \in G$$

For example, consider the finite point group C_{2v}, which is composed of four symmetry operations: the identity operation (**E**), a twofold symmetry axis (**C₂**), and two orthogonal mirror planes ($\sigma_\mathbf{v}$ and $\sigma'_\mathbf{v}$). We can then define ρ_m as a representation of this group over three-dimensional Euclidean space such that each operation corresponds to a 3 × 3 matrix:

$$\begin{array}{c|cccc}
C_{2v} & \mathbf{E} & \mathbf{C_2} & \sigma_\mathbf{v} & \sigma'_\mathbf{v} \\
\hline
\rho_m & \begin{pmatrix} 1 & 0 & 0 \\ 0 & 1 & 0 \\ 0 & 0 & 1 \end{pmatrix} & \begin{pmatrix} -1 & 0 & 0 \\ 0 & -1 & 0 \\ 0 & 0 & 1 \end{pmatrix} & \begin{pmatrix} 1 & 0 & 0 \\ 0 & -1 & 0 \\ 0 & 0 & 1 \end{pmatrix} & \begin{pmatrix} -1 & 0 & 0 \\ 0 & 1 & 0 \\ 0 & 0 & 1 \end{pmatrix}
\end{array}.$$

As another example, consider the infinite group of 2 × 2 orthogonal matrices with determinant +1, which is referred to as SO(2). This group may be represented as the set of two-dimensional rotation matrices,

$$R(\theta) = \begin{pmatrix} \cos\theta & -\sin\theta \\ \sin\theta & \cos\theta \end{pmatrix}.$$

Note that as SO(2) is an infinite group, this representation is also infinite. Additionally, the representations are parametrized by the angle θ, which may be smoothly varied to give any representation of the group. Multiplication in SO(2) corresponds to simply adding the angles, and inversion corresponds to a rotation in the opposite direction (i.e. by a negative angle), both of which are differentiable maps. SO(2) is thus an example of a Lie group.

2.2.4 Some Comments on Topology

For a more complete description of topics in algebraic topology, the reader is referred to Nakahara's *Geometry, Topology, and Physics*[12], Nash and Sen's *Geometry and Topology for Physicists*[13], and Frankel's *The Geometry of Physics: An Introduction*[14]. Here we only briefly touch on a few relevant definitions to help clarify a few relatively opaque topics that will influence our discussion in the next section.

A *manifold* is a topological space that is locally Euclidean, so that each point of an n-dimensional manifold has a neighborhood that is homeomorphic to $\mathbb{R}^n$. Then there is a *chart* at each point which is an invertible map between the manifold in neighborhood of said point and $\mathbb{R}^n$. The set of charts covering a manifold is called an *atlas*. As an example, the plane $\mathbb{R}^2$ is an example of a manifold, which may be charted by polar coordinates (with the exception of the positive x-axis and origin).

A *smooth manifold* (or *differentiable manifold*) is a manifold for which overlapping charts are smoothly compatible in such a way that the manifold is locally similar enough to a linear space to allow for differential calculus to be performed. That is, the transition between charts is differentiable, so the manifold must have a globally defined differential structure.

Lie groups are an important example of groups that are also differentiable manifolds. As a result, one can define a space of infinitesimal linear elements of the group localized at the identity element of the group, which is the corresponding *Lie algebra* of the group. Specifically, this may be treated as the tangent space at the identity. Because the elements of the Lie algebra have a differential relationship to the Lie group, the Lie algebra $\mathfrak{g}$ can be thought of as the elements X for which $\exp(tX) \in G$ for all t. Because of this connection, there is a one-to-one correspondence between the representations of a Lie algebra and the representations of the corresponding Lie group. The *center* of a Lie algebra $\mathfrak{g}$ consists of all elements $x \in \mathfrak{g}$ such that $[x, g] = 0$ for all $g \in \mathfrak{g}$.

We can also define the connectivity of a manifold (or any topological space). A *connected space* is a topological space that cannot be represented as the union of two or more disjoint nonempty open subsets. A *path-connected space* is a topological space where any two points in the space can be connected by a continuous function, or path. A topological space is *simply connected* if it is path-connected and every path between any two points can be continuously transformed within the space into any other path without moving the endpoints (the paths are then *homotopic* and the mapping between one path and another is a *homotopy*). An equivalent definition is that a space is simply connected if any closed path (i.e. a loop) can be smoothly contracted to a point. For example, the surface of a 3-dimensional ball is simply connected, but a torus is not simply-connected (imagine contracting a string tied around a donut such that the string goes through the hole).[1]

---

[1] I feel that I am obligated by topological tradition to point out that in terms of connectivity and homotopy, a donut

It is also possible to define a continuous map p from a topological space C to a topological space X such that each point in X has an open neighborhood evenly covered by p. The topological space C is then called the *covering space* of X, and the homeomorphic copies in C of an evenly covered neighborhood U are called the *sheets* over U. One example is that every space is trivially a cover of itself (with a single sheet). A more useful example is that SU(2) is the double cover of SO(3) (double cover meaning that there are two sheets). If a covering space is simply connected, it is a *universal covering space*. If X is a Lie group, then so is its universal covering group, and the mapping p is a group homomorphism. This is useful for quantum mechanics because representations of the universal covering group are projective representations of the classical group X.

We will also mention an interesting theorem from algebraic topology: *there is no nonvanishing continuous tangent vector field on even-dimensional* n*-spheres* [15].[2] As a result, it is not possible to define a smooth set of frames in all tangent spaces on even-dimensional n-spheres, so such manifolds (e.g. S^2) cannot be a Lie group manifold. We will see the influence of this theorem indirectly in our search for the symmetry-based origins of spin.

2.2.5 Spin and the Poincaré Group

One of the most fascinating developments in physics and mathematics of the 20th century is that particle Hilbert spaces are group representations of the symmetry group, G, of the universe (technically, projective Hilbert spaces are projective group representations of G, but one may generally neglect this minor subtlety). Because each type of particle corresponds to a representation of G, if we can classify the group representations of G, we can develop a powerful intuition about the possibilities and properties of particle Hilbert spaces, and thus the kinds of particles that can exist. This very connection between symmetry and physics is the basis for virtually all of modern particle physics, particularly the Standard Model. In fact, it essentially means that all we need to do to fully understand fundamental physics is to fully understand the symmetry of the universe.

Of course, the fact that not all problems in physics have been solved, and physicists are still doing research is fairly strong evidence that we do not, in fact fully understand fundamental physics. By extension, we can conclude that we do not fully understand the symmetry of the universe. While this may be disheartening to readers who were hoping that one small section of a chemistry Ph.D. dissertation would present a conclusive unified theory of physics, it is not at all surprising – the universe is notoriously difficult to understand, so we do not know all of the symmetries of the universe, or, for that matter, how the symmetries that we *do* know about all fit together. We have, however, determined a large number of apparent symmetries, which we may use to inform our current understanding of physics.

The symmetry group in which we are particularly interested for the purpose of this section is the group of isometries of space-time. For those of us who try to spend as little time as possible a long distance away from black holes or other particularly massive objects, we may generally approximate our local space-time geometry as Minkowski space [16] (technically, local space-

---

and coffee cup are topologically equivalent.

[2] This is often stated in more amusing language as “you can’t comb flat the hair on a coconut.”

time geometries are always isomorphic to Minkowski space so long as one avoids singularities or non-simply connected locales). We may define this space as a 4-dimensional manifold where distances between points are computed in terms of the differential length

$$ds^2 = -d\boldsymbol{e}_0^2 + d\boldsymbol{e}_1^2 + d\boldsymbol{e}_2^2 + d\boldsymbol{e}_3^2, \tag{2.10}$$

where $\boldsymbol{e}_0$ is the basis vector corresponding to time (which may be written $\boldsymbol{e}_0 = c \cdot t$ for those who prefer to set the speed of light to something other than $c = 1$), and $\boldsymbol{e}_i$ are the spatial basis vectors.

The group of isometries that leave ds^2 invariant is called the *Poincaré Group* [17], and is made up of ten basic group generators: translations in time, translations in one of the three spatial dimensions, rotations about any of the three spatial axes, or Lorentz boosts in any of the three spatial dimensions. Following the group axioms presented earlier, the product of any two isometries is also an isometry, and there is always an inverse that can be applied to an isometry to yield the identity. The Lie algebra of the Poincaré group is the Poincaré algebra, given by the following commutation relationships:

$$\begin{aligned}
\left[P_\mu, P_\nu\right] &= 0, \\
\left[M_{\mu\nu}, P_\rho\right] &= \eta_{\mu\rho} P_\nu - \eta_{\nu\rho} P_\mu, \\
\left[M_{\mu\nu}, M_{\rho\sigma}\right] &= \eta\mu\rho M_{\nu\sigma} - \eta\mu\sigma M_{\nu\rho} - \eta\nu\rho M_{\mu\sigma} + \eta\nu\sigma M_{\mu\rho},
\end{aligned} \tag{2.11}$$

where P is the generator of translations, M is the generator of Lorentz transformations, and η is the Minkowski metric. If we write rotations as $J_i = \epsilon_{imn} M^{mn}/2$ and boosts as $K_i = M_{i0}$, we can write this in a potentially more understandable form

$$\begin{aligned}
[J_m, P_n] &= i\epsilon_{mnk} P_k, \\
[J_i, P_0] &= 0, \\
[K_i, P_k] &= i\eta_{ik} P_0, \\
[K_i, P_0] &= -P_i, \\
[J_m, J_n] &= i\epsilon_{mnk} J_k, \\
[J_m, K_n] &= i\epsilon_{mnk} K_k, \\
[K_m, K_n] &= -i\epsilon_{mnk} J_k.
\end{aligned} \tag{2.12}$$

The Poincaré algebra has two Casimir invariants, $P_\mu P^\mu$ and $W_\mu W^\mu$, where P^μ is the four-momentum (the generator of translations), and W_μ is the *Pauli-Lubanski pseudovector*, defined as

$$W_\mu \equiv \frac{1}{2} \epsilon_{\mu\nu\rho\sigma} J^{\nu\rho} P^\sigma, \tag{2.13}$$

where $J^{\nu\rho}$ is the angular momentum tensor, which should not be confused with the J_i of Eq. (2.12). The Casimir invariants are members of the center of the universal enveloping algebra and, by definition, commute with all other elements of the Poincaré algebra. Because in any irreducible representation of a Lie algebra the Casimir operators are proportional to the identity (Schur's Lemma [18]), the constant of proportionality can be used to classify the representations of said Lie algebra, and by extension, its Lie group. In other words, the eigenvalues of the Casimir operators of a Lie algebra serve as indices of the irreducible representations of the Lie group.

In the case of the Poincaré algebra, the first Casimir invariant $P_\mu P^\mu$ has eigenvalues of mass, so one of the indices of the irreducible representations of the Poincaré group is mass, corresponding to the rest mass of a particle. In fact, we can write

$$P_\mu P^\mu = \eta_{\mu\nu} P^\mu P^\nu = |\mathbf{p}|^2 - \frac{E^2}{c^2} = -m^2 c^2, \tag{2.14}$$

where $\mathbf{p}$ is the 3-momentum, showing that the invariance of $P_\mu P^\mu$ directly leads to conservation of mass!

In the case of a massive particle, the Casimir invariant $W_\mu W^\mu$ has eigenvalues $W_\mu W^\mu = -m^2 s(s+1)$, where s is some kind of mysterious parameter that we refer to as "spin." The reason for its name is that if we look at the rest frame of the particle, $W^i = J^i$ and $W^0 = 0$, so $W_\mu W^\mu = -m^2 \mathbf{J}^2$, showing the connection to the 3-dimensional rotation group SO(3), which has Casimir invariant $\mathbf{J}^2$.

For massive particles in their rest frame, i.e. the non-relativistic case, we may consider spin in terms of SO(3). Perhaps the most important aspect for our purposes is that SO(3) is not simply connected, [3] so unlike geometric vectors, the irreducible representations that we are looking for are actually sensitive to the different homotopy classes of the underlying topology. Therefore, in order to determine the irreducible representations of SO(3), we consider the universal covering group, SU(2), which is diffeomorphic to the sphere S^3 (the 3-dimensional surface of a 4-dimensional ball), and is thus simply connected. More specifically, we will consider $\mathfrak{su}(2)$, the Lie algebra of SU(2), which is spanned by three elements J_+, J_-, and J_z with Lie brackets

$$[J_z, J_+] = J_+, \;\; [J_z, J_-] = -J_-, \;\; [J_+, J_-] = J_z. \tag{2.15}$$

We may then generalize the notion of eigenvalues of the representations of the algebra, called weights. If x is an eigenvector with weight α, then

$$\begin{aligned} J_z[x] &= \alpha x, \\ J_z[J_+[x]] &= (\alpha + 1)x, \\ J_z[J_-[x]] &= (\alpha - 1)x, \end{aligned} \tag{2.16}$$

showing that $J_\pm$ may simply be treated as ladder operators, and J_z used to read out the weight. As stated earlier, $\mathbf{J}^2 = J_z^2 + J_+J_- + J_-J_+$ is a Casimir invariant, and commutes with all other generators of the algebra. Furthermore, the action of $\mathbf{J}^2$ is proportional to the identity map for irreducible representations, with this proportionality constant written as $\lambda(\lambda + 1)$. For the representation x with the greatest weight, α_1, such that $J_+[x] = 0$, it is easily shown that

$$\left(J_z^2 + J_+J_- + J_-J_+\right) x = (\alpha_1^2 + \alpha_1)x = \lambda(\lambda + 1)x = \mathbf{J}^2 x, \tag{2.17}$$

---

[3] To see this, consider holding a half-filled glass of whiskey in your hand. It is possible to rotate the glass by 360°, without spilling any of your whiskey, by rotating your arm at the elbow such that your forearm passes either above or below your elbow, leaving your arm twisted. It is in fact impossible to smoothly deform your arm back to its untwisted state without rotating more about your elbow, or spilling your whiskey (obviously unacceptable). The only options to return to the original state are to rotate backward for an overall rotation of 0°, or to continue the rotation forward for an overall rotation of 720°.

so that α_1 equals either λ or $-(\lambda+1)$. For the representation x with the lowest weight, α_2, where $J_-[x]=0$, it may be similarly shown that $(\alpha_2^2-\alpha_2)x=\lambda(\lambda+1)x$, so α_2 equals either $-\lambda$ or $\lambda+1$.

For irreducible finite-dimensional representations, the highest weight must be greater than the lowest weight, and the difference between the two must be an integer. Considering the possible values for α_1 and α_2, this means that the highest weight must be λ and the lowest weight must be $-\lambda$. Based on these constraints, it is immediately apparent that the smallest non-zero weight representation of SU(2), and thus SO(3), is the fundamental representation with $\lambda=\frac{1}{2}$. It may be easily shown that states that transform under this representation acquire a phase shift following a rotation by 360°, and are only returned to their initial state by a 720° rotation [see, for example, Ref. [19]], thus corresponding to spin-$\frac{1}{2}$ fermions. Representations with $\lambda=1$ (the adjoint representations) are also faithful representations of SO(3), and correspond to massive spin-1 particles as well as 3-dimensional rotations. All representations with higher λ are faithful representations of SO(3), and are generally used to refer to composite particles/states.

The reader curious about the representations of spin *not* in the particle's rest frame[4] is referred to Section 19.3 of Frankel's *The Geometry of Physics: An Introduction*[14], which considers the topology of the Lorentz group.[5] The essential result is that the Lorentz group has double cover $\mathrm{SL}(2,\mathbb{C})$. Also, the complexification of the Lie algebra of the Lorentz group, $\mathfrak{so}(3,1)_C$ is isomorphic to $\mathfrak{sl}(2,\mathbb{C})\oplus\mathfrak{sl}(2,\mathbb{C})$ [20]. The representations $\pi_{(m,n)}:\mathfrak{so}(3,1)\to\mathfrak{gl}(V)$ are given in terms of the generators of rotations J_i and of boosts K_i by

$$\pi_{(m,n)}(J_i)=\mathbb{1}_{(2m+1)}\otimes J_i^{(n)}+J_i^{(m)}\otimes\mathbb{1}_{(2n+1)} \tag{2.18}$$

$$\pi_{(m,n)}(K_i)=i\left(\mathbb{1}_{(2m+1)}\otimes J_i^{(n)}-J_i^{(m)}\otimes\mathbb{1}_{(2n+1)}\right), \tag{2.19}$$

where the $\mathbf{J}^{(n)}=\left(J_1^{(n)},J_2^{(n)},J_3^{(n)}\right)$ are the $(2n+1)$-dimensional irreducible spin-n representations of $\mathfrak{su}(2)$ and $\mathbb{1}_n$ is the n-dimensional identity matrix (see Section 5.6 of Ref. [21]). Then $\pi_{(0,0)}$ is the Lorentz scalar representation and $\pi_{(\frac{1}{2},\frac{1}{2})}$ is the four-vector representation. $\pi_{(\frac{1}{2},0)}$ is the left-handed Weyl spinor representation, $\pi_{(0,\frac{1}{2})}$ is the right-handed Weyl spinor representation, and $\pi_{(\frac{1}{2},0)}\oplus\pi_{(0,\frac{1}{2})}$ is the Dirac bispinor representation [22]. The left- and right-handed representations are particularly important when considering the weak nuclear force, which only interacts with left-handed particles and right-handed antiparticles [23, 24, 25].

2.2.6 Nucleon Spin

All matter that is stable enough to be studied by chemistry consists of atoms having nuclei composed of two kinds of *nucleons*, protons and neutrons. Protons and neutrons are *baryons*,

---

[4] Generally not of practical importance for NMR, except for in cases where the weak nuclear force plays a role (important for possible measurements of parity violation), or of course, in cases where the sample and magnet are moving at relativistic speeds with respect to each other. The author is unaware of any examples of such a configuration, though it would be an impressive sight. Measurement of astronomical phenomena involving relativistic spins in strong magnetic fields (e.g. near to magnetars or supermassive black holes) may be possible, though strong gravitational effects altering space-time topology would have to be considered.

[5] For the mathematically talented (or masochistic) reader, Section 19.5 considers spin topology in *curved* space-time.

meaning that their properties are primarily determined by three valence quarks. Furthermore, protons and neutrons exist in the ground state having baryons angular momentum $L = 0$, so the total angular momentum of either nucleon is determined by its spin, which must be based on its constituent quarks. Quarks are massive spin-$\frac{1}{2}$ fundamental particles which possess an electric charge (weak hypercharge in the electroweak theory), a weak isospin, and a strong color charge, thus allowing quarks to interact with all four known fundamental forces. There are six different types of quark (up, down, strange, charm, top, and bottom), but the valence quarks of protons and neutrons are only up or down quarks. An up quark has electric charge $+\frac{2}{3}e$ (e is the charge of an electron) and a down quark has electric charge $-\frac{1}{3}e$. Specifically, a proton has two up valence quarks and a down valence quark, yielding a total electric charge of $+e$, and a neutron has one up valence quark and two down valence quarks, and so has a total electric charge of 0.

The total spin of a baryon is determined by the total spin of its constituent quarks. If one assumes that all "sea quarks" (non-valence quarks) are paired, then a baryon may only have a total spin of $\frac{1}{2}$ or $\frac{3}{2}$. Indeed, protons and neutrons are both spin-$\frac{1}{2}$ particles, though recent results from deep inelastic scattering experiments on polarized nuclear targets [26] indicate that the projections of valence quark spins add up in such a way that valence quarks only account for around one-third of the total proton spin, showing that the naive model is insufficient. In fact, it appears that one must include the relativistic motion of the valence quarks, the pion cloud of the nucleon, and the virtual excitation of anti-quarks in low energy p-states through the one-gluon-exchange hyperfine interaction in order to understand the quark contribution to the proton spin [27]. The remaining spin is presumably carried by polarized gluons and quark/gluon orbital angular momentum, though the question remains open [28].

As such, though it is clearly the case that both protons and neutrons are spin-$\frac{1}{2}$ particles, it is not yet possible to completely determine the sources of this spin. This becomes particularly important when trying to determine the source of nuclear magnetic moments. For example, the magnetic moment of the up and down quarks, as fundamental spin-$\frac{1}{2}$ particles, should be

$$\begin{aligned} \boldsymbol{\mu}_u &= \frac{g_s e}{3m_u}\mathbf{S}, \\ \boldsymbol{\mu}_d &= -\frac{g_s e}{6m_d}\mathbf{S}, \end{aligned} \tag{2.20}$$

where we have assumed that the g-factor should be the same as for the electron, being determined entirely by quantum electrodynamics. The difficulty is that these equations imply "free" quarks, which cannot be measured due to asymptotic freedom, a property of the strong nuclear force. Related to this issue is the difficulty in accurately measuring masses for quarks, which are generally poorly defined due to the strong confinement by the fields of quantum chromodynamics. In fact, the majority of the mass of the proton is due to massless gluons, which contribute to the quantum chromodynamics binding energy, with valence quark mass (due to the Higgs mechanism) contributing only about 1% of the total mass. Even if the quark masses were known well, the strong coupling in the low-energy regime of quantum chromodynamics makes calculations much more complicated than simply adding up apparent quark magnetic moments. While advances in Lattice QCD may eventually yield *ab initio* calculations in agreement with nucleon magnetic moments, calculations for larger nuclei may remain non-trivial, so for the foreseeable future we will express nuclear magnetic moments in terms of the nuclear magneton, μ_N:

$$\boldsymbol{\mu}_I = \frac{g_I \mu_N \mathbf{I}}{\hbar}, \tag{2.21}$$

where g_I is the g-factor of the nuclear spin $\mathbf{I}$.

2.3 Nuclear Magnetic Resonance

Now we return to a much more tangible reality, introducing quantum mechanics as needed for the description of nuclear magnetic resonance experiments. Comments and tangents related to the preceding sections will generally be confined to footnotes for the convenience of the casual reader, as the deeper fundamental mathematical understanding is useful, but not *necessary*. For a more complete introduction to quantum mechanics, the reader is referred to Sakurai's *Modern Quantum Mechanics*[19], which is recommended in particular due to the exceptional treatment of angular momentum and symmetry.

2.3.1 Nuclear Spin States

Nuclei are composed of protons and neutrons, which are spin-$\frac{1}{2}$ particles. Thus nuclei with unpaired nucleons will themselves possess spin. The term *nuclear spin* refers to the total angular momentum of a nucleus, which may be determined from the nuclear shell model [29], which models nuclear structure via a deformed harmonic oscillator potential including spin-orbit coupling. For a trivial example, the unpaired proton of ^{1}H is in the $1s_{1/2}$ state, so the total nuclear spin is $\frac{1}{2}$. Similarly, for ^{13}C, the six protons are are all paired, with two in the $1s_{1/2}$ state and four in the $1p_{3/2}$ state. Six of ^{13}C's neutrons are also paired (in the same $1s_{1/2}$ and $1p_{3/2}$ states), but the seventh neutron is unpaired in a $1p_{1/2}$ state, yielding a nuclear spin of $\frac{1}{2}$. In general, one needs only consider the last unpaired nucleon (or nucleons), as all other spins will pair up. For example, the spin of ^{27}Al is $\frac{5}{2}$ because the 13th proton is in a $1d_{5/2}$ state, and all 14 neutrons are paired. It is also important to consider the case where a nucleus has an odd number of both protons and neutrons, such as ^{14}N, which has nuclear spin 1 because the seventh proton and the seventh neutron are both in $1p_{1/2}$ states. The nuclear magnetic moment of a nucleus with non-zero spin is then given by Eq. (2.21). However, in NMR it is typically convenient to rewrite the nuclear magnetic moment in terms of a nucleus' *gyromagnetic ratio*,

$$\gamma_I = \frac{g_I \mu_N}{\hbar}, \tag{2.22}$$

where g_I is the nuclear g-factor and μ_N is the nuclear magneton, such that the magnetic moment may be written in condensed form as

$$\boldsymbol{\mu}_I = \gamma_I \mathbf{I}. \tag{2.23}$$

The state of a spin-$\frac{1}{2}$ nuclear spin may be written as a two-component spinor,

$$|\psi\rangle = \begin{pmatrix} \alpha \\ \beta \end{pmatrix}, \tag{2.24}$$

where α is the projection of the state onto the basis spinor

$$|\alpha\rangle = \begin{pmatrix} 1 \\ 0 \end{pmatrix}, \tag{2.25}$$

and β is the projection of the state onto the basis spinor

$$|\beta\rangle = \begin{pmatrix}0\\1\end{pmatrix}, \tag{2.26}$$

such that

$$|\psi\rangle = \alpha\begin{pmatrix}1\\0\end{pmatrix} + \beta\begin{pmatrix}0\\1\end{pmatrix}. \tag{2.27}$$

α and β are in general complex scalars, and are typically normalized such that $|\alpha|^2 + |\beta|^2 = 1$. In this notation, $|\psi\rangle$ is called a *ket*, and $|\alpha\rangle$, $|\beta\rangle$ are the *basis kets* for the vector space H. By defining an inner product operation, thus making our vector (ket) space a Hilbert space, we can further show that our basis is *orthonormal*,

$$|\alpha\rangle \cdot |\beta\rangle = \delta_{\alpha\beta}. \tag{2.28}$$

We may also define a dual space with elements

$$\langle\psi| = \begin{pmatrix}\alpha^* & \beta^*\end{pmatrix}, \tag{2.29}$$

where α^* is the projection of the covector onto the basis form

$$\langle\alpha| = \begin{pmatrix}1 & 0\end{pmatrix}, \tag{2.30}$$

and β^* is the projection of the covector onto the basis form

$$\langle\beta| = \begin{pmatrix}0 & 1\end{pmatrix}, \tag{2.31}$$

such that

$$\langle\psi| = \alpha^*\begin{pmatrix}1 & 0\end{pmatrix} + \beta^*\begin{pmatrix}0 & 1\end{pmatrix}. \tag{2.32}$$

Here $\langle\psi|$ is called a *bra*, and $\langle\alpha|$, $\langle\beta|$ are the *basis bras* for the dual space H^*. Furthermore, having defined the inner product space before, we can establish a correspondence between the bra and ket spaces such that

$$\langle\alpha|\beta\rangle = |\alpha\rangle \cdot |\beta\rangle = \delta_{\alpha\beta}. \tag{2.33}$$

The dual correspondence is generally defined in terms of the Hermitian conjugate, such that $\langle\psi| = |\psi\rangle^\dagger$ and α^* and β^* are the complex conjugates of α and β, respectively.

The Hilbert space describing a composite system of two (or more) spins is simply formed by the tensor product of the component spaces. For two spins, $H_{12} = H_1 \otimes H_2$, so the the basis kets may be defined in terms of

$$|\alpha\alpha\rangle = |\alpha\rangle\otimes|\alpha\rangle = \begin{pmatrix}1\\0\\0\\0\end{pmatrix},\ |\alpha\beta\rangle = |\alpha\rangle\otimes|\beta\rangle = \begin{pmatrix}0\\1\\0\\0\end{pmatrix},\ |\beta\alpha\rangle = |\beta\rangle\otimes|\alpha\rangle = \begin{pmatrix}0\\0\\1\\0\end{pmatrix}, |\beta\beta\rangle = |\beta\rangle\otimes|\beta\rangle = \begin{pmatrix}0\\0\\0\\1\end{pmatrix}, \tag{2.34}$$

and the basis of the dual space H_{12}^* may be readily formed via Hermitian conjugation of these basis vectors.

2.3.2 Operators

An *operator*, $\hat{A}$, is a function over the state of physical states. Any physical observable, A is associated with a self-adjoint linear operator with real eigenvalues, otherwise referred to as a *Hermitian* operator.[6] An operator may also be thought of as a "machine" that acts on a state vector to yield another state vector multiplied by a scalar. For an eigenket $|\phi\rangle$ of $\hat{A}$,

$$\hat{A}\,|\phi\rangle = a\,|\phi\rangle\,, \tag{2.35}$$

where a is the eigenvalue of $\hat{A}$, corresponding to the measured value of the observable A on the state $|\phi\rangle$. The expectation value of the observable A for a physical state $|\psi\rangle$ is

$$\langle A\rangle = \frac{\left\langle\psi|\hat{A}|\psi\right\rangle}{\langle\psi|\psi\rangle}, \tag{2.36}$$

where the denominator is equal to one may be omitted if the state vector is normalized. This condition is not generally necessary, but it does substantially clean up notation, so we will typically endeavor to use normalized vectors whenever possible.

It should be noted that operators may act on either bras or kets, acting on bras to the operator's left and on kets to the operator's right. So for an eigenket $|\phi\rangle$ of $\hat{A}$ with eigenvalue a, there also exists an eigenbra $\langle\phi|$ such that

$$\langle\phi|\,\hat{A} = a\,\langle\phi|\,, \tag{2.37}$$

due to the dual correspondence between the bra and ket spaces.

An important detail about operators is that they do not in general commute, so $\hat{A}\hat{B}\,|\psi\rangle \neq \hat{B}\hat{A}\,|\psi\rangle$. There is a super-operator, called the *commutator* that acts on operators such that

$$\left[\hat{A},\hat{B}\right] = \hat{A}\hat{B} - \hat{B}\hat{A}. \tag{2.38}$$

If the commutator of $\hat{A}$ and $\hat{B}$, $\left[\hat{A},\hat{B}\right] = 0$, then $\hat{A}$ and $\hat{B}$ are said to commute. It is worth noting that the commutator of two operators is itself an operator,

$$\left[\hat{A},\hat{B}\right]|\psi\rangle = \hat{A}\hat{B}\,|\psi\rangle - \hat{B}\hat{A}\,|\psi\rangle\,, \tag{2.39}$$

an important detail that will be of use in the study of angular momenta.

A particular operator that will be of fundamental importance is the *Hamiltonian*, $\mathcal{H}$, corresponding to the total energy of the system. Its eigenvalues are the energy levels and its eigenstates are the energy eigenstates of the system. This may be expressed as the time-independent Schrödinger equation:

$$\mathcal{H}\,|n\rangle = E_n\,|n\rangle\,. \tag{2.40}$$

The Hamiltonian is also extremely important for the description of a system's dynamics, because it is in general the generator of time-evolution, as per the time-dependent Schrödinger equation:

$$-i\hbar\frac{\partial}{\partial t}\,|\psi\rangle = \mathcal{H}\,|\psi\rangle\,. \tag{2.41}$$

---

[6] Outside of this section, we will frequently drop the "hat" from operators for notational convenience where there is no ambiguity between an observable and the corresponding operator.

From Wigner's Theorem, symmetry transformations on a quantum mechanical Hilbert space are represented by either unitary or antiunitary operators.[7] A *unitary* operator $\hat{U}$ is defined such that

$$\hat{U}^\dagger \hat{U} = \hat{U}\hat{U}^\dagger = \mathbb{1}, \tag{2.43}$$

where $\mathbb{1}$ is the identity operator. An equivalent definition also includes the fact that a unitary operator $\hat{U}$ preserves the inner product of the Hilbert space,[8] such that

$$\hat{U}\left|\phi\right\rangle \cdot \hat{U}\left|\psi\right\rangle = \left\langle\phi\right| \hat{U}^\dagger \hat{U} \left|\psi\right\rangle = \left\langle\phi|\psi\right\rangle = \left|\phi\right\rangle \cdot \left|\psi\right\rangle. \tag{2.44}$$

For infinitesimal transformations, a unitary operator may be written in the form

$$\hat{U}(\epsilon) = \mathbb{1} + \epsilon\hat{G} + O\left(\epsilon^2\right), \tag{2.45}$$

where $\mathbb{1}$ is the identity operator, ϵ is an infinitesimal parameter, $\hat{G}$ is called the *generator* of the transformation, and we can comfortably neglect higher order terms in ϵ. A finite transformation may then be expressed in terms of an infinite product of infinitesimal transformations,

$$\hat{U}(\theta)\left|\psi\right\rangle = \lim_{N\to\infty}\left[\mathbb{1} + \left(\frac{\theta}{N}\right)\hat{G}\right]^N \left|\psi\right\rangle, \tag{2.46}$$

which can be rewritten as an exponential:

$$\hat{U}(\theta)\left|\psi\right\rangle = e^{\theta\hat{G}}\left|\psi\right\rangle. \tag{2.47}$$

We will return to this definition of transformations as unitary operators later in Section 2.3.6.[9]

---

[7] An antiunitary operator $\hat{\Upsilon}$ is a bijective antilinear map such that

$$\hat{\Upsilon}\left|\phi\right\rangle \cdot \hat{\Upsilon}\left|\psi\right\rangle = \left|\psi\right\rangle \cdot \left|\phi\right\rangle = \left\langle\psi|\phi\right\rangle = \left\langle\phi|\psi\right\rangle^*. \tag{2.42}$$

The only notable antiunitary operator that shows up with any frequency in quantum mechanics is the time-reversal symmetry operator, which will not be used much in this dissertation.

[8] It should be pointed out for the mathematically interested reader that unitary operators therefore represent automorphisms of the Hilbert space, because they preserve the structure of the space and map from the Hilbert space to itself.

[9] We would also be remiss if we were to fail to comment on the immensely important connection from unitary transformation operators and their generators to Lie groups and Lie algebras. Because they are built from infinitesimal transformations, these unitary operators necessarily form a group that is also a differentiable manifold. By the definitions of Eqs. (2.45) and (2.46), multiplication and inversion must be smooth maps, so the group of transformations $\hat{U}(\theta)$ is a Lie group. Then the operator $\hat{G}$ is a generator of the corresponding Lie algebra $\mathfrak{g}$, such that the exponentiation in Eq. (2.47) is precisely the exponential map from a Lie algebra to the Lie group. The effects of multiple symmetry transformations may thus be studied in terms of the corresponding Lie algebras. This is particularly useful when the Lie bracket corresponds to the commutator of Eq. (2.38), such as for the study of three-dimensional rotations, where the generators are angular momentum operators, which generate a Lie algebra isomorphic to $\mathfrak{su}(2)$.

2.3.3 Density Matrix

Most NMR measurements are concerned not with the state of a single spin (or composite spin system), but with an ensemble of spins (or composite spin systems) large enough to be described by statistical distributions. If $|\psi_i\rangle$ is some set of normalized kets, where i is a discrete index to which probabilities $f_i \geq 0$ are assigned such that

$$\sum_i f_i = 1, \tag{2.48}$$

then the expectation value of an arbitrary operator is given by

$$\langle A\rangle = \sum_i f_i \langle\psi_i|A|\psi_i\rangle\,. \tag{2.49}$$

This expectation value can be rewritten in terms of the *density operator* ρ, defined in the discrete case by

$$\rho = \sum_i f_i \,|\psi_i\rangle\,\langle\phi_i|\,, \tag{2.50}$$

so that

$$\langle A\rangle = \mathrm{Tr}(\rho A). \tag{2.51}$$

Despite the apparent simplicity of this definition, the density operator contains a complete and minimal description of the information available about a given ensemble of identically prepared systems.

For a pure spin-$\frac{1}{2}$ state with $m_s = +\frac{1}{2}$, the density operator is $\rho = |\alpha\rangle\,\langle\alpha|$, which may be written as the outer product of the vector in Eq. (2.25) and the covector in Eq. (2.30):

$$\rho = \begin{pmatrix} 1 & 0 \\ 0 & 0 \end{pmatrix}. \tag{2.52}$$

An equal mixture of up and down spin states, on the other hand, would have the density operator

$$\rho = \begin{pmatrix} \frac{1}{2} & 0 \\ 0 & \frac{1}{2} \end{pmatrix}, \tag{2.53}$$

which, it is worth noting, is proportional to the identity matrix, and thus invariant to rotations.

It should also be pointed out that the density operator is Hermitian, nonnegative definite, and has unit trace. One may then consider its eigenkets $|n\rangle$ with eigenvalues p_n, such that

$$\rho\,|n\rangle = p_n\,|n\rangle\,. \tag{2.54}$$

Also, because ρ is nonnegative definite, we can write

$$\langle n|\,\rho\,|n\rangle = p_n \geq 0, \tag{2.55}$$

and because $\operatorname{Tr}\rho = 1$,

$$\sum_n p_n = 1. \tag{2.56}$$

As a result, we can treat these nonnegative numbers, p_n that sum to unity as probabilities, so an arbitrary density operator can be expressed in terms of a discrete orthonormal set of pure states.

We can also describe coherent superpositions of energy eigenstates in terms of a pure state of the form

$$|\psi\rangle = \sum_n c_n |n\rangle . \tag{2.57}$$

The density operator is then

$$\rho = |\psi\rangle \langle\psi| = \sum_{nm} c_n c_m^* |n\rangle \langle m| , \tag{2.58}$$

which, it should be noted, differs from our previous definition due to the inclusion of off-diagonal terms. It can be shown (see Section 2.3.6) that the time evolution of such a state can be written in terms of the time evolution of the coefficients c_n,

$$c_n(t) = c_n(0)e^{-iE_n t/\hbar}, \tag{2.59}$$

where E_n is the energy eigenvalue of state $|n\rangle$. The density matrix may then be written as

$$\rho(t) = \sum_{nm} |c_n(0)|\, |c_m(0)|\, e^{-i(E_n-E_m)t/\hbar} |n\rangle \langle m| . \tag{2.60}$$

For the diagonal terms, $E_n - E_n = 0$, meaning that they do not experience coherent evolution. For this reason, the diagonal terms of the density matrix are commonly referred to as *populations*, while the off-diagonal terms are called *coherences*. In the absence of other interactions, coherences should persist more or less indefinitely, but in practice, incoherent fluctuations of the energy eigenvalues E_n and E_m lead to a randomization of the phase, so that averaging over the entire ensemble leads to an elimination of coherences at thermal equilibrium. This process is commonly referred to as *dephasing* of the coherence.

At thermal equilibrium, the density operator for an ensemble with Hamiltonian $\mathcal{H}$ is in an *incoherent* superposition of energy eigenstates,

$$\rho = \frac{e^{-\frac{\mathcal{H}}{k_B T}}}{\operatorname{Tr} e^{-\frac{\mathcal{H}}{k_B T}}} = \sum_n \frac{e^{-\frac{E_n}{k_B T}}}{\Xi} |n\rangle \langle n| , \tag{2.61}$$

where k_B is the Boltzmann constant, T is the temperature of the system, and $\Xi = \operatorname{Tr} e^{-\mathcal{H}/k_B T}$ is the partition function of the ensemble.

For nuclear spins in a magnetic field, the population difference between the $m_s = \pm\frac{1}{2}$ states is given by the Boltzmann distribution, and is worked out in Chapter 4. For convenience, we will just refer to the polarization as P_0 such that the density matrix for an ensemble of uncoupled thermally polarized nuclear spins is

$$\rho = \frac{1}{2}\left[(1 + P_0)\,|\alpha\rangle \langle\alpha| + (1 - P_0)\,|\beta\rangle \langle\beta|\right] = \frac{1}{2}\left(|\alpha\rangle \langle\alpha| + |\beta\rangle \langle\beta|\right) + \frac{P_0}{2}\left(|\alpha\rangle \langle\alpha| - |\beta\rangle \langle\beta|\right), \tag{2.62}$$

which may be rewritten in terms of spin operators as

$$\rho = \frac{\mathbb{1}}{2} + P_0 I_z, \tag{2.63}$$

where $\mathbb{1}$ is the identity operator, and

$$I_z = \frac{1}{2}\begin{pmatrix} 1 & 0 \\ 0 & -1 \end{pmatrix} \tag{2.64}$$

is the nuclear spin projection operator on the z axis (equivalent to the Pauli matrix σ_z multiplied by one-half). Because thermal polarization in a magnetic field yields populations that can be described by I_z, it should be pointed out that coherences can then be described by a linear combination of I_x and I_y, defined as

$$I_x = \frac{1}{2}\begin{pmatrix} 0 & 1 \\ 1 & 0 \end{pmatrix}, \; I_x = \frac{1}{2}\begin{pmatrix} 0 & -i \\ i & 0 \end{pmatrix}, \tag{2.65}$$

which leads to the semi-classical description of NMR in terms of precessing vectors.[10]

2.3.4 High-Field and Zero-Field Energy Eigenstates

In order to ensure that the diagonal elements of a density operator do in fact represent stationary populations under the Hamiltonian of a given system, it is necessary that the density operator is defined in terms of the energy eigenstates. That is, it is preferable that the density matrix is defined $\rho = \sum_{nm} c_n c_m^* |n\rangle\langle m|$ where $|n\rangle$ and $|m\rangle$ are eigenstates of $\mathcal{H}$. For illustration we will consider an ensemble of two coupled nuclei **I** and **S** with $\gamma_I \neq \gamma_S$, in two different conditions: in the presence of a large external magnetic field (high-field), and in the absence of an applied field (zero-field).[11]

The high-field basis consists of the eigenstates of the high-field Hamiltonian, of which the Zeeman interaction is dominant. The high-field Hamiltonian may be written as

$$\mathcal{H}_Z + \mathcal{H}_{CS} = -\hbar \sum_j \gamma_j \mathbf{I}_j \cdot (\mathbf{1} - \boldsymbol{\sigma}) \cdot \mathbf{B}_0 \tag{2.66}$$

where

$$\mathcal{H}_Z = -\hbar \sum_j \gamma_j \mathbf{I}_j \cdot \mathbf{B}_0, \tag{2.67}$$

---

[10] It is occasionally noted that the ability to write a density operator in terms of the identity matrix and Pauli spin operators is trivial, because the density operator is a Hermitian operator and the set composed of the identity matrix and the Pauli matrices is the minimal basis for the construction of Hermitian operators. Moreover, *any* Hermitian matrix of *any* size may be constructed from tensor products of these four matrices. What is noted much less frequently is that this means that because any quantum mechanical ensemble has a Hermitian density operator and interacts according to a Hermitian Hamiltonian, the NMR spin formalism is totally general and can be extended to *any* system. Of course, while it would certainly work, it won't necessarily make anything easier. Still, once it's worked out, the ability to visualize a system's dynamics in terms of precessing spins can afford a powerful intuitive understanding of the system.

[11] The necessity of considering different basis constructions for the coupling of angular momenta in different perturbative regimes has been treated extensively in the past, a notable example being L-S vs. j-j coupling in the spin-orbit coupling of atomic states. There is also a particularly strong correspondence between the treatment presented here and that used to describe the Paschen-Back effect [30].

where γ_j is the gyromagnetic ratio of $\mathbf{I}_j$ and $\mathbf{B}_0$ is the external magnetic field, is the Zeeman Hamiltonian for a bare nucleus, which is modified by the chemical shift

$$\mathcal{H}_{CS} = \hbar \sum_j \gamma_j \mathbf{I}_j \cdot \boldsymbol{\sigma} \cdot \mathbf{B}_0, \tag{2.68}$$

where the chemical shielding tensor $\boldsymbol{\sigma}$ describes the effect of electrons producing counteracting magnetic fields that "shield" the nucleus from the external field. Because $\mathcal{H}_{CS}$ is typically 5-6 orders of magnitude smaller than $\mathcal{H}_Z$, and we will not be particularly concerned with the interpretation of high-field NMR spectra, we can safely consider the high-field Hamiltonian to be dominated by $\mathcal{H}_Z$. For two spins in a field aligned along the z-axis,

$$\mathcal{H}_Z = -\hbar \left(\gamma_I I_z + \gamma_S S_z\right) B_0 \tag{2.69}$$

Because the interaction with the magnetic field is much stronger than the interaction between the spins, the *uncoupled* basis is most appropriate, which has states written as $|M_I M_S\rangle$ that we will frequently done with up/down arrows as $|\uparrow\uparrow\rangle$, $|\uparrow\downarrow\rangle$, $|\downarrow\uparrow\rangle$, and $|\downarrow\downarrow\rangle$. The energies of these states are then

$$\begin{aligned}
\langle\uparrow\uparrow|\mathcal{H}_Z|\uparrow\uparrow\rangle &= -\hbar\left(\gamma_I + \gamma_S\right) B_0 \\
\langle\uparrow\downarrow|\mathcal{H}_Z|\uparrow\downarrow\rangle &= -\hbar\left(\gamma_I - \gamma_S\right) B_0 \\
\langle\downarrow\uparrow|\mathcal{H}_Z|\downarrow\uparrow\rangle &= \hbar\left(\gamma_I - \gamma_S\right) B_0 \\
\langle\downarrow\downarrow|\mathcal{H}_Z|\downarrow\downarrow\rangle &= \hbar\left(\gamma_I + \gamma_S\right) B_0.
\end{aligned} \tag{2.70}$$

To describe the general elements of a high-field density matrix for two coupled spins, we need a total of 16 operators. These are comprised of the identity operator, six one-spin operators, and nine two-spin operators. The one-spin operators, in terms of the 2 × 2 Pauli matrices are

$$\begin{aligned}
I_x &= \tfrac{1}{4}\sigma_x \otimes \mathbb{1} & I_y &= \tfrac{1}{4}\sigma_y \otimes \mathbb{1} & I_z &= \tfrac{1}{4}\sigma_z \otimes \mathbb{1} \\
S_x &= \tfrac{1}{4}\sigma_x \otimes \mathbb{1} & S_y &= \tfrac{1}{4}\sigma_y \otimes \mathbb{1} & S_z &= \tfrac{1}{4}\sigma_z \otimes \mathbb{1}
\end{aligned} \tag{2.71}$$

and the two-spin operators are

$$\begin{aligned}
I_x S_x &= \tfrac{1}{4}\sigma_x \otimes \sigma_x & I_y S_x &= \tfrac{1}{4}\sigma_y \otimes \sigma_x & I_z S_x &= \tfrac{1}{4}\sigma_z \otimes \sigma_x \\
I_x S_y &= \tfrac{1}{4}\sigma_x \otimes \sigma_y & I_y S_y &= \tfrac{1}{4}\sigma_y \otimes \sigma_y & I_z S_y &= \tfrac{1}{4}\sigma_z \otimes \sigma_y. \\
I_x S_z &= \tfrac{1}{4}\sigma_x \otimes \sigma_z & I_y S_z &= \tfrac{1}{4}\sigma_y \otimes \sigma_z & I_z S_z &= \tfrac{1}{4}\sigma_z \otimes \sigma_z
\end{aligned} \tag{2.72}$$

At zero magnetic field, the primary interaction for an isotropic liquid is the J-coupling (described more thoroughly in the next section), so the Hamiltonian has the form

$$\mathcal{H}_J = \hbar J_{IS} \mathbf{I} \cdot \mathbf{S}, \tag{2.73}$$

which, unlike Eq. (2.69), is spherically symmetric. Because there is no longer an external field to impose axial symmetry on the system, the zero-field density matrix should not be diagonal in the

z projection of each spin, but in the total angular momentum $\mathbf{F}^2 = (\mathbf{I} + \mathbf{S})^2$, and the projection of $\mathbf{F}$ onto a conveniently chosen axis, F_z. The eigenstates of $\mathcal{H}_J$ are related to the high-field basis by the Clebsch-Gordan coefficients $\langle I S m_I m_S | F m_F \rangle$,

$$|F m_F\rangle = \sum_{m_I m_J} |I S m_I m_S\rangle \langle I S m_I m_S | F m_F \rangle \,, \tag{2.74}$$

such that the zero-field eigenstates are the singlet and triplet states:

$$\begin{array}{ccc} |T_+\rangle = |\uparrow\uparrow\rangle & |T_0\rangle = \frac{1}{\sqrt{2}}\left(|\uparrow\downarrow\rangle + |\downarrow\uparrow\rangle\right) & |T_-\rangle = |\downarrow\downarrow\rangle \\ & |S_0\rangle = \frac{1}{\sqrt{2}}\left(|\uparrow\downarrow\rangle - |\downarrow\uparrow\rangle\right) & \end{array} \,, \tag{2.75}$$

where the triplet states have total angular momentum $F = 1$ and the singlet has total angular momentum $F = 0$. Writing

$$\mathbf{F}^2 = (\mathbf{I} + \mathbf{S}) = \mathbf{I}^2 + \mathbf{S}^2 + 2\mathbf{I} \cdot \mathbf{S} \tag{2.76}$$

allows us to write the rewrite the zero-field Hamiltonian as

$$\mathcal{H}_J = \frac{\hbar J_{IS}}{2} \left(\mathbf{F}^2 - \mathbf{I}^2 - \mathbf{S}^2 \right), \tag{2.77}$$

so that the energies may be calculated as

$$\langle F m_F | \mathcal{H}_J | F m_F \rangle = \frac{\hbar J_{IS}}{2} \left[F(F+1) - I(I+1) - S(S+1) \right] = \frac{\hbar J_{IS}}{2} \left[F(F+1) - \frac{3}{2} \right]. \tag{2.78}$$

Thus the three triplet states are degenerate with energy $E_T = \hbar J_{IS}/4$, and the singlet has energy $E_S = -3\hbar J_{IS}/4$. Most of the systems studied so far in ZULF-NMR have a Hamiltonian dominated by a strong one-bond J-coupling, so we will generally make use of coupled bases of this form.

2.3.5 NMR Spin-Coupling Hamiltonians

We will now consider the Hamiltonians for some of the spin-coupling interactions that we will encounter in the remainder of this dissertation.

Direct Dipolar Spin-Spin Coupling

The Hamiltonian describing the direct dipole-dipole coupling of nuclear spins is in general given by

$$\mathcal{H}_D = \hbar \sum_{N;N'>N} \mathbf{I}_N \cdot \mathbf{D}_{NN'} \cdot \mathbf{I}_{N'}, \tag{2.79}$$

where $\mathbf{D}_{NN'}$ is a rank-2 symmetric tensor. Because the interaction is purely geometric, it is rarely specified in terms of the tensor itself, but expanded as

$$\mathcal{H}_D = -\hbar^2 \frac{\mu_0}{4\pi} \sum_{N;N'>N} \frac{\gamma_N \gamma_{N'}}{r_{NN'}^3} \left[3\left(\mathbf{I}_N \cdot \hat{\mathbf{r}}_{NN'}\right)\left(\mathbf{I}_{N'} \cdot \hat{\mathbf{r}}_{NN'}\right) - \mathbf{I}_N \cdot \mathbf{I}_{N'} \right], \tag{2.80}$$

where γ_N and $\gamma_{N'}$ are the gyromagnetic ratios of the two nuclei N and N', and $\mathbf{r}_{NN'}$ is the vector connecting the two nuclei.

For two spins **I** and **S**, the dipolar coupling may be further expanded in terms of irreducible spherical tensors:

$$\mathcal{H}_D = -\hbar^2 \frac{\mu_0 \gamma_I \gamma_S}{4\pi r_{IS}^3} \left(D_0^{(2)} + D_{+1}^{(2)} + D_{-1}^{(2)} + D_{+2}^{(2)} + D_{-2}^{(2)} \right) \tag{2.81}$$

where

$$D_0^{(2)} = \left(\frac{3\cos^2\theta - 1}{2} \right) \left[2I_z S_z - \frac{1}{2} \left(I_+ S_- + I_- S_+ \right) \right], \tag{2.82}$$

$$D_{\pm 1}^{(2)} = \frac{3}{2} \sin\theta \cos\theta e^{\mp i\phi} \left(I_z S_\pm + I_\pm S_z \right), \tag{2.83}$$

$$D_{\pm 2}^{(2)} = \frac{3}{4} \sin^2\theta e^{\mp 2i\phi} I_\pm S_\pm, \tag{2.84}$$

where θ is the polar angle and ϕ is the azimuthal angle of $\mathbf{r}_{IS}$ in spherical coordinates, with the principle axis defined by the geometry of the system (e.g. the magnetic field axis in high-field NMR, or the molecular principle axis system in ZULF-NMR). It is worth noting that the only component of the dipolar coupling Hamiltonian that commutes with the high-field Zeeman Hamiltonian in general is $D_0^{(2)}$, and for heteronuclear systems, the so-called "flip-flop" term, $\frac{1}{2}\left(I_+ S_- + I_- S_+ \right)$, does not commute, leaving only

$$\mathcal{H}_D^{HF,\,\text{hetero}} = -\hbar^2 \frac{\mu_0 \gamma_I \gamma_S}{4\pi r_{IS}^3} \left(3\cos^2\theta - 1 \right) I_z S_z, \tag{2.85}$$

where θ is the angle between the magnetic field axis and $\mathbf{r}_{IS}$.

This truncation does not occur in ZULF-NMR, so the form of $\mathcal{H}_D$ is determined entirely by the geometry of the sample. The case of weak alignment in anisotropic media is discussed in Chapter 7. In all other cases, the dipole-dipole coupling is averaged to zero by rapid isotropic molecular motion.

Indirect Spin-Spin Coupling

For the purpose of this dissertation, the most important spin-spin interaction is the electron-mediated indirect spin-spin coupling, typically referred to as the J-coupling. The J-coupling may be thought of as a second-order hyperfine effect, where one nucleus N affects the electronic state of a molecule through hyperfine couplings to the molecular electron density, and this perturbation is then transmitted from the molecular electronic state to a second nucleus N' through its hyperfine interaction with the molecular electron density. The Hamiltonian may be written in the form

$$\mathcal{H}_J = \hbar \sum_{N;N' \neq N} \mathbf{I}_N \cdot \mathbf{J}_{NN'} \cdot \mathbf{I}_{N'}, \tag{2.86}$$

where $\mathbf{I}_N$ and $\mathbf{I}_{N'}$ are the spins of nuclei N and N', and $\mathbf{J}_{NN'}$ is the second-rank J-coupling tensor. $\mathbf{J}_{NN'}$ may in general be represented as a sum of irreducible spherical tensors

$$\mathbf{J}_{NN'} = \mathbf{J}_{NN'}^{iso} + \mathbf{J}_{NN'}^{anti} + \mathbf{J}_{NN'}^{sym}, \tag{2.87}$$

where the isotropic component $\mathbf{J}^{iso}_{NN'}$ transforms as a scalar, the antisymmetric component $\mathbf{J}^{anti}_{NN'}$ transforms as a bivector (or pseudovector), and the symmetric component $\mathbf{J}^{sym}_{NN'}$ transforms as a symmetric rank-2 spherical tensor. The reason that the J-coupling is of particular value for ZULF-NMR (and, for that matter, HF-NMR) is that the isotropic component persists in liquid samples where rapid molecular tumbling averages higher-order tensors to zero. There is also substantial interest in the possibility of measuring the antisymmetric component of the tensor because the sense of rotation of a bivector may permit absolute measurements of chirality, although such experiments have not yet been conducted.

In order to focus on the influence of electronic structure on the indirect coupling tensor, we define the isotope-independent *reduced indirect coupling tensor*,

$$\mathbf{K}_{NN'} = \frac{4\pi^2 \mathbf{J}_{NN'}}{h\gamma_N \gamma_{N'}}, \tag{2.88}$$

where γ_N and $\gamma_{N'}$ are the gyromagnetic ratios of the two nuclei N and N'. The elements of the reduced indirect spin-spin coupling tensor may be identified as the mixed second derivatives of the total electronic energy of the system with respect to the magnetic moments of nuclei N and N' [31]:

$$\mathbf{K}_{NN'} = \left.\frac{\partial^2 E\left(\boldsymbol{\mu}_N, \boldsymbol{\mu}_{N'}, \cdots\right)}{\partial \boldsymbol{\mu}_N \partial \boldsymbol{\mu}_{N'}}\right|_{\mu_N=\mu_{N'}=\cdots=0} \tag{2.89}$$

The contributions to $\mathbf{K}_{NN'}$ may be broken down into the four “Ramsey” terms [32], the diamagnetic spin-orbit operator $\mathbf{h}^{\mathrm{DSO}}_{NN'}$, the paramagnetic spin-orbit operator $\mathbf{h}^{\mathrm{PSO}}_{N}$, the Fermi-contact operator $\mathbf{h}^{\mathrm{FC}}_{N}$, and the spin-dipole operator $\mathbf{h}^{\mathrm{SD}}_{N}$. These are given, in atomic units, as [33]

$$\mathbf{h}^{\mathrm{DSO}}_{NN'} = \alpha^4 \sum_k \frac{\mathbf{1}\,\mathbf{r}_{kN} \cdot \mathbf{r}_{kN'} - \mathbf{r}_{kN}\mathbf{r}_{kN'}}{r^3_{kN} r^3_{kN'}}, \tag{2.90}$$

$$\mathbf{h}^{\mathrm{PSO}}_{N} = -i\alpha^2 \sum_k \frac{\mathbf{r}_{kN} \times \nabla_k}{r^3_{kN}}, \tag{2.91}$$

$$\mathbf{h}^{\mathrm{FC}}_{N} = \frac{8\pi\alpha^2}{3} \sum_k \delta\left(\mathbf{r}_{kN}\right) \mathbf{s}_k, \tag{2.92}$$

$$\mathbf{h}^{\mathrm{SD}}_{N} = \alpha^2 \sum_k \frac{3\mathbf{r}_{kN} \cdot \mathbf{r}_{kN} - r^2_{kN}}{r^5_{kN}} \mathbf{s}_k, \tag{2.93}$$

where α is the fine-structure constant, $\mathbf{r}_{kN}$ is the position of electron k relative to nucleus N, $\mathbf{1}$ is the 3×3 identity matrix, $\delta\left(\mathbf{r}_{kN}\right)$ is the Dirac delta function, and $\mathbf{s}_k$ is the spin of electron k.

One may then calculate $\mathbf{K}_{NN'}$ for the non-relativistic closed-shell case using second-order perturbation theory [32]:

$$\mathbf{K}_{NN'} = \left\langle 0 \middle| \mathbf{h}^{\mathrm{DSO}}_{NN'} \middle| 0 \right\rangle - 2 \sum_{n_S \neq 0} \frac{\left\langle 0 \middle| \mathbf{h}^{\mathrm{PSO}}_{N} \middle| n_S \right\rangle \left\langle n_S \middle| \mathbf{h}^{\mathrm{PSO}}_{N'} \middle| 0 \right\rangle}{E_{n_S} - E_0}$$

$$- 2 \sum_{n_T} \frac{\left\langle 0 \middle| \mathbf{h}^{\mathrm{FC}}_{N} + \mathbf{h}^{\mathrm{SD}}_{N} \middle| n_s \right\rangle \left\langle n_s \middle| \left(\mathbf{h}^{\mathrm{FC}}_{N'}\right)^{\mathrm{T}} + \left(\mathbf{h}^{\mathrm{SD}}_{N'}\right)^{\mathrm{T}} \middle| 0 \right\rangle}{E_{n_T} - E_0}, \quad (2.94)$$

where $|0\rangle$ is the ground state, $|n_S\rangle$ are excited singlet states, $|n_T\rangle$ are excited triplet states, and superscript T denotes the tensor transpose.

For the isotropic case,

$$\mathcal{H}^{iso}_{J} = \hbar \sum_{N;N' \neq N} J^{iso}_{NN'} \mathbf{I}_N \cdot \mathbf{I}_{N'}, \quad (2.95)$$

we are only concerned with $K^{iso}_{NN'} = \frac{1}{3} \operatorname{Tr} \mathbf{K}_{NN'}$, which is generally dominated by the Fermi-contact interaction. The mixed Fermi-contact – spin-dipole and spin-dipole – Fermi-contact terms only contribute to the anisotropic part of $\mathbf{K}_{NN'}$, and can thus be omitted when considering the isotropic Hamiltonian.

Quadrupolar Coupling

The quadrupolar coupling Hamiltonian has the form

$$\mathcal{H}_Q(\Theta) = \frac{eQ}{2I(2I-1)} \mathbf{I} \cdot \mathbf{V}(\Theta) \cdot \mathbf{I}, \quad (2.96)$$

where e is the electric charge, Q is the nuclear quadrupole moment, I is the nuclear spin quantum number, and $\mathbf{V}(\Theta)$ is the electric field gradient tensor for an arbitrary molecular orientation Θ [34]. As a rank-2 interaction, the quadrupolar coupling is non-zero only for nuclei with spin $I \geq 1$. This is one of the notable advantages of studying spin-$\frac{1}{2}$ nuclei, because the the coupling of quadrupolar nuclei to the electric field gradient is a major source of relaxation, leading to short coherence times and thus to broad resonance lines.

Of particular use is the first-order quadrupolar Hamiltonian, which is used in Chapter 7 to obtain information about molecular alignment in anisotropic media from the quadrupolar splitting of deuterated molecules:

$$\mathcal{H}^{(1)}_{Q}(\Theta) = \left(\frac{3eQ\overline{V_{zz}}}{2I(2I-1)} \right) \frac{1}{6} \left[3\boldsymbol{I}_z^2 - I(I+1)\mathbb{1} \right], \quad (2.97)$$

where $\overline{V_{zz}}$ denotes the average of the electric field gradient component V_{zz} over molecular motion. $\overline{V_{zz}}$ may be rewritten as

$$\overline{V_{zz}} = \frac{\left\langle 3\cos^2\theta - 1 \right\rangle}{2} V_{zz} = S_{zz} V_{zz}, \quad (2.98)$$

where S_{zz} is the *order parameter* quantifying the anisotropic effect of the alignment medium on the molecular motion. More specifically, S_{zz} describes the extent to which the z-axis of the molecular principal axis system aligns with the lab-frame z-axis.

2.3.6 Time-Evolution

The time-evolution of a quantum can be described using unitary operators corresponding to the symmetry transformation of temporal translation. The unitary operator for time-evolution can easily be constructed using Eqs. (2.45)-(2.47), coupled with the knowledge that the generator of time-evolution is proportional to the Hamiltonian of the system. Specifically, the operator for an infinitesimal translation forward in time is

$$U(\epsilon) = \mathbb{1} - \frac{i\epsilon}{\hbar}\mathcal{H} + O\left(\epsilon^2\right), \tag{2.99}$$

and the finite time evolution may be written as

$$U(t)\left|\psi\right\rangle = e^{-i\mathcal{H}t/\hbar}\left|\psi\right\rangle. \tag{2.100}$$

In general, we are more interested in the evolution of a density operator, which at initial time t_0 may be written

$$\rho(t_0) = \sum_i f_i \left|\psi_i(t_0)\right\rangle \left\langle\psi_i(t_0)\right|. \tag{2.101}$$

Applying the time-evolution operator of Eq. (2.100) to the kets and its Hermitian conjugate to the bras, the density operator at a time t is then

$$\rho(t) = \sum_i f_i \left|\psi_i(t)\right\rangle \left\langle\psi_i(t)\right| = U(t)\left[\sum_i f_i \left|\psi_i(t)\right\rangle \left\langle\psi_i(t)\right|\right] U(t)^\dagger = U(t)\rho(t_0)U(t)^\dagger. \tag{2.102}$$

Differentiating this result, it can be shown that we can then write the time evolution of the density matrix in a form analogous to that of the classical Liouville equation:

$$i\hbar\frac{\partial\rho}{\partial t} = [\mathcal{H},\rho]. \tag{2.103}$$

For time-independent Hamiltonians, this is easily solved in terms of Eq. (2.102), such that we can write the value of the density operator at time t as

$$\rho(t) = e^{-i\mathcal{H}t/\hbar}\rho(t_0)e^{i\mathcal{H}t/\hbar}. \tag{2.104}$$

In the case of time-dependent Hamiltonians, a path integral formalism is necessary [35], but fortunately for us, most NMR experiments can be described piecewise using Eq. (2.104).[12]

---

[12] A deeper understanding of the evolution of a quantum system can be extracted from Eq. (2.103) if the density operator and Hamiltonian can both be written in terms of the generators of a Lie algebra – for NMR, this is usually $\mathfrak{su}(2)$ – in which case the commutator corresponds directly to the Lie bracket. In this case, the evolution of the system is fully described by the Lie algebra.

2.3.7 Rotations and the Wigner-Eckart Theorem

The generators of spatial rotations are the angular momentum operators $\mathbf{J}$, so the unitary operator describing an infinitesimal rotation about a unit vector $\hat{\mathbf{n}}$ is

$$U_\epsilon(\hat{\mathbf{n}}) = \mathbb{1} - \frac{i\epsilon}{\hbar}\hat{\mathbf{n}} \cdot \mathbf{J}, \tag{2.105}$$

allowing us to define the operator for a finite rotation θ as

$$U(\hat{\mathbf{n}}, \theta) = e^{-i\,\hat{\mathbf{n}}\cdot\mathbf{J}/\hbar}. \tag{2.106}$$

In the standard angular momentum basis, we may write the irreducible representations of the rotation operators as

$$D^j_{mm'}(\hat{\mathbf{n}}, \theta) = \langle jm|U(\hat{\mathbf{n}}, \theta)|jm'\rangle. \tag{2.107}$$

With this definition in hand, we can define an irreducible tensor operator of rank k as a set of $2k+1$ operators $T^{(k)}_q$ for $q = -k, \cdots, +k$ that satisfy

$$UT^{(k)}_q U^\dagger = \sum_{q'} T^{(k)}_{q'} D^k_{q'q}(U), \tag{2.108}$$

for all rotation operators U. Because this must hold for infinitesimal rotations, we may define a *scalar operator* as an operator K such that

$$[\mathbf{J}, K] = 0. \tag{2.109}$$

Similarly, a vector operator $\mathbf{V}$ must satisfy

$$\left[J_i, V_j\right] = i\hbar\epsilon_{ijk}V_k. \tag{2.110}$$

For a general irreducible tensor operator, we may write the following commutation relations with the components of the angular momentum operator:

$$\left[J_z, T^{(k)}_q\right] = \hbar q T^{(k)}_q, \tag{2.111}$$

$$\left[J_\pm, T^{(k)}_q\right] = \hbar\sqrt{(k \mp q)(k \pm q + 1)}T^{(k)}_{q\pm1}, \tag{2.112}$$

$$\sum_i \left[J_i, \left[J_i, T^{(k)}_q\right]\right] = \hbar^2 k(k+1)T^{(k)}_q. \tag{2.113}$$

We write the matrix elements of an irreducible spherical tensor operator using the Wigner-Eckart theorem:

$$\left\langle jm\middle|T^{(k)}_q\middle|j'm'\right\rangle = \left\langle j\middle\|T^{(k)}\middle\|j'\right\rangle \left\langle j'km'q\middle|jm\right\rangle, \tag{2.114}$$

where $\left\langle j'km'q\middle|jm\right\rangle$ is a Clebsch-Gordan coefficient, and $\left\langle j\middle\|T^{(k)}\middle\|j'\right\rangle$ is the *reduced matrix element*, which depends only on j, j', and k. The Clebsch-Gordan coefficient in Eq. (2.114) allows us to define selection rules for the matrix element based on the symmetry rules for Clebsch-Gordan coefficients. The selection rules are that $\left\langle jm \middle| T_q^{(k)} \middle| j'm' \right\rangle = 0$ unless $m' = m + q$ and j' takes one of the values, $|j - k|, \cdots, j + k - 1, j + k$. For the useful special case of a scalar operator,[13] T_0^0, $k = q = 0$, so

$$\left\langle jm \middle| T_0^{(0)} \middle| j'm' \right\rangle = \left\langle j \middle\| T^{(0)} \middle\| j' \right\rangle \delta_{j'j} \delta_{m'm}. \tag{2.115}$$

2.3.8 Example: Evolution of Two Coupled Spins in High-Field and Zero-Field Regimes

We will make use of some of these quantum mechanical tools to compare the evolution two coupled spins in the two natural regimes for NMR measurements, high-field and zero-field. In both cases, we will begin with the high-field thermally polarized density matrix:

$$\rho_0 = \frac{\mathbb{1}}{4} + \frac{\gamma_I B_0}{k_B T} I_z + \frac{\gamma_S B_0}{k_B T} S_z, \tag{2.116}$$

where γ_I is the gyromagnetic ratio of nucleus **I**, and γ_S is the gyromagnetic ratio of nucleus **S**. For the case of ^{1}H and ^{13}C, $\gamma_H / \gamma_C \approx 1/4$.

Two Coupled Spins in High Field

In a large applied magnetic field, the spin Hamiltonian is

$$\mathcal{H}_{HF} = -\hbar \left(\gamma_I I_z + \gamma_S S_z \right) B_0 + \hbar J_{IS} I_z S_z, \tag{2.117}$$

where we have neglected the effect of chemical shift, and we have included only the component of the J-coupling Hamiltonian that commutes with the dominant Zeeman term. In a typical high-field NMR experiment, a resonant RF pulse is applied that transforms the density matrix by effectively applying a $\pi/2$ rotation about the y axis (in the rotating frame) to the **I** nuclei.[14] This yields a new density operator,

$$\rho_1 = \frac{\mathbb{1}}{4} + \frac{\gamma_I B_0}{k_B T} I_x + \frac{\gamma_S B_0}{k_B T} S_z, \tag{2.118}$$

where the only difference is a rotation of I_z into I_x. As discussed previously, the I_x element of the density operator corresponds to a coherence, so this term evolves according to Eq. (2.103):

$$\rho(t) = e^{-i\mathcal{H}t/\hbar} \rho_1 e^{i\mathcal{H}t/\hbar} = \frac{\mathbb{1}}{4} + \frac{\gamma_I B_0}{k_B T} e^{-i\mathcal{H}t/\hbar} I_x e^{i\mathcal{H}t/\hbar} + \frac{\gamma_S B_0}{k_B T} S_z. \tag{2.119}$$

Considering first the effect of the Zeeman Hamiltonian, $\mathcal{H}_Z = -\hbar \left(\gamma_I I_z + \gamma_S S_z \right) B_0$, this yields

$$\rho(t) = \frac{\mathbb{1}}{4} + \frac{\gamma_I B_0}{k_B T} \left[I_x \cos\left(\gamma_I B_0 t\right) - I_y \sin\left(\gamma_I B_0 t\right) \right] + \frac{\gamma_S B_0}{k_B T} S_z, \tag{2.120}$$

---

[13] This is a particularly useful case due to the fact that the Hamiltonian for any isolated system is necessarily a scalar operator.

[14] Because of the resonant condition, **S** nuclei are unaffected.

where one might note that the identity term is unaffected, along with the term corresponding to nucleus **S**. Including the effect of the J-coupling, $\mathcal{H}_{J,HF} = \hbar J_{IS} I_z S_z$,

$$\rho(t) = \frac{\mathbb{1}}{4} + \frac{\gamma_I B_0}{k_B T}\Big[I_x \cos(\gamma_I B_0 t)\cos(\pi J_{IS} t) - I_y \sin(\gamma_I B_0 t)\cos(\pi J_{IS} t) + I_y S_z \cos(\gamma_I B_0 t)\sin(\pi J_{IS} t) + I_x S_z \sin(\gamma_I B_0 t)\sin(\pi J_{IS} t)\Big] + \frac{\gamma_S B_0}{k_B T} S_z. \tag{2.121}$$

The detectable signal is then

$$\mathcal{S}(t) = \mathrm{Tr}(\rho I_+) = \frac{\gamma_I B_0}{4\sqrt{2}k_B T}\left[e^{i(\gamma_I B_0 + \pi J_{IS})t} + e^{i(\gamma_I B_0 - \pi J_{IS})t}\right], \tag{2.122}$$

which, after Fourier transformation, yields the expected doublet centered at $\omega = \gamma_I B_0$, with the peaks separated by a frequency J_{IS}. The same experiment may be carried out by pulsing RF resonant with **S** nuclei, and detecting S_+ coherences.

Two Coupled Spins in Zero Field

As shown in Chapter 4, the non-identity components[15] of the density matrix in Eq. (2.116) after adiabatic transfer to zero-field may be rewritten in the zero-field basis as

$$\rho_0 = \delta(I_z + S_z) - \epsilon 2(I_x S_x + I_y S_y), \tag{2.123}$$

which we may rewrite in terms of "zero-quantum operators,"

$$\begin{aligned} Z_x &= 2(I_x S_x + I_y S_y), \\ Z_y &= 2(I_x S_y - I_y S_x), \\ Z_z &= (I_z - S_z), \\ D_z &= (I_z + S_z), \end{aligned} \tag{2.124}$$

yielding

$$\rho_0 = \delta D_z - \epsilon Z_x. \tag{2.125}$$

In a typical zero-field NMR experiment, a magnetic field pulse of length t_p is applied in the z direction, yielding

$$\rho_z = \delta D_z - \epsilon(\cos\alpha Z_x + \sin\alpha Z_y), \tag{2.126}$$

where $\alpha = 2\pi B_z t_p(\gamma_I - \gamma_S)$, and the D_z term is unaffected. Evolution under the full J-coupling Hamiltonian

$$\mathcal{H}_{ZF} = \hbar J_{IS} \mathbf{I} \cdot \mathbf{S}, \tag{2.127}$$

---

[15] One can generally disregard the identity component, because it commutes with everything and will thus never give rise to observable signal.

which persists at zero-field, yields

$$\rho_z(t) = \delta D_z - \epsilon \Big[\cos\alpha Z_x + \sin\alpha \cos(2\pi J_{IS} t)\, Z_y - \sin\alpha \sin(2\pi J_{IS} t) Z_z \Big]. \tag{2.128}$$

The observable magnetization is then

$$M_z(t) = Nh\, \mathrm{Tr}\{\rho(t)(\gamma_I I_z + \gamma_S S_z)\} = \frac{Nh}{2}\epsilon(\gamma_S - \gamma_I) \sin\alpha \sin(2\pi J_{IS} t), \tag{2.129}$$

which, after Fourier transformation, yields a single peak at J_{IS}.

The reader might note that this description of the evolution of two coupled spins at zero magnetic field is very similar to the one-spin case in high magnetic fields, replacing the high-field Zeeman Hamiltonian with Z_x, the RF pulse with a DC z pulse, I_x with Z_y, and I_y with Z_z. This is indeed the motivation for the introduction of the zero-quantum operators – the commutation relations for Z_x, Z_y, and Z_z are identical to those for I_z, I_x, and I_y, so the *algebra* of the operators is exactly the same. Furthermore, the evolution of zero-quantum coherences for a system composed of two coupled spins in zero-field NMR is isomorphic to the evolution of a single spin in high-field NMR![16] While the evolution of the zero-field coherences does not actually correspond to precession in physical 3-dimensional space, the description of the evolution as procession in the zero-quantum space provides a valuable visualization heuristic for ZULF-NMR experiments.

2.3.9 Chemical vs. Magnetic Equivalence

Two spins are *chemically equivalent* if they have the same precession frequency and are exchanged by a molecular symmetry operation. In high-field NMR, chemically equivalent spins are defined as having identical chemical shifts. Because this thesis is concerned with the zero- and ultra-low-field regime where chemical shift is negligible, we use a more general definition. It is, however, worth pointing out that in the absence of magnetic field, all spins have the same precession frequency, because $\omega = \gamma(1-\sigma)B_0 = 0$ regardless of chemical shielding or gyromagnetic ratio.

Two spins are *magnetically equivalent* if they are (1) chemically equivalent, (2) have the same gyromagnetic ratio, and (3) have identical couplings to *all other* spins in the molecule. This definition is important for the interpretation of ZULF-NMR spectra because J-couplings between magnetically equivalent spins are unobservable.

2.4 Zero- and Ultra-Low-Field NMR Definitions and Conventions

2.4.1 What is "Zero-Field"? What is "Ultra-Low-Field"?

"Zero-field" is defined as the regime of magnetic fields where the Zeeman Hamiltonian has no discernible effect on the coherent evolution of nuclear spins that gives rise to the NMR spectrum.

---

[16] For those keeping score, both operator algebras are isomorphic to $\mathfrak{su}(2)$, and exponentiation of the infinitesimal rotations in either space produces the group of SU(2) rotations.

To quantify this further, we may say that in the zero-field regime, the sum of all Larmor frequencies is substantially less than the inherent linewidth of spectral peaks, which is proportional to the inverse of the spin-spin relaxation time, T_2. That is, the magnetic field is small enough such that

$$|\boldsymbol{B}_0| \sum_j \gamma_j \ll \frac{1}{T_2}. \tag{2.130}$$

In other words, the "zero-field" regime refers to magnetic field strengths where there is no practical or experimental difference between the given situation and a situation where the magnetic field is identically zero.

"Ultra-low-field" is defined as the regime of magnetic fields where the Zeeman Hamiltonian may be treated as a first-order perturbation on the dominant spin-spin interaction Hamiltonian. In this dissertation, the dominant spin interaction is generally the J-coupling, so we may define the ultra-low-field regime for fields that satisfy

$$|\boldsymbol{B}_0| \sum_j \gamma_j \ll J_{\mathrm{AX}}, \tag{2.131}$$

where J_{AX} is the largest heteronuclear J-coupling in the system (typically a one-bond coupling).

2.4.2 Naming Conventions for Spin Systems

Because the chemical shift vanishes at zero field, such that all spins have equivalent Larmor frequencies $\omega_j = \gamma_j B_0 = 0$, all zero-field spin systems are at the strong-coupling limit. As a result, the standard Pople nomenclature [36, 37, 38] for high-field NMR no longer suffices. The simplest systems observable in ZULF-NMR consist of a set of magnetically equivalent spins A_n (typically ^{1}H nuclei) coupled to a heteronucleus X (e.g. ^{13}C, ^{15}N, ^{31}P, etc.) with $\gamma_A \neq \gamma_X$ by a J-coupling J_{AX}, and are denoted XA_n spin systems. Chapter 5 describes the zero-field J-spectra for such systems, along with other systems in which the XA_n energy levels are perturbed by an additional set of magnetically equivalent spins B_m with $\gamma_A = \gamma_B$. The perturbative description suffices when the condition $J_{\mathrm{AX}} \gg J_{\mathrm{BX}}, J_{\mathrm{AB}}$, and such systems are denoted $(\mathrm{XA}_n)\mathrm{B}_m$. The spin system within parentheses is the "strongly coupled" system, and the spins outside of the parentheses interact perturbatively with the strongly coupled system. Thus a system consisting of three strongly coupled spins X, A, and B, weakly coupled to three magnetically equivalent spins C_3 would be denoted $(\mathrm{XAB})\mathrm{C}_3$. Chemically equivalent spins that are not magnetically equivalent are denoted $\mathrm{B}_m\ \mathrm{B}'_{m'}$, such that benzene-^{13}C is an (XA)BB′CC′D spin system and ethylene glycol-$^{13}\mathrm{C}_2$ is an $(\mathrm{XA}_2)(\mathrm{X'A'_2})$ spin system.

The spin operator for nucleus X is $\mathbf{S}$, with eigenvalue S (typically $S = \frac{1}{2}$, with a few exceptions, such as $^{14}\mathrm{NH}_4^+$) and the total angular momentum spin operators for A_n, B_m, etc. nuclei are $\mathbf{K}_A = \sum_j \mathbf{I}_{A,j}$, $\mathbf{K}_B = \sum_j \mathbf{I}_{B,j}$, with eigenvalues K_A, K_B. The total angular momentum of the strongly coupled system (XA_n) is $\mathbf{F}_A = \mathbf{K}_A + \mathbf{S}$, and the total angular momentum of an $(\mathrm{XA}_n)\mathrm{B}_m$ is $\mathbf{F} = \mathbf{F}_A + \mathbf{K}_B$.

Chapter 3

Detection of Zero-Field NMR

In order to keep our signals high,
Rotating light measures spins alkali.
There is some affection
For inductive detection,
By at low-field it just won't comply.

This chapter explains the techniques by which ZULF NMR signal may be measured. This includes a brief overview of the challenges involved in zero-field detection, along with some of the techniques have historically been employed to overcome these challenges. The bulk of the chapter then focuses on optical magnetometry using alkali vapor cells, and some of the specifics of our ZULF NMR spectrometer apparatus. This chapter includes content from:

- Blanchard, J.W. and Budker, D. Zero-Field NMR. *Encyclopedia of Magnetic Resonance*. In Preparation.

3.1 NMR Detection

3.1.1 Inductive Detection

One of the primary difficulties in measuring magnetic resonance at zero field is that J-coupling and dipolar coupling frequencies are many orders of magnitude smaller than the Larmor frequency in high-field NMR. That this is an issue becomes apparent when considering Faraday's law of induction,

$$|\epsilon| \propto \frac{d\Phi}{dt} \propto \omega M_x, \tag{3.1}$$

where ϵ is the electromotive force on an inductive coil and Φ is the magnetic flux through the coil, which for the case of NMR is proportional to the product of the precession frequency ω and the transverse magnetization M_x. At high field, inductive coils are sensitive detectors of oscillating magnetic fields because the Larmor frequency is proportional to the magnetic field, but at zero field, where ^{1}H-^{13}C J-coupling frequencies are on the order of hundreds of Hz and dipolar couplings are on the order of tens of kHz, inductive detection is not sensitive enough to observe magnetic resonance signals. Moreover, the magnetization M_x is typically proportional to the magnetic field, as discussed in Chapter 4.

3.1.2 History of Zero-Field NMR Detection: Field Cycling

When zero-field NMR was first introduced in 1983 [39], experiments were performed by preparing sample magnetization in a high-field instrument, transferring the sample to a zero-field region, allowing the magnetization to evolve at zero-field for some time τ, and then returning the sample to high-field to measure the signal resulting from zero-field evolution over a time τ [40]. Acquisition of the full evolution thus required that the sample be cycled between high-field and zero-field many times, detecting the signal point-by-point.

3.1.3 History of Zero-Field NMR Detection: SQUIDs

The situation is radically different for magnetometers that do not rely on Faraday induction. A notable example is the superconducting quantum interference device (SQUID), described in great detail in [41]. Implementation of SQUID-detected zero-field NMR fundamentally changed the way that zero-field NMR was performed, eliminating the need to cycle between zero-field and high-field, thus increasing the accessibility of zero-field NMR. Such methods are still used for low-field NMR [42, 43, 44], and, particularly, for imaging applications [45, 46, 47, 48]. One drawback, however, is that SQUIDs must operate at cryogenic temperatures, limiting the potential for miniaturization and portability.

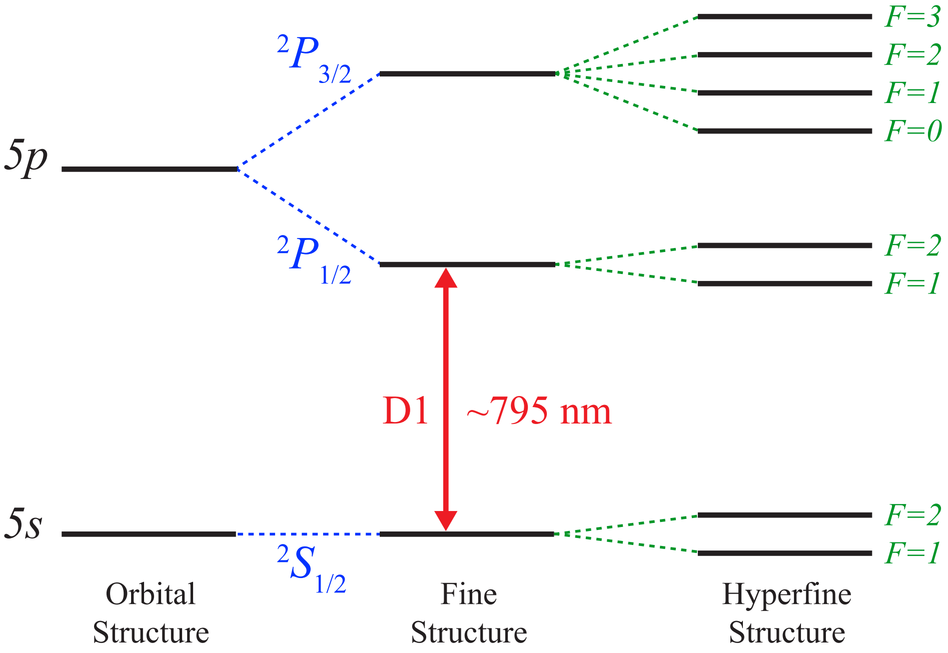

Figure 3.1: Energy levels of rubidium-87 including spin-orbit interactions (i.e. fine structure) and the hyperfine coupling to the nuclear spin.

3.2 Optical Magnetometry

Historically, the first non-inductive detector was an atomic magnetometer, where polarized ^{3}He atoms in a glass cell were detected via optically pumped Rb atoms in an adjacent cell [49]. Recent years have seen a revival of atomic magnetometry detection in NMR stimulated by developments in magnetometer technology. For NMR applications, the advent of spin-exchange relaxation free (SERF) magnetometry, allowing for unprecedented high sensitivity with a relatively small sensor, has been particularly influential [50].

3.2.1 Atomic States

The ground state and nearest excited state atomic energy levels for Rb-87 are shown in Fig. 3.1. The ground state valence electron is in a $5s$ orbital, and the lowest energy unoccupied orbital is $5p$. Including the effect of spin-orbit interactions, the $5s$ state is unaffected, but is relabeled using the term symbol $^2S_{1/2}$, and the $5p$ level splits into $^2P_{1/2}$ and $^2P_{3/2}$ states. The transition between $^2S_{1/2}$ and $^2P_{1/2}$ corresponds to light with a wavelength of 795 nm and is referred to as the D1 transition. Additional small splittings arise due to hyperfine coupling involving the Rb-87 nucleus, which has nuclear spin $I = 3/2$. For the purpose of this thesis, we may generally neglect the Rb-87 hyperfine effects.

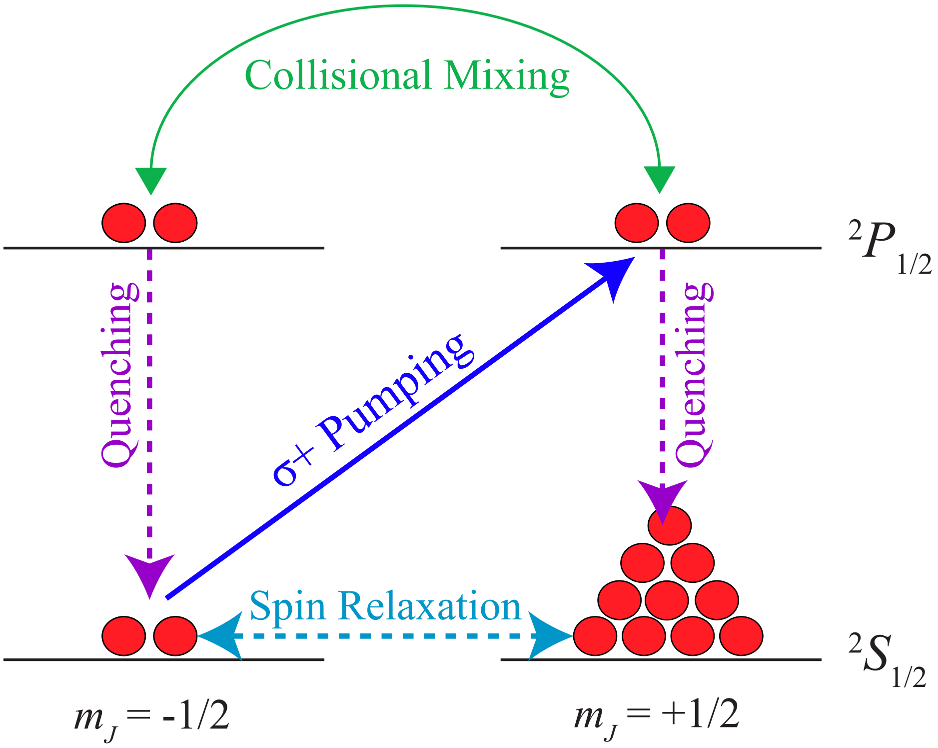

Figure 3.2: Optical pumping of the rubidium electron spin with D1 σ^+ circularly polarized light.

3.2.2 Optical Pumping

A general schematic diagram of the optical pumping process for rubidium atoms is shown in Fig. 3.2. 795 nm light directed in the $+y$ direction is used to excite the D1 transition from the $^2S_{1/2}$ ground state to the $^2P_{1/2}$ excited state. If the light is circularly polarized (here we describe σ^+ polarization, but the opposite handedness merely changes the sign), the photons carry $+1$ unit of angular momentum, so the only allowed transition is from $m_J = -\frac{1}{2}$ to $m_J = +\frac{1}{2}$, due to conservation of angular momentum. From the $^2P_{1/2}$ $m_J = +\frac{1}{2}$ state, the system may undergo collisional mixing to populate the $^2P_{1/2}$ $m_J = -\frac{1}{2}$ state, and quenching through interactions with buffer N_2 gas returns the Rb atoms to the ground state, conserving m_J. The rates of change of the spin state populations are

$$\frac{\mathrm{d}}{\mathrm{dt}}\rho\left(-\frac{1}{2}\right) = -2R_{\mathrm{OP}}\,\rho\left(-\frac{1}{2}\right) + 2(1-a)R_{\mathrm{OP}}\,\rho\left(-\frac{1}{2}\right), \tag{3.2}$$

$$\frac{\mathrm{d}}{\mathrm{dt}}\rho\left(+\frac{1}{2}\right) = +2aR_{\mathrm{OP}}\,\rho\left(-\frac{1}{2}\right), \tag{3.3}$$

where R_{OP} is the optical pumping rate and a is the optical pumping efficiency parameter, which can generally be set equal to 1/2, corresponding to the case of complete collisional mixing.

We may also define the spin polarization

$$\left\langle S_y \right\rangle = \frac{1}{2}\left[\rho\left(+\frac{1}{2}\right) - \rho\left(-\frac{1}{2}\right)\right] \tag{3.4}$$

such that

$$\frac{\mathrm{d}}{\mathrm{dt}}\left\langle S_y \right\rangle = \frac{1}{2}R_{\mathrm{OP}}\left(1 - 2\left\langle S_y \right\rangle\right), \tag{3.5}$$

where we have set $a = \frac{1}{2}$. If we include spin relaxation, this becomes

$$\frac{\mathrm{d}}{\mathrm{dt}}\left\langle S_y \right\rangle = \frac{1}{2}R_{\mathrm{OP}}\left(1 - 2\left\langle S_y \right\rangle\right) - R_{\mathrm{rel}}\left\langle S_y \right\rangle, \tag{3.6}$$

where R_{rel} is the relaxation rate. The equilibrium value is then

$$\left\langle S_y \right\rangle = \frac{1}{2}\frac{R_{\mathrm{OP}}}{R_{\mathrm{OP}} + R_{\mathrm{rel}}} \tag{3.7}$$

3.2.3 Magnetic Field Detection via Optical Rotation

In the presence of a magnetic field, an electron spin precesses as

$$\frac{\mathrm{d}}{\mathrm{dt}}\boldsymbol{S} = \frac{g_s\mu_{\mathrm{B}}}{\hbar(2I+1)}\boldsymbol{B}\times\boldsymbol{S}, \tag{3.8}$$

where g_s is the electron g-factor, μ_{B} is the Bohr magneton, and the factor $(2I + 1)$ is the "nuclear slowing down factor" due to coupling between the electron and nuclear spins.

The overall equation for the evolution of the atomic spin may then be written as

$$\frac{\mathrm{d}}{\mathrm{dt}}\boldsymbol{S} = \frac{1}{2I+1}\left[\frac{g_s\mu_{\mathrm{B}}}{\hbar}\boldsymbol{B}\times\boldsymbol{S} + R_{\mathrm{OP}}\left(\frac{1}{2}s\hat{\boldsymbol{y}} - \boldsymbol{S}\right) - R_{\mathrm{rel}}\boldsymbol{S}\right], \tag{3.9}$$

including the competing effects of optical pumping along the pumping axis (y), spin relaxation randomizing the spin direction, and spin precession induced by the magnetic field.

In the absence of a magnetic field, the equilibrium spin polarization is

$$S_0 = \frac{sR_{\mathrm{OP}}}{2\left(R_{\mathrm{OP}} + R_{\mathrm{rel}}\right)}. \tag{3.10}$$

In the limit of slowly varying magnetic fields (i.e. $\mathrm{d}\boldsymbol{S}/\mathrm{d}t = 0$), the steady state solution of Eq. (3.9) yields the following components of the spin:

$$S_x = S_0\frac{\beta_z + \beta_x\beta_y}{1 + \beta_x^2 + \beta_y^2 + \beta_z^2} \tag{3.11}$$

$$S_y = S_0\frac{1 + \beta_y^2}{1 + \beta_x^2 + \beta_y^2 + \beta_z^2} \tag{3.12}$$

$$S_z = S_0\frac{-\beta_x + \beta_x\beta_z}{1 + \beta_x^2 + \beta_y^2 + \beta_z^2}, \tag{3.13}$$

where, following Ref. [51], we have introduced the dimensionless magnetic field parameter $\boldsymbol{\beta}$ to clean up our notation,

$$\boldsymbol{\beta} = \left[\frac{g_s \mu_\mathrm{B}}{\hbar(R_\mathrm{OP} + R_\mathrm{rel})}\right] \boldsymbol{B}. \tag{3.14}$$

For a small field B_z orthogonal to the pump and probe directions, the steady state solution has the average atomic spin rotated a small angle

$$\tilde{\theta} \approx \frac{S_x}{S_0} \simeq \frac{g_s \mu_\mathrm{B}}{\hbar(R_\mathrm{OP} + R_\mathrm{rel})} B_z, \tag{3.15}$$

from the pumping direction into the x direction, proportional to the strength of the magnetic field B_z. Equivalently, we may describe the spin polarization in the x direction as

$$P_x = 2\langle S_x \rangle = \frac{g_s \mu_\mathrm{B} s R_\mathrm{OP}}{\hbar(R_\mathrm{OP} + R_\mathrm{rel})^2} B_z. \tag{3.16}$$

It can be shown [51] that the plane of polarization of linearly polarized light with frequency ν rotates by an angle

$$\theta = \frac{\pi \nu l}{c} \left[n_+(\nu) - n_-(\nu)\right], \tag{3.17}$$

after traveling a distance l through a birefringent medium with $n_+(\nu) \neq n_-(\nu)$.

For light at the D1 transition frequency, the indices of refraction of an alkali vapor are

$$n_\pm(\nu) = 1 + \rho\left(\mp\frac{1}{2}\right)\left(\frac{n r_e c^2 f_\mathrm{D1}}{4\nu}\right) \mathrm{Im}[\mathcal{V}(\nu - \nu_0)], \tag{3.18}$$

where n is the alkali vapor density, r_e is the classical electron radius, $f_\mathrm{D1} \approx 1/3$ is the oscillator strength of the D1 resonance, and $\mathrm{Im}[\mathcal{V}(\nu - \nu_0)]$ is the imaginary component of the Voigt profile of the pump laser beam [52]. Thus when $P_x = 2\langle S_x \rangle = \rho\left(+\frac{1}{2}\right) - \rho\left(-\frac{1}{2}\right) \neq 0$, the alkali vapor is birefringent. Combining Eqs. (3.17) and (3.18) yields

$$\theta = -\frac{\pi}{2} l\, n\, r_e\, c\, f_\mathrm{D1} P_x \mathrm{Im}[\mathcal{V}(\nu - \nu_0)]. \tag{3.19}$$

Plugging in P_x from Eq. (3.16) finally leads us to

$$\theta = -\frac{\pi g_s \mu_\mathrm{B} s}{2\hbar} l\, n\, r_e\, c\, f_\mathrm{D1} \mathrm{Im}[\mathcal{V}(\nu - \nu_0)] \frac{R_\mathrm{OP}}{(R_\mathrm{OP} + R_\mathrm{rel})^2} B_z. \tag{3.20}$$

If we approximate the Voigt profile with a Lorentzian,

$$\mathrm{Im}[\mathcal{V}(\nu - \nu_0)] \simeq \frac{1}{\pi(\nu - \nu_0)}, \tag{3.21}$$

and rewrite Eq. (3.20) as

$$\theta = -\frac{\pi g_s \mu_\mathrm{B} s}{2\hbar} l\, n\, r_e\, c\, f_\mathrm{D1} \frac{R_\mathrm{OP} + R_\mathrm{rel}}{(R_\mathrm{OP} + R_\mathrm{rel})^2 + \left(\frac{g_s \mu_\mathrm{B} B_z}{\hbar}\right)^2} B_z, \tag{3.22}$$

we see the full dependence of the rotation of the probe beam polarization on all parameters. For the purpose of NMR detection, we may summarize all of this as

$$\theta \propto B_z, \tag{3.23}$$

showing that measurement of the rotation of polarized light is equivalent to the measurement of a magnetic field. Because we are much more interested in measuring the dynamics of nuclear spins than in measuring absolute magnetic field strengths, we generally do not need to worry about the proportionality constant, except for when considering limitations on the signal-to-noise ratio.

3.2.4 The Spin-Exchange Relaxation-Free Regime

The fundamental sensitivity of an atomic magnetometer due to spin projection noise is given by [53]

$$\delta B = \frac{\hbar}{g_s \mu_{\mathrm{B}}} \frac{1}{\sqrt{nVT_2\tau}}, \tag{3.24}$$

where n is the alkali vapor density, V is the alkali vapor volume, T_2 is the spin decoherence (relaxation) correlation time, and τ is the measurement time. Thus, in order to maximize the magnetic field sensitivity per $\sqrt{s}$ of a magnetometer of given volume, it is desirable to maximize the product of the density and relaxation time. Increasing the alkali vapor density is straightforward – one needs only increase the temperature of the vapor cell to increase the number of atoms in the vapor phase. The relaxation time, however, is affected by several factors, including pumping rates from the pump and probe beams, wall collisions, spin-destruction collisions, and spin-exchange collisions. Furthermore, the contribution of spin-exchange collisions to the overall rate of decoherence increases as the vapor density increases, counteracting the benefit of having a higher vapor density!

All is not lost, however, as Happer and coworkers discovered that spin-exchange relaxation vanishes at extremely high alkali densities [54]. The effect may be described as akin to motional narrowing [55], where if the spin exchange rate is much faster than the precession frequency, individual atoms precess very little between collisions, and rapidly sample all ground-state sublevels, statistically weighted by the spin-temperature distribution. Considering hyperfine effects, atoms in two hyperfine levels may be thought of as "locked together" as they precess, so spin-exchange collisions no longer cause spin relaxation because the entire alkali ensemble precesses coherently [51].

Thus maximum sensitivity is obtained at high vapor densities and low magnetic fields, where the spin-exchange collision rate is much greater than the precession frequency. This is referred to as the Spin-Exchange Relaxation-Free (SERF) regime. Alkali vapor atomic magnetometers operating in this regime frequently reach sensitivities less than 1 fT/$\sqrt{\mathrm{Hz}}$ [56] and have reached sensitivities of 160 aT/$\sqrt{\mathrm{Hz}}$ [57]. Chip-scale SERF magnetometers have also been microfabricated [58, 59], with sensitivities on the order of 5-20 fT/$\sqrt{\mathrm{Hz}}$ [60], sufficient for ZULF-NMR.

3.3 Zero- and Ultra-Low-Field NMR Apparatus

3.3.1 Overview

A schematic of the ZULF NMR apparatus is shown in Fig. 3.3. Alkali atoms in a $0.6 \times 0.6 \times 1.0$ cm^3 ^{87}Rb vapor cell[1] are pumped by a circularly polarized laser beam at the D1 transition propagating in the $+y$ direction, and magnetic fields are measured by the rotation of a linearly polarized pump beam propagating in the x direction, such that the magnetometer is primarily sensitive to fields along the z axis, which is vertical in the lab frame. The magnetometer cell is affixed to a column of hexagonal boron nitride, which attains a stable temperature between 180-200°C by resistive heating. Magnetic fields are attenuated by 4-6 layers of μ-metal magnetic shielding. The most sensitive configuration also includes a ferrite shield to minimize thermal Johnson noise from the μ-metal shields, which otherwise limit sensitivity to ~40-50 fT/$\sqrt{\text{Hz}}$. A set of three orthogonal coils sits within the innermost layer of shielding for residual magnetic field compensation. Three additional low-inductance coils serve to apply magnetic field pulses.

In field-cycling experiments, samples are polarized in a permanent 2 T Halbach magnet, then shuttled pneumatically down to the zero-field detection region. Depending on the particular configuration, sample temperatures may be controlled by flowing dry nitrogen through either a cold bath or heated coil, and then to the bottom of the pneumatic shuttling tube. In this configuration, the backing pressure from the top of the shuttling tube must be carefully calibrated to ensure efficient sample transport. A "guiding field" solenoid may also be wound around the shuttling tube to ensure adiabatic transfer of the sample between the polarizing field region down to the zero-field region.

3.3.2 Polarimetry Optics

Two different methods for measuring the polarization of the probe beam have been employed in our ZULF-NMR experiments, one involving a balanced polarimeter and a polarizing beam splitter, and one employing a photoelastic modulator (PEM). In both cases, the pump beam optics are the same. First the pump beam is expanded using either collimation optics or a telescopic beam expander, after which the polarization of the beam is cleaned up using a linear polarizer, which is rotated so as to maximize optical transmission. The linearly polarized beam then passes through a quarter waveplate, producing circularly polarized light. Rotation of the quarter waveplate's fast vs. slow axes with respect to the linear polarizer can yield either right- or left-handed circular polarization.

The experimental optics configuration for polarimetry using a balanced polarimeter is shown in Fig. 3.4. The probe beam is passed through a linear polarizer to clean up the laser polarization, and then through a half waveplate, which serves to rotate the plane of the linearly polarized light, which should generally be at 45° to the polarizing beam splitter. After passing through the vapor cell, the probe beam is split into its vertical and horizontal components by a polarizing beam

---

[1] Microfabricated millimeter-scale cells have been used in the past, though we have since transitioned to larger cells manufactured by Twinleaf LLC.

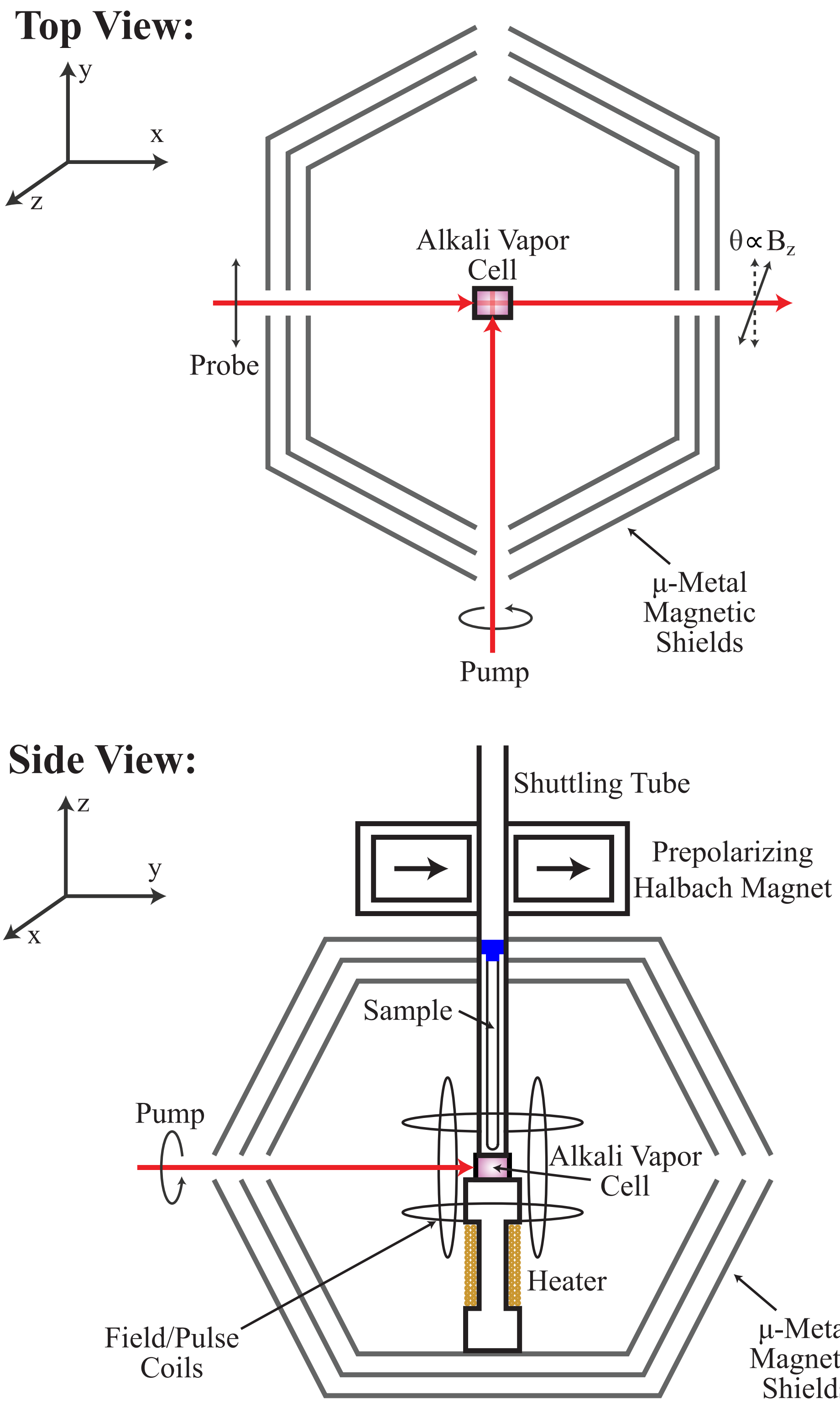

Figure 3.3: Schematic of the zero-field NMR apparatus.

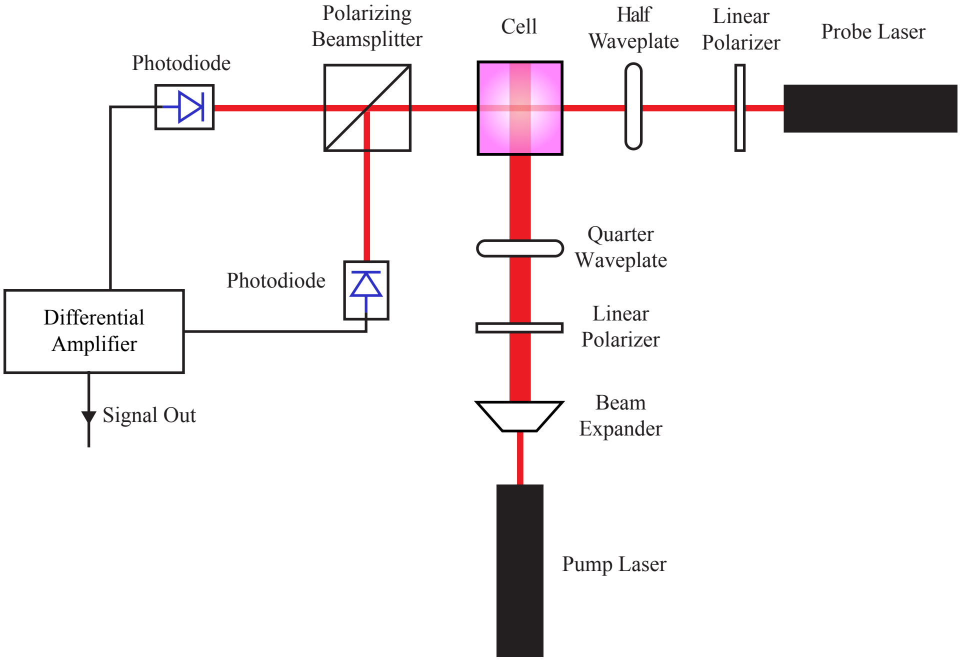

Figure 3.4: Experimental optics configuration using a balanced polarimeter.

splitter, and the intensity of each component beam is measured by a photodiode. The signals of the two photodiodes are fed into a differential amplifier, the output of which is proportional to the angle of rotation of the probe beam. It is in general necessary to balance the polarimeter by rotating the half waveplate to ensure that the output of the differential amplifier is zero when no field is applied. A quarter waveplate may also be placed after the half waveplate and before the cell in order to compensate for any ellipticity of the probe beam induced by the glass walls of the vapor cell.

The experimental optics configuration for polarimetry using a photoelastic modulator (PEM) is shown in Fig. 3.5. The probe beam is again passed through a linear polarizer and a half waveplate in order to yield polarization at 45° relative to the PEM. After passing through the vapor cell and experiencing a rotation of the linear polarization $\theta \propto B_z$, the beam is then passed through a quarter waveplate aligned parallel to the initial beam polarization, so any rotation of the linear polarization is transformed into ellipticity. If the beam does not experience rotation of the linear polarization in the vapor cell, the beam polarization is modulated by the PEM symmetrically between left- and right-handed circular polarization at the characteristic frequency of the PEM oscillation (typically around 50 kHz). If the beam experiences optical rotation in the cell, the modulation of the beam by the PEM is asymmetric so that after passing though a linear polarizer set at 90° relative to the initial polarization, the intensity of the light reaching the photodiode is

$$I = I_0 \sin^2\left[\theta + \beta \sin\left(\omega_{\mathrm{PEM}} t\right)\right], \tag{3.25}$$

so that for small rotations θ and modulation amplitudes β, the Fourier component of the detected

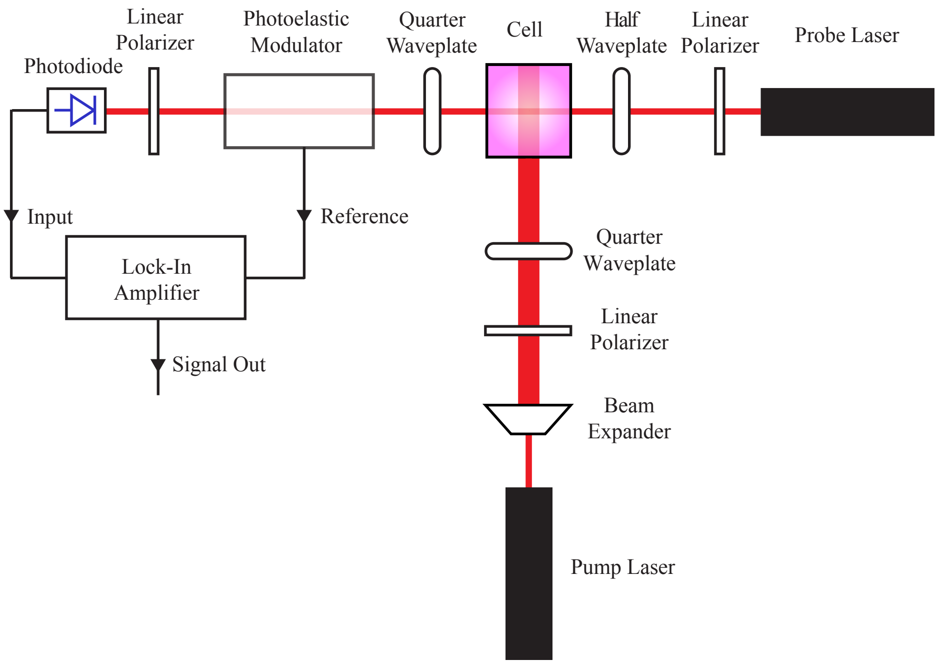

Figure 3.5: Experimental optics configuration using a photoelastic modulator.

intensity is proportional to the rotation angle,

$$I\left(\omega_{\mathrm{PEM}}\right) \approx 2I_0\theta\beta, \tag{3.26}$$

which is read out by feeding the photodiode signal into a lock-in amplifier referenced to the PEM modulation frequency. Because the measurement is performed at high frequency, polarimetry measurements performed using a PEM benefit from separation from $1/f$ and other low-frequency noise [51].

3.3.3 Vapor Cell Heating

To maximize sensitivity, our magnetometer cells are heated to 180-200 °C to obtain a high alkali vapor density. Higher temperatures are avoided due to breakdown of resistive heating elements and an increased likelihood of reactions between alkali atoms and the glass of the cell. The general design of the heater is shown in the lower view of Fig. 3.3, where 22 gauge copper wire (folded over and tightly twisted to minimize magnetic field noise) is wrapped around a column of hexagonal boron nitride (hBN) on which the vapor cell is affixed. Because of the high thermal conductivity of hBN, it is possible to separate the heating coil from the cell by multiple centimeters, further minimizing magnetic noise from the heater.

AC heating has been shown to be preferable to DC heating because it allows us to isolate magnetic noise from the heater at high frequencies outside of the detection bandwidth, and it minimizes temperature-dependent variations of the magnetometer signal. Further details of the current apparatus are given in Ref. [61].

Figure 3.6: Photograph of Phase-II magnetometer inner shields and coil housing.

3.3.4 Magnetic Field Pulses

Magnetic field pulses are applied by passing current pulses through low-inductance coils within the magnetic shields, as in Fig. 3.3. See Ref. [62] for a detailed description of coil and pulse circuit design. Major challenges involve pulse consistency, homogeneity, field strength, and rise time – most, if not all, of these should be solved by using commercially available instrumentation, such as high-frequency gradient amplifiers used in high-field magnetic resonance.

3.3.5 Phase-II Magnetometer Photographs

Figure 3.6 shows the innermost shields of the Phase-II magnetometer. The twisted purple wires are used for degaussing the magnetic shields. The insulation between the two innermost shields is substantially damaged by early unfocused heating methods.

Figure 3.7 shows several views of the Phase-II magnetometer's vapor cell housing. The topmost photograph shows the glass cell mounted on top of the white boron nitride heater, with a thermocouple affixed between the heater and cell. The pump beam enters the cell via the optical access channel from the top of the page, opposite the cell's stem (present in order to add rubidium to the cell). The probe beam propagates in the orthogonal direction. The second photograph shows the cell through the probe beam channel, and the third photograph shows the same view with the upper portion of the sample holder in place. The fourth photograph shows the top view of the cell housing including the hole bored most of the way to the vapor cell position, with $\sim$ 1 mm of material remaining to prevent samples from smashing the cell during shuttling.

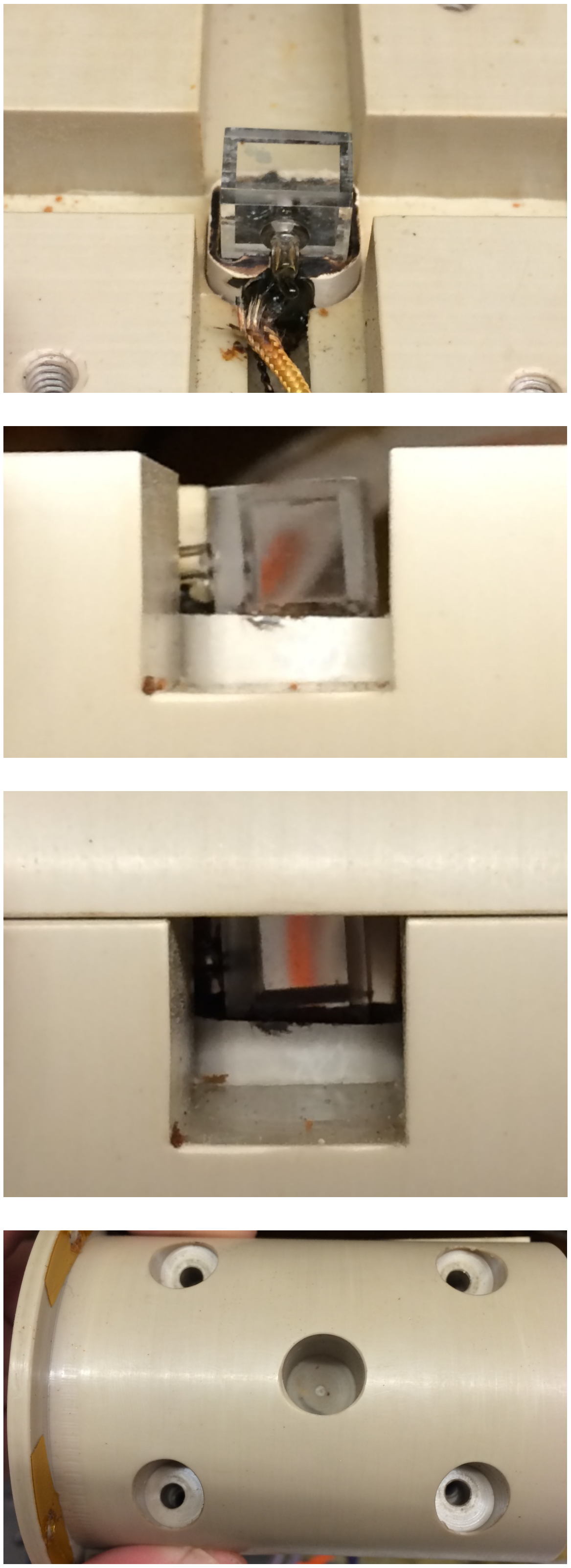

Figure 3.7: Photographs of Phase-II magnetometer cell holder.

3.3.6 Magnetic Field Compensation

Compensation Based on Magnetometer Response

Based on Eq. (3.11), the sensitivity of the magnetometer is linear in the z direction, and bilinear in the x and y directions. In order to zero the magnetic field in the z direction, one may simply balance the polarimeter (such that the DC offset due to the polarization optics is zero) with the pump beam blocked, and then readjust the z field to remove any DC offset upon unblocking the pump beam. If we apply small field modulations about the x and y axes such that [63]

$$\begin{aligned} \beta_x &= \beta_x^0 + \beta_x^{\mathrm{mod}} \sin\left(\omega_x t\right) \\ \beta_y &= \beta_y^0 + \beta_y^{\mathrm{mod}} \sin\left(\omega_y t\right), \end{aligned} \tag{3.27}$$

where β_x^0 and β_y^0 are components of the static ambient magnetic field, and β_x^{mod} and β_y^{mod} are the modulation amplitudes, then Eq. (3.11) may be expanded as

$$S_x \approx S_0 \left[\beta_z - \beta_x^0\beta_y^0 - \beta_x^0\beta_y^{\mathrm{mod}} \sin\left(\omega_y t\right) - \beta_y^0\beta_x^{\mathrm{mod}} \sin\left(\omega_x t\right)\right]. \tag{3.28}$$

Then lock-in amplifiers referenced to ω_y and ω_x yield signals proportional to β_x^0 and β_y^0, respectively. Thus the magnetic field along x (y) may be zeroed by minimizing the signal arising from a field modulation in the y (x) direction.

Compensation Based on Zeeman Splittings

One can also eliminate magnetic fields by measuring Zeeman splittings of the J-coupling spectrum induced by non-zero magnetic fields. In fact, the absence of observable Zeeman perturbation is, by definition, evidence that the sample is in the zero-field regime. By arraying the applied field strength, one can determine the parameters that correspond to zero magnetic field in terms of the equations listed in Chapter 6. Magnetic fields in the x and y directions will cause a splitting of the ${}^1J_{\mathrm{CH}}$ peak in ^{13}C-labeled formic acid, so eliminating this splitting ensures that the sample is not affected by x or y fields. Furthermore, the center peak at ${}^1J_{\mathrm{CH}}$ will reappear if a z field is applied while the spectrum is split by x or y fields, so minimizing the central peak in the presence of x or y fields allows one to zero the magnetic field in the z direction.

It should be noted that field compensation based on Zeeman splittings is generally the preferred method for fine-tuning to the zero-field condition, because we are generally more interested in the ambient field present at the sample than that present at the magnetometer cell, which are not necessarily the same. This is a notable difference between NMR measurements, where we are primarily interested in the spin dynamics of our sample, and precision fundamental physics measurements, where one is more often attempting to measure fields with a greater spatial homogeneity.

Chapter 4

Preparing Nuclear Spin Magnetization in Zero-Field NMR

NMR measures magnetization,
As per Boltzmann's exponentiation.
Though in ZULF-NMR,
This is lower by far,
So we need hyperpolarization.

This chapter describes the methods by which zero-field NMR signal is generated. Because thermal spin polarization is negligible in the absence of a magnetic field, the production of observable signal in ZULF NMR requires the formation of so-called "hyperpolarized" spin states, having spin polarization much greater than thermally equilibrated states. We will also consider the effects of magnetic field pulses to transform static states into superposition states yielding oscillating magnetization. This chapter includes content from the following publications:

- Blanchard, J.W. and Budker, D. Zero-Field NMR. *Encyclopedia of Magnetic Resonance*. In Preparation.
- Emondts, M., Ledbetter, M.P., Pustelny, S., Theis, T., Patton, B., Blanchard, J.W., Butler, M.C., Budker, D., and Pines, A. Long-Lived Heteronuclear Spin-Singlet States in Liquids at a Zero Magnetic field. *Phys. Rev. Lett.* **112** (7), 077601. (2014)
- Butler, M.C., Kervern, G., Theis, T., Ledbetter, M.P., Ganssle, P.J., Blanchard, J.W., Budker, D., and Pines, A. Parahydrogen-Induced Polarization at Zero Magnetic Field. *J. Chem. Phys.* **135** (9), 234201. (2013)

- Theis, T., Ledbetter, M.P., Kervern, G., Blanchard, J.W., Ganssle, P.J., Butler, M.C., Shin, H.D., Budker, D., and Pines, A. Zero-Field NMR Enhanced by Parahydrogen in Reversible Exchange. *J. Am. Chem. Soc.* **134** (9), 3987-3990. (2012)

4.1 Overview: Spin Polarization and Hyperpolarization

As described in the previous chapter, detection of a ZULF NMR signal amounts to the measurement of the magnetic field produced by nuclear spins in a sample, which is proportional to the net magnetization of those nuclear spins. The magnetic moment of a single spin **S** may be written

$$\boldsymbol{\mu} = \hbar\gamma\mathbf{S}, \tag{4.1}$$

where $\hbar$ is the reduced Planck constant and γ is the gyromagnetic ratio of the nuclear spin **S**. The total magnetization of an ensemble of spins can then be written as

$$\mathbf{M} = N\hbar\gamma\mathbf{S}P_0, \tag{4.2}$$

where N is the number density of nuclear spins, and P_0 is the ratio of the spin state population difference to the total population, generally referred to as the *spin polarization*. Explicitly, for spin-$\frac{1}{2}$ nuclei,

$$P_0 = \frac{n_\uparrow - n_\downarrow}{n_\uparrow + n_\downarrow}, \tag{4.3}$$

where $n_\uparrow$ is the fraction of spins with $m_s = +\frac{1}{2}$, and $n_\downarrow$ is the fraction of spins with $m_s = -\frac{1}{2}$. These populations are given by the Boltzmann distribution,

$$\begin{aligned} n_\uparrow &= e^{\frac{-E_+}{k_B T}} \\ n_\downarrow &= e^{\frac{-E_-}{k_B T}} \end{aligned} \tag{4.4}$$

where $E_\pm$ is the energy of the state with $m_s = \pm\frac{1}{2}$, k_B is the Boltzmann constant, and T is the temperature of the system. In a large magnetic field, the dominant energy term is the Zeeman interaction,

$$\mathcal{H}_Z = -\hbar\gamma\mathbf{B}_0 \cdot \mathbf{S}, \tag{4.5}$$

where $\mathbf{B}_0$ is the applied magnetic field. For a magnetic field in the z direction, the energy is

$$E = -\hbar\gamma B_0 m_s, \tag{4.6}$$

so Eq. (4.3) may be written as

$$\begin{aligned} P_0 &= \frac{e^{\frac{\hbar\gamma B_0}{2k_B T}} - e^{-\frac{\hbar\gamma B_0}{2k_B T}}}{e^{\frac{\hbar\gamma B_0}{2k_B T}} + e^{-\frac{\hbar\gamma B_0}{2k_B T}}} \\ P_0 &= \tanh\left(\frac{\hbar\gamma B_0}{2k_B T}\right). \end{aligned} \tag{4.7}$$

Under practically achievable conditions, this may be approximated by the leading term of the Taylor expansion of the hyperbolic tangent,

$$P_0 \approx \frac{\hbar\gamma B_0}{2k_B T}, \tag{4.8}$$

such that

$$\mathbf{M} \approx \frac{N\hbar^2\gamma^2 B_0}{2k_B T}\mathbf{S}. \tag{4.9}$$

Thus the magnitude of the observable NMR signal is dependent not only on the spin density and gyromagnetic ratio, but also varies linearly with the magnetic field strength.

The thoughtful reader may rightly realize that this result is rather disturbing for zero-field NMR, as Eq. (4.9) suggests that there should be no observable magnetization in the absence of a magnetic field! It is true that in the ZULF regime, the dominant spin interaction is no longer the Zeeman Hamiltonian, but is instead the J-coupling Hamiltonian,[1] which persists down to zero field. This interaction is, however, very small compared to the high-field Zeeman interaction, and does not produce much in the way of observable magnetization. For example, while the thermal equilibrium of ^{1}H nuclei in a 9.4 T magnet yields part-per-million spin polarization due to a 400 MHz splitting between energy levels, thermal polarization at zero field due to a J-coupling of only hundreds of Hz yields a spin polarization roughly a million times smaller, which is beyond the limit of the most sensitive detectors.

The solution is, however, rather straightforward: if the equilibrium spin polarization is insufficient for ZULF NMR, we clearly need some kind of non-equilibrium spin polarization. In the following sections, we explore some of the methods for generating so-called "hyperpolarized" states where the polarization level substantially exceeds that obtained by thermal polarization.

Also, much as high-field NMR is not actually sensitive to the static magnetization aligned with the field, but to the transverse magnetization precessing in the orthogonal plane, we must consider how to transform static magnetization at zero-field into an evolving magnetization that yields useful information. In high-field NMR, the static equilibrium magnetization corresponds to an eigenstate of the Zeeman Hamiltonian, so it is necessary to apply a resonant radio-frequency pulse to "rotate" the density matrix into a superposition state that will precess under the Zeeman Hamiltonian to produce observable magnetization in the xy plane. Similarly, in zero-field NMR, the initial state will generally be an eigenstate of the J-coupling Hamiltonian and must be transformed into a superposition state that will evolve under the J-coupling Hamiltonian to produce an observable oscillating magnetization. As we will see in the following sections, this may be achieved using DC magnetic field pulses.[2]

4.2 Field Cycling, or "Pneumatic Hyperpolarization"

The most commonly used polarization scheme in ZULF NMR is cycling (e.g. by pneumatic shuttling) a sample from a high-field polarization region to a zero-field region, after which co-

---

[1] That is, in isotropic liquids. In solids, the direct dipole-dipole or quadrupolar couplings typically dominate. While the dipolar coupling Hamiltonian is also generally insufficient for the generation of measurable spin polarization, the quadrupolar coupling is typically on the order of MHz, leading to the possibility of measurement without the need for alternative polarization methods. It is for this reason that nuclear quadrupole resonance (NQR) is sometimes referred to – somewhat erroneously – as "zero-field NMR."

[2] A DC magnetic field pulse may be considered the equivalent of a resonant radio-frequency pulse with zero frequency because at zero field, the Larmor frequencies $\omega = \gamma B_0$ of all nuclei are identically zero.

herences are generated and observed. In a typical experiment,[64, 65, 66, 67] a sample inside of normal 5 mm NMR tubes are polarized in a 2 T permanent Halbach cylinder magnet located on top of the ZULF NMR apparatus, outside of the magnetic shielding, as shown in Fig. 3.3. The sample is then shuttled out of the polarizing field and down into the zero-field region for detection. During the shuttling, a “guiding field” may be applied in the vertical direction (z axis in Fig. 3.3) by a solenoid wrapped around the shuttling tube – upon reaching the detection region, the field is suddenly turned off. Alternatively, the sample may be shuttled slowly in the absence of a guiding field, providing an adiabatic transition.

For illustration, we examine the case of a coupled heteronuclear spin-$\frac{1}{2}$ pair, **I** and **S**, following the approach laid out in the Supporting Information of Ref. [67]. For simplicity, we include only the J-coupling in the local Hamiltonian, and we neglect relaxation effects. We will also work in a unit system with $\hbar = 1$.

At the beginning of the experiment, in the polarizing field, the eigenstates of the spin system are given by the uncoupled basis $|M_I M_S\rangle$, which we further denote using up/down arrow notation as $|\uparrow\uparrow\rangle$, $|\uparrow\downarrow\rangle$, $|\downarrow\uparrow\rangle$, and $|\downarrow\downarrow\rangle$. The populations of these states $P_{M_I,M_S} = \langle M_I M_S|\rho|M_I M_S\rangle$ are given by the Boltzmann distribution:

$$P_{M_I,M_S} = \frac{1}{4}e^{\frac{B_p(\gamma_I M_I+\gamma_S M_S)}{kT}} \approx \frac{1}{4}(1+\frac{\gamma_I}{kT}\mathbf{B}_p\cdot\mathbf{I}+\frac{\gamma_S}{kT}\mathbf{B}_p\cdot\mathbf{S}), \tag{4.10}$$

where B_p is the strength of the polarizing field, k is the Boltzmann constant, and M_I and M_S are $\pm\frac{1}{2}$. We then write the populations of each state as

$$P_{\uparrow\uparrow} = \frac{1}{4}+\delta,\ P_{\uparrow\downarrow} = \frac{1}{4}+\epsilon,\ P_{\downarrow\uparrow} = \frac{1}{4}-\epsilon,\ P_{\downarrow\downarrow} = \frac{1}{4}-\delta, \tag{4.11}$$

where $\delta = B_p(\gamma_I+\gamma_S)/(8kT)$ and $\epsilon = B_p(\gamma_I-\gamma_S)/(8kT)$.

At zero field, the local Hamiltonian is $H_J = J\mathbf{I}\cdot\mathbf{S}$, and the eigenstates consist of the singlet and triplet states, $|S_0\rangle$, $|T_0\rangle$, and $|T_{\pm1}\rangle$, which are indexed by the total angular momentum $\mathbf{F} = \mathbf{I}+\mathbf{S}$. Note that the formalism is similar to that used for atomic hyperfine coupling [68]. In terms of the high-field states, these are written as

$$\begin{aligned} |T_{+1}\rangle = |\uparrow\uparrow\rangle,\ |T_0\rangle &= \frac{1}{\sqrt{2}}(|\uparrow\downarrow\rangle+|\downarrow\uparrow\rangle),\ |T_{-1}\rangle = |\downarrow\downarrow\rangle, \\ |S_0\rangle &= \frac{1}{\sqrt{2}}(|\uparrow\downarrow\rangle-|\downarrow\uparrow\rangle). \end{aligned} \tag{4.12}$$

4.2.1 Adiabatic Transition to Zero Field

Following adiabatic transport to zero field, the populations of the high-field states $|\uparrow\uparrow\rangle$, $|\downarrow\uparrow\rangle$, $|\uparrow\downarrow\rangle$, and $|\downarrow\downarrow\rangle$ are converted to populations of the zero-field states $|T_{+1}\rangle$, $|T_0\rangle$, $|S_0\rangle$, and $|T_{-1}\rangle$, respectively. Henceforward, we will represent these populations using the operators $T_{0,\pm1} = \left|T_{0,\pm1}\right\rangle\left\langle T_{0,\pm1}\right|$ and $S_0 = |S_0\rangle\langle S_0|$. For convenience, we express these populations in the spin-operator formalism:

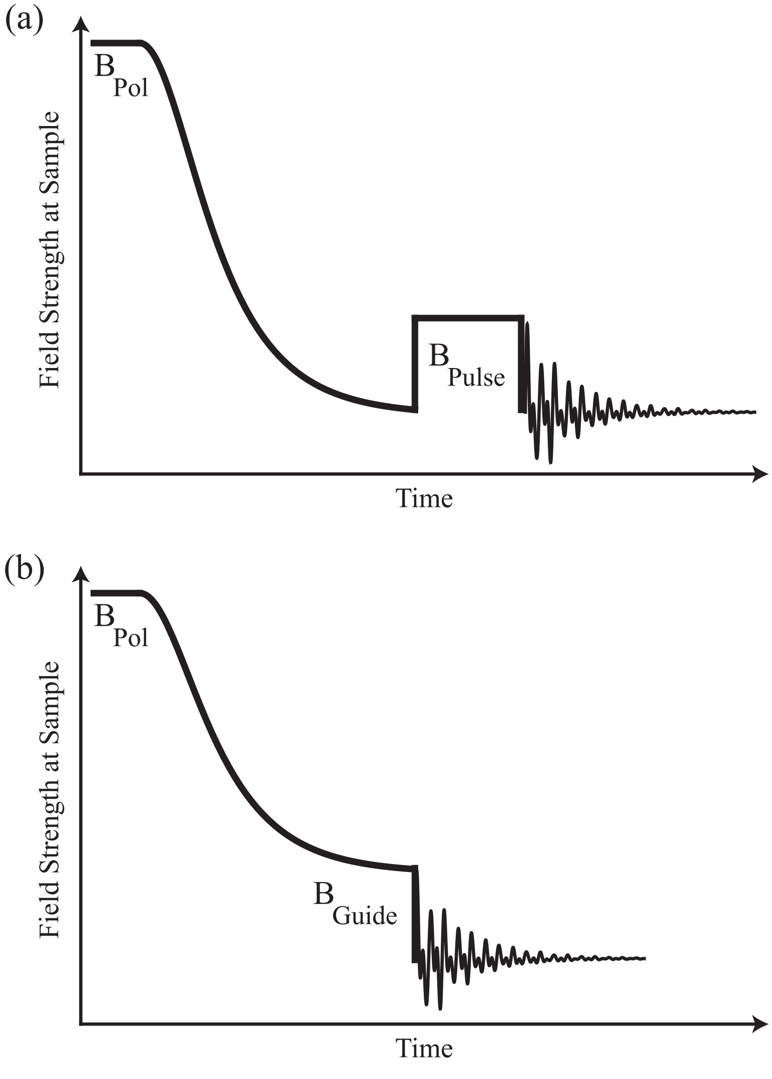

Figure 4.1: Magnetic field experienced by the sample during pneumatic shuttling for (a) adiabatic transfer, (b) sudden transfer.

$S_0 = \mathbb{1}/4 - \mathbf{I}\cdot\mathbf{S}$, $T_0 = \mathbb{1}/4 + I_xS_x + I_yS_y - I_zS_z$, $T_{\pm 1} = \mathbb{1}/4 \pm (I_z + S_z)/2 + I_zS_z$. The initial density matrix following adiabatic transport to zero field can then be written as

$$\rho_0 = \delta(I_z + S_z) - 2\epsilon(\mathbf{I}\cdot\mathbf{S} - I_zS_z). \tag{4.13}$$

We also introduce a set of zero-quantum and double-quantum operators:

$$\begin{aligned} Z_x &= 2(I_xS_x + I_yS_y), \\ Z_y &= 2(I_xS_y - I_yS_x), \\ Z_z &= (I_z - S_z), \\ D_z &= (I_z + S_z)\,. \end{aligned} \tag{4.14}$$

In terms of these operators, the initial density matrix can be written as

$$\rho_0 = \delta D_z - \epsilon Z_x. \tag{4.15}$$

The reason for using these operators becomes apparent when considering the commutation relations with the scalar-coupling Hamiltonian:

$$\begin{gathered} [Z_x, H_J] = [D_Z, H_J] = 0, \\ [Z_z, H_J] = -iJZ_y, [Z_y, H_J] = iJZ_z. \end{gathered} \tag{4.16}$$

For the purpose of visualization, these commutation relations define an algebra identical to that of the single-spin operators in high-field NMR, with the J-coupling Hamiltonian viewed as "parallel" to Z_x in place of the high-field Zeeman Hamiltonian. Thus Z_z coherences evolving into Z_y (and vice versa) under H_J can be viewed as analogous to the evolution of spins precessing about a magnetic field.

Because all terms in the initial density matrix in Eq. (4.15) commute with H_J, it is necessary to transform the density matrix into a state that will evolve in order to generate an NMR signal. Analogous to high-field NMR, this is done by applying a magnetic-field pulse. However, in this case, it is a DC pulse rather than RF, because the Larmor frequency in the absence of magnetic field is zero. The Hamiltonian for a magnetic-field pulse in the z-direction is the Zeeman Hamiltonian,

$$H_z = B_z(\gamma_I I_z + \gamma_S S_z)\,, \tag{4.17}$$

and the commutation relations with the pulse Hamiltonian are

$$\begin{gathered} [Z_z, H_z] = [D_z, H_z] = 0, \\ [Z_y, H_z] = iB_z(\gamma_I - \gamma_S)Z_x, \\ [Z_x, H_z] = -iB_z(\gamma_I - \gamma_S)Z_y. \end{gathered} \tag{4.18}$$

Thus applying a magnetic field in the z direction causes evolution between Z_x and Z_y, analogous to a high-field RF x pulse rotating magnetization from I_z into I_y. Following a z pulse of duration t_p, the density matrix is

$$\rho_z = \delta D_z - \epsilon(\cos\alpha Z_x + \sin\alpha Z_y), \tag{4.19}$$

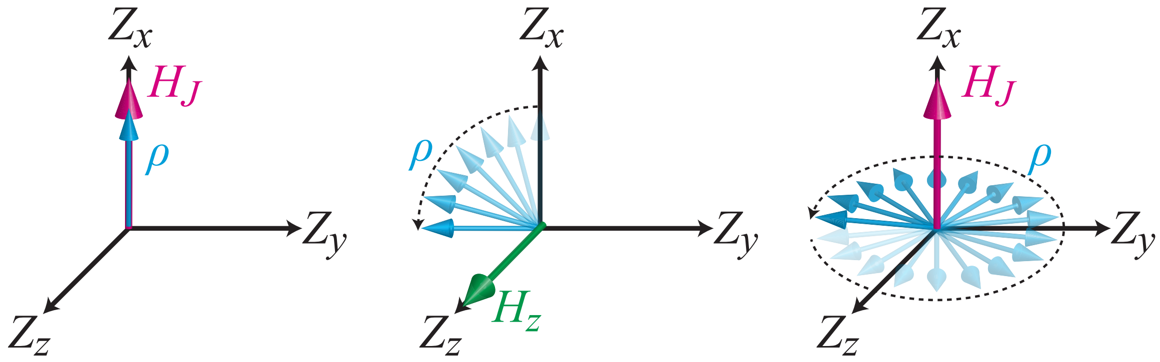

Figure 4.2: Visualization of the evolution of a two-spin system during the pulse and detection period. As described in the text, the initial state is an eigenstate of H_J, depicted here as a pseudospin collinear with H_J. The Hamiltonian describing a magnetic-field pulse in the z direction is perpendicular to H_J and rotates the pseudospin through an angle of $\pi/2$ into $-Z_y$. Following the pulse, the pseudospin then evolves under H_J, depicted here as precession about the Z_x axis. Adapted with permission from Ref. [69]. ©2013 American Institute of Physics.

where $\alpha = 2\pi B_z t_p(\gamma_I - \gamma_S)$.

Evolution under the J-coupling Hamiltonian yields

$$\rho_z(t) = \delta D_z - \epsilon \left[\cos\alpha Z_x + \sin\alpha \cos(2\pi J t)\, Z_y - \sin\alpha \sin(2\pi J t) Z_z \right]. \tag{4.20}$$

The sample magnetization in the z direction is $M_z(t) = Nh\,\mathrm{Tr}\{\rho(t)(\gamma_I I_z + \gamma_S S_z)\}$, where N is the molecular number density and h is Planck's constant. Inserting Eq. (4.20) and ignoring the D_z term, which does not evolve, we obtain

$$M_z(t) = \frac{Nh}{2}\epsilon(\gamma_S - \gamma_I)\sin\alpha \sin(2\pi J t). \tag{4.21}$$

We can also apply a magnetic-field pulse in the x (or, equivalently, y) direction. Working with pulses orthogonal to z is less convenient, as the pulse Hamiltonian does not have a simple projection onto the operators in Eq. (4.14), but it can be shown that an x (y) pulse converts the term of the density operator proportional to ϵ into magnetization oscillating in the x (y) direction. Because the magnetometer is only sensitive to z magnetic fields, we can ignore this part and focus instead on the term proportional to δ, which is of the form $I_z + S_z$. Using the standard commutation relations for angular momentum, we find that, following the pulse, the relevant part of the density matrix is

$$\rho_x = \delta \left[\frac{D_z}{\sqrt{2}}(\cos\theta_I + \cos\theta_S) + \frac{Z_z}{\sqrt{2}}(\cos\theta_I - \cos\theta_S) \right], \tag{4.22}$$

where $\theta_{I,S} = B_x t_p \gamma_{I,S}$. As before, D_z commutes with H_J and so does not evolve. Z_z does not, however, commute with H_J, so it will evolve and give rise to a time-dependent magnetization:

$$M_z(t) = \frac{Nh}{2}\delta(\gamma_I - \gamma_S)(\cos\theta_I - \cos\theta_S)\cos(2\pi J t). \tag{4.23}$$

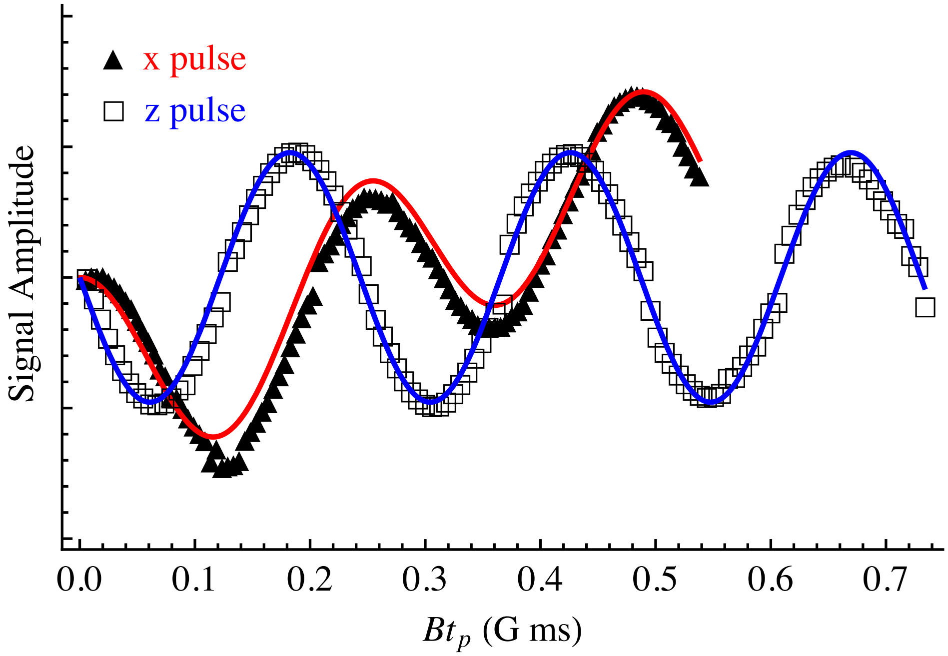

Figure 4.3: Dependence of ZULF NMR signal amplitude on the “pulse area” $B_z t_p$ for pulses of magnetic field in the x and z directions for a model two-spin system, formic acid-^{13}C. The solid curves overlaying the data are fits to Eqs. (4.21) and (4.23). Adapted with permission from Ref. [67]. ©2014 American Physical Society.

So a pulse in the x or y direction generates an signal evolving as $\cos(2\pi Jt)$ proportional to δ, the population difference between the $|T_{+1}\rangle$ and $|T_{-1}\rangle$ states, and a pulse in the z direction generates a signal evolving as $\sin(2\pi Jt)$ proportional to ϵ, the population difference between the $|T_0\rangle$ and $|S_0\rangle$ states. Following Fourier transformation, these produce spectral features described by absorptive and dispersive peaks, respectively.

4.2.2 Sudden Transition to Zero Field

The initial density operator following a sudden transition to zero-field is obtained by projecting the high-field density operator onto the zero-field basis:

$$\rho_0 = \delta D_z + \epsilon Z_z. \tag{4.24}$$

In this case, the Z_z term will begin to evolve immediately, without any pulses, yielding a time-dependent magnetization signal:

$$M_z(t) = \frac{Nh}{2}\epsilon(\gamma_I - \gamma_S)\cos(2\pi Jt). \tag{4.25}$$

As shown in Eq. (4.18), both terms in the initial density operator commute with a magnetic field pulse in the z direction, so such a pulse has no effect. However, as shown in Eq. (4.22), a pulse in the x direction interconverts the D_z and Z_z populations

$$\rho_x = D_z\left[\frac{\delta}{\sqrt{2}}(\cos\theta_I + \cos\theta_S) + \frac{\epsilon}{\sqrt{2}}(\cos\theta_I - \cos\theta_S)\right] + Z_z\left[\frac{\delta}{\sqrt{2}}(\cos\theta_I - \cos\theta_S) + \frac{\epsilon}{\sqrt{2}}(\cos\theta_I + \cos\theta_S)\right] \quad (4.26)$$

The Z_z term then produces an oscillating magnetization due to evolution under H_J:

$$M_z(t) = \frac{Nh}{2}\left[\frac{\delta}{\sqrt{2}}(\cos\theta_I - \cos\theta_S) + \frac{\epsilon}{\sqrt{2}}(\cos\theta_I + \cos\theta_S)\right]\cos(2\pi Jt). \quad (4.27)$$

This is particularly useful in cases where $\delta > \epsilon$, i.e. when γ_I and γ_S are of the same sign, as a pulse length selected such that $\cos\theta_I = -\cos\theta_S$ generates a signal proportional to δ, whereas the sudden transition alone generates a signal proportional to ϵ.

4.3 Parahydrogen-Induced Polarization

While zero-field NMR has been demonstrated for many systems using thermal polarization in a permanent magnet, the signal is typically too small for anything other than isotopically labeled liquids. Alternatively, significant nuclear spin polarization can be achieved via parahydrogen-induced polarization (PHIP). Because the ground state of molecular hydrogen has a symmetric rotational wavefunction, the Pauli Exclusion Principle requires that it possesses an antisymmetric singlet nuclear spin state. This nuclear spin state of hydrogen is referred to as parahydrogen, and the symmetric triplet spin state is referred to as orthohydrogen. The energy spacing between the ground state and the next lowest rotational state is equivalent to approximately 170 K, so a nearly pure singlet nuclear spin state of molecular hydrogen can be prepared by cooling H_2 substantially below this temperature (for example, 98% para-enriched at 30 K). This process is impractically slow (~ 2 weeks) in pure hydrogen [70], so in practice a magnetic catalyst is used to break the local magnetic symmetry of the molecule. If the catalyst is confined to a low temperature region, hydrogen may then be flowed through the catalyst to produce parahydrogen, which may then be stored at room temperature for multiple days without substantial loss of para-enrichment.

When parahydrogen reacts with a substrate (e.g. addition across a double bond), the nuclear spin states formed by the coupling of the singlet state to the other spin angular momenta in the molecule have substantially higher populations than those formed by coupling with the triplet states. However, the state formed by addition of angular momenta to the singlet state has no magnetic moment and thus produces no NMR signal. Yet if the substrate contains at least one spin-$\frac{1}{2}$ nucleus **S** with $\gamma_\mathrm{S} \neq \gamma_\mathrm{H}$, the symmetry is broken and observable coherences can be excited by a DC magnetic field pulse in the z-direction. While heteronuclear couplings are still necessary for the generation of observable magnetization, PHIP leads to a signal enhancement of up to 4 orders of magnitude over high-field thermal polarization, allowing for detection of dilute samples at natural isotopic abundance. Zero-field PHIP using catalytic hydrogenation has been reported previously in Ref. [71] and is described in-depth in Ref. [61].

4.3.1 Non-Hydrogenative Parahydrogen-Induced Polarization

While hydrogenative PHIP generates very large polarization at zero magnetic field, it is far from generalizable, and furthermore requires modification of the analyte, which is often undesirable for analytical techniques. It is, however, possible to transfer the non-equilibrium singlet spin order from parahydrogen to an analyte without chemical modification using a technique appropriately called non-hydrogenative parahydrogen-induced polarization (NH-PHIP), sometimes referred to as signal amplification by reversible exchange (SABRE) [73]. The basic principle behind NH-PHIP is the transfer of spin order through the J-coupling network of a transient complex formed between a parahydrogen molecule, a metal center, and the molecule of interest, usually making use of an iridium-based "polarization transfer catalyst" such as Crabtree's catalyst, (1,5-cyclooctadiene)(pyridine)-(tricyclohexylphosphine)-iridium(I) hexafluorophosphate.

We have demonstrated NH-PHIP at zero magnetic field for the polarization of pyridine-^{15}N, yielding single-shot spectra of samples at natural isotopic abundance [72]. The general mechanism for the NH-PHIP spin order transfer mechanism is shown in Fig. 4.4(a). Hydrogen and pyridine bind reversibly to the catalytic intermediate and singlet spin order is transferred from parahydrogen to pyridine through the J-coupling network. This then yields spectra like those of Fig. 4.4(b) in a single scan for unenriched pyridine-^{15}N, corresponding to a 40 mM concentration of the actual analyte. For comparison, Fig. 4.4(c) shows the spectrum of neat isotopically-enriched pyridine-^{15}N (14 M concentration) thermally polarized in a 1.6 T magnet, after averaging 128 transients. Factoring in the differences in concentration and the number of averages, NH-PHIP yields a signal enhancement of $\sim 1.7 \times 10^4$. The limit of detection in a single scan was shown to be $\sim$ 6mM, demonstrating that NH-PHIP extends the capability of ZULF-NMR even to reasonably dilute samples. Furthermore, for an enriched sample of pyridine-^{15}N, NH-PHIP, the resulting magnetization was on the order of 10^{-10} T, within the detection range of less-sensitive magnetometers such as those based on nitrogen-vacancy centers in diamond.

In the case of pyridine-^{15}N polarized by NH-PHIP, the density matrix may be treated as a sum of two-spin singlet states,

$$\rho_0 = \sum_{j \neq k} p_{jk} \mathbf{I}_j \cdot \mathbf{I}_k, \tag{4.28}$$

where p_{jk} is a population weight for each spin pair population produced by incoherent averaging during the bubbling phase of the experiment.[3] Based on the treatment in the previous section, this may be modeled as a sum of two-spin density matrices which in zero-field may be mapped

---

[3] This is related to the fact any density matrix can be described in terms of tensor products of the Pauli spin matrices, and the "spread of non-thermal singlet order" terminology used in PHIP literature generally refers to the increased population of two-spin singlet operators. This is expected because the singlet order is spread by the J-coupling Hamiltonian of the transient complex with the polarization transfer catalyst, which should leave the geometric form of the parahydrogen density matrix invariant, simply distributing the increased population amongst states of the same symmetry. This can be seen in Ref. [69], where the generator of the algebra describing the redistribution of singlet order for a three-spin system corresponds to a pseudoscalar operator that does not decrease the sum of the amplitudes

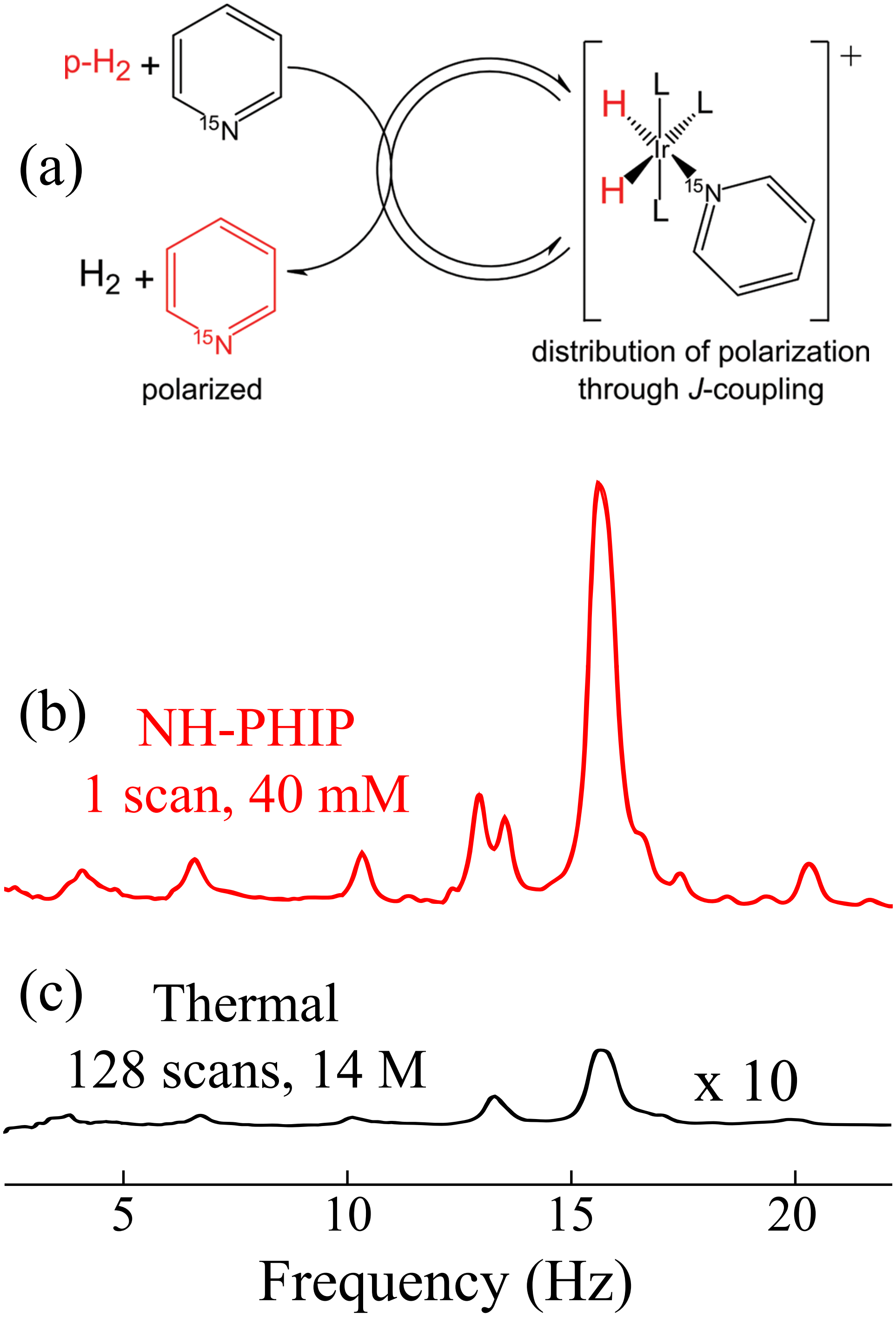

Figure 4.4: (a) NH-PHIP transfer mechanism – polarization is transferred from parahydrogen to pyridine via *J*-couplings during reversible binding to the iridium polarization transfer catalyst. Demonstration of NH-PHIP signal enhancement comparing (b) a single shot spectrum of a 40 mM solution of pyridine-^{15}N polarized using NH-PHIP to (c) the average of 128 transients of a 14 M solution of pyridine-^{15}N polarized thermally in a 1.6 T permanent magnet. Adapted from Ref. [72]. ©2012 American Chemical Society.

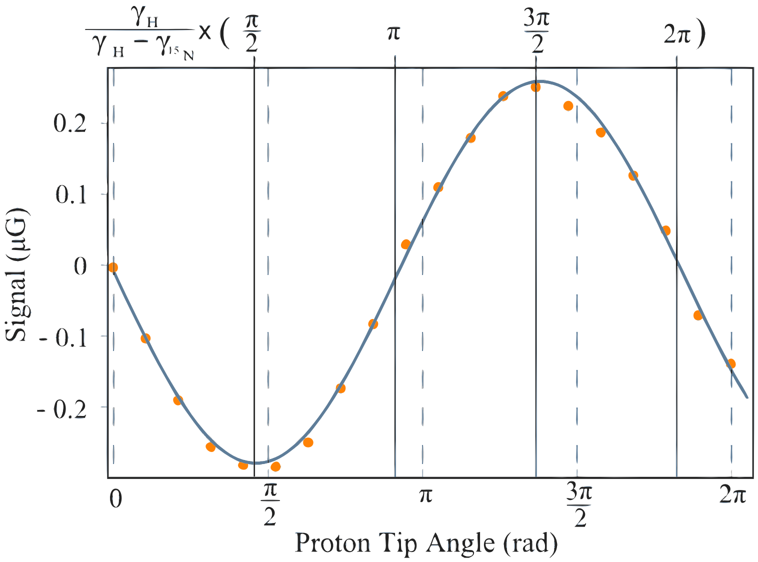

Figure 4.5: Dependence of zero-field NH-PHIP signal amplitude on the z magnetic field pulse length for pyridine-^{15}N. The pulse length is given in terms of the rotation angle experienced by a proton, calibrated in terms of a pulse train producing an alternating magnetization in a water sample, as described in Ref. [61]. The curve is a fit to $\sin(\eta_{NH}\theta_H)$, where $\eta_{NH} = -(\gamma_{^1H} - \gamma_{^{15}N})/\gamma_{^1H}$ and θ_H is the proton rotation angle.

onto Z_x, such that the magnetization in the z direction following a z magnetic field pulse may be described in terms of some product of sine functions that feature the same dependence on pulse length as that described in Eq. (4.21). Evidence that this model is consistent in describing the NH-PHIP experiment is provided in Fig. 4.5, showing the dependence of the zero-field NH-PHIP signal amplitude on the z field pulse length for pyridine-^{15}N. The behavior is analogous to that of the z pulses on formic acid-^{13}C in Fig. 4.3, supporting the validity of treating the pyridine-^{15}N NH-PHIP polarized density matrix as a direct product of two-spin singlet states.

4.4 Other Hyperpolarization Schemes

In addition to the techniques discussed above, many other spin-polarization methodologies are applicable to zero-field NMR. One example is dynamic nuclear polarization (DNP), where a much higher electron spin polarization is transferred to nuclear spins [74]. One disadvantage of DNP is that it typically requires a separate expensive and immobile instrument based on a superconducting magnet to achieve high electron polarization, eliminating the potential portability

---

of the two-spin operators because the algebra contains no representations corresponding to higher-order operators other than the $\Gamma = \mathbf{I}_1 \cdot \mathbf{I}_2 \times \mathbf{S}$ pseudoscalar. For the sake of posterity, it may be worth pointing out that because the Γ operator in Ref. [69] is a pseudoscalar, it changes sign under parity inversion, so chiral molecules may demonstrate different polarization dynamics for different enantiomers.

of ZULF-NMR. Another difficulty is that the presence of paramagnetic radicals in DNP samples is necessary to provide accessible electron polarization, and these paramagnetic species would likely lead to dramatically reduced coherence times in ZULF-NMR due to paramagnetic relaxation effects.

One could also imagine transferring polarization from optically pumped nuclear spins, such as ^{129}Xe [75] or ^{13}C nuclei near to nitrogen-vacancy centers in diamond [76, 77, 78], via the nuclear Overhauser effect [79, 80] or low-field thermal mixing due to dipole-dipole coupling [81, 82, 83]. These techniques do not require the contamination of samples with paramagnetic species, are miniaturizable [84], and operate near to room temperature.

Another possibility is photochemically induced dynamic nuclear polarization (CIDNP) [85], which relies on spin selection rules in the decay of photo-excited triplet radical pairs [86] and often achieves optimal signal enhancement at low magnetic fields [87]. Similar techniques have been used to generate long-lived states at variable magnetic field, which were studied via field cycling for high-field NMR detection [88]. By eliminating the need for high-field detection, and thus allowing for more coherent control over the hyperpolarized spin system, ZULF-NMR may be particularly useful for the study of systems hyperpolarized by CIDNP.

Furthermore, future experiments using miniaturized detectors (e.g. nitrogen-vacancy defect centers in diamond) to detect a small number of nuclear spins [89] may be able to acquire spectra without the need for sample polarization, instead relying on spin noise [90]. Spin noise is usually small compared to other sources of signal, but in the limit of extremely small samples, statistical fluctuations are dominant [91]. An related statement is that a single spin is always perfectly polarized, because it can only point in one direction. Similarly, a sample of, say 11 spins, has a minimum polarization of $1/11 \approx 9\%$ – for sufficiently small samples, the *statistical* polarization is actually larger than the equilibrium polarization achievable even in the most powerful superconducting magnets.

Chapter 5

J-Spectroscopy

At low-field there's no chemical shift,
So are chemists to be left adrift?
Electrons still have sway,
So our spectrum's from J –
Now to just make the analysis swift...

This chapter will provide a description of the current state of the art in the interpretation of zero-field NMR J-spectra. We will begin with spin systems having simple XA_n topologies, and perturbation theory will be used to extend to more complicated $(XA_n)B_m$ spin topologies. In order to demonstrate the further applicability to more complex topologies, necessary for chemical analysis, we will conclude with a discussion of benzene derivatives, where the consistent perturbation of the phenyl ring protons yields a clear spectral fingerprint. This chapter includes content from the following three publications:

- Theis, T., Blanchard, J.W., Butler, M.C., Ledbetter, M.P., Budker, D., and Pines, A. Chemical Analysis Using J-Coupling Multiplets in Zero-Field NMR. *Chem. Phys. Lett.* **580**, 160-165. (2013)

- Butler, M.C., Ledbetter, M.P., Theis, T., Blanchard, J.W., Budker, D., and Pines, A. Multiplets at zero magnetic field: The geometry of zero-field NMR. *J. Chem. Phys.* **138** (18), 184202. (2013)

- Blanchard, J.W., Ledbetter, M.P., Theis, T., Butler, M.C., Budker, D., and Pines, A. High-Resolution Zero-Field NMR J-Spectroscopy of Aromatic Compounds. *J. Am. Chem. Soc.* **135** (9), 3607-3612. (2013)

In the absence of magnetic fields, the Zeeman interaction, and thus the chemical shift, vanishes, leaving an isotropic fluid system to evolve only under electron-mediated scalar couplings (J-couplings) between spins in a molecule. Even in the absence of chemical shifts, the high sensitivity of J-couplings to subtle changes in geometry and electronic structure makes them a valuable source of chemical information. Owing to continued progress in quantum chemical calculations of spin–spin couplings [92, 31, 93], there now exists a number of techniques for analysis and interpretation of J-coupling constants, ranging from empirical Karplus[94]-type equations to newer techniques involving spin–spin coupling density surfaces [95, 96], double finite perturbation theory calculations [97], and decomposition of J-couplings and the Ramsey [32] terms (Fermi contact, spin dipole, diamagnetic spin orbit, and paramagnetic spin orbit) into orbital contributions [98, 99]. Using these techniques, it has been possible to solve problems of molecular configuration [100, 101, 102, 103], bond character [104], molecular motion [105, 106], and intermolecular interactions [107, 108].

This section will detail a method for the interpretation of zero-field J-spectra wherein a preferred basis set for the spins is determined by the one-bond coupling between two heteronuclei, and smaller long-range couplings are treated as perturbations on this primary zeroth-order interaction. For systems consisting of three sets of magnetically equivalent spins, this analysis leads to simple analytical expressions that fully describe the zero-field spectra. In order to demonstrate the viability of J-spectroscopy for chemical fingerprinting, high-resolution zero-field J-spectra for a series of labeled aromatic molecules have been measured. The general qualitative structures of the spectra are consistent with patterns for simpler spin systems, and furthermore, the spectra for different molecules are unique and easily distinguished from one another. The narrow linewidths (as low as 11 mHz for benzene-$^{13}C_1$) permit precise measurement of long-range J-couplings, which encompass a wealth of chemically relevant information.

5.1 XA_n Systems

5.1.1 Energy Levels

In Section (4.2) we discussed the eigenstates for a two-spin system, XA, which consist of three triplet states and a singlet state separated by the J-coupling energy. We now demonstrate how to obtain the eigenstates and energies for XA_n systems. For XA_n spin systems in isotropic solutions, the J-coupling Hamiltonian is written as

$$\mathcal{H}^{(0)} = \hbar J_{AX} \mathbf{K}_A \cdot \mathbf{S}, \tag{5.1}$$

where $\mathbf{K}_A = \sum_j \mathbf{I}_{A,j}$ is the total angular momentum of spins A and $\mathbf{S}$ is the angular momentum of spin X.

The eigenstates of $\mathcal{H}_0$ are those of $\mathbf{F}_A^2$ and $\mathbf{F}_{A,z}$, where

$$\mathbf{F}_A = \mathbf{K}_A + \mathbf{S} \tag{5.2}$$

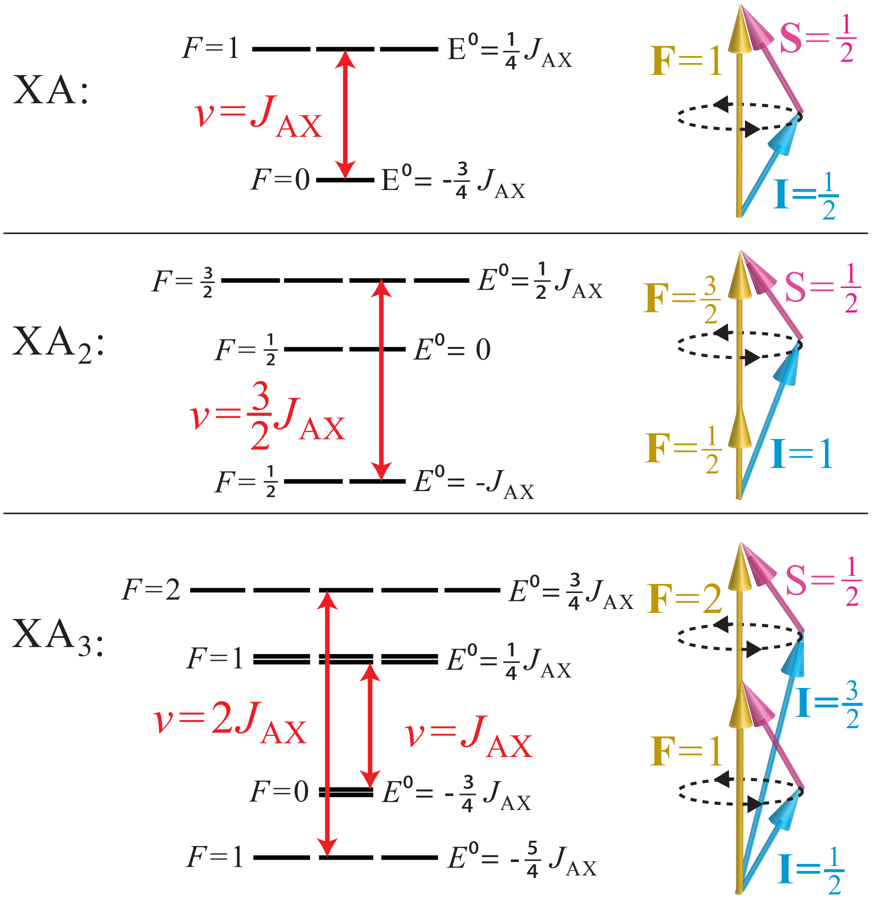

Figure 5.1: Eigenstates, energies, and allowed transitions for XA_n spin systems. Right panel shows geometric model for the addition of angular momenta and precession about the total angular momentum. Double lines represent degenerate energy levels. For clarity, only a single transition is shown for each frequency.

is the total spin angular momentum, and may be written as $|K_A, S, F_A, m_{F_A}\rangle$ where K_A, S, F_A, and m_{F_A} are the eigenvalues of $\mathbf{K}_A$, $\mathbf{S}$, $\mathbf{F}_A^2$, and $\mathbf{F}_{A,z}$, respectively. K_A and S are only kept for bookkeeping purposes, and will generally be omitted for clarity.

In order to compute the scalar product in Eq. (5.1), we write

$$\mathbf{F}_A^2 = (\mathbf{K}_A + \mathbf{S})^2 = \mathbf{K}_A^2 + \mathbf{S}^2 + 2\mathbf{K}_A \cdot \mathbf{S}, \tag{5.3}$$

so that the scalar product may be written as

$$\mathbf{K}_A \cdot \mathbf{S} = \frac{1}{2}\left(\mathbf{F}_A^2 - \mathbf{K}_A^2 - \mathbf{S}^2\right). \tag{5.4}$$

Using Eq. (5.4) in Eq. (5.1), we find that the states $|F_A, m_{F_A}\rangle$ have energy

$$\begin{aligned} E^{(0)} =& \frac{J_{AX}}{2} \langle F_A, m_{F_A}| \left(\mathbf{F}_A^2 - \mathbf{K}_A^2 - \mathbf{S}^2\right) |F_A, m_{F_A}\rangle \\ =& \frac{J_{AX}}{2} \left[F_A(F_A + 1) - K_A(K_A + 1) - S(S + 1)\right] \end{aligned} \tag{5.5}$$

and degeneracy $2F_A + 1$. The energy levels for XA, XA$_2$, and XA$_3$ systems are shown in Fig. 5.1, along with a geometric model for the addition of angular momenta and precession about the total angular momentum.

5.1.2 Selection Rules and Amplitudes

Because the detected magnetization, $M_z(t) \propto \mathrm{Tr}\left[\rho(t) \sum_j \gamma_j I_{j,z}\right]$, is a sum of vector operators with magnetic quantum number zero, observable coherences only arise between states that differ by one quantum of total angular momentum $\mathbf{F}_A$, $\Delta F_A = 0, \pm 1$ with $\Delta m_{F_A} = 0$. The equivalence of the spins A$_n$ imposes an additional selection rule, $\Delta K_A = 0$, because the Hamiltonian commutes with $\mathbf{K}_A^2$. Using these considerations, one may derive [109] that the spectrum for an XA system consists of one peak at J_{AX}, the spectrum for an XA$_2$ system consists of one peak at $\frac{3}{2}J_{AX}$, and the spectrum for an XA$_3$ system consists of two peaks at J_{AX} and $2J_{AX}$.

Relative amplitudes can be determined by comparing the transition matrix elements,

$$A_{nm} = \left\langle n \middle| \sum_j \gamma_j I_{j,z} \middle| m \right\rangle^2, \tag{5.6}$$

where $|m\rangle$ and $|n\rangle$ are shorthand for the initial ($|K_A, S, F', m_F\rangle$) and final ($|K_A, S, F, m_F\rangle$) states, respectively. The transition matrix elements may then be computed in terms of the uncoupled basis as

$$\begin{aligned} A_{nm} &= \left[\sum_{\substack{m_{K_A} m_S \\ m'_{K_A} m'_S}} \langle F_A m_{F_A} | K_A S\, m_{K_A} m_S \rangle \langle K_A S\, m_{K_A} m_S | B_z(\gamma_A K_{A,z} + \gamma_A S_z) | K_A S\, m'_{K_A} m'_S \rangle \right. \\ &\qquad\qquad \left. \times \langle K_A S\, m'_{K_A} m'_S | F'_A m_{F_A} \rangle \right]^2 \\ &= \left[\sum_{m_{K_A} m_S} \langle K_A S\, m_{K_A} m_S | F_A m_{F_A} \rangle \langle K_A S\, m_{K_A} m_S | F'_A m_{F_A} \rangle (\gamma_A m_{K_A} + \gamma_S m_S) \right]^2 , \end{aligned} \tag{5.7}$$

where $\langle K_A S\, m_{K_A} m_S | F_A m_{F_A} \rangle$, etc. are the Clebsch-Gordan coefficients, and where we have made use of the selection rules $\Delta K = \Delta S = \Delta m_S = \Delta m_{K_A} = \Delta m_{F_A} = 0$.

5.1.3 Example XA_n Spectra

Figure 5.2 shows spectra for formic acid-^{13}C, an XA system; formaldehyde-^{13}C, an XA_2 system; and methanol-^{13}C, an XA_3 system. The formic acid spectrum consists of a single peak at $^1J_{\mathrm{CH}} = 221.1$ *Hz*, as expected for an XA system. Formaldehyde, an XA_2 system, has a single peak at $\frac{3}{2} \times {}^1J_{\mathrm{CH}} = 245.8$ *Hz*. The methanol spectrum consists of two peaks at $^1J_{\mathrm{CH}} = 141.0$ *Hz* and $2 \times {}^1J_{\mathrm{CH}} = 282.0$ *Hz*, as predicted by the previous sections for an XA_3 spin system. The specific transitions are those depicted in Fig. 5.1.

5.1.4 $^{14}NH_4^+$ and $^{15}NH_4^+$: Variations on XA_4

An interesting example of basic zero-field J-spectroscopy is given by the ammonium ion NH_4^+, an XA_4 system where X may be either spin-1 or spin-$\frac{1}{2}$ if the nitrogen nucleus is ^{14}N or ^{15}N, respectively. The tetrahedral symmetry of NH_4^+ prevents rapid quadrupolar relaxation from the ^{14}N nucleus, yielding one of very few cases where sharp zero-field spectra may be measured for molecules containing quadrupolar nuclei. Figure 5.3 shows the zero-field J-spectrum for a roughly 60:40 mixture of $^{15}NH_4Cl$ and $^{14}NH_4Cl$ dissolved in an acidic aqueous solution ($\sim$ 6 M NH_4Cl, $\sim$ 1 M HCl).

The spectrum in Fig. 5.3 is readily understood through application of Eq. (5.5) for the possible states that can be formed via angular momentum addition rules. For an XA_4 system, $K_A = 0, 1, 2$ yielding in all cases three separate angular momentum manifolds due to the $\Delta K_A = 0$ selection rule discussed previously. For $^{15}NH_4^+$, $S = 1/2$, so the possible states are $K_A = 0$, $F_A = \frac{1}{2}$; $K_A = 1$,

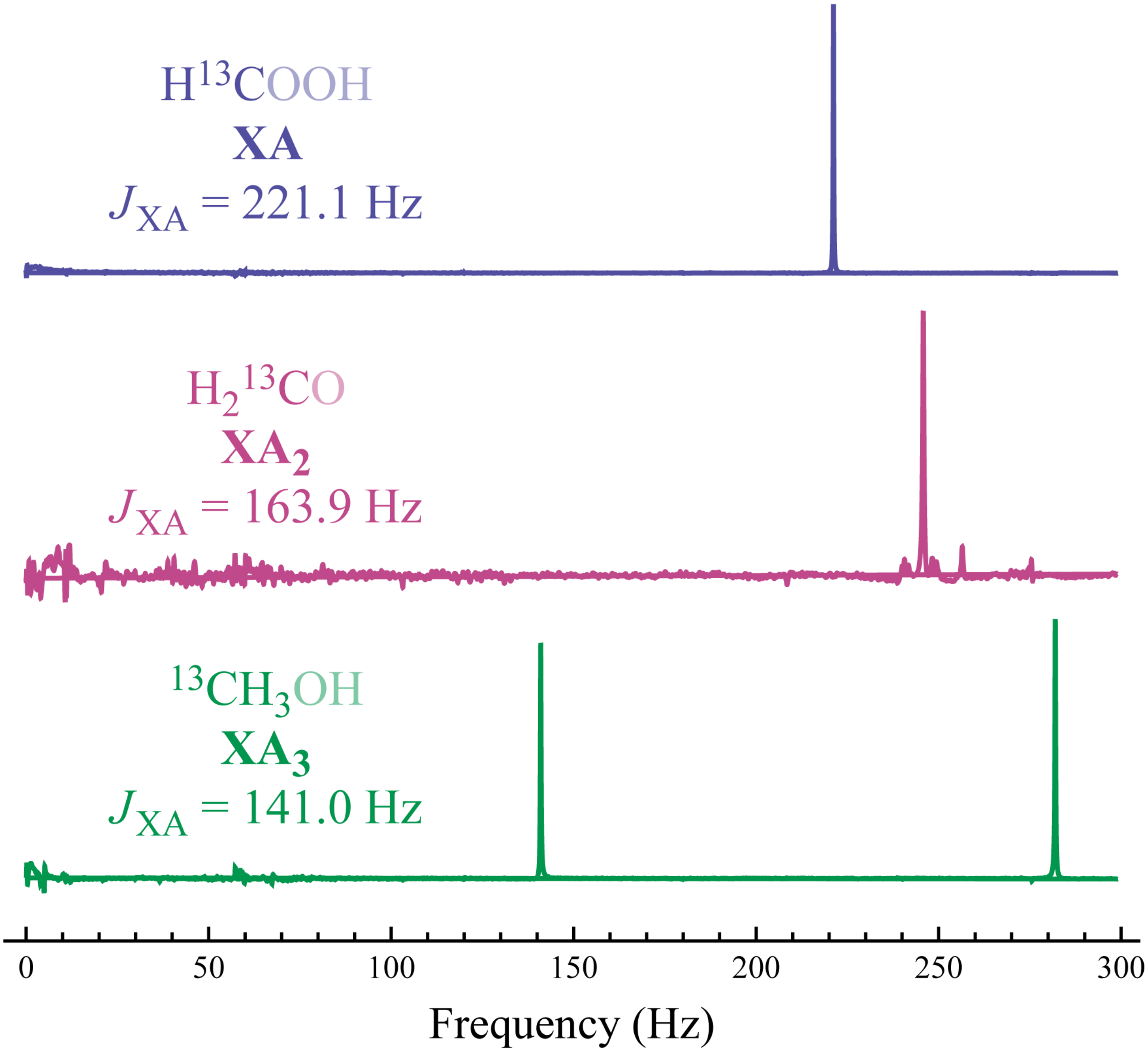

Figure 5.2: Zero-field *J*-spectra of formic acid-^{13}C, formaldehyde-^{13}C, and methanol-^{13}C, as examples of XA, XA_2, and XA_3 spin systems, respectively.

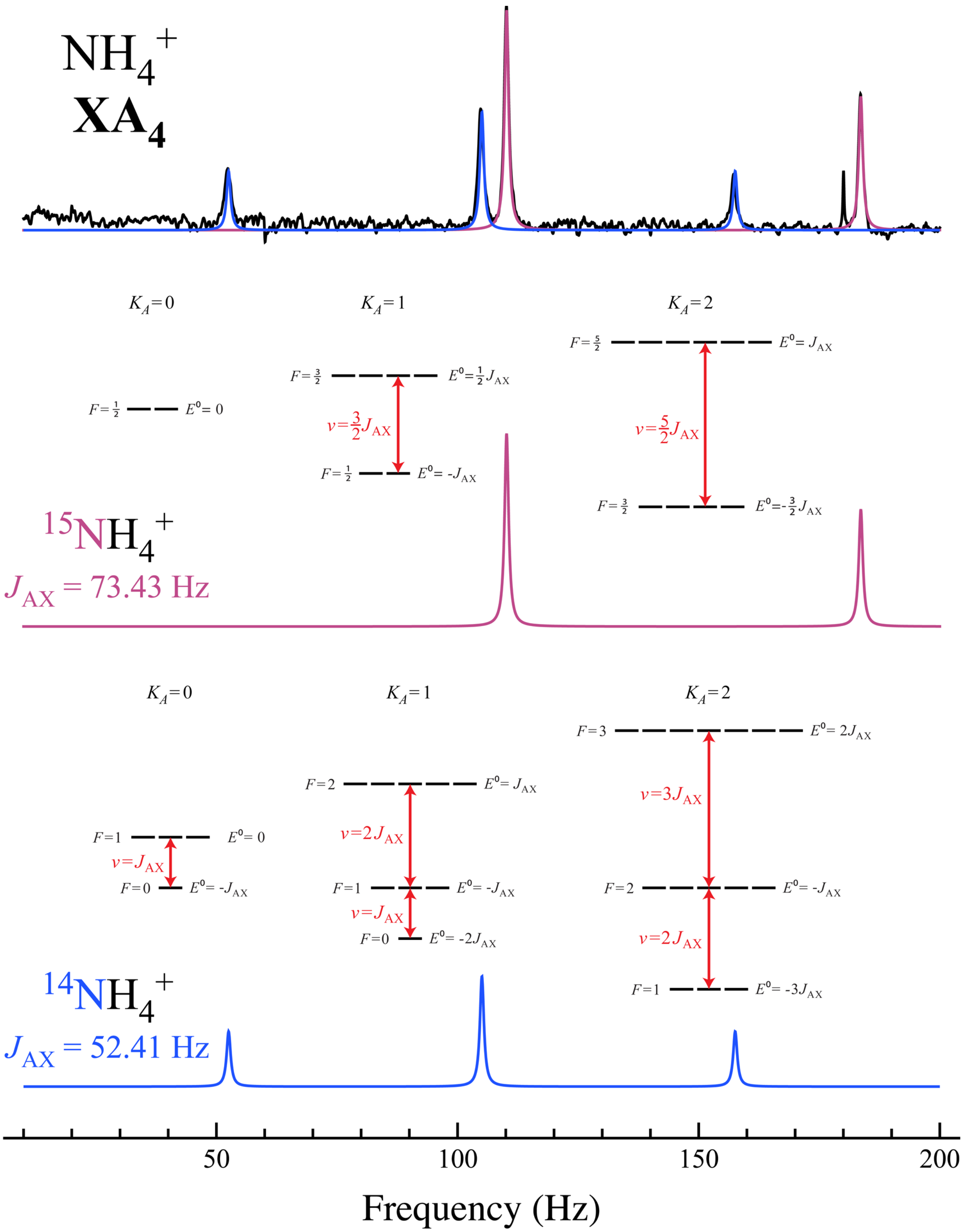

Figure 5.3: Zero-field J-spectra of a mixture of $^{14}NH_4Cl$ and $^{15}NH_4Cl$, as examples of XA_4 spin systems containing spin-1 and spin-$\frac{1}{2}$ heteronuclei, respectively.

$F_A = \frac{1}{2}, \frac{3}{2}$; $K_A = 2$, $F_A = \frac{3}{2}, \frac{5}{2}$. The energies of these states are

$$\begin{aligned}
E^{(0)}\left(K_A = 0, S = \frac{1}{2}, F_A = \frac{1}{2}\right) &= 0, \\
E^{(0)}\left(K_A = 1, S = \frac{1}{2}, F_A = \frac{1}{2}\right) &= -J_{\mathrm{AX}}, \\
E^{(0)}\left(K_A = 1, S = \frac{1}{2}, F_A = \frac{3}{2}\right) &= \frac{1}{2}J_{\mathrm{AX}}, \\
E^{(0)}\left(K_A = 2, S = \frac{1}{2}, F_A = \frac{3}{2}\right) &= -\frac{3}{2}J_{\mathrm{AX}}, \\
E^{(0)}\left(K_A = 2, S = \frac{1}{2}, F_A = \frac{5}{2}\right) &= J_{\mathrm{AX}}.
\end{aligned} \tag{5.8}$$

Then applying the selection rules from section 5.1.2, there are two allowed transitions, one in the $K_A = 1$ manifold between $F_A = \frac{1}{2} \leftrightarrow F_A = \frac{3}{2}$ states with frequency $\nu = \frac{3}{2} \times {}^1J_{^{15}\mathrm{N-H}}$, and one in the $K_A = 2$ manifold between $F_A = \frac{3}{2} \leftrightarrow F_A = \frac{5}{2}$ states with frequency $\nu = \frac{5}{2} \times {}^1J_{^{15}\mathrm{N-H}}$. For the spectrum in Fig. 5.3, these frequencies are $\left|\frac{3}{2} \times {}^1J_{^{15}\mathrm{N-H}}\right| = 110.45$ Hz and $\left|\frac{5}{2} \times {}^1J_{^{15}\mathrm{N-H}}\right| = 183.58$ Hz.

For $^{14}\mathrm{NH}_4^+$, $S = 1$, and the possible states are $K_A = 0$, $F_A = 0, 1$; $K_A = 1$, $F_A = 0, 1, 2$; $K_A = 2$, $F_A = 1, 2, 3$. The energies of these states are

$$\begin{aligned}
E^{(0)}\left(K_A = 0, S = 1, F_A = 0\right) &= -J_{\mathrm{AX}}, \\
E^{(0)}\left(K_A = 0, S = 1, F_A = 1\right) &= 0, \\
E^{(0)}\left(K_A = 1, S = 1, F_A = 0\right) &= 2J_{\mathrm{AX}}, \\
E^{(0)}\left(K_A = 1, S = 1, F_A = 0\right) &= -J_{\mathrm{AX}}, \\
E^{(0)}\left(K_A = 1, S = 1, F_A = 2\right) &= 0, \\
E^{(0)}\left(K_A = 2, S = 1, F_A = 1\right) &= -3J_{\mathrm{AX}}, \\
E^{(0)}\left(K_A = 2, S = 1, F_A = 2\right) &= -J_{\mathrm{AX}}, \\
E^{(0)}\left(K_A = 2, S = 1, F_A = 3\right) &= 2J_{\mathrm{AX}}.
\end{aligned} \tag{5.9}$$

There are then five transitions, one in the $K_A = 0$ manifold, two in the $K_A = 1$ manifold, and two in the $K_A = 2$ manifold. The $K_A = 0$ transition is between $F_A = 0 \leftrightarrow F_A = 1$ states with frequency $\nu = {}^1J_{^{14}\mathrm{N-H}}$. The $K_A = 1$ transitions are between $F_A = 0 \leftrightarrow F_A = 1$ states with frequency $\nu = {}^1J_{^{14}\mathrm{N-H}}$ and between $F_A = 1 \leftrightarrow F_A = 2$ states with frequency $\nu = 2 \times {}^1J_{^{14}\mathrm{N-H}}$. The $K_A = 2$ transitions are between $F_A = 1 \leftrightarrow F_A = 2$ states with frequency $\nu = 2 \times {}^1J_{^{14}\mathrm{N-H}}$ and between $F_A = 2 \leftrightarrow F_A = 3$ states with frequency $\nu = 3 \times {}^1J_{^{14}\mathrm{N-H}}$. The transitions at ${}^1J_{^{14}\mathrm{N-H}}$ and $2 \times {}^1J_{^{14}\mathrm{N-H}}$ of course overlap, so Fig. 5.3 has three peaks arising from $^{14}\mathrm{NH}_4^+$ at frequencies ${}^1J_{^{14}\mathrm{N-H}} = 52.41$ Hz, $2 \times {}^1J_{^{14}\mathrm{N-H}} = 104.82$ Hz, and $3 \times {}^1J_{^{14}\mathrm{N-H}} = 157.23$ Hz.

The difference in the ^{14}N−H and ^{15}N−H J-coupling frequencies is primarily due to the different gyromagnetic ratios of the two nuclei. From multiple measurements of the same $\mathrm{NH_4Cl}$ sample, the ratio of the J-couplings is $|J_{^{15}\mathrm{N-H}}/J_{^{14}\mathrm{N-H}}| = 1.4012 \pm 0.0002$, as compared to $|\gamma_{^{15}\mathrm{N-H}}/\gamma_{^{14}\mathrm{N-H}}| = 1.4027$. The small difference between the ratios of $|J_{^{15}\mathrm{N-H}}/J_{^{14}\mathrm{N-H}}|$ and $|\gamma_{^{15}\mathrm{N-H}}/\gamma_{^{14}\mathrm{N-H}}|$ is likely due to the different vibrational energies of $^{14}NH_4^+$ and $^{15}NH_4^+$, leading to a slight difference in electron densities.

Additionally, the ^{14}N lines are generally 1.36±0.05 times broader than the ^{15}N lines, suggesting that the T_2 for $^{14}NH_4^+$ is slightly shorter than for $^{15}NH_4^+$. A rough measurement of T_1 times was performed by varying the sample polarization time between 5 and 40 s, yielding $T_1(^{14}N) = 12.5$ s, $T_1(^{15}N) = 15.5$ s.

5.2 (XA$_n$)B$_m$ Systems

5.2.1 First-Order Energy Levels

Because one-bond J-couplings are generally substantially larger than couplings to more distant spins, many molecular spin systems can be decomposed into an (XA$_n$) subgroup and another group of spins with smaller couplings to the X and A$_n$ spins [110]. An illustrative example are spin systems of the form (XA$_n$)B$_m$ where $J_{AX} \gg J_{AB}, J_{BX}$. To zeroth-order, where J_{AB} and J_{BX} are neglected, the system is described by $\mathcal{H}_0$, with energy levels as described in the previous section. The first-order perturbing Hamiltonian is then

$$\mathcal{H}^{(1)} = J_{BX}\mathbf{K}_B \cdot \mathbf{S} + J_{AB}\mathbf{K}_A \cdot \mathbf{K}_B. \tag{5.10}$$

In the same way that the evolution of XA$_n$ systems can be visualized in terms of vectors $\mathbf{S}$ and $\mathbf{K}_A$ precessing about $\mathbf{F}_A$, we can visualize (XA$_n$)B$_m$ systems to first order in terms of $\mathbf{F}_A$ and $\mathbf{I}_B$ precessing about the total angular momentum [110],

$$\mathbf{F} = \mathbf{F}_A + \mathbf{K}_B. \tag{5.11}$$

Because the motion of $\mathbf{S}$ and $\mathbf{K}_A$ about $\mathbf{F}_A$ is much faster than that of $\mathbf{F}_A$ and $\mathbf{I}_B$ about $\mathbf{F}$, the effect of the perturbing Hamiltonian is truncated so that, to first order, only the “parallel” components are preserved. This geometric picture corresponds to the formal description where the vectors are replaced with spin operators:

$$\mathcal{H}^{(1)} = J_{XB}\mathbf{S}^{\|} \cdot \mathbf{K}_B + J_{AB}\mathbf{K}_A^{\|} \cdot \mathbf{K}_B, \tag{5.12}$$

where

$$\mathbf{S}^{\|} = \frac{\langle \mathbf{S} \cdot \mathbf{F}_A \rangle}{\langle \mathbf{F}_A \cdot \mathbf{F}_A \rangle}\mathbf{F}_A \tag{5.13}$$

and

$$\mathbf{K}_A^{\|} = \frac{\langle \mathbf{K}_A \cdot \mathbf{F}_A \rangle}{\langle \mathbf{F}_A \cdot \mathbf{F}_A \rangle}\mathbf{F}_A \tag{5.14}$$

are the projections of $\mathbf{S}$ and $\mathbf{K}_A$ onto $\mathbf{F}_A$. Following algebraic manipulations along the lines of Eqs. (5.2)-(5.5), the perturbing Hamiltonian can then be written as

$$\mathcal{H}^{(1)} = \left(J_{XB}^{\|} + J_{AB}^{\|}\right)\mathbf{F}_A \cdot \mathbf{K}_B, \tag{5.15}$$

where

$$\begin{aligned} J_{BX}^{\|} &= J_{BX}\left[\frac{F_A(F_A+1) + S(S+1) - K_A(K_A+1)}{2F_A(F_A+1)}\right], \\ J_{AB}^{\|} &= J_{AB}\left[\frac{F_A(F_A+1) + K_A(K_A+1) - S(S+1)}{2F_A(F_A+1)}\right] \end{aligned} \tag{5.16}$$

$\lvert K_A, F_A, K_B, F\rangle$	$E^{(0)}$	$\Delta E^{(1)}$	$\Delta E^{(2)}$
$\left\lvert \frac{1}{2}, 1, \frac{3}{2}, \frac{5}{2}\right\rangle$	$\frac{1}{4}J_{\mathrm{AX}}$	$+\frac{3}{4}(J_{\mathrm{BX}} + J_{\mathrm{AB}})$	0
$\left\lvert \frac{1}{2}, 1, \frac{1}{2}, \frac{3}{2}\right\rangle$	$\frac{1}{4}J_{\mathrm{AX}}$	$+\frac{1}{4}(J_{\mathrm{BX}} + J_{\mathrm{AB}})$	0
$\left\lvert \frac{1}{2}, 1, \frac{3}{2}, \frac{3}{2}\right\rangle$	$\frac{1}{4}J_{\mathrm{AX}}$	$-\frac{1}{2}(J_{\mathrm{BX}} + J_{\mathrm{AB}})$	$\frac{15(J_{\mathrm{BX}}-J_{\mathrm{AB}})^2}{16J_{\mathrm{AX}}}$
$\left\lvert \frac{1}{2}, 1, \frac{1}{2}, \frac{1}{2}\right\rangle$	$\frac{1}{4}J_{\mathrm{AX}}$	$-\frac{1}{2}(J_{\mathrm{BX}} + J_{\mathrm{AB}})$	$\frac{3(J_{\mathrm{BX}}-J_{\mathrm{AB}})^2}{16J_{\mathrm{AX}}}$
$\left\lvert \frac{1}{2}, 1, \frac{1}{2}, \frac{1}{2}\right\rangle$	$\frac{1}{4}J_{\mathrm{AX}}$	$-\frac{5}{4}(J_{\mathrm{BX}} + J_{\mathrm{AB}})$	0
$\left\lvert \frac{1}{2}, 0, \frac{3}{2}, \frac{3}{2}\right\rangle$	$-\frac{3}{4}J_{\mathrm{AX}}$	0	$-\frac{15(J_{\mathrm{BX}}-J_{\mathrm{AB}})^2}{16J_{\mathrm{AX}}}$
$\left\lvert \frac{1}{2}, 0, \frac{1}{2}, \frac{1}{2}\right\rangle$	$-\frac{3}{4}J_{\mathrm{AX}}$	0	$-\frac{3(J_{\mathrm{BX}}-J_{\mathrm{AB}})^2}{16J_{\mathrm{AX}}}$

Table 5.1: Energy levels for an $(XA)B_3$ system (e.g. methyl formate-^{13}C) from first and second order perturbation theory.

are couplings scaled by the projections of $\mathbf{S}$ and $\mathbf{K}_A$ onto $\mathbf{F}_A$. The first-order energy corrections are then

$$\Delta E^{(1)} = \frac{1}{2}\left(J_{BX}^{\parallel} + J_{AB}^{\parallel}\right)\left[F(F+1) - F_A\left(F_A+1\right) - K_B\left(K_B+1\right)\right]. \tag{5.17}$$

As an example, we consider methyl formate-^{13}C, an $(XA)B_3$ spin system, the spectrum for which is shown in Fig. 5.4(a). To zeroth order, the ^{13}C and formyl proton form an XA system, with $^1J_{\mathrm{CH}} = 226.8$ Hz [110] and energy levels as shown in Fig. 5.4(b). The three equivalent methyl protons are coupled to the XA system via $^3J_{\mathrm{CH}} = 4.0$ Hz and $^4J_{\mathrm{HH}} = -0.8$ Hz [110]. Assuming that these protons possess a single spin $\mathrm{K}_B = 3/2$ yields the energy levels shown in Fig. 5.4(c), and the $\mathrm{K}_B = 1/2$ case yields those shown in Fig. 5.4(d). The spectrum simulated using first-order perturbation theory largely agrees with the experimental spectrum, through full numerical diagonalization reveals higher-order effects that cause small frequency shifts and lift degeneracies between some of the energy levels.

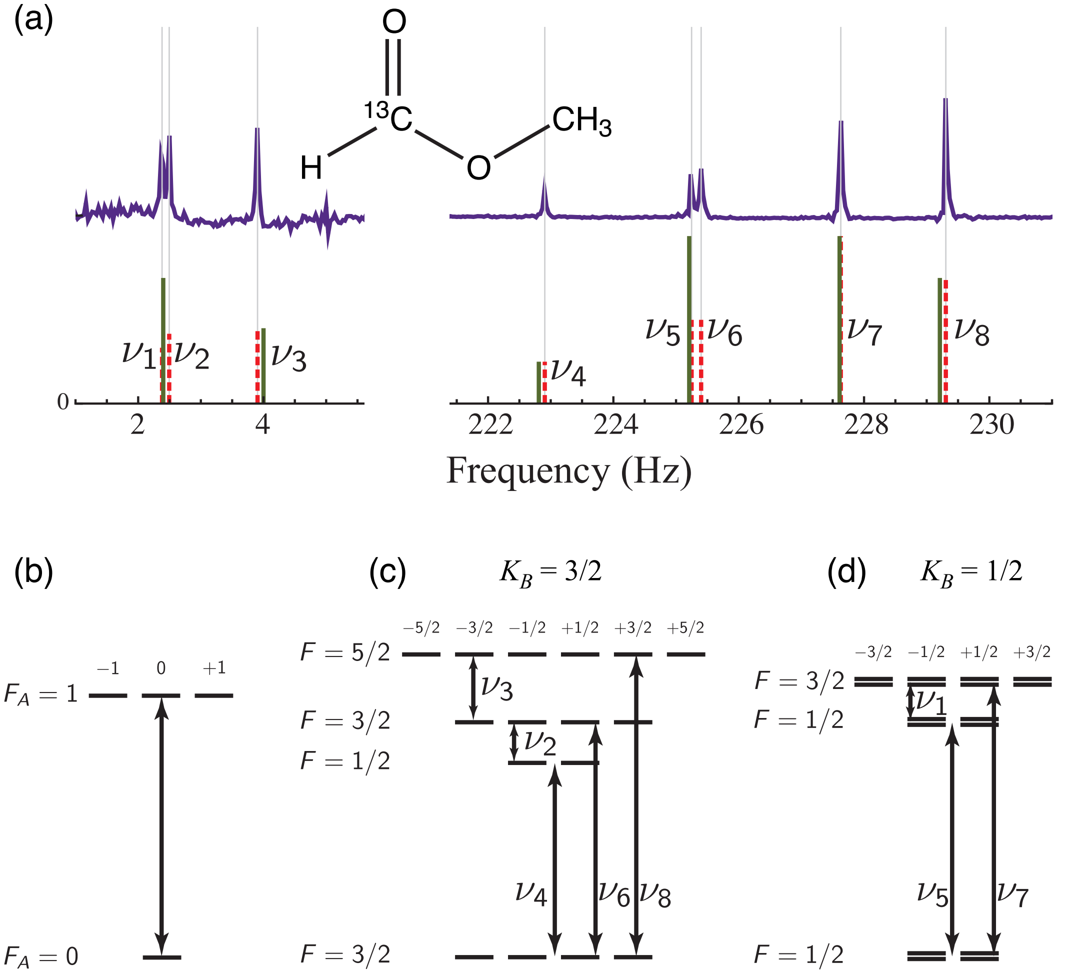

Figure 5.4: (a) Comparison of zero-field J-spectrum of methyl formate-^{13}C to the predicted spectrum simulated using first-order perturbation theory (dashed lines) and exact numerical diagonalization (solid lines). Eigenstates and allowed transitions are shown for (b) an unperturbed XA spin system (^{13}C-H) and an XA spin system perturbed by three equivalent methyl protons (B_3) with (c) $K_B = 3/2$ and (d) $K_B = 1/2$. Double lines represent degenerate energy levels due to the existence of two $K_B = 1/2$ representations of the methyl protons. Adapted with permission from Ref. [110]. ©2013 American Institute of Physics.

	$\lvert K_A, F_A, K_B, F\rangle_i$	$\lvert K_A, F_A, K_B, F\rangle_f$	Transition Frequency	2nd Order Correction
ν_1	$\left\lvert\frac{1}{2}, 1, \frac{1}{2}, \frac{1}{2}\right\rangle$	$\left\lvert\frac{1}{2}, 1, \frac{1}{2}, \frac{3}{2}\right\rangle$	$0 + \frac{3}{4}(J_{\text{BX}} + J_{\text{AB}})$	$-\frac{3(J_{\text{BX}}-J_{\text{AB}})^2}{16J_{\text{AX}}}$
ν_2	$\left\lvert\frac{1}{2}, 1, \frac{3}{2}, \frac{1}{2}\right\rangle$	$\left\lvert\frac{1}{2}, 1, \frac{3}{2}, \frac{3}{2}\right\rangle$	$0 + \frac{3}{4}(J_{\text{BX}} + J_{\text{AB}})$	$+\frac{15(J_{\text{BX}}-J_{\text{AB}})^2}{16J_{\text{AX}}}$
ν_3	$\left\lvert\frac{1}{2}, 1, \frac{3}{2}, \frac{3}{2}\right\rangle$	$\left\lvert\frac{1}{2}, 1, \frac{3}{2}, \frac{5}{2}\right\rangle$	$0 + \frac{5}{4}(J_{\text{BX}} + J_{\text{AB}})$	$-\frac{15(J_{\text{BX}}-J_{\text{AB}})^2}{16J_{\text{AX}}}$
ν_4	$\left\lvert\frac{1}{2}, 0, \frac{3}{2}, \frac{3}{2}\right\rangle$	$\left\lvert\frac{1}{2}, 1, \frac{3}{2}, \frac{1}{2}\right\rangle$	$J_{\text{AX}} - \frac{5}{4}(J_{\text{BX}} + J_{\text{AB}})$	$+\frac{15(J_{\text{BX}}-J_{\text{AB}})^2}{16J_{\text{AX}}}$
ν_5	$\left\lvert\frac{1}{2}, 0, \frac{1}{2}, \frac{1}{2}\right\rangle$	$\left\lvert\frac{1}{2}, 1, \frac{1}{2}, \frac{1}{2}\right\rangle$	$J_{\text{AX}} - \frac{1}{2}(J_{\text{BX}} + J_{\text{AB}})$	$+\frac{3(J_{\text{BX}}-J_{\text{AB}})^2}{8J_{\text{AX}}}$
ν_6	$\left\lvert\frac{1}{2}, 0, \frac{3}{2}, \frac{3}{2}\right\rangle$	$\left\lvert\frac{1}{2}, 1, \frac{3}{2}, \frac{3}{2}\right\rangle$	$J_{\text{AX}} - \frac{1}{2}(J_{\text{BX}} + J_{\text{AB}})$	$+\frac{15(J_{\text{BX}}-J_{\text{AB}})^2}{8J_{\text{AX}}}$
ν_7	$\left\lvert\frac{1}{2}, 0, \frac{1}{2}, \frac{1}{2}\right\rangle$	$\left\lvert\frac{1}{2}, 1, \frac{1}{2}, \frac{3}{2}\right\rangle$	$J_{\text{AX}} + \frac{1}{4}(J_{\text{BX}} + J_{\text{AB}})$	$+\frac{3(J_{\text{BX}}-J_{\text{AB}})^2}{16J_{\text{AX}}}$
ν_8	$\left\lvert\frac{1}{2}, 0, \frac{3}{2}, \frac{3}{2}\right\rangle$	$\left\lvert\frac{1}{2}, 1, \frac{3}{2}, \frac{5}{2}\right\rangle$	$J_{\text{AX}} + \frac{3}{4}(J_{\text{BX}} + J_{\text{AB}})$	$+\frac{15(J_{\text{BX}}-J_{\text{AB}})^2}{16J_{\text{AX}}}$

Table 5.2: Transition frequencies for an $(XA)B_3$ system (e.g. methyl formate-^{13}C) from first and second order perturbation theory.

5.2.2 General Matrix Elements

While the "geometric" approach presented above for understanding the first-order perturbation theory for (XA$_n$)B$_m$ is formally accurate and conveniently intuitive, it is also worthwhile to establish a more rigorous method for calculating the effect of the perturbing Hamiltonian. To this end, we will briefly review the derivation of analytical expressions for the matrix elements of the perturbing Hamiltonian for a general (XA$_n$)B$_m$ system. As before, we work in the basis eigenstates that are also eigenstates of $\mathbf{S}^2$, $\mathbf{K}_A^2$, $\mathbf{K}_B^2$, $\mathbf{F}_A^2$, $\mathbf{F}^2$, and F_z. We denote these states as $|K_A S\,(F_A) K_B F m_F\rangle$, though we will drop the S index for all systems where $\mathbf{S}$ is a spin-$\frac{1}{2}$ nucleus, and we will neglect m_F because the energy levels at zero field only depend on K_A, F_A, K_B, and F. Beginning with the term $\langle J_{\mathrm{BX}} \mathbf{K}_B \cdot \mathbf{S} \rangle$,

$$
\begin{aligned}
\langle K_A S\,(F_A) K_B F m_F | J_{\mathrm{BX}} \mathbf{K}_B \cdot \mathbf{S} | K_A S\,(F'_A) K_B F' m'_F \rangle = \\
\sum_{\substack{F'', m''_F, F''_B \\ F''', m'''_F, F'''_B}} \langle K_A S\,(F_A) K_B F m_F | K_A S\, K_B (F''_B) F'' m''_F \rangle \times \\
\left\langle K_A S\, K_B (F''_B) F'' m''_F \right| J_{\mathrm{BX}} \mathbf{K}_B \cdot \mathbf{S} \left| K_A S\, K_B (F'''_B) F''' m'''_F \right\rangle \times \\
\langle K_A S\, K_B (F'''_B) F''' m'''_F | K_A S\,(F'_A) K_B F' m'_F \rangle
\end{aligned}
\tag{5.18}
$$

where we have introduced $\mathbf{F}_B = \mathbf{K}_B + \mathbf{S}$. We can reduce some of our indices using some handy delta functions $\left\langle K_A S\,(F_A) K_B F m_F | K_A S\, K_B (F''_B) F'' m''_F \right\rangle \propto \delta_F^{F''} \delta_{m_F}^{m''_F}$ and we use $\mathbf{K}_B \cdot \mathbf{S} = 1/2(\mathbf{F}_B^2 - \mathbf{K}_B^2 - \mathbf{S}^2)$ to write

$$
\langle K_A S\, K_B (F''_B) F m_F | \mathbf{K}_B \cdot \mathbf{S} | K_A S\, K_B (F'''_B) F' m'_F \rangle = \frac{1}{2} \left[F''_B (F''_B + 1) - K_B (K_B + 1) - S\,(S+1) \right] \delta_F^{F'} \delta_{F''_B}^{F'''_B},
$$

thus obtaining

$$
\begin{aligned}
\langle K_A S\,(F_A) K_B F m_F | J_{\mathrm{BX}} \mathbf{K}_B \cdot \mathbf{S} | K_A S\,(F'_A) K_B F' m'_F \rangle = \\
\frac{J_{\mathrm{BX}}}{2} \sum_{F''_B} \langle K_A S\,(F_A) K_B F m_F | K_A S\, K_B (F_B) F m_F \rangle \times \left[F''_B (F''_B + 1) - K_B (K_B + 1) - S\,(S+1) \right] \times \\
\langle K_A S\, K_B (F''_B) F' m'_F | K_A S\,(F'_A) K_B F' m'_F \rangle\, \delta_F^{F'} \delta_{m_F}^{m'_F}.
\end{aligned}
\tag{5.19}
$$

For the sake of more comfortable notation we make the change $F''_B \to F_B$, and transform between bases with the Wigner 6-j symbols,

$$
\begin{aligned}
\langle K_A S\,(F_A) K_B F m_F | J_{\mathrm{BX}} \mathbf{K}_B \cdot \mathbf{S} | K_A S\,(F'_A) K_B F' m'_F \rangle = \\
\frac{J_{\mathrm{BX}}}{2} \sum_{F_B} (-1)^{K_A + K_B + S + F} \sqrt{(2F_A + 1)(2F_B + 1)} \begin{Bmatrix} K_A & S & F_A \\ K_B & F & F_B \end{Bmatrix} \times \\
\left[F_B (F_B + 1) - K_B (K_B + 1) - S\,(S+1) \right] \times \\
(-1)^{K_A + K_B + S + F'} \sqrt{(2F'_A + 1)(2F_B + 1)} \begin{Bmatrix} K_A & S & F'_A \\ K_B & F' & F_B \end{Bmatrix} \delta_F^{F'} \delta_{m_F}^{m'_F}.
\end{aligned}
\tag{5.20}
$$

This can then be simplified to

$$\begin{aligned}&\langle K_A S(F_A) K_B F m_F | J_{\rm BX} \mathbf{K}_B \cdot \mathbf{S} | K_A S(F'_A) K_B F' m'_F \rangle = \\ &\quad \frac{J_{\rm BX}}{2} \sum_{F_B} (2F_B+1)\sqrt{(2F_A+1)(2F'_A+1)} \begin{Bmatrix} K_A & S & F_A \\ K_B & F & F_B \end{Bmatrix} \times \begin{Bmatrix} K_A & S & F'_A \\ K_B & F' & F_B \end{Bmatrix} \times \\ &\qquad [F_B(F_B+1) - K_B(K_B+1) - S(S+1)]\, \delta_F^{F'} \delta_{m_F}^{m'_F}. \end{aligned} \tag{5.21}$$

The same procedure may be used for the $\langle J_{\rm AB} \mathbf{K}_A \cdot \mathbf{K}_B \rangle$ term:

$$\begin{aligned}&\langle K_A S(F_A) K_B F m_F | J_{\rm AB} \mathbf{K}_A \cdot \mathbf{K}_B | K_A S(F'_A) K_B F' m'_F \rangle = \\ &\quad \frac{J_{\rm AB}}{2} \sum_{K_{AB}} (2K_{AB}+1)\sqrt{(2F_A+1)(2F'_A+1)} \begin{Bmatrix} K_A & S & F_A \\ K_B & F & K_{AB} \end{Bmatrix} \times \begin{Bmatrix} K_A & S & F'_A \\ K_B & F' & K_{AB} \end{Bmatrix} \times \\ &\qquad [F_B(F_B+1) - K_B(K_B+1) - S(S+1)]\, \delta_F^{F'} \delta_{m_F}^{m'_F}, \end{aligned} \tag{5.22}$$

where K_{AB} is the combined angular momentum of the A and B spins. However, as K_{AB} is only used as a summation index, its physical meaning is of little consequence.

Note that the perturbing Hamiltonian is diagonal in K_A, K_B, S, F, and m_F, but not in F_A. In terms of perturbation theory, the off-diagonal terms mix states with different F_A, leading to second-order energy shifts, as discussed in the next subsection. First order shifts in the general basis are given as

$$\Delta E^{(1)} = \langle K_A S(F_A) K_B F m_F | (J_{\rm BX} \mathbf{K}_B \cdot \mathbf{S} + J_{\rm AB} \mathbf{K}_A \cdot \mathbf{K}_B) | K_A S(F'_A) K_B F m_F \rangle \tag{5.23}$$

and are readily computed by making use of Eqs. (5.21) and (5.22). Adventurous ZULF NMR practitioners could in principle extend this method to larger systems using 9-j, 12-j symbols, etc. (for N sets of equivalent spins X, A_n, B_m, C_r, D_s etc., the $3(N-1)$-j symbols are necessary).

5.2.3 Second-Order Corrections

Terms in $\mathcal{H}^{(1)}$ that connect states with the same K_A, S, K_B, F, but with different F_A give rise to second-order energy shifts, which may be calculated using non-degenerate perturbation theory:

$$\Delta E^{(2)}(n) = \sum_{m \neq n} \frac{\langle n | \mathcal{H}^{(1)} | m \rangle^2}{\langle n | \mathcal{H}^{(0)} | n \rangle - \langle m | \mathcal{H}^{(0)} | m \rangle} \tag{5.24}$$

where $|m\rangle \neq |n\rangle$ are states $\left|K_A, F_A, K_B, F\right\rangle \neq \left|K'_A, F'_A, K'_B, F'\right\rangle$, written in contracted form for convenience. For all $(\mathrm{XA}_n)\mathrm{B}_m$ systems that we have studied, second-order perturbation theory appears to reproduce exact numerical simulations almost perfectly.

5.2.4 Selection Rules and Transition Amplitudes

The selection rules for (XA$_n$)B$_m$ systems are simply a generalization of those presented in section 5.1.2, and are equivalently based on the calculation of non-zero elements of the transition matrix in Eq. (5.6).

$$\begin{aligned}
A_{nm} &= \Bigg[\sum_{m_S m_{K_A} m_{K_B}} \langle F_A, K_B, m_{F_A}, m_{K_B} | F, m_F \rangle \langle K_A, S, m_{K_A}, m_S | F_A, m_{F_A} \rangle \\
&\qquad \times \langle F'_A, K_B, m_{F_A}, m_{K_B} | F', m_F \rangle \langle K_A, S, m_{K_A}, m_S | F'_A, m_{F_A} \rangle (\gamma_A m_{K_A} + \gamma_B m_{K_B} + \gamma_S m_S) \Bigg]^2 \\
&= \Bigg[\sum_{m_S m_{K_A} m_{K_B}} \langle F_A, K_B, m_{K_A} + m_S, m_{K_B} | F, m_F \rangle \langle K_A, S, m_{K_A}, m_S | F_A, m_{F_A} \rangle \\
&\qquad \times \langle F'_A, K_B, m_{K_A} + m_S, m_{K_B} | F', m_F \rangle \langle K_A, S, m_{K_A}, m_S | F'_A, m_{F_A} \rangle (\gamma_A m_{K_A} + \gamma_B m_{K_B} + \gamma_S m_S) \Bigg]^2,
\end{aligned} \tag{5.25}$$

where $\langle K_A S m_{K_A} m_S | F_A m_{F_A} \rangle$, etc. are the Clebsch-Gordan coefficients. The relevant selection rules are $\Delta K_A = \Delta K_B = \Delta S = \Delta m_F = 0$, $\Delta F_A = 0, \pm 1$, and $\Delta F = 0, \pm 1$

5.2.5 Example $(XA_n)B_m$ Spectra

(XA_2)B: Formamide-^{15}N

The zero-field J-spectrum and energy levels for formamide-^{15}N, an (XA_2)B system, are shown in Fig. 5.5, along with spectra predicted using first-order perturbation and exact numerical diagonalization. The J-coupling values used in the simulation are $J_{\mathrm{AX}} = -89.3$ Hz, $J_{\mathrm{BX}} = -13.5$ Hz, and $J_{\mathrm{AB}} = 8$ Hz. Analytical expressions for the (XA_2)B energy levels from first and second order perturbation theory are listed in Table 5.3. The frequencies of allowed transitions are listed in Table 5.4, including corrections up to second order.

$\lvert K_A, F_A, K_B, F\rangle$	$E^{(0)}$	$\Delta E^{(1)}$	$\Delta E^{(2)}$
$\left\lvert 1, \frac{3}{2}, \frac{1}{2}, 2\right\rangle$	$\frac{1}{2}J_{\mathrm{AX}}$	$+\frac{1}{4}J_{\mathrm{BX}} + \frac{1}{2}J_{\mathrm{AB}}$	0
$\left\lvert 1, \frac{3}{2}, \frac{1}{2}, 1\right\rangle$	$\frac{1}{2}J_{\mathrm{AX}}$	$-\frac{5}{12}J_{\mathrm{BX}} - \frac{5}{6}J_{\mathrm{AB}}$	$+\frac{4(J_{\mathrm{BX}}-J_{\mathrm{AB}})^2}{27J_{\mathrm{AX}}}$
$\left\lvert 0, \frac{1}{2}, \frac{1}{2}, 1\right\rangle$	0	$+\frac{1}{4}J_{\mathrm{BX}}$	0
$\left\lvert 0, \frac{1}{2}, \frac{1}{2}, 0\right\rangle$	0	$-\frac{3}{4}J_{\mathrm{BX}}$	0
$\left\lvert 1, \frac{1}{2}, \frac{1}{2}, 1\right\rangle$	$-J_{\mathrm{AX}}$	$-\frac{1}{12}J_{\mathrm{BX}} + \frac{1}{3}J_{\mathrm{AB}}$	$-\frac{4(J_{\mathrm{BX}}-J_{\mathrm{AB}})^2}{27J_{\mathrm{AX}}}$
$\left\lvert 1, \frac{1}{2}, \frac{1}{2}, 0\right\rangle$	$-J_{\mathrm{AX}}$	$+\frac{1}{4}J_{\mathrm{BX}} - J_{\mathrm{AB}}$	0

Table 5.3: Energy levels for an (XA_2)B system (e.g. formamide-^{15}N) from first and second order perturbation theory.

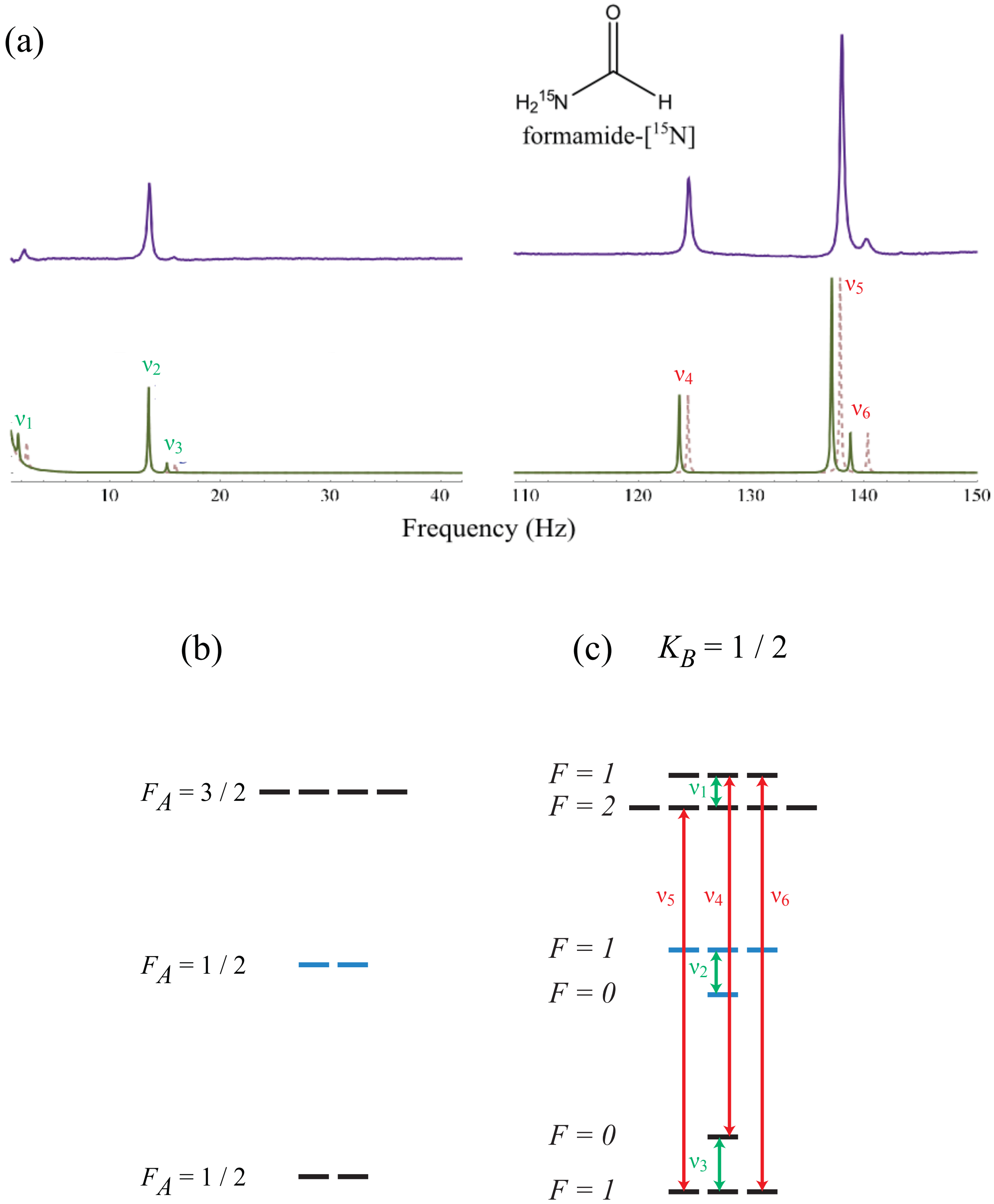

Figure 5.5: (a) Comparison of zero-field J-spectrum of formamide-^{15}N to the predicted spectrum simulated using first-order perturbation theory (solid lines) and exact numerical diagonalization (dashed lines). Eigenstates and allowed transitions are shown for (b) an unperturbed XA_2 spin system ($^{15}N\text{-}H_2$) and (c) an XA_2 spin system perturbed by a single proton (B) with $K_B = 1/2$. Blue lines denote states with $K_A = 0$, black lines denote states with $K_A = 1$. Adapted with permission from Ref. [66]. ©2013 Elsevier.

	$\lvert K_A, F_A, K_B, F\rangle_i$	$\lvert K_A, F_A, K_B, F\rangle_f$	Transition Frequency	2nd Order Correction
ν_1	$\left\lvert 1, \frac{3}{2}, \frac{1}{2}, 2\right\rangle$	$\left\lvert 1, \frac{3}{2}, \frac{1}{2}, 1\right\rangle$	$-\frac{2}{3}J_{\mathrm{BX}} - \frac{4}{3}J_{\mathrm{AB}}$	$+\frac{4(J_{\mathrm{BX}}-J_{\mathrm{AB}})^2}{27J_{\mathrm{AX}}}$
ν_2	$\left\lvert 0, \frac{1}{2}, \frac{1}{2}, 0\right\rangle$	$\left\lvert 0, \frac{1}{2}, \frac{1}{2}, 1\right\rangle$	$+J_{\mathrm{BX}}$	0
ν_3	$\left\lvert 1, \frac{1}{2}, \frac{1}{2}, 1\right\rangle$	$\left\lvert 1, \frac{1}{2}, \frac{1}{2}, 0\right\rangle$	$+\frac{1}{3}J_{\mathrm{BX}} - \frac{4}{3}J_{\mathrm{AB}}$	$+\frac{4(J_{\mathrm{BX}}-J_{\mathrm{AB}})^2}{27J_{\mathrm{AX}}}$
ν_4	$\left\lvert 1, \frac{1}{2}, \frac{1}{2}, 0\right\rangle$	$\left\lvert 1, \frac{3}{2}, \frac{1}{2}, 1\right\rangle$	$\frac{3}{2}J_{\mathrm{AX}} - \frac{2}{3}J_{\mathrm{BX}} + \frac{1}{6}J_{\mathrm{AB}}$	$+\frac{4(J_{\mathrm{BX}}-J_{\mathrm{AB}})^2}{27J_{\mathrm{AX}}}$
ν_5	$\left\lvert 1, \frac{1}{2}, \frac{1}{2}, 1\right\rangle$	$\left\lvert 1, \frac{3}{2}, \frac{1}{2}, 2\right\rangle$	$\frac{3}{2}J_{\mathrm{AX}} + \frac{1}{3}J_{\mathrm{BX}} + \frac{1}{6}J_{\mathrm{AB}}$	$+\frac{4(J_{\mathrm{BX}}-J_{\mathrm{AB}})^2}{27J_{\mathrm{AX}}}$
ν_6	$\left\lvert 1, \frac{1}{2}, \frac{1}{2}, 1\right\rangle$	$\left\lvert 1, \frac{3}{2}, \frac{1}{2}, 1\right\rangle$	$\frac{3}{2}J_{\mathrm{AX}} - \frac{1}{3}J_{\mathrm{BX}} - \frac{7}{6}J_{\mathrm{AB}}$	$+\frac{8(J_{\mathrm{BX}}-J_{\mathrm{AB}})^2}{27J_{\mathrm{AX}}}$

Table 5.4: Transition frequencies for an $(XA_2)B$ system (e.g. formamide-^{15}N) from first and second order perturbation theory.

$(XA_2)B_3$: Ethanol-1-^{13}C

The zero-field J-spectrum and energy levels for ethanol-1-^{13}C, an $(XA_2)B_3$ system, are shown in Fig. 5.6, along with spectra predicted using first-order perturbation and exact numerical diagonalization. The J-coupling values used in the simulation are $J_{\mathrm{AX}} = 141$ Hz, $J_{\mathrm{BX}} = -4.65$ Hz, and $J_{\mathrm{AB}} = 7.1$ Hz. Analytical expressions for the $(XA_2)B_3$ energy levels from first and second order perturbation theory are listed in Table 5.5. The frequencies of allowed transitions are listed in Table 5.6, including corrections up to second order.

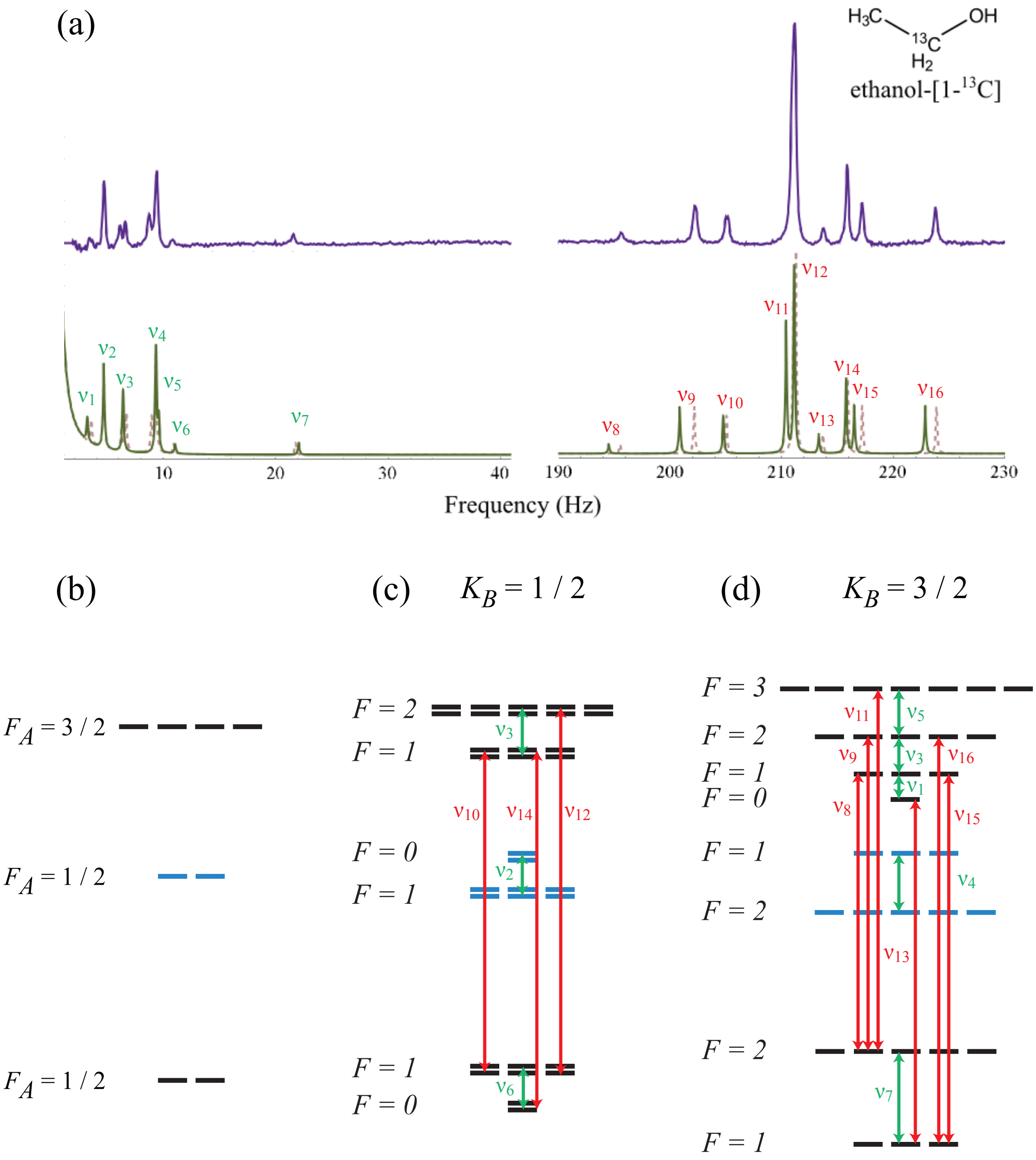

Figure 5.6: (a) Comparison of zero-field J-spectrum of ethanol-1-^{13}C to the predicted spectrum simulated using first-order perturbation theory (solid lines) and exact numerical diagonalization (dashed lines). Eigenstates and allowed transitions are shown for (b) an unperturbed XA_2 spin system (^{13}C-H_2) and an XA_2 spin system perturbed by three equivalent methyl protons (B_3) with (c) $K_B = 3/2$ and (d) $K_B = 1/2$. Blue lines denote states with $K_A = 0$, black lines denote states with $K_A = 1$. Double lines represent degenerate energy levels due to the existence of two $K_B = 1/2$ representations of the methyl protons. Adapted with permission from Ref. [66]. ©2013 Elsevier.

$\lvert K_A, F_A, K_B, F\rangle$	$E^{(0)}$	$\Delta E^{(1)}$	$\Delta E^{(2)}$
$\left\lvert 1, \frac{3}{2}, \frac{3}{2}, 3\right\rangle$	$\frac{1}{2}J_{\mathrm{AX}}$	$+\frac{3}{4}J_{\mathrm{BX}} + \frac{3}{2}J_{\mathrm{AB}}$	0
$\left\lvert 1, \frac{3}{2}, \frac{3}{2}, 2\right\rangle$	$\frac{1}{2}J_{\mathrm{AX}}$	$-\frac{1}{4}J_{\mathrm{BX}} - \frac{1}{2}J_{\mathrm{AB}}$	$+\frac{2(J_{\mathrm{BX}}-J_{\mathrm{AB}})^2}{3J_{\mathrm{AX}}}$
$\left\lvert 1, \frac{3}{2}, \frac{3}{2}, 1\right\rangle$	$\frac{1}{2}J_{\mathrm{AX}}$	$-\frac{11}{12}J_{\mathrm{BX}} - \frac{11}{6}J_{\mathrm{AB}}$	$+\frac{10(J_{\mathrm{BX}}-J_{\mathrm{AB}})^2}{27J_{\mathrm{AX}}}$
$\left\lvert 1, \frac{3}{2}, \frac{3}{2}, 0\right\rangle$	$\frac{1}{2}J_{\mathrm{AX}}$	$-\frac{5}{4}J_{\mathrm{BX}} - \frac{5}{2}J_{\mathrm{AB}}$	0
$\left\lvert 1, \frac{3}{2}, \frac{1}{2}, 1\right\rangle$	$\frac{1}{2}J_{\mathrm{AX}}$	$-\frac{5}{12}J_{\mathrm{BX}} - \frac{5}{6}J_{\mathrm{AB}}$	$+\frac{4(J_{\mathrm{BX}}-J_{\mathrm{AB}})^2}{27J_{\mathrm{AX}}}$
$\left\lvert 1, \frac{3}{2}, \frac{1}{2}, 0\right\rangle$	$\frac{1}{2}J_{\mathrm{AX}}$	$-\frac{3}{4}J_{\mathrm{BX}} - \frac{3}{2}J_{\mathrm{AB}}$	0
$\left\lvert 0, \frac{1}{2}, \frac{3}{2}, 1\right\rangle$	0	$-\frac{5}{4}J_{\mathrm{BX}}$	0
$\left\lvert 0, \frac{1}{2}, \frac{1}{2}, 0\right\rangle$	0	$-\frac{3}{4}J_{\mathrm{BX}}$	0
$\left\lvert 0, \frac{1}{2}, \frac{1}{2}, 1\right\rangle$	0	$+\frac{1}{4}J_{\mathrm{BX}}$	0
$\left\lvert 0, \frac{1}{2}, \frac{3}{2}, 2\right\rangle$	0	$+\frac{3}{4}J_{\mathrm{BX}}$	0
$\left\lvert 1, \frac{1}{2}, \frac{3}{2}, 2\right\rangle$	$-J_{\mathrm{AX}}$	$-\frac{1}{4}J_{\mathrm{BX}} + J_{\mathrm{AB}}$	$-\frac{2(J_{\mathrm{BX}}-J_{\mathrm{AB}})^2}{3J_{\mathrm{AX}}}$
$\left\lvert 1, \frac{1}{2}, \frac{3}{2}, 1\right\rangle$	$-J_{\mathrm{AX}}$	$+\frac{5}{12}J_{\mathrm{BX}} - \frac{5}{3}J_{\mathrm{AB}}$	$-\frac{10(J_{\mathrm{BX}}-J_{\mathrm{AB}})^2}{27J_{\mathrm{AX}}}$
$\left\lvert 1, \frac{1}{2}, \frac{1}{2}, 1\right\rangle$	$-J_{\mathrm{AX}}$	$-\frac{1}{12}J_{\mathrm{BX}} + \frac{1}{3}J_{\mathrm{AB}}$	$-\frac{4(J_{\mathrm{BX}}-J_{\mathrm{AB}})^2}{27J_{\mathrm{AX}}}$
$\left\lvert 1, \frac{1}{2}, \frac{1}{2}, 0\right\rangle$	$-J_{\mathrm{AX}}$	$+\frac{1}{4}J_{\mathrm{BX}} - J_{\mathrm{AB}}$	0

Table 5.5: Energy levels for an $(XA_2)B_3$ system (e.g. ethanol-1-^{13}C) from first and second order perturbation theory.

$(XA_3)B_2$: Ethanol-2-^{13}C

The zero-field J-spectrum and energy levels for ethanol-2-^{13}C, an $(XA_3)B_2$ system, are shown in Fig. 5.7, along with spectra predicted using first-order perturbation and exact numerical diagonalization. The J-coupling values used in the simulation are $J_{\mathrm{AX}} = 125.4$ Hz, $J_{\mathrm{BX}} = -2.2$ Hz, and $J_{\mathrm{AB}} = 7.0$ Hz. Analytical expressions for the $(XA_3)B_2$ energy levels from first order perturbation theory are listed in Table 5.7. The frequencies of allowed transitions are listed in Table 5.8.

	$\lvert K_A, F_A, K_B, F\rangle_i$	$\lvert K_A, F_A, K_B, F\rangle_f$	Transition Frequency	2nd Order Correction
ν_1	$\left\lvert 1, \frac{3}{2}, \frac{3}{2}, 0\right\rangle$	$\left\lvert 1, \frac{3}{2}, \frac{3}{2}, 1\right\rangle$	$\frac{1}{3}J_{\mathrm{BX}} + \frac{2}{3}J_{\mathrm{AB}}$	$+\frac{10(J_{\mathrm{BX}}-J_{\mathrm{AB}})^2}{27J_{\mathrm{AX}}}$
ν_2	$\left\lvert 0, \frac{1}{2}, \frac{1}{2}, 0\right\rangle$	$\left\lvert 0, \frac{1}{2}, \frac{1}{2}, 1\right\rangle$	$+J_{\mathrm{BX}}$	0
ν_3	$\left\lvert 1, \frac{1}{2}, \frac{1}{2}, 1\right\rangle$	$\left\lvert 1, \frac{1}{2}, \frac{1}{2}, 0\right\rangle$	$+\frac{1}{3}J_{\mathrm{BX}} - \frac{4}{3}J_{\mathrm{AB}}$	$-\frac{4(J_{\mathrm{BX}}-J_{\mathrm{AB}})^2}{27J_{\mathrm{AX}}}$
ν_3'	$\left\lvert 1, \frac{3}{2}, \frac{3}{2}, 1\right\rangle$	$\left\lvert 1, \frac{3}{2}, \frac{3}{2}, 2\right\rangle$	$+\frac{1}{3}J_{\mathrm{BX}} - \frac{4}{3}J_{\mathrm{AB}}$	$+\frac{8(J_{\mathrm{BX}}-J_{\mathrm{AB}})^2}{27J_{\mathrm{AX}}}$
ν_4	$\left\lvert 0, \frac{1}{2}, \frac{3}{2}, 2\right\rangle$	$\left\lvert 0, \frac{1}{2}, \frac{3}{2}, 1\right\rangle$	$-2J_{\mathrm{BX}}$	0
ν_5	$\left\lvert 1, \frac{3}{2}, \frac{3}{2}, 1\right\rangle$	$\left\lvert 1, \frac{3}{2}, \frac{3}{2}, 3\right\rangle$	$J_{\mathrm{BX}} + 2J_{\mathrm{AB}}$	$-\frac{2(J_{\mathrm{BX}}-J_{\mathrm{AB}})^2}{3J_{\mathrm{AX}}}$
ν_6	$\left\lvert 1, \frac{1}{2}, \frac{1}{2}, 1\right\rangle$	$\left\lvert 1, \frac{1}{2}, \frac{1}{2}, 0\right\rangle$	$+\frac{1}{3}J_{\mathrm{BX}} - \frac{4}{3}J_{\mathrm{AB}}$	$-\frac{4(J_{\mathrm{BX}}-J_{\mathrm{AB}})^2}{27J_{\mathrm{AX}}}$
ν_7	$\left\lvert 1, \frac{1}{2}, \frac{3}{2}, 1\right\rangle$	$\left\lvert 1, \frac{1}{2}, \frac{3}{2}, 2\right\rangle$	$-\frac{2}{3}J_{\mathrm{BX}} + \frac{8}{3}J_{\mathrm{AB}}$	$-\frac{8(J_{\mathrm{BX}}-J_{\mathrm{AB}})^2}{27J_{\mathrm{AX}}}$
ν_8	$\left\lvert 1, \frac{1}{2}, \frac{3}{2}, 2\right\rangle$	$\left\lvert 1, \frac{3}{2}, \frac{3}{2}, 1\right\rangle$	$\frac{3}{2}J_{\mathrm{AX}} - \frac{2}{3}J_{\mathrm{BX}} - \frac{17}{6}J_{\mathrm{AB}}$	$+\frac{28(J_{\mathrm{BX}}-J_{\mathrm{AB}})^2}{27J_{\mathrm{AX}}}$
ν_9	$\left\lvert 1, \frac{1}{2}, \frac{3}{2}, 2\right\rangle$	$\left\lvert 1, \frac{3}{2}, \frac{3}{2}, 2\right\rangle$	$\frac{3}{2}J_{\mathrm{AX}} + \frac{3}{2}J_{\mathrm{AB}}$	$+\frac{4(J_{\mathrm{BX}}-J_{\mathrm{AB}})^2}{3J_{\mathrm{AX}}}$
ν_{10}	$\left\lvert 1, \frac{1}{2}, \frac{1}{2}, 1\right\rangle$	$\left\lvert 1, \frac{3}{2}, \frac{1}{2}, 1\right\rangle$	$\frac{3}{2}J_{\mathrm{AX}} - \frac{1}{3}J_{\mathrm{BX}} - \frac{7}{6}J_{\mathrm{AB}}$	$+\frac{8(J_{\mathrm{BX}}-J_{\mathrm{AB}})^2}{27J_{\mathrm{AX}}}$
ν_{11}	$\left\lvert 1, \frac{1}{2}, \frac{3}{2}, 2\right\rangle$	$\left\lvert 1, \frac{3}{2}, \frac{3}{2}, 3\right\rangle$	$\frac{3}{2}J_{\mathrm{AX}} + J_{\mathrm{BX}} + \frac{1}{2}J_{\mathrm{AB}}$	$+\frac{2(J_{\mathrm{BX}}-J_{\mathrm{AB}})^2}{3J\mathrm{AX}}$
ν_{12}	$\left\lvert 1, \frac{1}{2}, \frac{1}{2}, 1\right\rangle$	$\left\lvert 1, \frac{3}{2}, \frac{1}{2}, 2\right\rangle$	$\frac{3}{2}J_{\mathrm{AX}} + \frac{1}{3}J_{\mathrm{BX}} + \frac{1}{6}J_{\mathrm{AB}}$	$+\frac{4(J_{\mathrm{BX}}-J_{\mathrm{AB}})^2}{27J_{\mathrm{AX}}}$
ν_{13}	$\left\lvert 1, \frac{1}{2}, \frac{3}{2}, 1\right\rangle$	$\left\lvert 1, \frac{3}{2}, \frac{3}{2}, 0\right\rangle$	$\frac{3}{2}J_{\mathrm{AX}} - \frac{5}{3}J_{\mathrm{BX}} - \frac{5}{6}J_{\mathrm{AB}}$	$+\frac{10(J_{\mathrm{BX}}-J_{\mathrm{AB}})^2}{27J_{\mathrm{AX}}}$
ν_{14}	$\left\lvert 1, \frac{1}{2}, \frac{1}{2}, 0\right\rangle$	$\left\lvert 1, \frac{3}{2}, \frac{1}{2}, 1\right\rangle$	$\frac{3}{2}J_{\mathrm{AX}} - \frac{2}{3}J_{\mathrm{BX}} + \frac{1}{6}J_{\mathrm{AB}}$	$+\frac{4(J_{\mathrm{BX}}-J_{\mathrm{AB}})^2}{27J_{\mathrm{AX}}}$
ν_{15}	$\left\lvert 1, \frac{1}{2}, \frac{3}{2}, 1\right\rangle$	$\left\lvert 1, \frac{3}{2}, \frac{3}{2}, 1\right\rangle$	$\frac{3}{2}J_{\mathrm{AX}} - \frac{4}{3}J_{\mathrm{BX}} - \frac{1}{6}J_{\mathrm{AB}}$	$+\frac{20(J_{\mathrm{BX}}-J_{\mathrm{AB}})^2}{27J_{\mathrm{AX}}}$
ν_{16}	$\left\lvert 1, \frac{1}{2}, \frac{3}{2}, 1\right\rangle$	$\left\lvert 1, \frac{3}{2}, \frac{3}{2}, 2\right\rangle$	$\frac{3}{2}J_{\mathrm{AX}} - \frac{2}{3}J_{\mathrm{BX}} + \frac{7}{6}J_{\mathrm{AB}}$	$+\frac{28(J_{\mathrm{BX}}-J_{\mathrm{AB}})^2}{27J_{\mathrm{AX}}}$

Table 5.6: Transition frequencies for an (XA$_2$)B$_3$ system (e.g. ethanol-1-^{13}C) from first and second order perturbation theory.

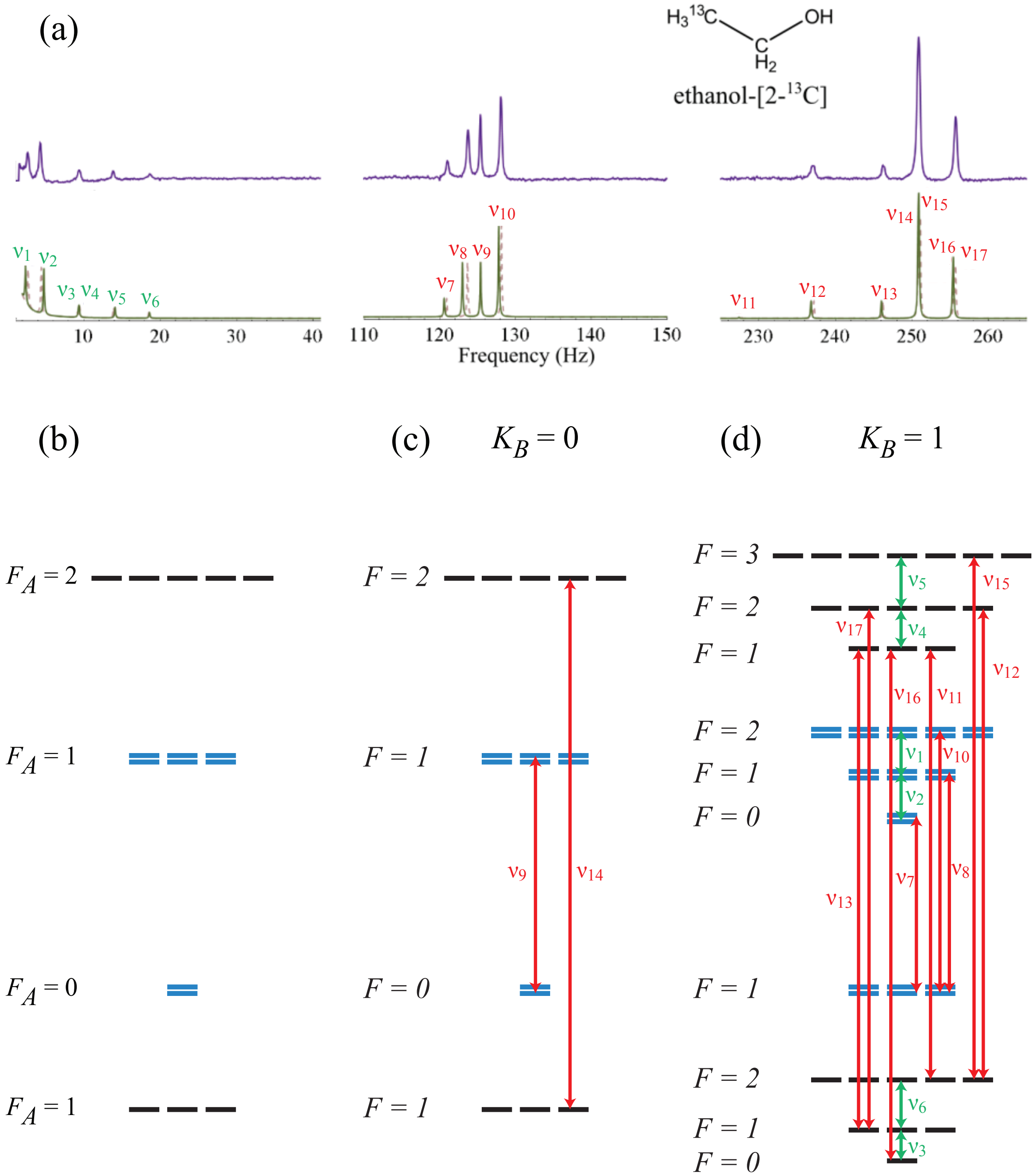

Figure 5.7: (a) Comparison of zero-field J-spectrum of ethanol-2-^{13}C to the predicted spectrum simulated using first-order perturbation theory (solid lines) and exact numerical diagonalization (dashed lines). Eigenstates and allowed transitions are shown for (b) an unperturbed XA_3 spin system (^{13}C-H_3) and an XA_3 spin system perturbed by two equivalent methyl protons (B_2) with (c) $K_B = 0$ and (d) $K_B = 1$. Blue lines denote states with $K_A = 1/2$, black lines denote states with $K_A = 3/2$. Double lines represent degenerate energy levels due to the existence of two $K_A = 1/2$ representations of the methyl protons. Adapted with permission from Ref. [66]. ©2013 Elsevier.

$\lvert K_A, F_A, K_B, F\rangle$	$E^{(0)}$	$\Delta E^{(1)}$
$\left\lvert\frac{3}{2},2,1,3\right\rangle$	$\frac{3}{4}J_{AX}$	$+\frac{1}{2}J_{BX}+\frac{3}{2}J_{AB}$
$\left\lvert\frac{3}{2},2,1,2\right\rangle$	$\frac{3}{4}J_{AX}$	$-\frac{1}{4}J_{BX}-\frac{3}{4}J_{AB}$
$\left\lvert\frac{3}{2},2,1,1\right\rangle$	$\frac{3}{4}J_{AX}$	$-\frac{3}{4}J_{BX}-\frac{9}{4}J_{AB}$
$\left\lvert\frac{3}{2},2,0,2\right\rangle$	$\frac{3}{4}J_{AX}$	0
$\left\lvert\frac{1}{2},1,1,2\right\rangle$	$\frac{1}{4}J_{AX}$	$+\frac{1}{2}J_{BX}+\frac{1}{2}J_{AB}$
$\left\lvert\frac{1}{2},1,1,1\right\rangle$	$\frac{1}{4}J_{AX}$	$-\frac{1}{2}J_{BX}-\frac{1}{2}J_{AB}$
$\left\lvert\frac{1}{2},1,1,0\right\rangle$	$\frac{1}{4}J_{AX}$	$-J_{BX}-J_{AB}$
$\left\lvert\frac{1}{2},1,0,1\right\rangle$	$\frac{1}{4}J_{AX}$	0
$\left\lvert\frac{1}{2},0,0,0\right\rangle$	$-\frac{3}{4}J_{AX}$	0
$\left\lvert\frac{1}{2},0,1,1\right\rangle$	$-\frac{3}{4}J_{AX}$	0
$\left\lvert\frac{3}{2},1,1,2\right\rangle$	$-\frac{5}{4}J_{AX}$	$-\frac{1}{4}J+\frac{5}{4}J_{BX}$
$\left\lvert\frac{3}{2},1,1,1\right\rangle$	$-\frac{5}{4}J_{AX}$	$+\frac{1}{4}J_{BX}-\frac{5}{4}J_{AB}$
$\left\lvert\frac{3}{2},1,1,0\right\rangle$	$-\frac{5}{4}J_{AX}$	$+\frac{1}{2}J_{BX}-\frac{5}{2}J_{AB}$
$\left\lvert\frac{3}{2},1,0,1\right\rangle$	$-\frac{5}{4}J_{AX}$	0

Table 5.7: Energy levels for an (XA$_3$)B$_2$ system (e.g. ethanol-2-^{13}C) from first order perturbation theory.

(XA)B$_4$: Glycerol-2-^{13}C

The zero-field J-spectrum and energy levels for glycerol-2-^{13}C, an (XA)B$_4$ system, are shown in Fig. 5.8, along with spectra predicted using first-order perturbation and exact numerical diagonalization. The J-coupling values used in the simulation are J_{AX} = 142.9 Hz, J_{BX} = −3.1 Hz, and J_{AB} = 6.3 Hz. Analytical expressions for the (XA)B$_4$ energy levels from first order perturbation theory are listed in Table 5.9. The frequencies of allowed transitions are listed in Table 5.10.

In general, one might expect the spin system of glycerol-2-^{13}C to be (XA)B$_2$B$'_2$ rather than (XA)B$_4$, with the magnetic equivalence broken by the four-bond $^4J_{HH}$ coupling between the two methylene groups. However, rotations about molecular bonds at frequencies much greater than $^4J_{HH}$ average away this symmetry-breaking effect, restoring magnetic equivalence. This does not occur in molecules with a more rigid topology, and it is possible that at lower temperatures, intramolecular hydrogen bonding in glycerol could hinder rotation sufficiently to make the two methylene groups magnetically inequivalent.

	$\lvert K_A, F_A, K_B, F\rangle_i$	$\lvert K_A, F_A, K_B, F\rangle_f$	Transition Frequency
ν_1	$\left\lvert\frac{1}{2}, 1, 1, 1\right\rangle$	$\left\lvert\frac{1}{2}, 1, 1, 2\right\rangle$	$J_{\mathrm{BX}} + J_{\mathrm{AB}}$
ν_2	$\left\lvert\frac{1}{2}, 1, 1, 1\right\rangle$	$\left\lvert\frac{1}{2}, 1, 1, 1\right\rangle$	$\frac{1}{2}J_{\mathrm{BX}} + \frac{1}{2}J_{\mathrm{AB}}$
ν_3	$\left\lvert\frac{3}{2}, 1, 1, 0\right\rangle$	$\left\lvert\frac{3}{2}, 1, 1, 1\right\rangle$	$-\frac{1}{4}J_{\mathrm{BX}} + \frac{5}{4}J_{\mathrm{AB}}$
ν_4	$\left\lvert\frac{3}{2}, 2, 1, 1\right\rangle$	$\left\lvert\frac{3}{2}, 2, 1, 2\right\rangle$	$\frac{1}{2}J_{\mathrm{BX}} + \frac{3}{2}J_{\mathrm{AB}}$
ν_5	$\left\lvert\frac{3}{2}, 2, 1, 2\right\rangle$	$\left\lvert\frac{3}{2}, 2, 1, 3\right\rangle$	$\frac{3}{4}J_{\mathrm{BX}} + \frac{9}{4}J_{\mathrm{AB}}$
ν_6	$\left\lvert\frac{3}{2}, 1, 1, 1\right\rangle$	$\left\lvert\frac{3}{2}, 1, 1, 2\right\rangle$	$-\frac{1}{2}J_{\mathrm{BX}} + \frac{5}{2}J_{\mathrm{AB}}$
ν_7	$\left\lvert\frac{1}{2}, 0, 1, 1\right\rangle$	$\left\lvert\frac{1}{2}, 1, 1, 0\right\rangle$	$J_{\mathrm{AX}} - J_{\mathrm{BX}} - J_{\mathrm{AB}}$
ν_8	$\left\lvert\frac{1}{2}, 0, 1, 1\right\rangle$	$\left\lvert\frac{1}{2}, 1, 1, 1\right\rangle$	$J_{\mathrm{AX}} - \frac{1}{2}J_{\mathrm{BX}} - \frac{1}{2}J_{\mathrm{AB}}$
ν_9	$\left\lvert\frac{1}{2}, 0, 0, 0\right\rangle$	$\left\lvert\frac{1}{2}, 1, 0, 1\right\rangle$	J_{AX}
ν_{10}	$\left\lvert\frac{1}{2}, 0, 1, 1\right\rangle$	$\left\lvert\frac{3}{2}, 1, 1, 2\right\rangle$	$J_{\mathrm{AX}} + \frac{1}{2}J_{\mathrm{BX}} + \frac{1}{2}J_{\mathrm{AB}}$
ν_{11}	$\left\lvert\frac{3}{2}, 1, 1, 2\right\rangle$	$\left\lvert\frac{3}{2}, 2, 1, 1\right\rangle$	$2J_{\mathrm{AX}} - \frac{1}{2}J_{\mathrm{BX}} - \frac{7}{2}J_{\mathrm{AB}}$
ν_{12}	$\left\lvert\frac{3}{2}, 1, 1, 2\right\rangle$	$\left\lvert\frac{3}{2}, 2, 1, 2\right\rangle$	$2J_{\mathrm{AX}} - 2J_{\mathrm{AB}}$
ν_{13}	$\left\lvert\frac{3}{2}, 1, 1, 1\right\rangle$	$\left\lvert\frac{3}{2}, 2, 1, 1\right\rangle$	$2J_{\mathrm{AX}} - J_{\mathrm{BX}} - J_{\mathrm{AB}}$
ν_{14}	$\left\lvert\frac{3}{2}, 1, 0, 1\right\rangle$	$\left\lvert\frac{3}{2}, 2, 0, 2\right\rangle$	$2J_{\mathrm{AX}}$
ν_{15}	$\left\lvert\frac{3}{2}, 1, 1, 2\right\rangle$	$\left\lvert\frac{3}{2}, 2, 1, 3\right\rangle$	$2J_{\mathrm{AX}} + \frac{3}{4}J_{\mathrm{BX}} + \frac{1}{4}J_{\mathrm{AB}}$
ν_{16}	$\left\lvert\frac{3}{2}, 1, 1, 0\right\rangle$	$\left\lvert\frac{3}{2}, 2, 1, 1\right\rangle$	$2J_{\mathrm{AX}} - \frac{5}{4}J_{\mathrm{BX}} + \frac{1}{4}J_{\mathrm{AB}}$
ν_{17}	$\left\lvert\frac{3}{2}, 1, 1, 1\right\rangle$	$\left\lvert\frac{3}{2}, 2, 1, 2\right\rangle$	$2J_{\mathrm{AX}} - \frac{1}{2}J_{\mathrm{BX}} + \frac{1}{2}J_{\mathrm{AB}}$

Table 5.8: Transition frequencies for an $(XA_3)B_2$ system (e.g. ethanol-2-^{13}C) from first order perturbation theory.

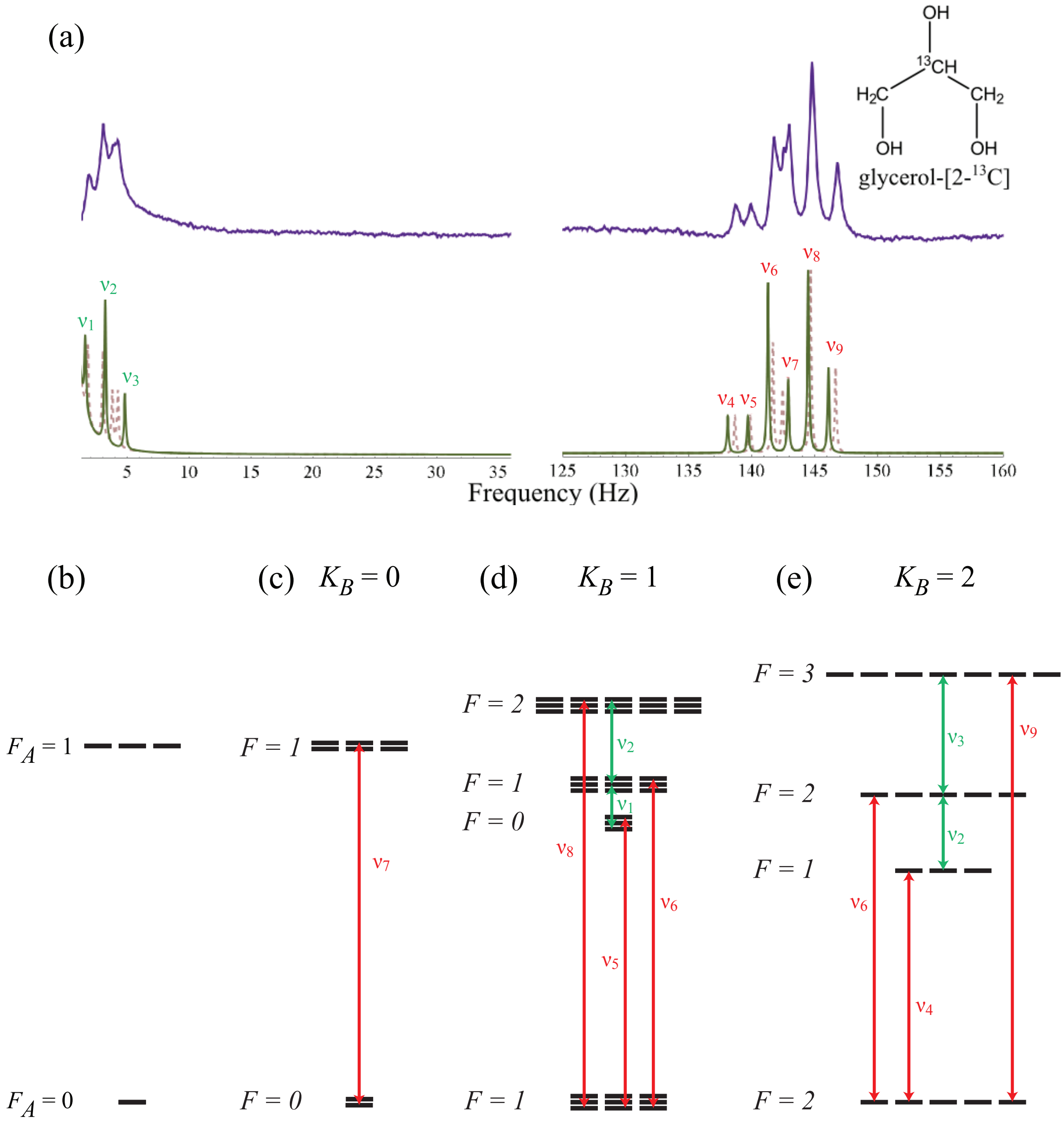

Figure 5.8: (a) Comparison of zero-field J-spectrum of glycerol-2-^{13}C to the predicted spectrum simulated using first-order perturbation theory (solid lines) and exact numerical diagonalization (dashed lines). Eigenstates and allowed transitions are shown for (b) an unperturbed X spin system (^{13}C-H) and an XA spin system perturbed by four equivalent protons (B_4) with (c) $K_B = 0$, (d) $K_B = 1$, and (e) $K_B = 2$. Double/triple lines represent degenerate energy levels due to the existence of two $K_B = 1$ and three $K_B = 2$ representations of the B_4 protons. Adapted with permission from Ref. [66]. ©2013 Elsevier.

$\lvert K_A, F_A, K_B, F\rangle$	$\mathrm{E}^{(0)}$	$\Delta\mathrm{E}^{(1)}$
$\left\lvert\frac{1}{2}, 1, 2, 3\right\rangle$	$\frac{1}{4}J_{\mathrm{AX}}$	$+(J_{\mathrm{BX}} + J_{\mathrm{AB}})$
$\left\lvert\frac{1}{2}, 1, 2, 2\right\rangle$	$\frac{1}{4}J_{\mathrm{AX}}$	$-\frac{1}{2}(J_{\mathrm{BX}} + J_{\mathrm{AB}})$
$\left\lvert\frac{1}{2}, 1, 2, 1\right\rangle$	$\frac{1}{4}J_{\mathrm{AX}}$	$-\frac{3}{2}(J_{\mathrm{BX}} + J_{\mathrm{AB}})$
$\left\lvert\frac{1}{2}, 1, 1, 2\right\rangle$	$\frac{1}{4}J_{\mathrm{AX}}$	$\frac{1}{2}(J_{\mathrm{BX}} + J_{\mathrm{AB}})$
$\left\lvert\frac{1}{2}, 1, 1, 1\right\rangle$	$\frac{1}{4}J_{\mathrm{AX}}$	$-\frac{1}{2}(J_{\mathrm{BX}} + J_{\mathrm{AB}})$
$\left\lvert\frac{1}{2}, 1, 1, 0\right\rangle$	$\frac{1}{4}J_{\mathrm{AX}}$	$-(J_{\mathrm{BX}} + J_{\mathrm{AB}})$
$\left\lvert\frac{1}{2}, 1, 0, 1\right\rangle$	$\frac{1}{4}J_{\mathrm{AX}}$	0
$\left\lvert\frac{1}{2}, 0, 2, 2\right\rangle$	$-\frac{3}{4}J_{\mathrm{AX}}$	0
$\left\lvert\frac{1}{2}, 0, 1, 1\right\rangle$	$-\frac{3}{4}J_{\mathrm{AX}}$	0
$\left\lvert\frac{1}{2}, 0, 0, 0\right\rangle$	$-\frac{3}{4}J_{\mathrm{AX}}$	0

Table 5.9: Energy levels for an (XA)B_4 system (e.g. glycerol-2-^{13}C) from first order perturbation theory.

5.3 More Complex Systems: Benzene Derivatives

In order to demonstrate the viability of J-spectroscopy for chemical fingerprinting, we measured high-resolution zero-field J-spectra for a series of labeled aromatic molecules: benzene-$^{13}C_1$, benzaldehyde-α-$^{13}C_1$, benzyl alcohol-α-$^{13}C_1$, toluene-α-$^{13}C_1$, and acetophenone-β-$^{13}C_1$. The general qualitative structures of the spectra are consistent with patterns reported previously for simpler spin systems, and furthermore, the spectra for different molecules are unique and easily distinguished from one another. The narrow linewidths (as low as 11 mHz for benzene-$^{13}C_1$) permit precise measurement of long-range J-couplings, which encompass a wealth of chemically-relevant information.

5.3.1 General XA$_n$ Structures

The zero-field J-spectra for the indicated compounds are shown in Fig. 5.9. For ease of comparison, the vertical axis has been normalized. The signal-to-noise ratio in the benzyl alcohol spectrum is somewhat lower on account of broader lines, which we suspect is related to hydrogen-bonding. The spectrum for each molecule is dominated by a strong 1-bond heteronuclear J-coupling, which is then perturbed by long-range couplings involving the phenyl-ring protons. Differences in molecular structure (i.e. functional groups) give rise to significantly different spectra, with little overlap between spectra for different molecules. The general qualitative structure, being dependent on the strong one-bond coupling, provides information about the substituent functional group (peaks around $^1J_{\mathrm{CH}}$ for CH, $3/2 \times {}^1J_{\mathrm{CH}}$ for CH_2, and two sets of peaks around $^1J_{\mathrm{CH}}$ and $2 \times {}^1J_{\mathrm{CH}}$ for CH_3),

	$\lvert K_A, F_A, K_B, F\rangle_i$	$\lvert K_A, F_A, K_B, F\rangle_f$	Transition Frequency
ν_1	$\left\lvert\frac{1}{2}, 1, 1, 0\right\rangle$	$\left\lvert\frac{1}{2}, 1, 1, 1\right\rangle$	$\frac{1}{2}(J_{\mathrm{BX}} + J_{\mathrm{AB}})$
ν_2	$\left\lvert\frac{1}{2}, 1, 1, 1\right\rangle$	$\left\lvert\frac{1}{2}, 1, 1, 2\right\rangle$	$J_{\mathrm{BX}} + J_{\mathrm{AB}}$
ν_3	$\left\lvert\frac{1}{2}, 1, 2, 2\right\rangle$	$\left\lvert\frac{1}{2}, 1, 2, 3\right\rangle$	$\frac{3}{2}(J_{\mathrm{BX}} + J_{\mathrm{AB}})$
ν_4	$\left\lvert\frac{1}{2}, 0, 2, 2\right\rangle$	$\left\lvert\frac{1}{2}, 1, 2, 1\right\rangle$	$J_{\mathrm{AX}} - \frac{3}{2}(J_{\mathrm{BX}} + J_{\mathrm{AB}})$
ν_5	$\left\lvert\frac{1}{2}, 0, 1, 1\right\rangle$	$\left\lvert\frac{1}{2}, 1, 1, 0\right\rangle$	$J_{\mathrm{AX}} - (J_{\mathrm{BX}} + J_{\mathrm{AB}})$
ν_6	$\left\lvert\frac{1}{2}, 0, 2, 2\right\rangle$	$\left\lvert\frac{1}{2}, 1, 2, 2\right\rangle$	$J_{\mathrm{AX}} - \frac{1}{2}(J_{\mathrm{BX}} + J_{\mathrm{AB}})$
ν_7	$\left\lvert\frac{1}{2}, 0, 0, 0\right\rangle$	$\left\lvert\frac{1}{2}, 1, 0, 1\right\rangle$	J_{AX}
ν_8	$\left\lvert\frac{1}{2}, 0, 1, 1\right\rangle$	$\left\lvert\frac{1}{2}, 1, 1, 2\right\rangle$	$J_{\mathrm{AX}} + \frac{1}{2}(J_{\mathrm{BX}} + J_{\mathrm{AB}})$
ν_9	$\left\lvert\frac{1}{2}, 0, 2, 2\right\rangle$	$\left\lvert\frac{1}{2}, 1, 2, 3\right\rangle$	$J_{\mathrm{AX}} + \frac{3}{2}(J_{\mathrm{BX}} + J_{\mathrm{AB}})$

Table 5.10: Transition frequencies for an (XA)B_4 system (e.g. glycerol-2-^{13}C) from first order perturbation theory.

and the measurement of splittings from long range J-couplings provides quantitative information about electronic structure and molecular configuration, as discussed below. Because nearly all peaks are resolved (with the exception of the peaks in acetophenone, where the couplings to the methyl group are small), the high-frequency portion of the spectrum (generally 100 – 300 Hz) is sufficient to fully determine all coupling frequencies without the need for consideration of the lower frequency peaks, which are often affected by low-frequency noise and potentially by spectral overlap in mixtures.

The basic qualitative structures of these spectra are consistent with previous work, with peaks at non-zero frequency arising due to J-couplings in molecules containing spins with at least two different gyromagnetic ratios. The simplest examples include ^{13}C-^{1}H in formate (^{13}CHOO^{-}), ^{13}C-^{1}H$_2$ in formaldehyde (^{13}CH$_2$O), and ^{13}C-^{1}H$_3$ in methanol (^{13}CH$_3$OH). We refer to these systems as XA, XA$_2$, and XA$_3$, respectively, where X is ^{13}C and A$_n$ represents a set of equivalent protons. Neglecting all couplings other than $^{1}J_{\mathrm{CH}}$, the molecules in this study have spectra that correspond to these simple XA$_n$ systems. The energy levels are given by Eq. (5.5)

Because the observable in our experiment is a vector operator, the selection rule for observable coherences is $\Delta F_A = 0, \pm 1$. Also, because the zero-field Hamiltonian commutes with both $\mathbf{K}^2$ and $\mathbf{S}^2$, $\Delta K = \Delta S = 0$. As a result, the allowed non-zero transition frequencies are $^{1}J_{\mathrm{CH}}$ for XA systems, $3/2 \times {}^{1}J_{\mathrm{CH}}$ for XA$_2$ systems, and both $^{1}J_{\mathrm{CH}}$ and $2 \times {}^{1}J_{\mathrm{CH}}$ for XA$_3$ systems. Similarly, the structure of the zero-field J-spectra for benzene-^{13}C$_1$ and benzaldehyde-α-^{13}C$_1$ both of which are zeroth-order XA systems consists of a cluster of peaks near $^{1}J_{\mathrm{CH}}$. The spectrum for benzyl alcohol-α-^{13}C$_1$, to zeroth-order an XA$_2$ system, consists of peaks near $3/2 \times {}^{1}J_{\mathrm{CH}}$, and the spectra of toluene-α-^{13}C$_1$ and acetophenone-β-^{13}C$_1$, which are zeroth-order XA$_3$ systems, consist of peaks near $^{1}J_{\mathrm{CH}}$ and $2 \times {}^{1}J_{\mathrm{CH}}$.

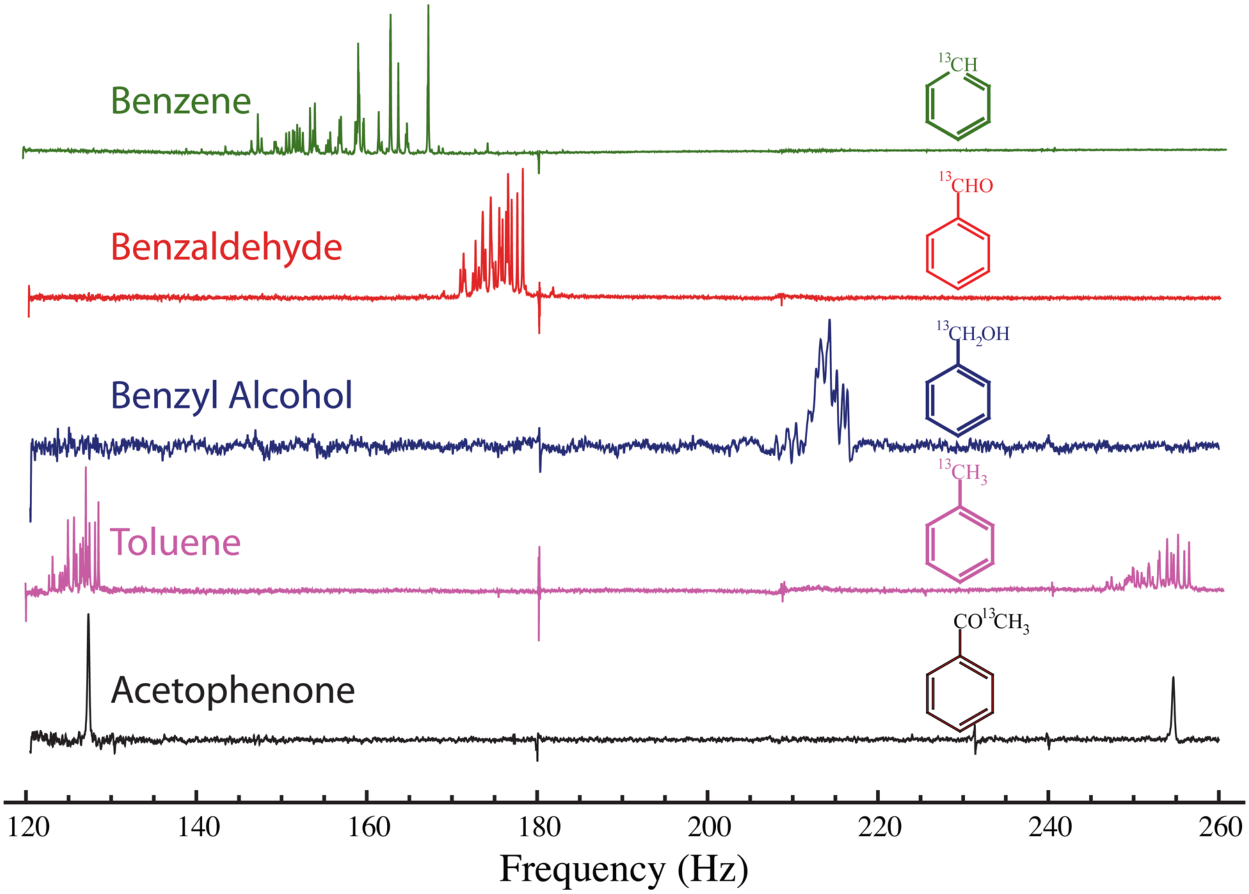

Figure 5.9: J-spectra of a series of benzene derivatives, highlighting the effects of different ^{13}CH$_n$ groups and their increasing displacement from the aromatic ring. Clusters of peaks appear at J for CH groups, at $3J/2$ for CH$_2$ groups, and at J and $2J$ for CH$_3$ groups. The spread of the peaks within the clusters decreases as the distance of the ^{13}C label from the aromatic ring increases. Signals at multiples of 60 Hz are the result of line noise. ©2013 American Chemical Society.

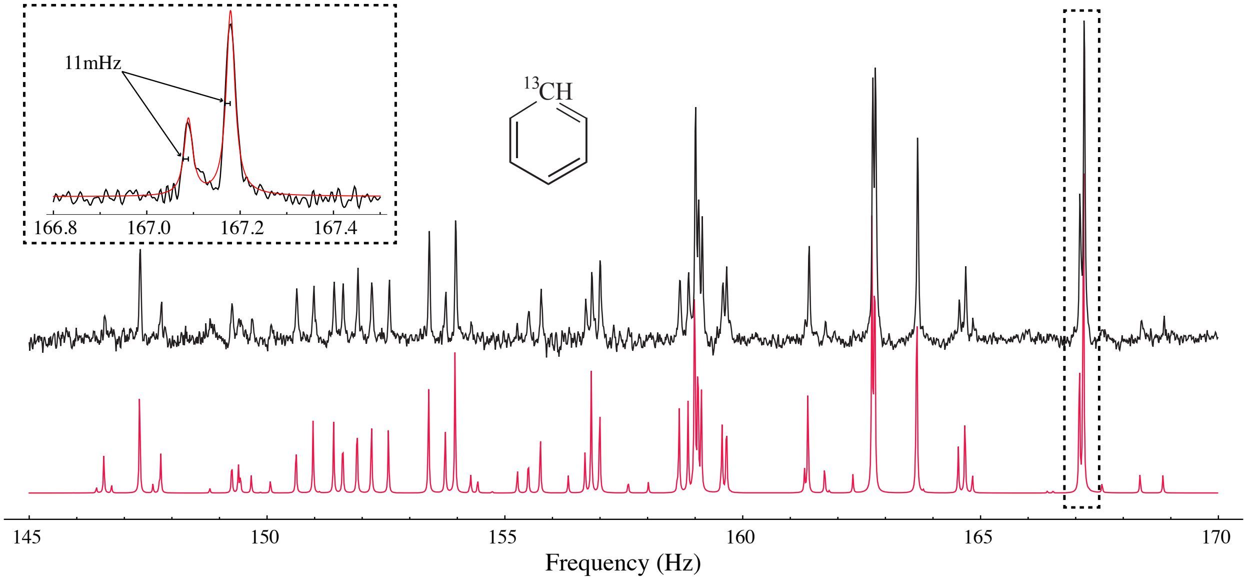

Figure 5.10: Experimental (upper trace) and simulated (lower trace) spectrum of benzene-$^{1}3C_{1}$ in the neighborhood of $^{1}J_{CH}$. Inset shows fitting of two high-frequency peaks with 11 mHz half-width at half-maximum, consistent with Fourier resolution limited by 80 s acquisition time. ©2013 American Chemical Society.

5.3.2 High Resolution from Narrow Resonances

The experimental spectra are in excellent agreement with simulations (performed via numerical diagonalization of the density matrix), as demonstrated in Figure 2 for the high-frequency portion of the zero- field J-spectrum of benzene-$^{13}C_1$. The simulated spectrum fully reproduces the multiplet structure, with peak frequencies in agreement to within ~10 mHz. Achieving this level of agreement between experiment and simulation required the use of precise values of the benzene J-coupling constants presented in Ref. [111], which include the influence of ^{13}C isotope effects. Small frequency differences are likely artifacts of limited precision in the literature values for the coupling constants or slight differences in sample preparation. Peak intensities are well-reproduced, with small variations likely arising due to insufficient prepolarization time or nonadiabatic shuttling between the prepolarization field and the detection region.

Because we operate in zero magnetic field, the absolute field homogeneity is exceptional, and extensive magnetic-field shimming is not required. Inhomogeneous broadening is negligible and spectral lines are extremely narrow, which allows for very precise measurements of line positions and coupling parameters. The zoomed inset in Fig. (5.10) shows the two peaks at 167.089 Hz and 167.179 Hz fit to the sum of two Lorentzians, each with a half-width at half-maximum of 11 mHz. This linewidth is comparable to the Fourier resolution of the spectrum, which is limited by the 80 s acquisition time. It is likely that the intrinsic linewidth is actually narrower, as the near-zero-field $T_2^\star$ of unlabeled benzene has been measured on the same instrument to be 21 s [112], corresponding to a half-width at half-maximum of ~7.6 mHz. Since the zero-field $T_2^\star$ is probably

C-H Couplings (Hz)	H-H Couplings (Hz)
$^1J_{\mathrm{CH}} = 158.354$	$^3J_{\mathrm{HH}}(H1, H2) = 7.540$
$^3J_{\mathrm{CH}} = 1.133$	$^3J_{\mathrm{HH}}(H2, H3) = 7.543$
$^4J_{\mathrm{CH}} = 7.607$	$^4J_{\mathrm{HH}}(H3, H4) = 7.535$
$^5J_{\mathrm{CH}} = -1.296$	$^4J_{\mathrm{HH}}(H1, H3) = 1.380$
	$^4J_{\mathrm{HH}}(H2, H4) = 1.377$
	$^5J_{\mathrm{HH}}(H2, H6) = 1.373$
	$^5J_{\mathrm{HH}}(H3, H5) = 1.382$
	$^5J_{\mathrm{HH}}(H1, H4) = 0.661$
	$^5J_{\mathrm{HH}}(H2, H5) = 0.658$

Table 5.11: Spin-spin couplings in benzene-$^{13}C_1$, from Ref. [111].

similar to this value, we expect that the intrinsic linewidth is less than 10 mHz.

5.3.3 The Phenyl Perturbation

Beyond the zero-order structure of the zero-field spectra, additional splittings arise due to couplings between the XA_n spin systems and the ring protons. Because all couplings involving the ring protons are at least 15 times smaller than $^1J_{\mathrm{CH}}$ (see Tables (5.11)-5.13), these couplings may be treated as a perturbation to the XA_n system. In keeping with notation described previously, the molecules studied in this report may be considered $(XA_n)BB'CC'D$ spin systems, where B and B′ are the ring protons in the ortho positions, C and C′ are the protons in the meta positions, and D is the proton in the para position. It is apparent from Fig. (5.9) that as the ^{13}C label is further displaced from the aromatic ring, the spreading of the peaks decreases, with the greatest peak spreading for benzene-$^{13}C_1$, in which the label is part of the ring, and almost no spreading for acetophenone-β-$^{13}C_1$, in which the label is four bonds from the nearest spin on the ring.

For the -$^{13}C(=O)H$ functional group (XA subsystem) and -$^{13}CH_3$ functional group (XA_3 subsystem), addition of angular momentum yields states with $K = 1/2$ and $F_A = 0, 1$. The zero-order spectrum of these groups includes a peak at frequency $^1J_{\mathrm{CH}}$, which corresponds to a transition with $\Delta F_A = \pm 1$ between states with $K = 1/2$. When the spins of either functional group are weakly coupled to the spins of a phenyl group, the perturbation splits this peak into a consistent multiplet pattern. To demonstrate that the effect of the ring proton perturbation is qualitatively similar for different functional groups, Fig. (5.11) shows a comparison of the $K = 1/2$ peaks in the spectra of benzaldehyde-α-$^{13}C_1$ (red trace) and toluene-α-$^{13}C_1$ (blue trace), with the benzaldehyde spectrum shifted without scaling to lower frequency for the purpose of illustration. The smooth black traces show simulated spectra, obtained by smoothly interpolating J-coupling parameters, as discussed below. While there are small differences in the multiplet structures, many features are present in the spectra of both molecules for example, the three peaks at the lower-frequency end of the spectrum (around 123 Hz for toluene) and the three larger peaks at the higher-frequency end (around 128 Hz for toluene). The multiplets have a similar structure because the network of couplings involving the ring couplings is (BB′CC′D) is topologically identical for any molecule containing a

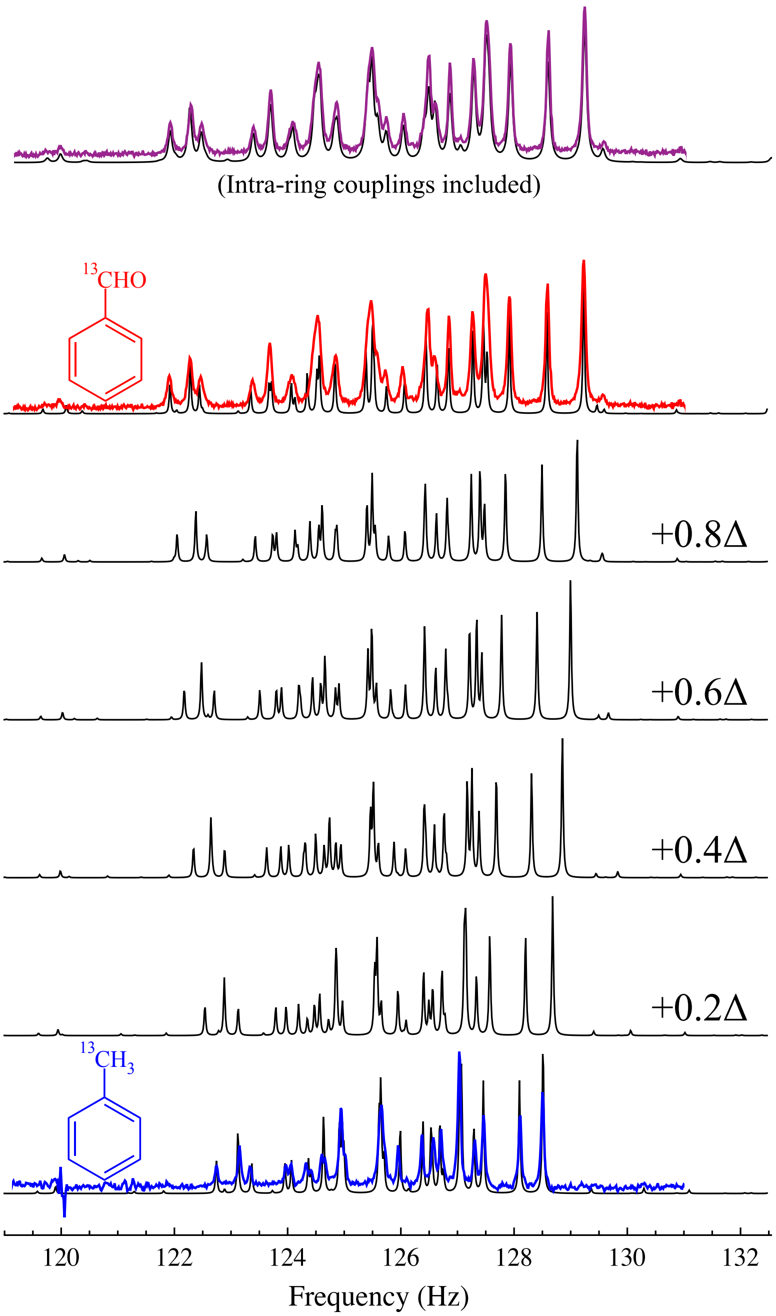

Figure 5.11: Comparison of $K = 1/2$ peaks of benzaldehyde-α-$^{13}C_1$ (red trace) and toluene-α-$^{13}C_1$ (blue trace) spectra. The benzaldehyde-α-$^{13}C_1$ spectrum has been shifted to lower frequency by 48.86 Hz for the purpose of illustration, but it has not been scaled. Intermediate simulated spectra are produced by incrementally varying the long-range substituent-to-ring ^{13}C–^{1}H and ^{1}H–^{1}H coupling constants by a uniform fraction of the differences between the values for the two molecules (Δ). The general structure of the peaks is similar because of the identical spin topology, with small quantitative differences arising due to geometric differences and substituent effects. The fit is in reasonable agreement with the benzaldehyde spectrum, even when adjustments to the intraring couplings constants are not included. ©2013 American Chemical Society.

phenyl group The qualitative similarity of the multiplet patterns facilitates chemical fingerprinting analysis. Variations in the splittings and central frequencies of multiplets allow for differentiation between the spectra of similar molecules.

5.3.4 Differences between Toluene and Benzaldehyde Spectra

The differences that arise between the $K = 1/2$ multiplets in the benzaldehyde-α-$^{13}C_1$ and toluene-α-$^{13}C_1$ spectra are associated with important differences between the two molecules. Specifically, the J-coupling constants depend on electronic structure, which in turn depends on substituent electron-donating/withdrawing effects and the spatial orientation of the substituent with respect to the plane of the ring. The variation in the $^nJ_{CH}$ couplings is primarily dependent on the electronegativity of the substituent, with a more strongly-electron-withdrawing substituent leading to a larger coupling between the substituent ^{13}C and ring protons. The $^nJ_{CH}$ couplings in benzaldehyde-α-$^{13}C_1$ are thus larger than in toluene–α-$^{13}C_1$, as the more electronegative aldehyde substituent more strongly attracts the -electron density of the aromatic ring, increasing the overlap with the ^{13}C nucleus. The $^nJ_{HH}$ benzylic couplings between the substituent protons and the aromatic protons have been studied, [113, 114, 115, 116] and they feature a dependence on the angle by which the substituent protons are rotated out of the plane of the ring. The couplings are given as

$$^4J(H, CH_n) = 6.90p\langle\sin^2\theta\rangle - 0.32\langle\cos^2\theta\rangle, \tag{5.26}$$

$$^5J(H, CH_n) = {}^5J^{\pi}\langle\sin^2\theta\rangle + {}^5J^{\sigma}\langle\sin^2(\theta/2)\rangle, \tag{5.27}$$

and

$$^6J(H, CH_n) = {}^6J_{90}\langle\sin^2\theta\rangle, \tag{5.28}$$

where θ is the angle by which the substituent C-H bond twists out of the benzene plane, p is the mutual atom-atom polarizability, $^5J^{\pi}$ is the $\sigma - \pi$ electron contribution to the $^5J(\mathrm{H}, \mathrm{CH_n})$ coupling, $^5J^{\sigma}$ is the σ-electron component, and $^6J_{90}$ is the value of $^6J(\mathrm{H}, \mathrm{CH_n})$ when the substituent C-H bond is perpendicular to the plane of the benzene ring. Key differences between the toluene and benzaldehyde $^nJ_{HH}$ couplings arise because of differences in these parameters. The most striking differences are related to the angle θ, and the $^6J(\mathrm{H}, \mathrm{CH_n})$ coupling is an illustrative example. Because the methyl group in toluene rotates freely, the expectation value of $\langle\sin^2\theta\rangle$ is 0.5, for a coupling of -0.52 Hz, whereas in benzaldehyde, the formyl proton is essentially in the benzene plane, and the coupling is only -0.018 Hz.

The intermediate calculated spectra in Fig. (5.11) were produced by varying the $^nJ_{CH}$ and $^nJ_{HH}$ couplings in linear fractional increments between the values for toluene-α-$^{13}C_1$ and benzaldehyde-α-$^{13}C_1$, leaving the intra-ring couplings constant. The agreement with the benzaldehyde spectrum is good, with the simulation fully reproducing the multiplet structure. Slight disagreements are the result of minute differences in intra-ring couplings that are affected by differences in aromatic ring electron densities induced by substituent effects. Including these effects, which cause changes of 0.02 0.2 Hz (the effects are strongest for the four-bond couplings, followed by the three- and then five-bond couplings) gives full agreement, as indicated by the uppermost traces in Fig. (5.11).

J-couplings measured in these zero-field experiments agree with the values determined by high-field NMR [Figs. (5.12-5.13)], though the zero-field experiments provided greater resolution and thus higher precision. Because the zero-field spectra generally have enough peaks to determine all J-coupling frequencies and thus provide enough information for chemical identification and elucidation of electronic structure, topology, and spatial configuration the presence of chemical shifts may not always be necessary for chemical identification and analysis.

5.3.5 Materials and Methods

Sample Preparation

Benzene-$^{13}C_1$, benzaldehyde-α-$^{13}C_1$, benzyl alcohol-α-$^{13}C_1$, toluene-α-$^{13}C_1$, and acetophenone-β-$^{13}C_1$ were obtained from Cambridge Isotopes Laboratory. Samples were degassed via several freeze-thaw cycles under vacuum and flame-sealed in 5 mm NMR tubes.

Zero-Field NMR Measurements

Samples were thermally polarized in a 2 T magnet and pneumatically shuttled into a zero-field detection region where the field of the nuclear spins was measured using an alkali-vapor atomic magnetometer. As the sample was shuttled to the detection region, a solenoid produced a guiding field in order to keep the initial magnetization aligned vertically. Once the sample reached the detection region, the solenoid was turned off and a DC magnetic field pulse with area $\gamma_H Bt \approx 4\pi$ was applied in an orthogonal direction to maximize the $\mathbf{I}_z - \mathbf{S}_z$ components of the density matrix, thus maximizing the signal.

Spectra for benzene-$^{13}C_1$, benzaldehyde-α-$^{13}C_1$, toluene-α-$^{13}C_1$, and acetophenone-β-$^{13}C_1$ were acquired without heating or cooling the sample, at roughly 35°C. To avoid hydrogen-bonding line-broadening effects in benzyl alcohol-α-$^{13}C_1$, the spectrum was taken at 70°C. The benzene-$^{13}C_1$ spectrum is the result of averaging 220 transients, each with 100 s polarization time and 80 s acquisition time. The benzaldehyde-α-$^{13}C_1$ spectrum was the result of averaging 256 transients, each with 60 s polarization time and 40 s acquisition time. The toluene-α-$^{13}C_1$ spectrum was the result of averaging 222 transients, each with 60 s polarization time and 40 s acquisition time. The acetophenone-β-$^{13}C_1$ spectrum was the result of averaging 1180 transients, each with 20 s polarization time and 16 s acquisition time. The benzyl alcohol-α-$^{13}C_1$ spectrum was the result of averaging 2300 transients, each with 20 s polarization time and 8 s acquisition time. It is worth noting that while these experiments require several hours of signal averaging using thermal polarization at 2 T, improvements in magnetometric sensitivity and sample polarization may significantly reduce acquisition times.

High-Field NMR Measurements

High-field NMR spectra [Figs. (5.12)-5.13] of labeled benzaldehyde and toluene were collected on a Bruker Avance 300 MHz (7.04 T) spectrometer with a Bruker 5 mm $^1H/^{13}C$ liquids probe. No ^{13}C or ^1H decoupling was performed. Careful FID shimming was performed in order

C-H Couplings (Hz)	Benzylic Couplings (Hz)	Intra-Ring Couplings (Hz)
${}^{1}J_{\mathrm{CH}} = 174.85$	${}^{4}J_{\mathrm{HH}} = -0.152$	${}^{3}J_{\mathrm{HH}}(H2, H3) = 7.695$
${}^{3}J_{\mathrm{CH}} = 4.92$	${}^{5}J_{\mathrm{HH}} = 0.431$	${}^{3}J_{\mathrm{HH}}(H3, H4) = 7.443$
${}^{4}J_{\mathrm{CH}} = 0.72$	${}^{6}J_{\mathrm{HH}} = -0.018$	${}^{4}J_{\mathrm{HH}}(H2, H4) = 1.333$
${}^{5}J_{\mathrm{CH}} = 0.69$		${}^{4}J_{\mathrm{HH}}(H2, H6) = 1.738$
		${}^{4}J_{\mathrm{HH}}(H3, H5) = 1.236$
		${}^{5}J_{\mathrm{HH}}(H2, H5) = 0.624$

Table 5.12: Spin-spin couplings in benzaldehyde-α-${}^{13}C_1$. Determined by manual refinement, using values from Ref. [117] and high-field ${}^{13}C$ spectrum [see Fig. 5.12] as a starting point.

C-H Couplings (Hz)	Benzylic Couplings (Hz)	Intra-Ring Couplings (Hz)
${}^{1}J_{\mathrm{CH}} = 125.99$	${}^{4}J_{\mathrm{HH}} = -0.69$	${}^{3}J_{\mathrm{HH}}(H2, H3) = 7.655$
${}^{3}J_{\mathrm{CH}} = 4.53$	${}^{5}J_{\mathrm{HH}} = 0.30$	${}^{3}J_{\mathrm{HH}}(H3, H4) = 7.417$
${}^{4}J_{\mathrm{CH}} = 0.63$	${}^{6}J_{\mathrm{HH}} = -0.52$	${}^{4}J_{\mathrm{HH}}(H2, H4) = 1.273$
${}^{5}J_{\mathrm{CH}} = 0.56$		${}^{4}J_{\mathrm{HH}}(H2, H6) = 1.902$
		${}^{4}J_{\mathrm{HH}}(H3, H5) = 1.442$
		${}^{5}J_{\mathrm{HH}}(H2, H5) = 0.610$

Table 5.13: Spin-spin couplings in toluene-α-${}^{13}C_1$. Determined by manual refinement, using values from Ref. [113] and high-field ${}^{13}C$ spectrum [see Fig. 5.13] as a starting point.

to maximize resolution for the observation of $J_{\mathrm{CH}}/J_{\mathrm{HH}}$ splitting patterns. Long acquisitions (4 s) were performed and negative Lorentzian line-broadening (−0.1 Hz) was applied to enhance spectral resolution. The same degassed samples used for the low-field measurements were used for the high-field measurements.

Simulations

Zero-field J-spectra were simulated by numerical diagonalization of the density matrix. The time-dependent magnetization was determined by evolving the initial thermally-polarized density matrix under the J-coupling Hamiltonian as described in Ref. 29. Specific J-coupling frequencies were either taken directly from the literature (as in the case of benzene-${}^{13}C_1$) or were determined by manually refining literature and/or measured values to optimize agreement with experimental spectra (for benzaldehyde J_{CH} and toluene J_{CH}). No iterative fitting algorithms were used, though such methods may allow for easier extraction of high-precision J-coupling frequencies in the future.

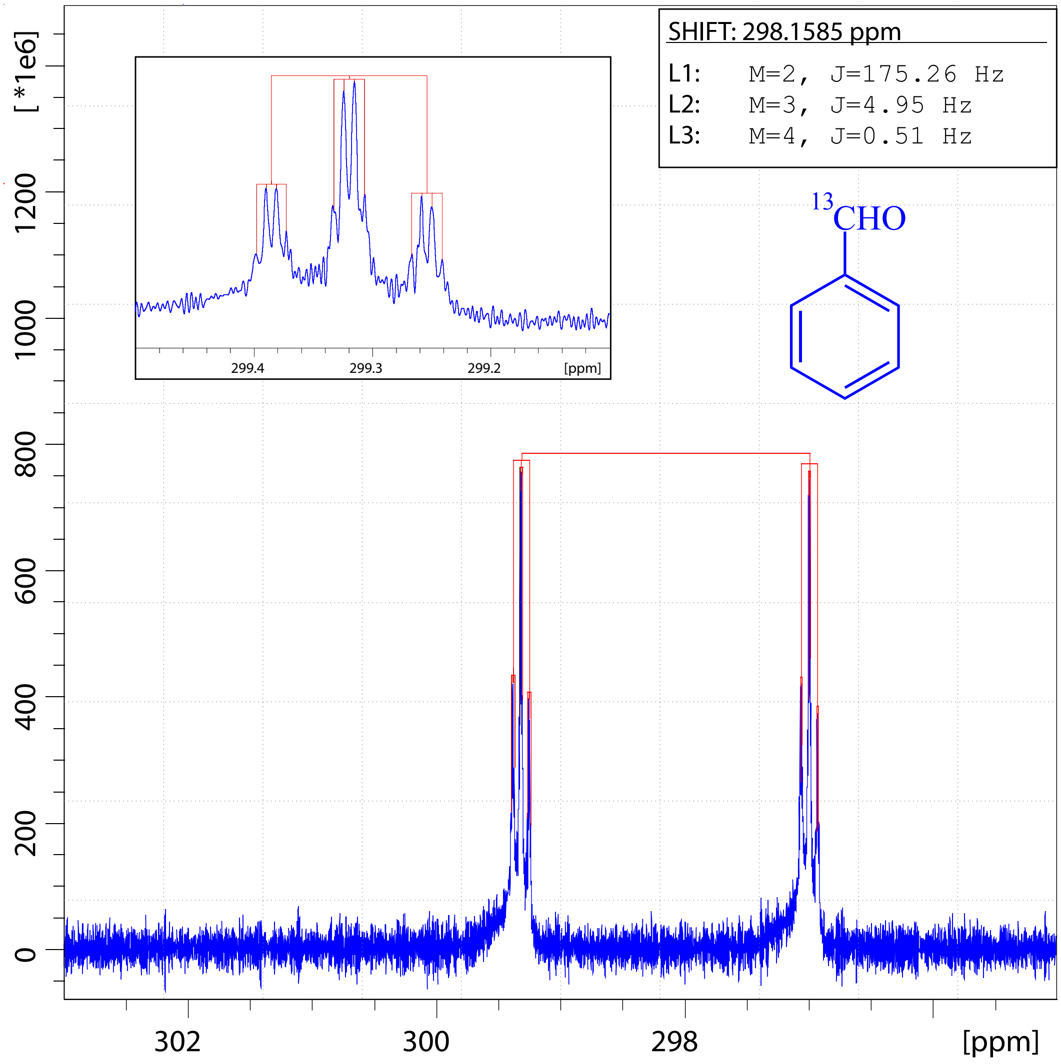

Figure 5.12: Benzaldehyde-α-$^{13}C_1$ high-field (7 T) ^{13}C spectrum without ^1H-decoupling. The overall structure of the multiplet is a doublet of triplets of doublets of triplets, though it appears to be a doublet of triplets of quartets because $^4J_{CH}$ and $^5J_{CH}$ are too close to be resolved at high field. The chemical shift axis is referenced arbitrarily, as we are only concerned with the J-coupling multiplet structure and splittings. ©2013 American Chemical Society.

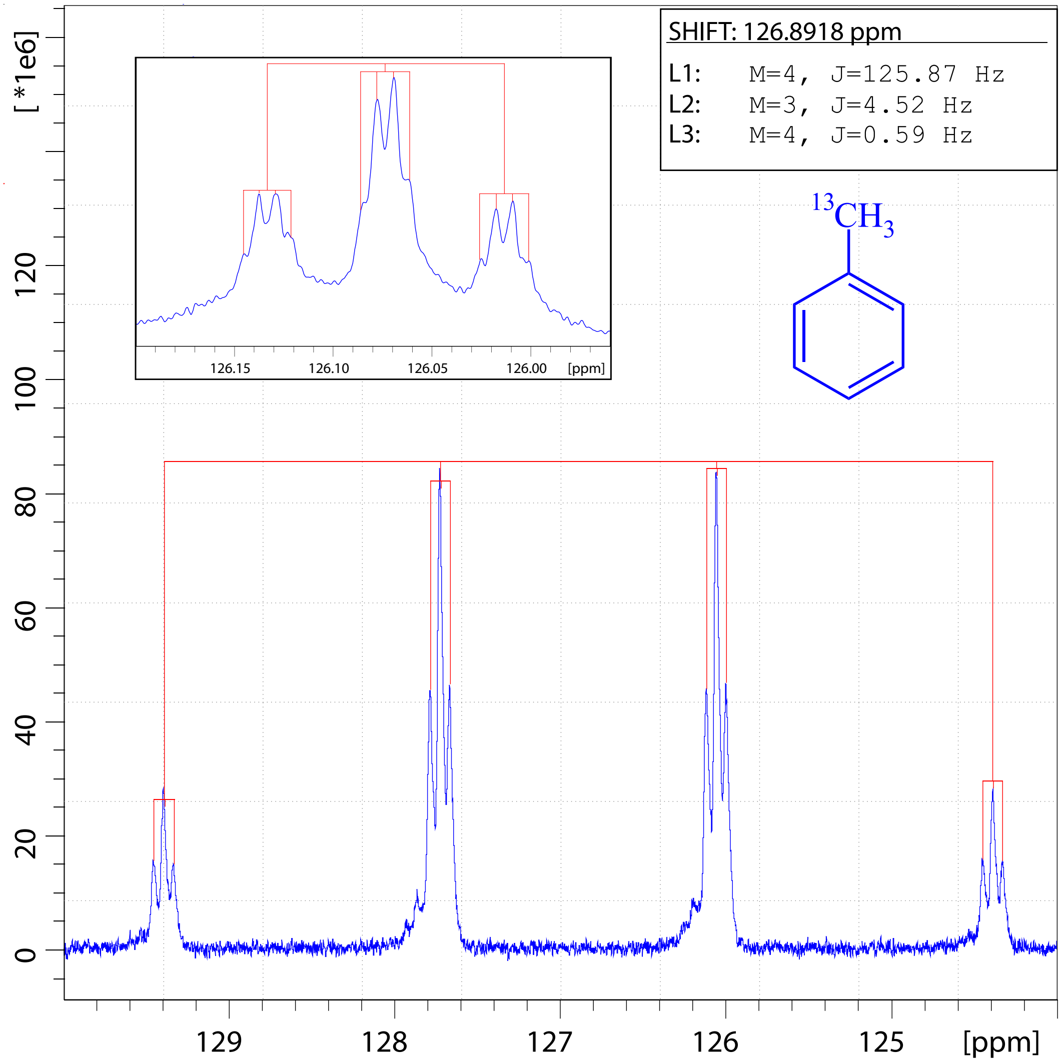

Figure 5.13: Toluene-α-$^{13}C_1$ high-field (7 T) ^{13}C spectrum without ^1H-decoupling. The overall structure of the multiplet is a quartet of triplets of doublets of triplets, though it appears to be a doublet of triplets of quartets because $^4J_{CH}$ and $^5J_{CH}$ are too close to be resolved at high field. The chemical shift axis is referenced arbitrarily, as we are only concerned with the J-coupling multiplet structure and splittings. ©2013 American Chemical Society.

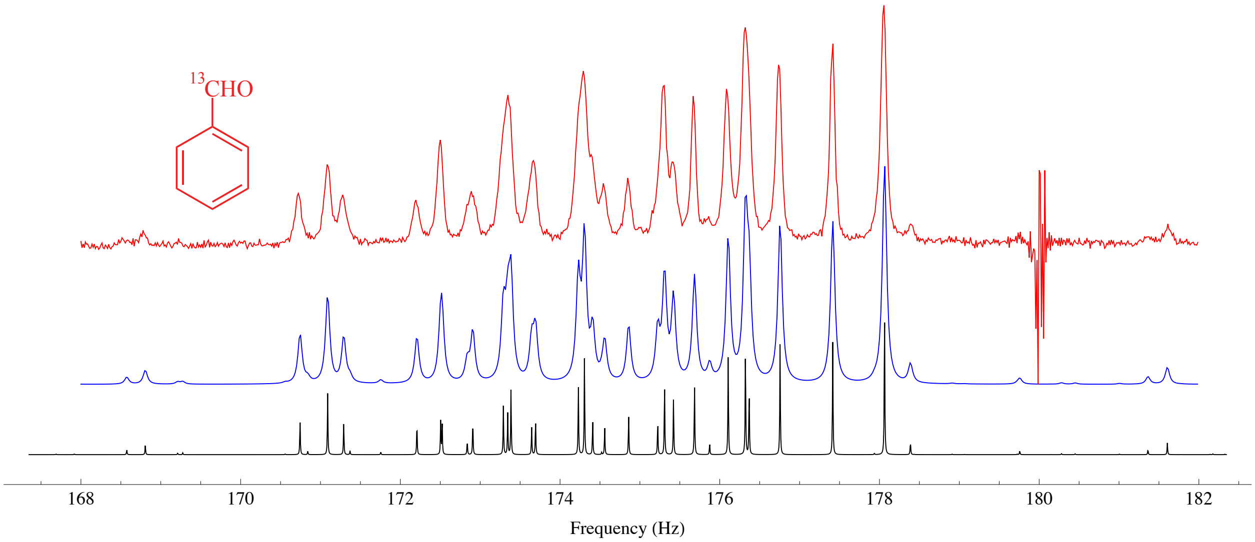

Figure 5.14: Overlay of benzaldehyde-α-$^{13}C_1$ experimental spectrum (top, red trace), spectrum simulated using couplings in Table S1 with linewidth set so as to best reproduce experiment (middle, blue trace), and simulated spectrum with decreased linewidth to show substructure (bottom, black trace). ©2013 American Chemical Society.

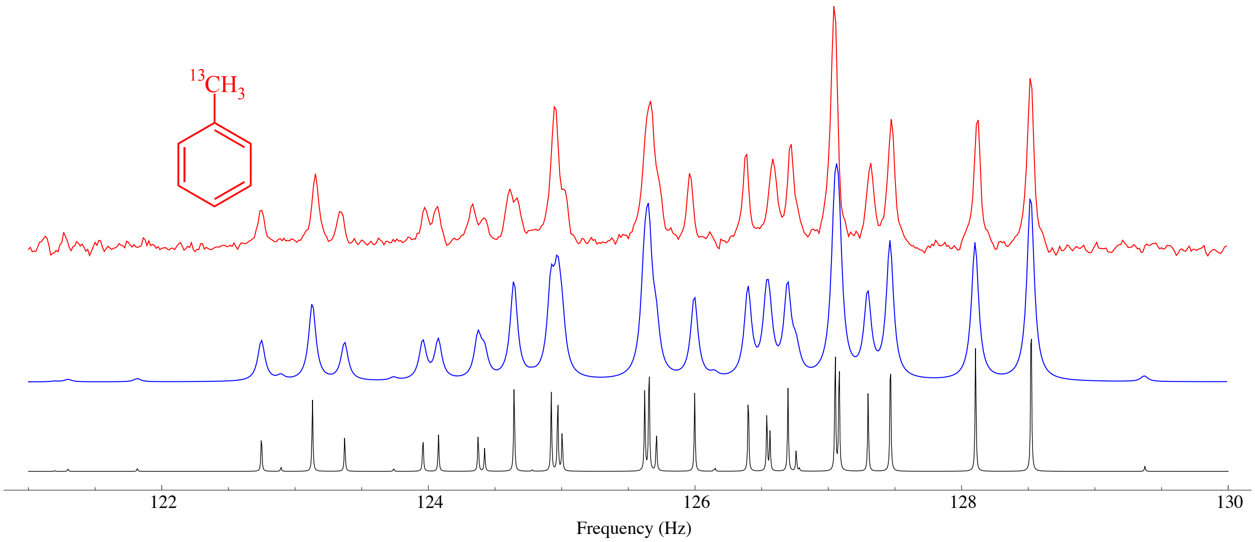

Figure 5.15: Overlay of toluene-α-$^{13}C_1$ experimental spectrum (top, red trace), spectrum simulated using couplings in Table S2 with linewidth set so as to best reproduce experiment (middle, blue trace), and simulated spectrum with decreased linewidth to show substructure (bottom, black trace). ©2013 American Chemical Society.

5.4 Conclusions: Zero-Field NMR for Chemical Analysis

Zero-field NMR J-spectroscopy has been demonstrated for a series of molecules with various spin topologies, yielding unique, well-resolved, and information-rich spectra that are well suited for chemical fingerprinting. Long relaxation times and consistent field homogeneity give rise to extremely narrow resonance linewidths and enhanced resolution. The narrow linewidths allow for measurement of J-coupling frequencies with greater precision than is typically achieved using other techniques. Conveniently, in the molecules studied here, zero-field spectra are all non-overlapping, which facilitates analysis of mixtures without the need for higher-dimensional spectroscopy.

The existence of consistent qualitative spectral patterns allows for quick assignment of spin system topology [(XA_n), $(XA_n)B_m$, $(XA_n)BB'CC'D$, etc.], so that implementation of search algorithms with zero-field simulations should yield precise J-coupling values. While all samples measured so far consist of molecules selectively labeled with spin-$\frac{1}{2}$ heteronuclei, ideally one would have the capability to measure samples with ^{13}C, ^{15}N, etc. in natural abundance. This may be achieved by incorporating hyperpolarization techniques or by improvements in magnetometric sensitivity. Regarding the latter, we estimate that the fundamental limits of sensitivity are 100 times lower than the present noise level [53]. Implementation of hyperpolarization techniques should extend the applicability of zero-field NMR experiments to more normal (dilute, natural abundance) samples, as has been demonstrated for systems amenable to parahydrogen-induced polarization [71, 72].

Combining this new technique for the precise measurement of electron-mediated scalar couplings with quantum chemistry calculations should provide detailed information about molecular conformation and electronic structure. This contribution supports the development of zero-field NMR as a technique complementary to high field NMR, enabling precision measurement of couplings. Furthermore, the absence of superconducting magnets in zero-field NMR facilitates cost effectiveness and portability.

Chapter 6

Near-Zero-Field NMR: The Zeeman Perturbation

When probing the chemist's creation,
Zeeman splittings can assuage frustration.
It's no chemical shift,
But degen'racies lift,
So the spectrum yields more information.

In this chapter, we consider the effects of small magnetic fields on ultra-low-field NMR spectra. In the regime where the Zeeman effect can be treated as a perturbation, we observe high-resolution spectra with easy-to-understand splitting patterns that are in good qualitative and quantitative agreement with first-order perturbation theory. This may be thought of as a dualistic compliment to conventional high-field NMR, where heteronuclear couplings are almost always treated as a small perturbation to the much larger Zeeman interaction. Thus analogous to J-splitting in spectra dominated by the chemical shift, we see Zeeman splitting of near-zero-field J-spectra. We also examine the case in which the Zeeman interaction is of comparable strength to the J-coupling, resulting in spectra of maximal complexity. These results have been published previously:

- Ledbetter, M.P., Theis, T., Blanchard, J.W., Ring, H., Ganssle, P., Appelt, S., Blümich, B., Pines, A., and Budker, D. Near-Zero-Field Nuclear Magnetic Resonance. *Phys. Rev. Lett.* **107** (10), 107601. (2011)

- Ledbetter, M.P., Pustelny, S., Budker, D., Romalis M.V., Blanchard, J.W., and Pines, A. Liquid-State Nuclear Spin Comagnetometers. *Phys. Rev. Lett.* **108** (24), 243001. (2012)

6.1 Motivation

As shown in the previous chapter, the J-coupling Hamiltonian encodes a great deal of useful chemical information which can be accessed in zero-field NMR spectra, but some ambiguity does remain due to the absence of any direct measurement of which nuclei are present [118]. For example, the zero-field J-spectrum of an XA_2 spin system composed of a ^{15}N nucleus bound to two ^{1}H nuclei consists of a single peak at $\frac{3}{2}J_{\mathrm{NH}}$, which – based on the coupling strengths of formamide-^{15}N presented in the previous chapter – will appear around 140 Hz. Alternatively, the zero-field J-spectrum of an XA system composed of a ^{13}C nucleus bound to a ^{1}H nucleus far from any electron-withdrawing groups will consist of a single peak at J_{CH}, which is also around 140 Hz. Thus zero-field NMR is incapable of differentiating between even these two substantially different systems!

It turns out that it is possible to remove this ambiguity by applying weak magnetic fields, which results in splitting of the zero-field lines, restoring information about gyromagnetic ratios that is otherwise lost by operating at zero magnetic field. The perturbation also reveals specific information about the topology of the angular momentum manifolds involved in the transitions corresponding to each peak in the zero-field spectrum. By operating near to zero field, the atomic magnetometer still operates in the SERF regime, and coupling between the nuclear spins in the sample and the alkali spins in the detector is enhanced by better matching the electron Larmor frequency to the J-coupling frequency.

6.2 Theory

The Hamiltonian in the presence of J-couplings and a magnetic field is

$$\mathcal{H} = \hbar \sum_{j;k>j} J_{jk} \mathbf{I}_j \cdot \mathbf{I}_k - \hbar \sum_j \gamma_j \mathbf{I}_j \cdot \mathbf{B}. \tag{6.1}$$

Here $\mathbf{I}_j$ represent both like and unlike spins with gyromagnetic ratio γ_j and J_{jk} is the scalar coupling between spins j and k. In the absence of magnetic fields, the spherical symmetry of the Hamiltonian dictates that eigenstates $|\phi_a\rangle$ are also eigenstates of $\mathbf{f}^2$ and f_z, where $\mathbf{f}$ is the total angular momentum $\mathbf{f} = \sum_j \mathbf{I}_j$, with energy E_a, and degeneracy $2f + 1$. Application of a magnetic field B_z lifts this degeneracy, splitting the ZF NMR lines.

The signal in our experiment is the x component of the magnetization

$$M_x(t) = n\hbar \mathrm{Tr}\left[\rho(t) \sum_j \gamma_j I_{jx}\right], \tag{6.2}$$

where $\rho(t)$ is the time dependent density matrix and n is the molecular density. The initial density matrix ρ_0 can be expressed in terms of the operators $|\phi_a\rangle\langle\phi_b|$, each of which evolves as $e^{i\omega_{ab}t}$, where $\omega_{ab} = (E_a - E_b)/\hbar$. Equation (6.2) can be rewritten

$$M_x(t) = n\hbar \sum_{a,b,j} \frac{\gamma_j}{2} \rho_{ab} \langle\phi_b| \left(I_{j+} + I_{j-}\right) |\phi_a\rangle e^{-i\omega_{ab}t}, \tag{6.3}$$

where $\rho_{ab} = \langle\phi_a|\rho_0|\phi_b\rangle$ and $I_{j\pm} = I_{jx} \pm iI_{jy}$ are the usual raising and lowering operators. For arbitrary scalar-coupling networks and arbitrary magnetic fields, eigenstates and eigenvalues can be calculated numerically. In the limit where the magnetic field is very small, such that $|\gamma_i B_z| \ll |J_{jk}|$ for all values of i, j, and k, its effects on the spectra can be calculated analytically using first-order perturbation theory, lending considerable physical insight to the problem.

We first examine the effects of very small magnetic fields on a ^{13}CH$_n$ system, with n equivalent protons, using perturbation theory. In zero field, the unperturbed energy levels are given by $E(F,K) = J/2[F(F+1) - K(K+1) - S(S+1)]$, [109] where $K = 1/2, 1, 3/2...$ are the possible spin quantum numbers of the operator $\mathbf{K}$ describing the sum of the equivalent proton spins, and $S = 1/2$ is the spin quantum number associated with the operator $\mathbf{S}$, representing the ^{13}C spin. To first order in B_z, eigenstates are those of the unperturbed Hamiltonian, and Zeeman shifts of the eigenvalues can be read from the diagonal matrix elements of the Zeeman perturbation. One finds:

$$\begin{aligned}
\Delta E\,(F,K,m_F) &= -\langle Fm_F|B_z(\gamma_h K_z + \gamma_c S_z)|Fm_F\rangle, \\
&= -\sum_{\substack{m_K m_S \\ m'_K m'_S}} \langle Fm_F|KS\,m_K m_S\rangle\langle KS\,m_K m_S|B_z(\gamma_h K_z + \gamma_c S_z)|KS\,m'_K m'_S\rangle\langle KS\,m'_K m'_S|Fm_F\rangle \\
&= -\sum_{m_K,m_S} B_z\langle KS\,m_K m_S|Fm_F\rangle^2(\gamma_h m_K + \gamma_c m_S). \qquad (6.4)
\end{aligned}$$

Here γ_h and γ_c are the proton and ^{13}C gyromagnetic ratios, and $\langle KS\,m_K m_S|Fm_F\rangle$ are the Clebsch-Gordan coefficients. The observable in our experiment is the total x magnetization, $M_x(t) \propto \mathrm{Tr}\rho(t)\sum_j I_{jx}\gamma_j$, where $\rho(t)$ is the time dependent density matrix. Writing I_{jx} in terms of the raising and lowering operators, we obtain selection rules for observable coherences: $\Delta F = 0, \pm1$ and $\Delta m_F = \pm1$, valid in the limit where $|\gamma_j B| << |J|$. In the case at hand with n equivalent protons, there is an additional selection rule, $\Delta K = 0$, since, in the absence of chemical shifts, the Hamiltonian commutes with $\mathbf{K}^2$.

For $n = 1$, $K = 1/2$, and the zero-field levels are a singlet with $F = 0$ and a triplet with $F = 1$. In the presence of a small magnetic field, the singlet level is unperturbed, while the triplet levels split,

$$\begin{aligned}
E\left(0, \frac{1}{2}, 0\right) &= -3J/4, \\
E\left(1, \frac{1}{2}, m_F\right) &= J/4 - m_F B_z\left(\gamma_h + \gamma_c\right)/2. \qquad (6.5)
\end{aligned}$$

as shown by the manifolds on the left of Fig. 6.1(a). In the following, ν_{F,m_F}^{F',m'_F} denotes the frequency of transitions between the states $|F, m_F\rangle$ and $|F', m'_F\rangle$. Employing Eq. 6.4 and the selection rules, one finds a single line for transitions with $\Delta F = 0$ between states with $F = 1$, and a doublet for transitions with $\Delta F = \pm1$ between states with $F = 1$ and $F = 0$:

$$\nu_{1,m_F}^{1,m_F\pm1} = B_z\left(\gamma_h + \gamma_c\right)/2, \qquad (6.6)$$

$$\nu_{0,0}^{1,\pm1} = J \pm B_z\left(\gamma_h + \gamma_c\right)/2. \qquad (6.7)$$

For the case of $n = 2$, K is either 0 or 1 (please note that experimental data are presented only for $n = 1$ and 3 – we only present the $n = 2$ case here for completeness). Adding the ^{13}C spin to the system yields a zero-field manifold with $F = 1/2$ for $K = 0$ and unperturbed energy 0. For $K = 1$, the zero-field manifolds have $F = 3/2, 1/2$ with energies $J/2$ and $-J$, respectively. A small magnetic field perturbs these levels according to Eq. 6.4

$$E\left(\frac{1}{2}, 0, m_F\right) = -m_F B_z \gamma_c / 2 \tag{6.8}$$

$$E\left(\frac{1}{2}, 1, m_F\right) = -J - m_F B_z \left(4\gamma_h - \gamma_c\right)/3 \tag{6.9}$$

$$E\left(\frac{3}{2}, 1, m_F\right) = J/2 - m_F B_z \left(2\gamma_h + \gamma_c\right)/3. \tag{6.10}$$

Thus, there are three lines corresponding to transitions with $\Delta f = 0$:

$$\nu^{\frac{1}{2},m_F}_{\frac{1}{2},m_F\pm1} = B_z \gamma_c; K = 0 \tag{6.11}$$

$$\nu^{\frac{1}{2},m_F}_{\frac{1}{2},m_F\pm1} = B_z \left(4\gamma_h - \gamma_c\right)/3; K = 1 \tag{6.12}$$

$$\nu^{\frac{3}{2},m_F}_{\frac{3}{2},m_F\pm1} = B_z \left(2\gamma_h + \gamma_c\right)/3; K = 1. \tag{6.13}$$

Transitions with $\Delta f = \pm 1$ and $\Delta m_f = \pm 1$ between states with $f = 1/2$ and $f = 3/2$ for $k = 1$ yield four lines, at frequencies given by

$$\nu^{3/2,m_f\pm1}_{1/2,m_f} = 3J/2 + 2B_z m_f \left(\gamma_h - \gamma_c\right)/3 \mp B_z \left(2\gamma_h + \gamma_c\right)/3. \tag{6.14}$$

For the case of $n = 3$, K is either 1/2 or 3/2. The $K = 1/2$ transition frequencies are given by Eq. 6.7. For the $K = 3/2$ manifolds, evaluating Eq. (6.4), we find

$$\begin{aligned} E\left(1, \frac{3}{2}, m_F\right) &= -5J/4 - m_F B_z \left(5\gamma_h - \gamma_c\right)/2, \\ E\left(2, \frac{3}{2}, m_F\right) &= 3J/4 - m_F B_z \left(3\gamma_h + \gamma_c\right)/4. \end{aligned} \tag{6.15}$$

The $K = 3/2$ manifolds are shown on the right of Fig. 6.1(a), and coherences between $|F = 1, m_F\rangle$ and $|F = 2, m_F \pm 1\rangle$ occur at frequencies given by

$$\nu^{2,m_F\pm1}_{1,m_F} = 2J + m_F \frac{B_z}{4}\left(-7\gamma_h + 6\gamma_c\right) \pm \frac{B_z}{4}\left(3\gamma_h + \gamma_c\right). \tag{6.16}$$

There are two additional transitions for states with $K = 3/2$ with $\Delta F = 0$ that occur near zero frequency,

$$\nu^{2,m_F\pm1}_{2,m_F} = \left(3\gamma_h + \gamma_c\right)\frac{B_z}{4}; K = \frac{3}{2}, \tag{6.17}$$

$$\nu^{1,m_F\pm1}_{1,m_F} = \left(5\gamma_h - \gamma_c\right)\frac{B_z}{4};; K = \frac{3}{2}. \tag{6.18}$$

Equations. (6.6)-(6.7) and (6.16)-(6.18) constitute a set of eleven transitions, three appearing near zero frequency, two near J, and six near $2J$, representing the NZF NMR spectrum of a $^{13}CH_3$ group.

In the presently considered limit of small magnetic fields, the amplitude of a peak corresponding to a transition between states $|\phi_a\rangle$ and $|\phi_b\rangle$ can be found from the coefficients in front of $e^{i\omega_{ab}t}$ in Eq. (6.3), $a_{ab} = \langle\phi_a|\rho_0|\phi_b\rangle\langle\phi_b|(P_+ + P_-)|\phi_a\rangle$, where $P_\pm = \sum_j \gamma_j I_{j\pm}$. The polarized part of the initial density matrix corresponding to high-field magnetization with $\mathbf{B}_0 = B_0\hat{\mathbf{x}}$ is $\rho \propto \sum_j \gamma_j I_{jx} = P_+ + P_-$. Hence, amplitudes are given by $\langle\phi_b|(P_+ + P_-)|\phi_a\rangle^2$. These matrix elements can be found using the Wigner-Eckart theorem for rank 1 vector operators with magnetic quantum number ±1:

$$\langle F, m_F|(P_+ + P_-)|F', m_F'\rangle^2 = \langle F||(P_+ + P_-)||F'\rangle^2\langle F, m_F|F', 1, m_F', \pm 1\rangle^2.$$

In the case of a $1 \leftrightarrow 0$ transition, the two peaks corresponding to transitions with $\Delta m_F = \pm 1$ have equal intensities. In the case of a $1/2 \leftrightarrow 3/2$ transition, the four peaks have intensities in the ratio of 1:3:3:1. For the $2 \leftrightarrow 1$ transitions, we find that the six peaks are in the ratio of 1:3:6:6:3:1.

We now make two observations: (1) Even in more complex molecules with additional nonequivalent spins, the zero-field eigenstates are also those of $\mathbf{F}^2$ and F_z. Therefore, the NZF splitting patterns can be used to identify the angular momenta of the states involved in the zero-field transitions: Transitions between levels with $F = 0$ and 1 will produce doublets, transitions between levels with $f = F$ and 2 will produce a multiplet with six lines, and so on. (2) The selection rules presented here break down as the magnetic field becomes large enough to produce significant mixing of the zero-field eigenstates. Reference [118] shows theoretically that the maximum number of lines for a $^{13}CH_n$ group is $(n + 1)^2$, most clearly visible when $|(\gamma_h + \gamma_c)B_z| \approx J$.

6.3 Zeeman Perturbation on XA_n Systems

Experiments were performed using an apparatus similar to that of Refs. [109, 71] and depicted in Fig. 6.1. Samples (typically $\approx 200\ \mu$L) were contained in a 5 mm NMR tube, and pneumatically shuttled between a 1.8 T prepolarizing magnet and a magnetically shielded enclosure, housing a microfabricated ^{87}Rb vapor cell, the central component of the atomic magnetometer. The cell is optically pumped by z-directed, circularly polarized laser light, tuned to the center of the D1 transition, and probed by y-directed, linearly polarized light, tuned about 100 GHz to the blue of the D1 transition. Optical rotation of the probe light is monitored by a balanced polarimeter. Bias fields and DC pulses of magnetic field, used to excite NMR spin coherences, are applied via a set of coils. At zero field, the magnetometer is primarily sensitive to fields in the x direction with noise floor of about $40 - 50$ fT/$\sqrt{Hz}$. As the bias field is increased, the magnetometer response moves to higher frequencies, compromising the low-frequency sensitivity by about a factor of 5 for $B_z = 3$ mG. To maintain a quantization axis during transit of the sample, a solenoid provides a “guiding” field. The guiding field is turned off suddenly prior to acquisition of data, and a pulse applied in the z-direction with area such that the proton spins rotate through $\approx 4\pi$ and the carbon spins rotate through $\approx \pi$ (about 480 μs), maximizing the amplitude of zero-field signals.

ZF and NZF spectra for formic acid (H^{13}COOH) are shown in Fig. 6.2. The ZF spectrum consists of a single line at $J = 222$ Hz, as well as a DC component, suppressed here for clarity. The

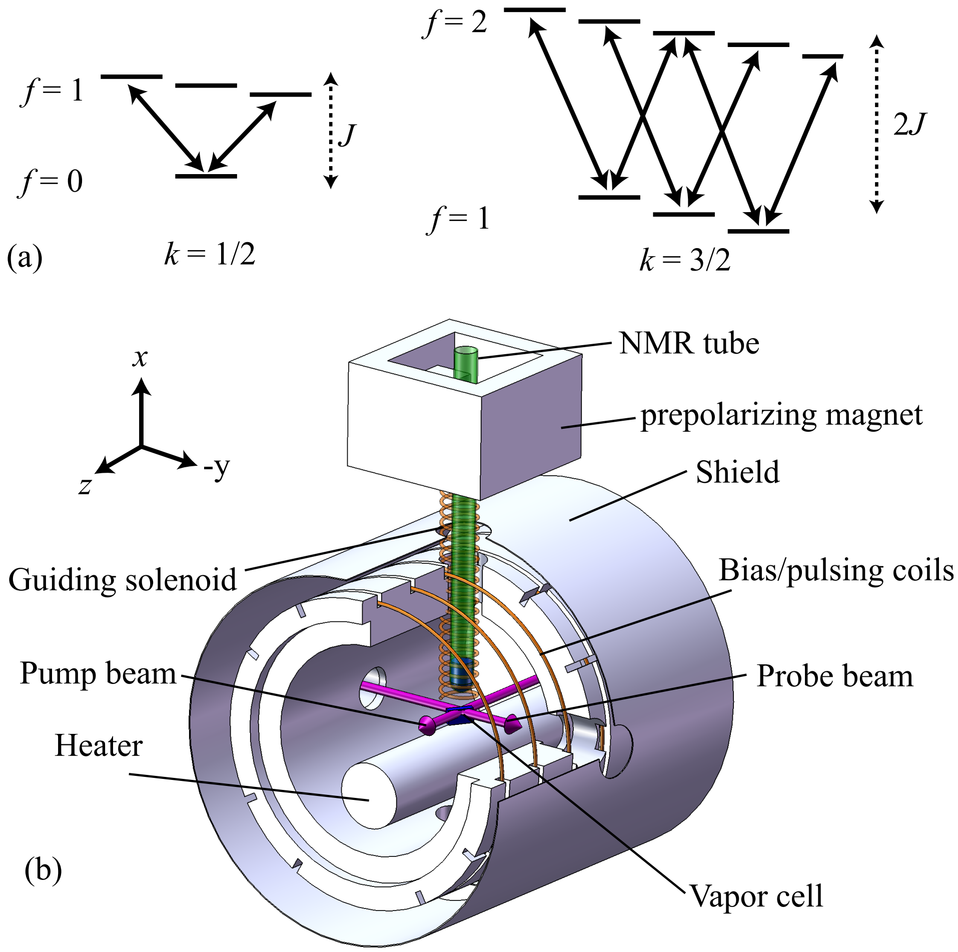

Figure 6.1: (a) Energy levels for a $^{13}CH_3$ group. Energy levels for a ^{13}CH group are given by the manifold on the left. (b) Experimental setup for near-zero-field spectroscopy, described in the text. Adapted with permission from Ref. [64]. ©2011 American Physical Society.

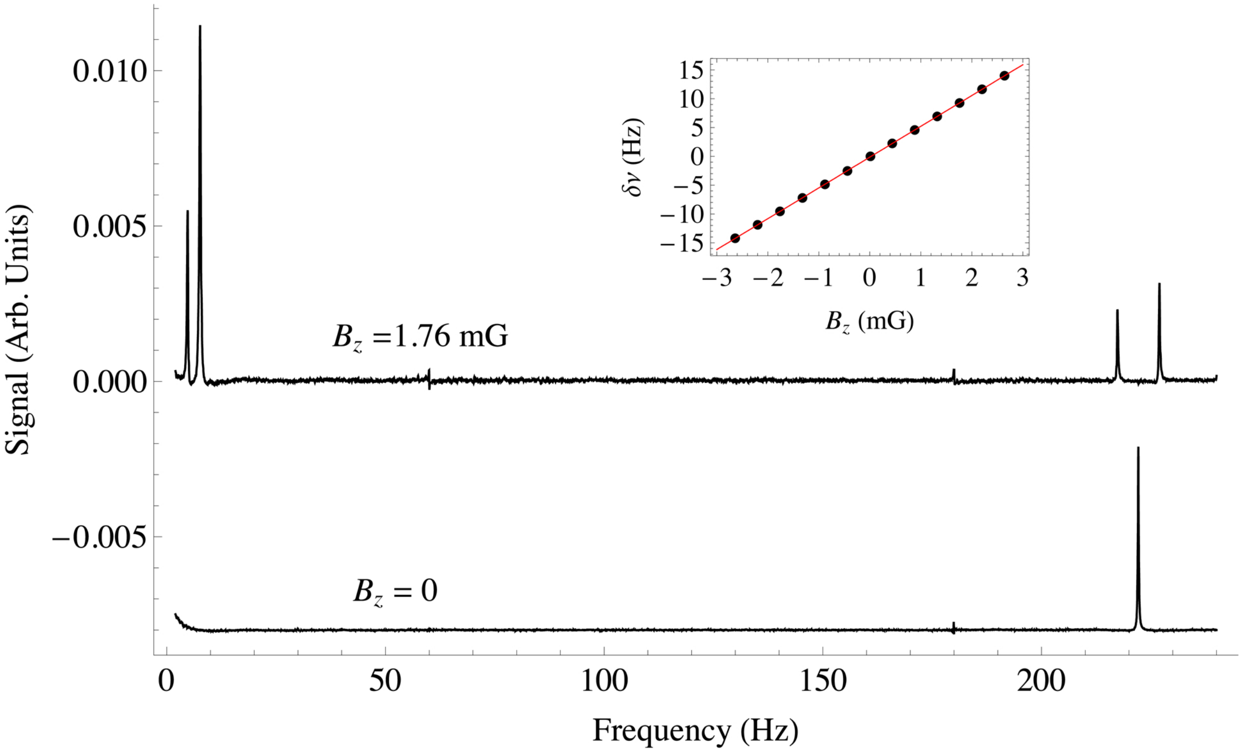

Figure 6.2: Spectra for ^{13}C labeled formic acid, H^{13}COOH, in the indicated magnetic fields. The spectra are the result of averaging eight transients. The inset shows the splitting of the two lines centered about J as a function of magnetic field. Adapted with permission from Ref. [64]. ©2011 American Physical Society

NZF spectrum arising from the ^{13}CH group is as discussed above: a doublet with frequencies $J \pm B_z(\gamma_h+\gamma_c)/2$ and an additional line at $B_z(\gamma_h+\gamma_c)/2 \approx 4.7$ Hz. The large peak at 7.5 Hz corresponds to the uncoupled OH group. The asymmetry in the doublet centered about J, reproduced by a full numerical calculation, is due to higher-order corrections to the eigenstates. The peaks are well described by Lorentzians, with half-width at half-maximum $\approx$ 0.1 Hz, and the locations of the peaks can be determined with an uncertainty of about 1 mHz. The inset shows the splitting of the line at J as a function of magnetic field, displaying a linear dependence. The slope is in agreement with that predicted by Eq. (6.7), $(\gamma_h + \gamma_c)$, at the level of about 0.1%.

To illustrate the case of a ^{13}CH$_3$ system, ZF and NZF spectra for acetonitrile-2-^{13}C (^{13}CH$_3$CN) are shown in Fig 6.3. For $B_z = 0$, the spectrum consists of a zero-frequency peak, a peak at J, and a peak at $2J$. Application of a magnetic field splits the zero-frequency peak into three lines, whose frequencies are given by Eqs. (6.6),(6.17), and (6.18).[1] The line at J splits into a doublet, whose frequencies are given by Eq. (6.7), and the line at $2J$ splits into six lines, whose frequencies are given by Eq. (6.16). The splitting of the lines at J and $2J$ clearly reveals the degeneracy of the zero-field levels. As with the formic acid spectrum, there is some asymmetry present in the multiplets centered about J and $2J$, which is reproduced by numerical simulation. Nevertheless, the relative amplitudes of the lines centered about $2J$ are roughly in the ratio 1:3:6:6:3:1 as expected from first-order perturbation theory (see previous section).

6.4 Zeeman Perturbation on Larger Systems

To illustrate the utility of near-zero-field NMR, we examine the case of fully labeled acetonitrile (^{13}CH$_3$^{13}C^{15}N). The zero-field spectrum is shown in the bottom trace of Fig. 6.4. It is not immediately clear which lines correspond to which zero-field transitions. An expanded view of the zero-field spectrum in the range of 110 to 180 Hz is provided and compared to the spectrum obtained in the indicated finite magnetic fields. We see the appearance of doublets centered at 114, 126, and 151 Hz, indicating that these transitions occur between manifolds with $F = 0$ and $F = 1$. It is interesting to note that these doublets display different splittings due to differences in the Landé g factors for the different manifolds involved in these transitions. The line at 131 Hz splits first into a doublet, which split into a pair of doublets. One can show that such a splitting pattern arises for a $F = 1 \leftrightarrow F = 1$ (see Supplementary Information). The small zero-field peak at 168 Hz splits into four lines, barely above the noise, indicating an additional $F = 1 \leftrightarrow F = 1$ transitions. Finally, the zero-field peak at 155.5 Hz splits into a sextet indicating the transition is $F = 1 \leftrightarrow F = 2$. The six lines in this multiplet appear “inside-out” compared to the six line multiplet observed at $2J$ in 2-acetonitrile due to a reversal in relative magnitude of the Landé g factor.

The multiplicity of the peaks in this part of the spectrum can be understood as follows: Suppose we start with a ^{13}CH$_3$ group, and confine our attention to the $1 \leftrightarrow 0$ transition with total proton spin = 1/2, yielding transitions in the neighborhood of $^1J_{\mathrm{CH}}$. Addition of the second ^{13}C splits

---

[1] An additional peak at 11.2 Hz may correspond to a vibrational resonance of the building or to an uncoupled proton due to an unknown solvent in the sample

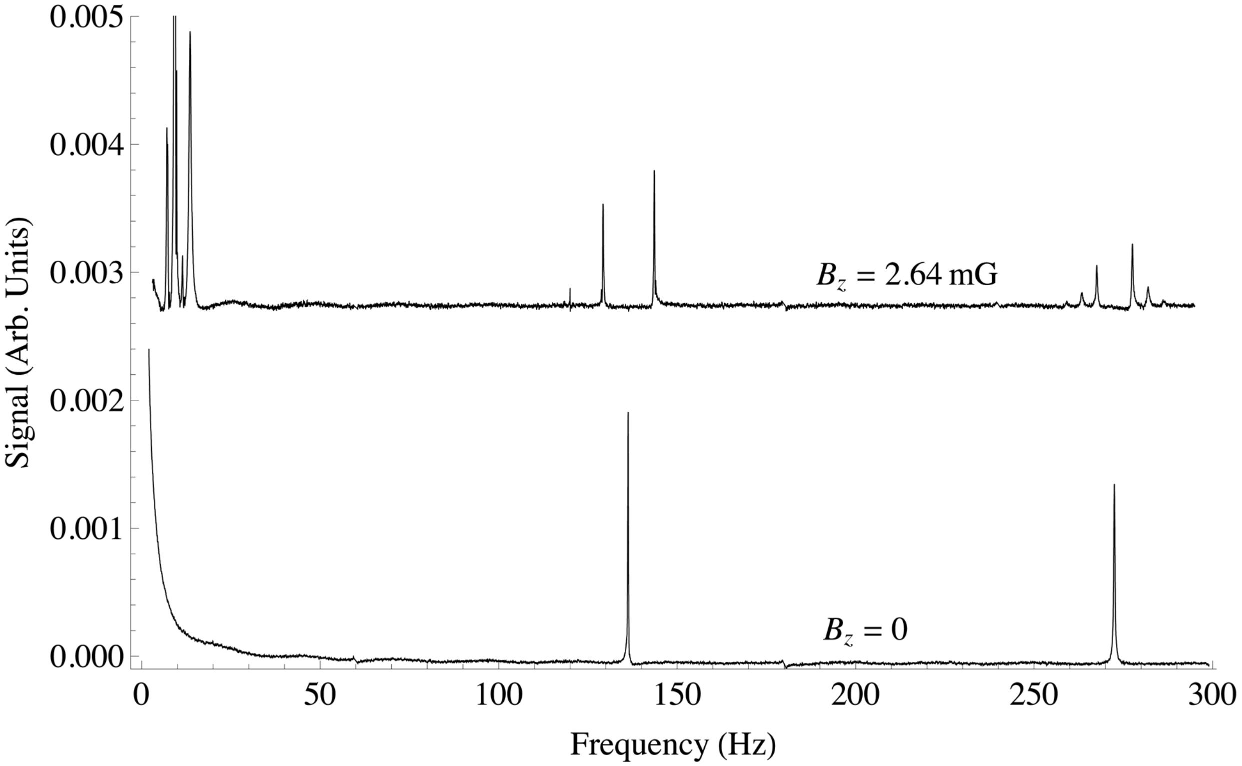

Figure 6.3: Spectra for singly labeled acetonitrile-2-^{13}C, ^{13}CH$_3$CN in zero-field and in a field of 2.64 mG. The positions of all peaks are well described by Eqs. (6.6)-(6.18). Adapted with permission from Ref. [64]. ©2011 American Physical Society

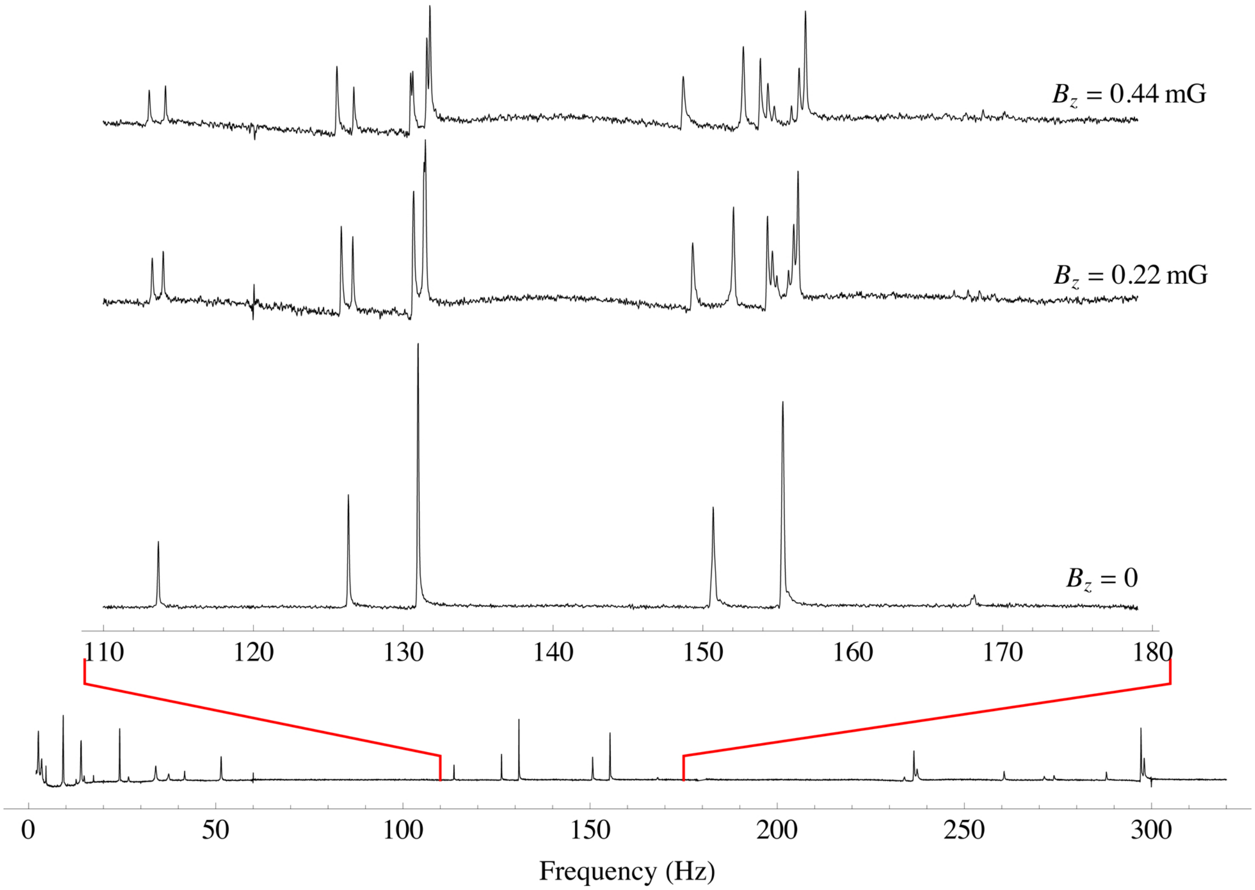

Figure 6.4: Effects of small magnetic fields on fully labeled acetonitrile $^{13}CH_3^{13}C^{15}N$. The bottom trace shows the entire zero-field spectrum. The upper traces show an expanded view of the central part of the zero-field spectrum, as well as the spectra in the indicated finite fields. Adapted with permission from Ref. [64]. ©2011 American Physical Society

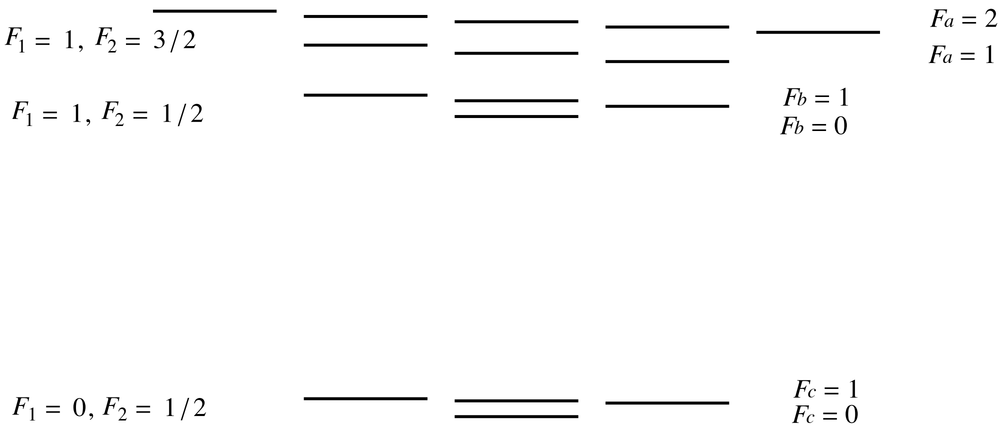

Figure 6.5: Energy levels for fully labeled acetonitrile with protons in $K = 1/2$ manifolds. Adapted with permission from Ref. [64]. ©2011 American Physical Society

these levels: $F = 1$ splits to 3/2, 1/2 manifolds, and $F = 0$ manifolds splits to 1/2. Addition of the ^{15}N splits these so we now have $F_a = 2$ or 1, $F_b = 1$ or 0, and $F_c = 1$ or 0. For now, we ignore transitions between $F_a \leftrightarrow F_b$ because they occur at low frequency. Employing the $\Delta F = 1$ rule we expect three $1 \leftrightarrow 0$ transitions, producing doublets: $F_a = 1 \leftrightarrow F_c = 0$, $F_b = 1 \leftrightarrow F_c = 0$, and $F_b = 0 \leftrightarrow F_c = 1$. Transitions between $F_a = 2 \leftrightarrow F_c = 1$ yields a multiplet with six lines, and transitions with $\Delta F = 0$ between $F_a = 1 \leftrightarrow F_c = 1$ and between $F_b = 1 \leftrightarrow F_c = 1$ yield multiplets with four lines.

For a more rigorous description, we proceed as follows: we have analytically calculated the first-order corrections to the energy eigenvalues and the splitting patterns for the case of the $\mathrm{CH_N}$ group, so we wish to extend this to larger spin systems in a straightforward way. We now proceed to analyze the case of fully labeled acetonitrile $^{13}\mathrm{CH}_3\,^{13}\mathrm{C}^{15}\mathrm{N}$.

The energy eigenstates $|\phi_a\rangle$ can be approximately constructed by iteratively adding additional spins to the spin pair with the largest spin coupling. This treatment is valid in the limit where the coupling of each additional spin to the previous spin system is small compared to that of all the previous couplings. In the following, $\mathbf{k}$ is the sum of the equivalent proton spins, $\mathbf{S}_1$ is the methyl ^{13}C, $\mathbf{S}_2$ is the second ^{13}C, and $\mathbf{N}$ is the ^{15}N spin. In zero magnetic field, the eigenstates of the strong one bond ^{13}CH coupling are those of $\mathbf{F}_1^2$ and F_{1z} (here $\mathbf{F}_1 = \mathbf{S} + \mathbf{K}$), which can be expressed in terms of the uncoupled states via the Clebsch-Gordan coefficients:

$$|F_1, m_1\rangle = \sum_{m_K, m_S} \langle F_1 m_1 | K S_1 m_K m_S\rangle |K m_K\rangle |S m_S\rangle. \tag{6.19}$$

Adding $\mathbf{S}_2$ to $\mathbf{F}_1$ yields the states

$$|F_2, m_2\rangle = \sum_{m_1, m_{S_2}} \langle F_2 m_2; K | F_1 S_2 m_1 m_{S_2}\rangle |F_1 m_1\rangle |S_2 m_{S_2}\rangle. \tag{6.20}$$

The quantity $\langle F_2 m_2; K | F_1 S_2 m_1 m_{S_2}\rangle$ is the usual Clebsch Gordan coefficient for addition of angular momenta $\mathbf{F}_1$ and $\mathbf{S_2}$; the quantum number K is included because the same value of F_1 can be

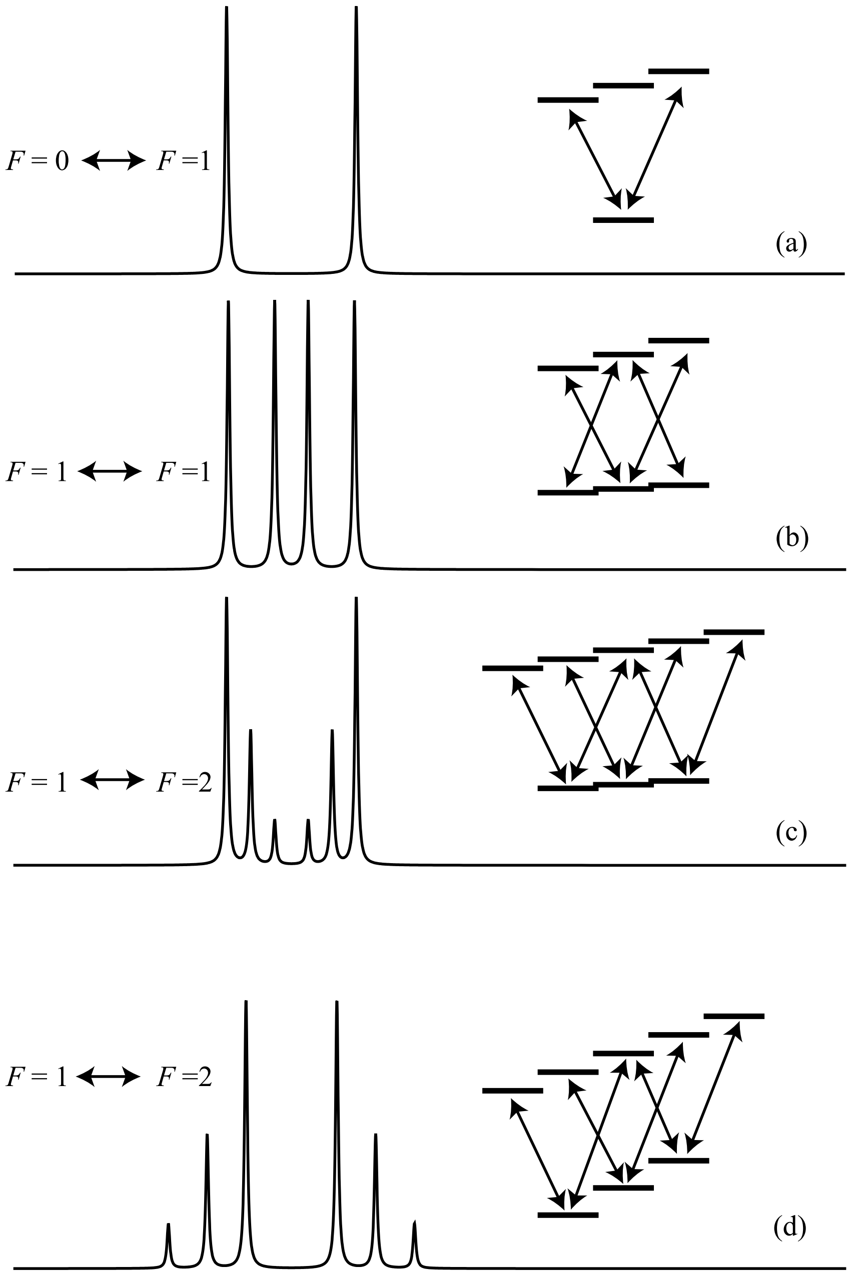

Figure 6.6: Near-zero-field NMR multiplets arising from several different transitions, as indicated. The upper three multiplets correspond approximately to those found in the fully labeled acetonitrile spectra. Trace (d) corresponds to the $K = 3/2$ transitions of labeled acetonitrile-2, displaying an "inside-out" pattern compared to the $F = 1 \leftrightarrow F' = 2$ transition of fully labeled acetonitrile. Adapted with permission from Ref. [64]. ©2011 American Physical Society

obtained with different values of K. Finally, adding $\mathbf{N}$ to $\mathbf{F}_2$ yields the states

$$|F, m\rangle = \sum_{m_2, m_N} \langle Fm; F_1, K|F_2 N m_2 m_N\rangle |F_2 m_2\rangle |N m_N\rangle. \tag{6.21}$$

Now, to find the first-order energy shifts, we calculate the diagonal matrix elements $\langle Fm|H_Z|Fm\rangle$. Inserting the expressions for the eigenstates, we find

$$\begin{aligned}\langle Fm|\mathcal{H}_Z|Fm\rangle = -\sum_{m_1 m_2 m_N}\sum_{m_K m_{S_1} m_{S_2}} &\langle Fm; F_2 F_1 K|F_2 N m_2 m_N\rangle^2 \\ &\times \langle F_2 m_2; F_1 K|F_1 S_2 m_1 m_{S_2}\rangle^2 \langle F_1 m_1; K|K S_1 m_K m_{S_1}\rangle^2 \\ &\times \left(\gamma_c m_{S_1} + \gamma_c m_{S_2} + \gamma_n m_N + \gamma_p m_K\right) B_z.\end{aligned} \tag{6.22}$$

We now connect this with the discussion above regarding the fully labeled acetonitrile spectrum. The proton spins can be either $K = 1/2$ or $K = 3/2$. Confining our attention to the latter, adding the first carbon $\mathbf{S}_1$ to the system yields $F_1 = 0$ and 1, separated by ${}^1J_{\mathrm{CH}}$. Adding $\mathbf{S}_2$ to the system produces manifolds with $F_2 = 1/2$ and 3/2 for $F_1 = 1$ and $F_2 = 1/2$ for $F_1 = 0$. Finally, adding the nitrogen spin $\mathbf{N}$ to the system produces manifolds with $F_a = F = 2, 1$ for $F_2 = 3/2$ and $F_1 = 1$, $F_b = F = 1, 0$ for $F_2 = 1/2$ and $F_1 = 1$, and $F_c = F = 1, 0$ for $F_2 = 1/2$ and $F_1 = 0$. These energy levels are shown schematically in Fig. 6.5, along with small Zeeman shifts. Lines that occur in the neighborhood of ${}^1J_{\mathrm{CH}}$ must be due to transitions between states with $\Delta F_1 = 1$.

The splitting patterns for a particular multiplet can be determined by applying the selection rules $\Delta F = 0, \pm 1$ and $\Delta m_F = \pm 1$, with amplitudes determined by Eq. (6.19). Traces (a)-(c) in Fig. 6.6 show the energy levels and splitting patterns for several of the transitions in fully labeled acetonitrile for protons in the $K = 1/2$ state. For contrast, trace (d) shows the splitting pattern for the $F = 1 \leftrightarrow F = 2$ transition for acetonitrile-2 (${}^{13}\mathrm{CH_3CN}$), displaying an "inside-out" pattern compared to the $F = 1 \leftrightarrow F = 2$ transition shown for fully labeled acetonitrile. This is because of the reversal in relative magnitudes of the Landé g factors for the $F = 1$ and $F = 2$ states.

6.5 Not-So-Near-Zero-Field

In systems with small couplings, such as 1-acetic acid ($\mathrm{CH_3}\,{}^{13}\mathrm{COOH}$) which has a two-bond coupling, ${}^2J_{\mathrm{CH}} = 6.8$ Hz, it is possible to explore the regime in which the Zeeman interaction is comparable to the J-coupling. Figure 6.7 shows experimental spectra for 1-acetic acid for the indicated magnetic fields. The large peak that does not split is due to the uncoupled OH group, while the rest of the spectrum corresponds to the $\mathrm{CH_3}\,{}^{13}\mathrm{C}$ part of the molecule. Initially, the spectrum appears similar to the 2-acetonitrile spectrum, with a doublet at J, and an additional doublet at $2J$ composed of several unresolved lines. As the magnetic field is increased, additional lines in the multiplet at $2J$ become resolved. At the highest magnetic fields, the spectrum displays the highest complexity, and is no longer recognizable from the perturbative treatment presented above. The smooth trace at the top of the plot shows the log of the absorptive component of a high resolution numerical simulation, reproducing all features of the data, to the extent that lines are

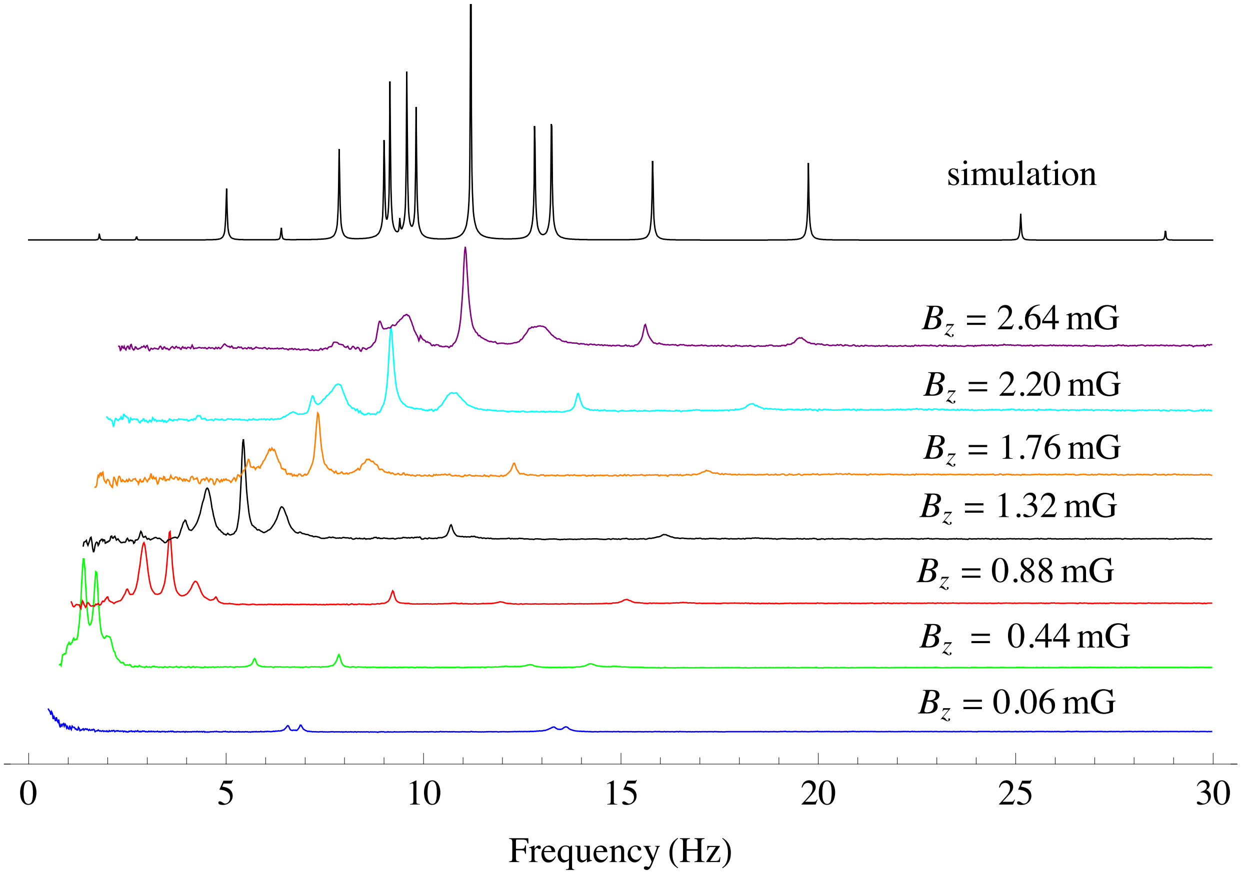

Figure 6.7: Experimental spectra for 1-acetic acid, ($CH_3\,{}^{13}COOH$) in the indicated magnetic fields. The smooth curve at the top of the plot presents the result of a full numerical simulation with high resolution. Adapted with permission from Ref. [64]. ©2011 American Physical Society

resolved. Careful examination reveals 17 lines, 1 for the OH group and $(N + 1)^2 = 16$ lines, as theoretically predicted in Ref. [118].

6.6 Significance of Near-Zero-Field NMR

In conclusion, we have investigated near-zero-field nuclear magnetic resonance, where the effects of magnetic fields can be treated as a perturbation to the scalar J-couplings. This work represents a new form of NMR spectroscopy, complementary to high-field NMR, in which heteronuclear scalar couplings are almost always treated as a small perturbation to the dominant Zeeman interaction. We find that the presence of small fields produces splitting of zero-field lines. The splitting patterns have easy-to-understand rules and data are in excellent agreement with the predictions of first-order perturbation theory. It is interesting to note that the phenomenology observed here is similar to that of atomic spectroscopy of multi-electron atoms, and intuition developed in the latter field may be applied to interpretation of NZF NMR spectra. We have also investigated the case where Zeeman and J-couplings are comparable, resulting in signals with much higher complexity, potentially useful for NMR quantum computing [118].

Chapter 7

Zero-Field NMR in Anisotropic Media

This chapter might seem a bit whimsical,
But dipolar terms are certainly critical.
It takes no wizardry
In the ZULF symmetry...
Well at least if the coupling's residual.

ZULF-NMR permits the measurement of nuclear spin-spin interactions free from effects of large magnetic fields, such as truncation of terms that do not commute with the Zeeman Hamiltonian. One such interaction, the magnetic dipole-dipole coupling, is a valuable source of spatial information in NMR, though many terms are unobservable in high-field NMR, and the interaction averages to zero under isotropic molecular tumbling. Under partial orientational ordering, this information is retained in the form of so-called residual dipolar couplings. This chapter describes zero- and ultra-low-field NMR measurements of residual dipolar couplings in acetonitrile-2-^{13}C aligned in stretched polyvinyl acetate gels. This allows investigation of dipolar couplings as a perturbation on the indirect spin-spin J-coupling in the absence of an applied magnetic field. As a consequence of working at zero magnetic field, we observe terms of the dipole-dipole coupling Hamiltonian that are invisible in conventional high-field NMR. This technique expands the capabilities of zero- and ultra-low-field NMR and may have applications in chemical analysis, precision measurement of subtle physical interactions, and characterization of local mesoscale structure in materials. These results of this chapter have been compiled into a manuscript awaiting submission:

- Blanchard, J.W., Sjolander, T.F., King, J.P., Ledbetter, M.P., Levine, E.H., Budker, D., and Pines, A. Residual Dipolar Couplings in Zero- to Ultra-Low-Field NMR. In Preparation.

7.1 Motivation and Overview

Nuclear magnetic resonance (NMR) experiments are conventionally performed in large magnetic fields in order to increase chemical shift resolution and to maximize signal via higher nuclear spin polarization and improved inductive detection sensitivity [119]. Recently, NMR experiments have been carried out in the opposite regime of very small magnetic fields [120, 118, 64, 121], taking advantage of advances in hyperpolarization [71, 72, 122, 123] and new detection modalities [53, 124, 56, 125, 42, 50, 126]. In the zero-field limit, spin dynamics are determined by local spin-spin interactions, in contrast to conventional high-field NMR where the coupling to the external field is dominant, so that only truncated parts of the spin-spin interactions can be measured. For example, in the case of heteronuclear magnetic dipole-dipole coupling at high-field, only terms of the Hamiltonian that conserve all magnetic quantum numbers are observable. Conversely, at zero-field, where we are no longer constrained by a uniaxial field geometry, it is in principle possible to measure all coupling terms. Thus zero-field NMR grants access to additional spectral information otherwise unavailable in magnetic resonance spectroscopy.

In this section we report the observation of the effect of dipolar couplings as a perturbation on the indirect spin-spin J-coupling in the absence of an external magnetic field. Dipolar couplings have long been used in high-field NMR to provide structural information in addition to the chemical shift. Previously work has demonstrated zero-field J-spectroscopy of several systems for chemical analysis [65, 66, 110]. Additional information may also be obtained from zero-field NMR spectra via application of weak magnetic fields [64]. In the regime where dipole-dipole coupling can be treated as a perturbation to J-coupling, zero- and ultra-low-field (ZULF) NMR allows sensitive measurement of the dipole-dipole coupling tensor. However, direct dipole-dipole couplings observed in solids are typically on the order of tens of kHz, substantially larger than J-couplings, and coherence and polarization lifetimes are often too short for current ZULF methodology. Furthermore, all dipole-dipole coupling terms average to zero in isotropic liquids. Smaller, scaled couplings are obtained by weakly aligning the molecule of interest in anisotropic media, such as liquid crystals [127, 128, 129] or stretched gels [130, 131], where molecular motion is partially restricted, yielding residual couplings. Such techniques have found widespread use in high-field NMR for structural measurements of proteins and small organic molecules [132, 133, 134, 135]. Here, we investigate the effects of residual dipole-dipole couplings (RDCs) on the zero-field spectrum of a model spin system: acetonitrile-2-^{13}C ($^{13}CH_3CN$) aligned in stretched crosslinked polyvinyl acetate (PVAc) gels.

7.2 Preparation of Stretched Gel Samples

Polyvinyl acetate (PVAc) polymer sticks containing between 1-6% v/v divinyl adipate (DVA) cross-linker were prepared in 5 mm NMR tubes by adding the radical initiator azobisisobutyronitrile (AIBN) to a solution of 60% vinyl acetate and 40% acetone by volume. The presence of

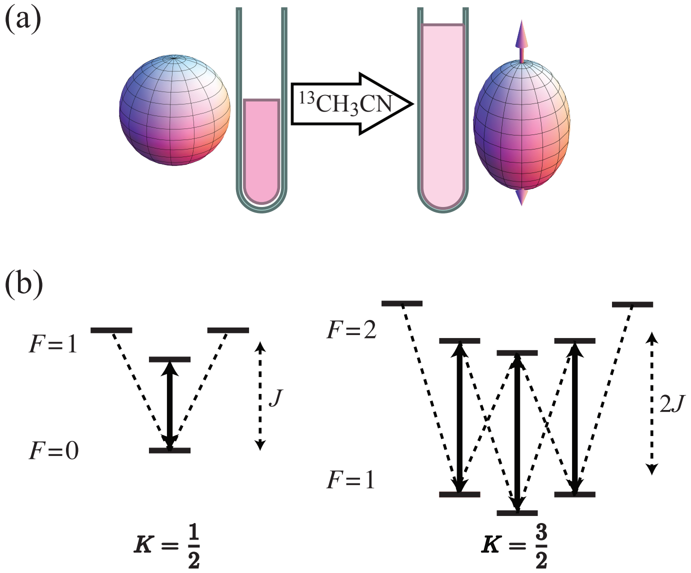

Figure 7.1: a) Schematic illustration of the change in symmetry that occurs during uniaxial stretching of the gel environment due to swelling with acetonitrile-2-^{13}C. The change in the order parameter is illustrated by the different three-dimensional shapes. b) Energy level structure of a partially ordered XA_3 spin system. F is the total spin angular momentum, K is the total proton angular momentum, and J is the one-bond ^{13}C – ^{1}H J-coupling. Solid arrows indicate allowed transitions, dashed lines indicate forbidden transitions.

the acetone was prompted by synthetic considerations.[1] Samples with varying alignment strength were prepared by adding a variable amount of the cross-linker DVA to the mixture before transfer to standard 5mm NMR tubes – increased cross-linking was found to correlate with increased alignment. The samples were then heated in an oven at 45°C for 7 days to initiate polymerization via the thermal decomposition of AIBN, followed by 2 days at 55°C in order to ensure that the reaction went to completion.[2]

Anisotropic gels were prepared by adding acetonitrile to the tubes and allowing the polymers to swell for 2 weeks. Because the polymers were confined to the NMR tubes in which they were cast, swelling was uniaxial and equivalent to stretching along the axis of the NMR tube. A schematic representation of the process is shown in Fig. 7.1(a).

In order to maximize the ZULF NMR signal the samples were prepared using labeled acetonitrile-2-^{13}C to which was added 5% v/v deuterated acetonitrile for the purpose of high-field NMR char-

---

[1] It was found that performing the polymerization reaction without an additional solvent frequently led to cracks or bubbles in the resulting polymer sticks. Presumably, carrying out the reaction in the presence of acetone allowed the reaction to continue to completion in an essentially solution phase without nonlinear issues related to phase transitions occurring during the reaction. The acetone is then easily removed by evaporation.

[2] After preparing the samples used for this study, additional "backup" polymer samples were prepared via slightly different means, the most successful of which involved a nearly identical procedure, but with sample heating performed in a temperature-controlled sand bath. The polymer sticks produced using the sand bath were consistently of high quality, so we suggest that this method is generally preferable for future applications of this work.

acterization. The molecular order parameter [136, 137] for acetonitrile in the stretched gel environment was determined by analyzing the quadrupolar splitting of the deuterium resonance [127, 138] using a 14.1 T NMR spectrometer with deuterium frequency 92.1 MHz. The value for the electric-field gradient around the deuterium nuclei in acetonitrile was obtained from the literature [138].

The ZULF-NMR apparatus has been described previously [109, 71, 64]. Samples were prepolarized in a 2 T permanent magnet located outside of the magnetic shielding for ≈20 s and then shuttled pneumatically to the zero-field region over 0.5 - 1 s. NMR signals were detected with an atomic magnetometer featuring a 0.6 × 0.6 × 1.0 cm ^{87}Rb vapor cell operating at 180°C. Transient signals were collected over ≈20 s. The spectra in Fig. 7.2 are the average of between 256 and 1024 transients, and the spectra in Fig. 7.3 are the average of 8 transients.

7.3 Theory of Residual Dipolar Couplings in Zero-Field NMR

The spin Hamiltonian in the presence of J-couplings and dipole-dipole interactions is

$$\mathcal{H} = \hbar \sum_{j;k>j} J_{jk} \mathbf{I}_j \cdot \mathbf{I}_k - \hbar^2 \frac{\mu_0}{4\pi} \sum_{j;k>j} \frac{\gamma_j \gamma_k}{r_{jk}^3} \left[3 \left(\mathbf{I}_j \cdot \hat{\mathbf{r}}_{jk} \right) \left(\mathbf{I}_k \cdot \hat{\mathbf{r}}_{jk} \right) - \mathbf{I}_j \cdot \mathbf{I}_k \right], \tag{7.1}$$

where $\hbar$ is the reduced Planck constant, μ_0 is the vacuum permeability, γ_j and γ_k are the gyromagnetic ratios of spins $\mathbf{I}_j$ and $\mathbf{I}_k$, and $\mathbf{r}_{jk}$ is the internuclear vector connecting the spins. In the case of isotropic liquids, the dipole-dipole interaction term averages to zero. However, in aligned samples, such as stretched gels, the motional averaging of the dipole-dipole term is incomplete. For the system studied here, the swelling of the polymer gel with acetonitrile along the axis of the NMR tube leads to an orientational probability distribution of the solvent molecules that is slightly anisotropic, with the preferential alignment axis (the director) determined by the swelling direction [130, 131]. This axis is collinear with the sensitive direction of the detector, and is denoted z. Because of the rapid rotation of the acetonitrile methyl group and the axial symmetry of the alignment medium, the x and y components of the $\mathbf{r}_{jk}$ vectors are averaged to zero, and the z components are scaled by the degree of alignment. Considering these averaging effects on the second term of Eq. (7.1), the residual dipolar coupling Hamiltonian is

$$\mathcal{H}_{RDC} = -\hbar \sum_{j;k>j} D_{jk} \left(3 I_{j,z} I_{k,z} - \mathbf{I}_j \cdot \mathbf{I}_k \right), \tag{7.2}$$

where

$$D_{jk} = \frac{\mu_0}{8\pi} \frac{\gamma_j \gamma_k \hbar}{r_{jk}^3} \left\langle 3 \cos^2 \theta_{jk} - 1 \right\rangle. \tag{7.3}$$

We may also define the coupling as being directly proportional to the molecular order parameter $\mathcal{S}_{zz} = \frac{1}{2} \left\langle 3 \cos^2 \theta_z - 1 \right\rangle$ [136, 137], a measure of the extent to which acetonitrile's C_3-axis is aligned with the laboratory z-axis, such that

$$D_{jk} = \frac{\mu_0}{4\pi} \frac{\gamma_j \gamma_k \hbar}{r_{jk}^3} \left(3 \cos^2 \phi_{jk} - 1 \right) \mathcal{S}_{zz}, \tag{7.4}$$

where ϕ_{jk} is the angle between $\mathbf{r}_{jk}$ and the C_3 axis, $\pi/2$ for D_{HH} and the tetrahedral angle ($2\arctan\sqrt{2}$) for D_{CH}.

In the regime where $D_{jk} \ll J_{jk}$, the residual dipolar couplings may be treated as a perturbation on the J-coupling. For acetonitrile-2-^{13}C, it is convenient to write the first term of Eq. (7.1) as

$$\mathcal{H}^{(0)} = \hbar\, {}^1J_{\mathrm{CH}} \mathbf{K} \cdot \mathbf{S}, \tag{7.5}$$

where $^1J_{CH}$ is the one-bond J-coupling, $\mathbf{K} = \sum_j \mathbf{I}_j$ is the total proton spin angular momentum, and $\mathbf{S}$ is the ^{13}C spin angular momentum [64]. The eigenstates of $\mathcal{H}^{(0)}$ are also eigenstates of $\mathbf{F}^2$ and F_z, where $\mathbf{F} = \mathbf{K} + \mathbf{S}$ is the total spin angular momentum. The eigenstates have degeneracy $2F + 1$ and energy

$$E^{(0)} = \frac{\hbar\, {}^1J_{\mathrm{CH}}}{2} \left[F(F+1) - K(K+1) - S(S+1)\right]. \tag{7.6}$$

To explore the effect of the residual dipolar coupling on the J-coupling eigenstates, it is convenient to decompose Eq. (7.2) into two heteronuclear terms,

$$\mathcal{H}^{(1a)} = -3\hbar D_{\mathrm{CH}} K_z S_z \tag{7.7}$$

and

$$\mathcal{H}^{(1b)} = \hbar D_{\mathrm{CH}} \mathbf{K} \cdot \mathbf{S}, \tag{7.8}$$

and a homonuclear term,

$$\mathcal{H}^{(1c)} = -\hbar D_{\mathrm{HH}} \sum_{j \neq k} \left(3 I_{j,z} I_{k,z} - \mathbf{I}_j \cdot \mathbf{I}_k\right). \tag{7.9}$$

It is worth noting that Eqs. (7.7) and (7.8) group the terms of the heteronuclear dipolar coupling Hamiltonian differently from the typical high-field NMR approach, because the only term that survives at high-field is

$$\mathcal{H}^{(trunc)} = -2\hbar D_{\mathrm{CH}} K_z S_z, \tag{7.10}$$

wherein a term of the form

$$\mathcal{H}_{RDC} - \mathcal{H}^{(trunc)} = \frac{\hbar}{2}\left(I_+ S_- + I_- S_+\right), \tag{7.11}$$

is truncated because it does not commute with the high-field Zeeman Hamiltonian. The zero-field Hamiltonian is untruncated, and thus includes this so-called “heteronuclear flip-flop” term that is invisible to high-field NMR.

To first order in D_{CH}, the energy shifts due to the heteronuclear residual dipolar coupling are

$$\begin{aligned}\Delta E^{(1a)} &= -3\hbar D_{\mathrm{CH}} \langle F m_F | K_z S_z | F m_F \rangle \\ &= -3\hbar D_{\mathrm{CH}} \sum_{m_K, m_S} \langle K S m_K m_S | F m_F \rangle^2 m_K m_S,\end{aligned} \tag{7.12}$$

where $\langle KS\, m_K m_S | F m_F \rangle$ are the Clebsch-Gordan coefficients, and

$$\begin{aligned}\Delta E^{(1b)} &= \hbar \frac{D_{\mathrm{CH}}}{2} \langle F m_F | \left(\mathbf{F}^2 - \mathbf{K}^2 - \mathbf{S}^2 \right) | F m_F \rangle \\ &= \hbar \frac{D_{\mathrm{CH}}}{2} \left[F(F+1) - K(K+1) - \frac{3}{4} \right]. \end{aligned} \tag{7.13}$$

For all $K = \frac{1}{2}$ states, the homonuclear residual dipolar coupling has no effect, as the rank-2 spherical-tensor operator of Eq. (7.9) defined in terms of proton angular momentum can only connect two states having total proton angular momentum K and K' such that $K + K' \geq 2$. The total energy shifts for the $K = \frac{1}{2}$ states are thus

$$\Delta E^{(1)} \left(F = 0, m_f = 0 \right) = 0, \tag{7.14}$$

$$\Delta E^{(1)} \left(F = 1, m_f = 0 \right) = \hbar D_{\mathrm{CH}}, \tag{7.15}$$

$$\Delta E^{(1)} \left(F = 1, m_f = \pm 1 \right) = -\frac{\hbar}{2} D_{\mathrm{CH}}. \tag{7.16}$$

The first-order energy shifts due to the homonuclear residual dipolar couplings for the $K = \frac{3}{2}$ may be calculated in a similar method to that of Eqs. (7.12) and (7.13), though the effects of couplings between equivalent spins must be considered. The total shifts for the $K = \frac{3}{2}$ states are

$$\Delta E^{(1)} \left(F = 1, m_F = 0 \right) = -\frac{\hbar}{2} \left(D_{\mathrm{CH}} - 3 D_{\mathrm{HH}} \right), \tag{7.17}$$

$$\Delta E^{(1)} \left(F = 1, m_F = \pm 1 \right) = \frac{\hbar}{4} \left(D_{\mathrm{CH}} - 3 D_{\mathrm{HH}} \right), \tag{7.18}$$

$$\Delta E^{(1)} \left(F = 2, m_F = 0 \right) = \frac{3\hbar}{2} \left(D_{\mathrm{CH}} + D_{\mathrm{HH}} \right), \tag{7.19}$$

$$\Delta E^{(1)} \left(F = 2, m_F = \pm 1 \right) = \frac{3\hbar}{4} \left(D_{\mathrm{CH}} + D_{\mathrm{HH}} \right), \tag{7.20}$$

$$\Delta E^{(1)} \left(F = 2, m_F = \pm 2 \right) = -\frac{3\hbar}{2} \left(D_{\mathrm{CH}} + D_{\mathrm{HH}} \right). \tag{7.21}$$

Because the observable in this experiment is the z-magnetization $M_z(t) \propto \mathrm{Tr}\, \{\rho(t) \sum_j I_{jz} \gamma_j\}$, the detectable coherences are those with $\Delta F = 0, \pm 1$ and $\Delta m_F = 0$. An additional selection rule, $\Delta K = 0$, arises in the case of equivalent spins (e.g. the methyl protons in acetonitrile) because $\mathbf{K}^2$ commutes with the Hamiltonian [109, 64].

It follows that there is one allowed transition between $K = \frac{1}{2}$ states, between the $|F = 0, m_F = 0\rangle$ and $|F = 1, m_F = 0\rangle$ states with frequency

$$\nu_{0,0}^{1,0} =^1 J_{CH} + D_{CH}. \tag{7.22}$$

In addition, there are nominally forbidden (assuming that the detector is only sensitive in the z-direction) $\Delta m_F = \pm 1$ transitions with frequency

$$\nu_{0,0}^{1,\pm 1} =^1 J_{CH} - \frac{D_{CH}}{2}. \tag{7.23}$$

For the transitions between $K = \frac{3}{2}$ states, there are allowed transitions with frequencies

$$\nu_{1,0}^{2,0} = 2^1J_{CH} + 2D_{CH}, \tag{7.24}$$

$$\nu_{1,\pm1}^{2,\pm1} = 2^1J_{CH} + \frac{1}{2}\left(D_{CH} + 3D_{HH}\right), \tag{7.25}$$

and nominally forbidden transitions $\Delta m_F = \pm 1$ with frequencies

$$\nu_{1,0}^{2,\pm1} = 2^1J_{CH} - \frac{1}{4}\left(7D_{CH} + 3D_{HH}\right), \tag{7.26}$$

$$\nu_{1,\pm1}^{2,\pm2} = 2^1J_{CH} + \frac{1}{4}\left(5D_{CH} - 3D_{HH}\right), \tag{7.27}$$

$$\nu_{1,\pm1}^{2,0} = 2^1J_{CH} + \frac{1}{4}\left(5D_{CH} + 9D_{HH}\right). \tag{7.28}$$

If the detector axis is not exactly aligned with the director/quantization axis, the nominally forbidden transitions become observable.

7.4 Zero-Field Spectra of Acetonitrile-2-^{13}C in Stretched Gels

Zero-field spectra of acetonitrile-2-^{13}C (^{13}CH$_3$CN) in polyvinyl acetate are shown in Fig. 7.2(a) for increasing values of the order parameter corresponding to the C_3 axis. As the order parameter increases, the $K = \frac{1}{2}$ peaks corresponding to the ordered portion of the sample split, while the $K = \frac{1}{2}$ peak corresponding to excess isotropic liquid external to the gel, remains unchanged. The lower-frequency peak in Fig. 7.2(a) corresponds to the $\Delta m_F = 0$ transition described by Eq. (7.22) and the higher-frequency peak corresponds to the $\Delta m_F = \pm 1$ transition described by Eq. (7.23). The phase of the $\Delta m_F = \pm 1$ peak is determined by the projection of the initial spin-state population onto the transverse component of the detection operator, and is thus an arbitrary signature of imperfections in the experimental configuration. Because the $\Delta m_F = \pm 1$ peaks are consistently narrower than the $\Delta m_F = 0$ peaks in Fig. 7.2(a), it appears that the linewidth is affected by imperfections in the gel producing an inhomogeneous order parameter and thus a spread in transition frequencies proportional to D_{CH}.

Figure 7.2(b) shows four $K = \frac{3}{2}$ peaks, three from the aligned acetonitrile-2-^{13}C, and one from the isotropic liquid. The two lower-frequency peaks arise from the $\Delta m_F = 0$ transitions described by Eqs. (7.24-7.25) and the small higher-frequency peak corresponds to the $\Delta m_F = \pm 1$ transition described by Eq. (7.26). Transitions corresponding to Eqs. (7.27-7.28) are not resolved.

In high-field NMR, terms in the Hamiltonian that do not commute with the Zeeman Hamiltonian are neglected, due to their immeasurably small effect on the NMR spectrum. Due to the absence of a large Zeeman interaction, ZULF NMR provides spectroscopic access to all spin-coupling terms [140]. In traditional high-field NMR, only part of the heteronuclear dipolar coupling, $\mathcal{H}^{(trunc)}$, from Eq. (7.10), yields measurable effects in the spectrum. By itself, this term would yield no shift of the $|F = 0, m_F = 0\rangle \leftrightarrow |F = 1, m_F = 0\rangle$ transition. In these data [Fig. 7.2(a)] the residual dipolar couplings clearly shift the peak relative to the isotropic liquid showing the

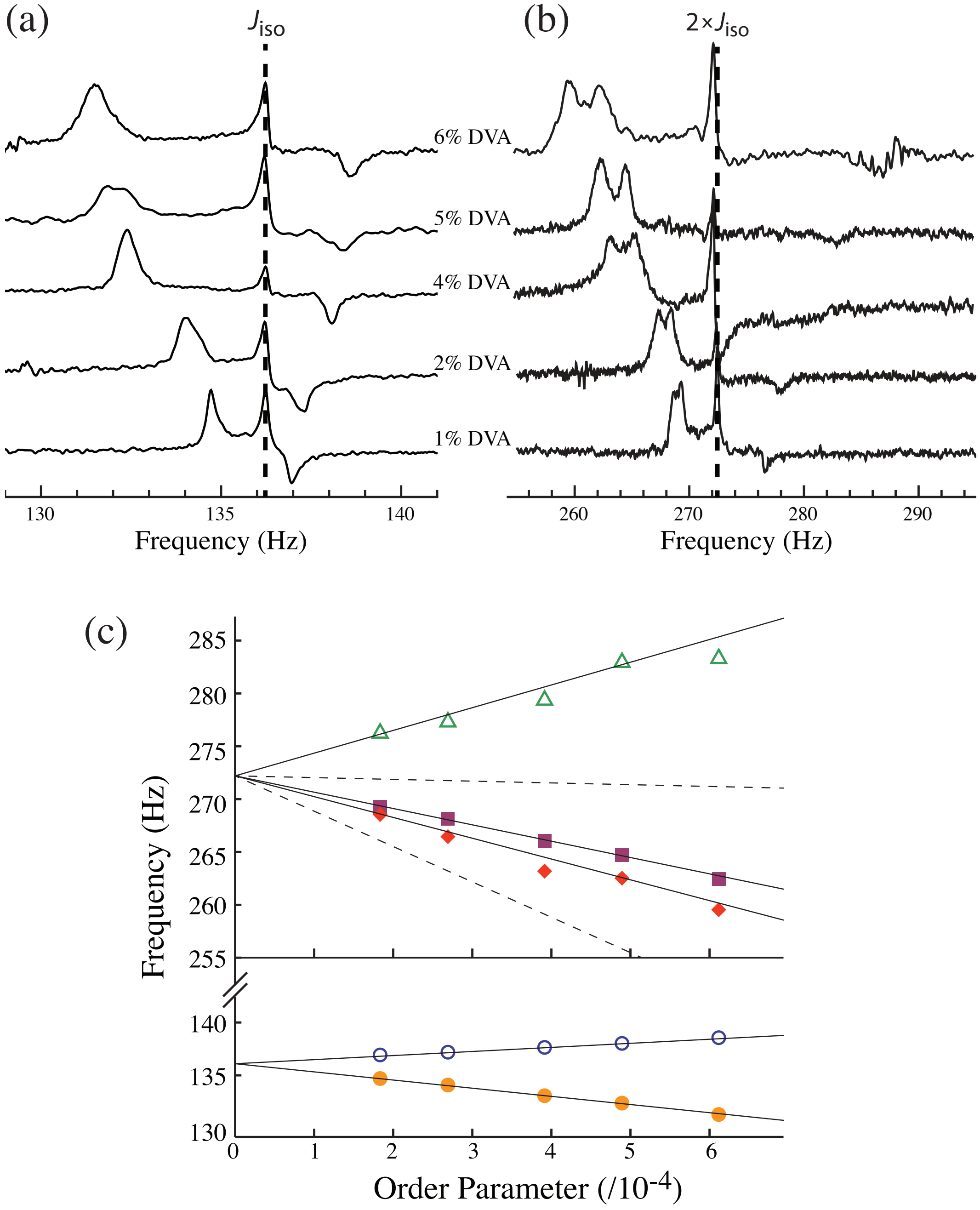

Figure 7.2: Zero-field spectra of acetonitrile-2-^{13}C with different degrees of ordering arising from the concentration of the cross-linker divinyl adipate (DVA). (a) $K = \frac{1}{2}$ and (b) $K = \frac{3}{2}$ peaks. (c) Peak positions as a function of order parameter. The lines are calculated transition frequencies based on literature values for the electric field gradient [138] and bond lengths [139] with no free parameters. Solid symbols represent allowed $\Delta m_f = 0$ transitions, open symbols represent transitions with $\Delta m_f = \pm 1$. Dashed lines indicate possible transitions that are not resolved.

observation of the untruncated Hamiltonian of Eq. (7.2), including the contribution of Eq. (7.11), an interaction “invisible” to traditional NMR. The absence of truncation that permits observation of this term has also been demonstrated via the preparation of heteronuclear spin-singlet states in Ref. [67].

As shown in Fig. 7.2(c), the frequency shift varies linearly with the order parameter. The data closely match the simulated curves, which are calculated from the order parameter using Eqs. (7.4) and (7.22-7.28).

In the situation where the sensitive axis of the magnetometer is parallel to the director of the gel orientation, only the $\Delta m_F = 0$ transitions are detected. If the detection axis (or direction of orientation) is rotated, the $\Delta m_F = \pm 1$ transitions are also observable, leading to peaks at higher frequency, with intensity dependent on the initial spin state populations and the angle between the detection and orientation axes. The additional peaks appear in Fig. 7.2 because the measurements were carried out using a magnetometer configuration that featured a rotated axis of detection due to a non-zero effective field at the Rb cell. We attribute this effect to imperfections in the magnetometer configuration, potentially related to laser alignment, AC Stark shifts, or a combination of the two. We point out that the effect was diminished after expanding the pump beam (thus decreasing the laser power density) and subsequently realigning the optics for the experiments in Fig. 7.3. It is worth noting that the rotation of the detection axis is necessary for the detection of the higher-frequency peaks only due to the axial symmetry of the system under study, which causes the terms of the dipolar coupling Hamiltonian that depend on the azimuthal angle to be averaged to zero. If these terms are not averaged to zero (e.g. in a biaxial ordered phase), they will further lift degeneracy and yield additional peaks [141].

7.5 Combination of Residual Dipolar Couplings and Zeeman Perturbation

We have also investigated the effect of applied magnetic fields on the spectrum, as shown in Fig. 7.3. When the effective detection operator is collinear with the gel director axis, only the $\Delta m_F = 0$ transition is observed (corresponding here to a 10 nT applied field). As the field is increased, however, states with different m_F are mixed, and the effects of imperfections in the magnetometer optics may be amplified via rotation of electron spins. The overall result is that as the field is increased, the vectors defining the detection operator and the quantization axis cease to be collinear. This in turn leads to the observation of $\Delta m_F = \pm 1$ transitions, which become dominant at fields of 60 nT and above, at which point the effective detection operator has been rotated substantially away from the director axis.

In the regime where the Zeeman interaction strength is on the order of the residual dipolar coupling, the peak frequencies in Fig. 7.3 do not vary linearly with the applied field strength. This is because the dipole-dipole coupling Hamiltonian does not commute with the Zeeman Hamiltonian, and thus first-order perturbation is no longer sufficient to describe the system.

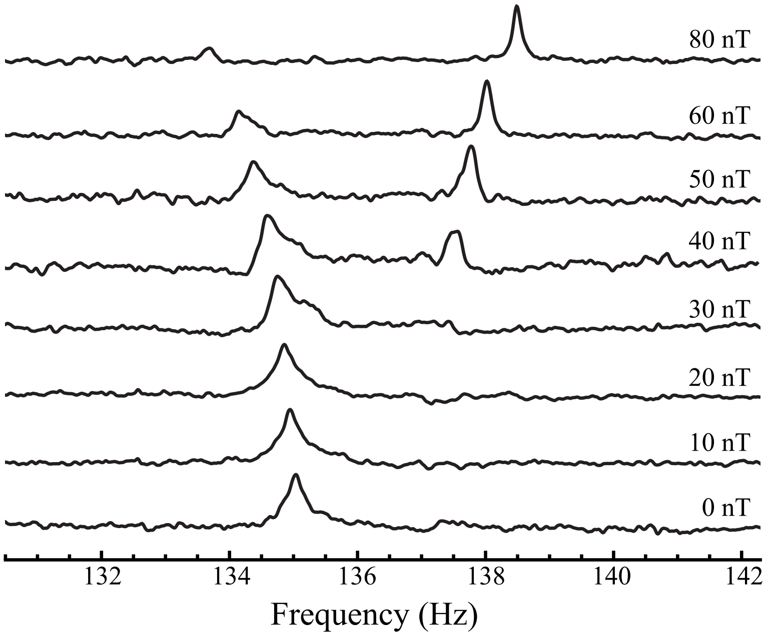

Figure 7.3: Acetonitrile-2-^{13}C $K = \frac{1}{2}$ peaks as a function of applied magnetic field.

7.6 Significance and Future Applications

We have detected residual dipolar couplings in zero- and ultra-low-field NMR spectra, including terms that are not directly observable in the high-field regime. The results are in strong agreement with a zero-free-parameter simulation utilizing literature values of internuclear distances and the electric field gradient of acetonitrile, the latter being used to determine the order parameter via high-field ^{2}H NMR. The sub-Hz resolution of ZULF NMR may be of future use for high-precision chemical analysis of small molecules.

We have also demonstrated the direct influence of the heteronuclear dipole-dipole coupling "flip-flop" term on ZULF NMR spectra. In principle, all terms of the spin coupling Hamiltonian are observable in ZULF NMR, increasing the information potentially available in NMR spectra. With appropriate systems (e.g. aligned chiral molecules) and continuing improvements in polarization and magnetometer sensitivity, ZULF NMR may be a promising method to measure subtle interactions such as the as-yet-unobserved antisymmetric components of the J-coupling tensor [142]. Based on calculations in Ref. [143], measurement of a non-zero antisymmetric J-coupling could permit the observation of a first-order energy shift arising from parity non-conservation in the molecular Hamiltonian.

This technique may also find application as a probe of material structure, allowing for the measurement of interactions with lower than azimuthal symmetry. For example, measurement of the full anisotropic spin-spin coupling tensor of small molecular probes within porous materials may provide a more complete description of local geometry than do measurements of total surface area or average pore diameter.

Chapter 8

Heteronuclear Singlets

If a state of two spins is beset,
One need not fear the dipolar threat,
Since one state that's revealed
By removing the field,
Is a heteronuclear singlet

This chapter reports the observation of long-lived spin-singlet states in a ^{13}C $-^{1}$ H spin pair in zero magnetic field. In ^{13}C-labeled formic acid, we observe spin-singlet lifetimes as long as 37 s, about a factor of three longer than the T_1 lifetime of dipole polarization in the triplet state. In contrast to common high-field experiments, the lifetime of the observed singlet-triplet coherence, T_2, is found to be longer than T_1, where the relaxation times, T_1 and T_2, are defined appropriately for the zero-field experiment. Moreover, we demonstrate that heteronuclear singlet states formed between a proton and a ^{13}C nucleus can exhibit longer lifetimes than the respective triplet states even in the presence of additional spins that couple to the spin pair of interest. Although long-lived homonuclear spin-singlet states have been extensively studied, this was the first experimental observation of analogous singlet states in heteronuclear spin-pairs. These results have been published previously:

- Emondts, M., Ledbetter, M.P., Pustelny, S., Theis, T., Patton, B., Blanchard, J.W., Butler, M.C., Budker, D., and Pines, A. Long-Lived Heteronuclear Spin-Singlet States in Liquids at a Zero Magnetic field. *Phys. Rev. Lett.* **112** (7), 077601. (2014)

8.1 Long-Lived Nuclear Spin States

Long-lived spin-singlet states have recently attracted considerable attention both experimentally [144, 145, 146, 147, 148, 149, 150, 151, 152, 153, 154] and theoretically [155, 156, 157, 158, 159]. Such states are of practical interest for their ability to store hyperpolarization for more than an order of magnitude longer than T_1 [152, 153] and for their utility in tracking slow chemical and biological processes [146, 148]. Long-lived spin states offer a wide range of applications to medicine, materials science, physiology and chemistry such as in vitro targetting of neuroscience relevant molecules [160], monitoring of protein unfolding [161] and probing of slow motion diffusion of biomolecules [162]. For recent reviews of long-lived states in nuclear magnetic resonance (NMR), see Refs. [163, 158].

In the case where two coupled spins are magnetically equivalent, the singlet state does not relax through their intramolecular dipole-dipole coupling, often the dominant source of relaxation in NMR. This is because the dipole-dipole interaction is symmetric with respect to exchange of particles and therefore cannot produce transitions between the antisymmetric singlet and symmetric triplet states. Other sources of relaxation, such as chemical-shift anisotropy, spin-rotation, and effects from paramagnetic impurities are also often suppressed for the singlet compared to the triplet states. As a result, singlet lifetimes can significantly exceed triplet lifetimes. The most dramatic case of a long-lived nuclear spin singlet state is parahydrogen, which has a lifetime of weeks, compared to the T_1 lifetime of orthohydrogen, which is on the order of seconds under typical experimental conditions (6 bar hydrogen pressure at room temperature in the absence of paramagnetic impurities).

8.2 Heteronuclear Spin-Singlet States at Zero Magnetic Field

In high-field NMR such singlet states must be composed of same-species (homonuclear) spin pairs, since the magnetic field breaks the equivalence of spin pairs formed by two different spin species. Here we demonstrate the existence of heteronuclear spin singlets at zero magnetic field; the spin singlet in question is formed by a strongly coupled ^{13}C-^{1}H pair in ^{13}C-labeled formic acid (^{13}CHOOH).[1] We show that the lifetime of this spin singlet, T_s, can exceed the relaxation time of the triplet-state dipole moment, T_1, by a factor of three. Furthermore, the transverse relaxation time of the singlet-triplet coherence, T_2, exceeds the longitudinal relaxation lifetime of the triplet states T_1, an unusual situation in NMR. The zero-field NMR experiments detect transitions between a triplet state and a singlet state that is protected from relaxation mechanisms; whereas in high-field NMR the observed transitions generally are between two states equally exposed to all relaxation mechanisms. We also show that the extended singlet-state lifetimes are not limited to isolated heteronuclear pairs. In benzene-^{13}C$_1$, with a strongly coupled heteronuclear spin pair weakly coupled to several distant spins, we show that the lifetime of manifolds where the strongly coupled spins are in the singlet state exceeds the lifetime of manifolds where the strongly coupled spins are in

---

[1] Note, the carboxyl proton can be ignored because 2- and 3-bond couplings between the $^{13}\mathrm{C} -^{1}\mathrm{H}$ system and the acidic proton can be neglected due to rapid exchange in protic solvents.

the triplet states by about a factor of 1.5. An appealing application for long-lived heteronuclear spin singlets may be in metabolic studies, along the lines of research employing hyperpolarized ^{13}C-labeled pyruvate [164].

In the present experiments the samples are polarized in a permanent magnet and then pneumatically shuttled to zero field immediately next to the detection cell. DC magnetic field pulses are used to manipulate the polarization in the singlet and triplet manifolds. This is in contrast to the case of low-field homonuclear singlet spin pairs [145], which require more elaborate multipulse sequences for the interconversion of singlet and triplet states. In the experiments we present here the phase of the resulting signals can be used to identify the type of nuclear spin polarization from which the signal arises. The use of a sensitive alkali-vapor magnetometer as a detector allows us to directly probe the resulting spin state.

In liquids, inter- and intra-molecular dipolar interactions average to zero due to fast Brownian motion, hence the Hamiltonian for two spins **I** and **S** in the presence of the Zeeman interaction and scalar coupling is well approximated by

$$H = J\mathbf{I}\cdot\mathbf{S} + (\gamma_I\mathbf{I} + \gamma_S\mathbf{S})\cdot\mathbf{B}. \tag{8.1}$$

Here, γ_I and γ_S are the gyromagnetic ratios of the respective spins, and J is the scalar coupling between them. In the high-field limit, eigenstates are those of I_z and S_z, $|M_I M_S\rangle$. In zero field, the eigenstates are those of F^2 and F_z where $\mathbf{F} = \mathbf{I} + \mathbf{S}$ is the total angular momentum. We denote the triplet states with $F = 1$ as $|T_{+1,0,-1}\rangle$, and the singlet state with $F = 0$ as $|S_0\rangle$, where the subscript indicates the magnetic quantum number, M_F. The manifolds are separated in energy by J. In zero field, the triplets are symmetric and the singlet is antisymmetric with respect to interchange of the spin labels. Therefore, transitions between the two manifolds due to the symmetric dipole-dipole interaction are forbidden. As the magnetic field is increased, the $|T_0\rangle$ and $|S_0\rangle$ levels are mixed and dipole-dipole relaxation is gradually turned on.

The energy levels of this two-spin system are shown as a function of magnetic field in Fig. 8.1. Polarization of the zero-field levels is achieved in our experiment by transferring the sample from thermal equilibrium in a prepolarizing magnet (20 kG) through a guiding field (solenoid generating a magnetic field of 10 mG) into the shielded magnetometer to zero field. The rate of transit (occurring over 1.5 s) is slow compared to J, populations of the thermally polarized high-field states are adiabatically transferred to those of the low-field states. This results in an excess population of the $|S_0\rangle$ state over the $|T_0\rangle$ state, and an excess of $|T_{+1}\rangle$ state over $|T_{-1}\rangle$. The latter corresponds to the dipole moment of the triplet state oriented in the direction of the quantization axis (z). We choose the z-direction as the direction of detection such that z-magnetization is defined as the observable. Also, the magnetic field inside the solenoid, used for adiabatic transfer and preparation of the probed populations is aligned with z. The x and y directions are transverse to z. More details of polarization via adiabatic transfer are included in Section 4.2. After adiabatic transfer from high to zero field, the sample stays in zero field for a certain storage time τ. In order to preserve the polarization of the sample, the guiding field stayed switched on during storage, producing a residual field at the sample ~1 mG. As the Zeeman shifts due to this residual guiding field are much smaller than the J-coupling, the singlet lifetime T_s as well as the dipole lifetime T_1 stay unaffected, as was verified experimentally by taking data at different values of the guiding

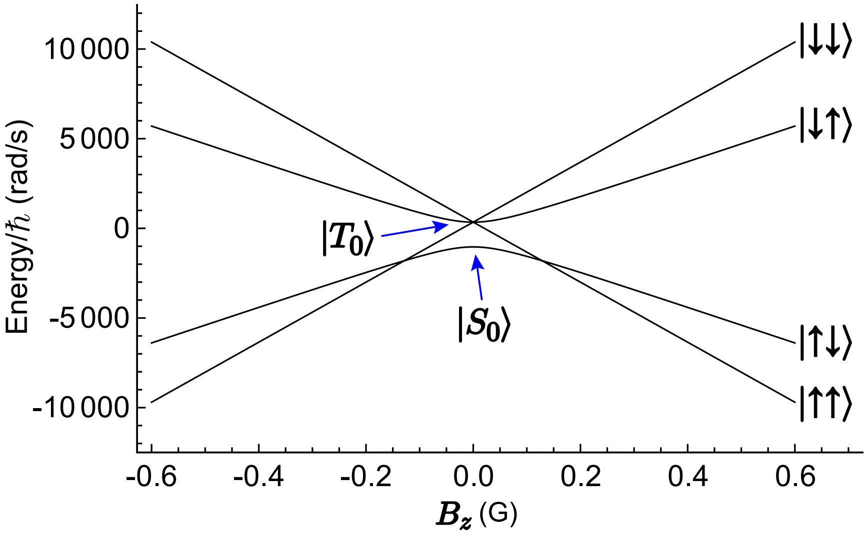

Figure 8.1: Energy levels for two spins, **I** and **S**, $I = S = 1/2$, in the presence of a scalar coupling and a Zeeman interaction. Here, $J = 220$ Hz, and gyromagnetic ratios correspond to carbon and hydrogen. High-field eigenstates are those of the uncoupled basis, as indicated by the kets on the right. Adapted with permission from Ref. [67]. ©2014 American Physical Society.

field. The frequency difference between the ^{1}H and ^{13}C nuclei are given as $(\gamma(^1\text{H})\text{-}\gamma(^{13}\text{C})\cdot\mathbf{B}) = 3.2$ Hz at 1 mG. This is sufficiently small compared to the ^{1}H-^{13}C J-coupling of 219.3 Hz, such that the singlet state remains very close to an eigenstate of the Hamiltonian and does not evolve into states not protected from relaxation.

DC magnetic-field pulses are used to excite a coherence between zero-field substates and to manipulate the polarization in the singlet and triplet manifolds. The use of a sensitive alkali-vapor magnetometer (described in [64]) allows us to directly probe the resulting spin state. We observe the z component of the nuclear magnetization, proportional to the trace of $\rho(\gamma_I I_z + \gamma_S S_z)$. Since the term in parenthesis is a vector operator with magnetic quantum number equal to zero, observable transitions are those with $\Delta F = \pm 1$ and $\Delta M_F = 0$. These are transitions between the $|T_0\rangle$ and $|S_0\rangle$ states, which produce magnetization oscillating in the z direction with frequency J.

Coherences between $|T_0\rangle$ and $|S_0\rangle$ can be established from excess population in the singlet state by application of a DC pulse of magnetic field in the z direction, resulting in z magnetization proportional to $\sin(2\pi J t)$. This corresponds to a dispersive peak in the real part of the Fourier transform of the magnetometer signal. The amplitude of the signal in this case is proportional to the difference in population between the $|T_0\rangle$ and $|S_0\rangle$ states. Coherences between $|T_0\rangle$ and $|S_0\rangle$ can also be established from dipole polarization in the triplet state by application of a pulse of magnetic field in the x direction, resulting in z magnetization proportional to $\cos(2\pi J t)$, corresponding to an absorptive peak in the real part of the Fourier transform. In this case, the amplitude is proportional to the difference in population between the $|T_{+1}\rangle$ and $|T_{-1}\rangle$ states. Note that a y-pulse would have the same effect as an x-pulse; they are both transverse to the privileged z-direction. Details of how coherences are produced from the different polarization moments and the resulting signals are

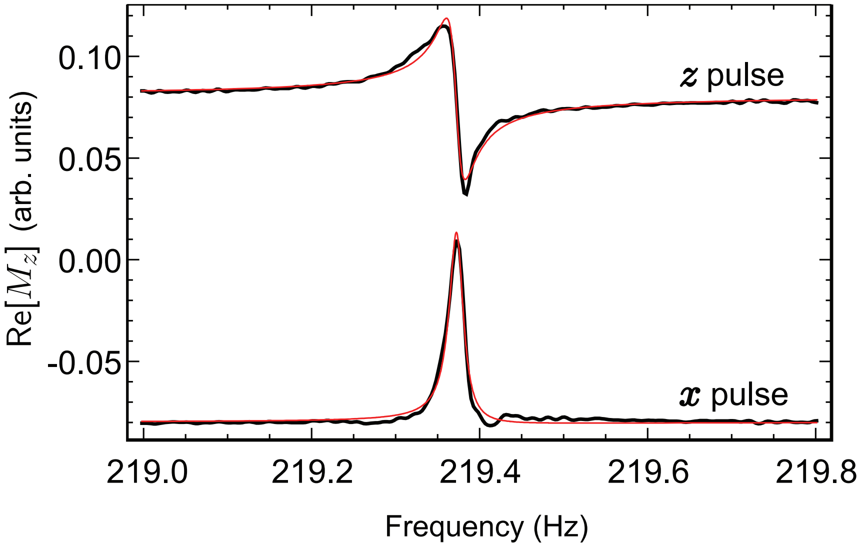

Figure 8.2: Zero-field NMR signals of formic acid (sample FAIII). The real part of the signal following a pulse in the z direction originates from an initial population imbalance between the $|S_0\rangle$ and $|T_0\rangle$ states and is dispersive. The real part of the signal due to a pulse in the x direction originates from dipole moment in the triplet manifold (excess of $|T_{+1}\rangle$ over $|T_{-1}\rangle$ states), and is absorptive. The curves have been vertically offset by +0.075 (z-pulse) and -0.075 (x-pulse) to avoid overlap. Adapted with permission from Ref. [67]. ©2014 American Physical Society.

presented in Section 4.2.

Figure 8.2 shows the real part of the Fourier transform of the magnetometer signal following adiabatic transition of the formic acid sample (FAIII) to zero field and subsequent application of magnetic-field pulses in either x or z direction. The phase is in agreement with the discussion above, with absorptive and dispersive lineshapes for x and z pulses, respectively. Overlaying each trace is the real part of a fit to a complex Lorentzian, with half-width at half-max (HWHM) linewidth equal to about 10 mHz, corresponding to coherence lifetime $T_2 = 16$ s. In both cases there is a small deviation from Lorentzian line shape. We attribute this to variations in J across the sample due to temperature gradients.

The amplitude of the zero-field NMR signal as a function of the storage time τ for application of magnetic field pulses in the x or z directions is shown in Fig. 8.3 for sample FAIII. The decay of the signal amplitude obtained by application of x pulses is well described by a single decaying exponential, with time constant $T_1 = 11.8(1)$ s. We note that our definition of T_1 deviates slightly from the high-field case, which usually corresponds to the lifetime of population difference between single-particle Zeeman eigenstates. Here, T_1 is the lifetime of the difference in population between the triplet states $|T_{+1}\rangle$ and $|T_{-1}\rangle$ in the coupled system. The singlet lifetime T_s was determined by fitting the decay curve (Fig. 8.3) of the signal amplitude after application of a z pulse. The decay is well described by a double exponential with fast and slow time constants $T_f = 10(3)$ and $T_s = 37(2)$ s. The slow decay is due to transitions between the singlet and triplet

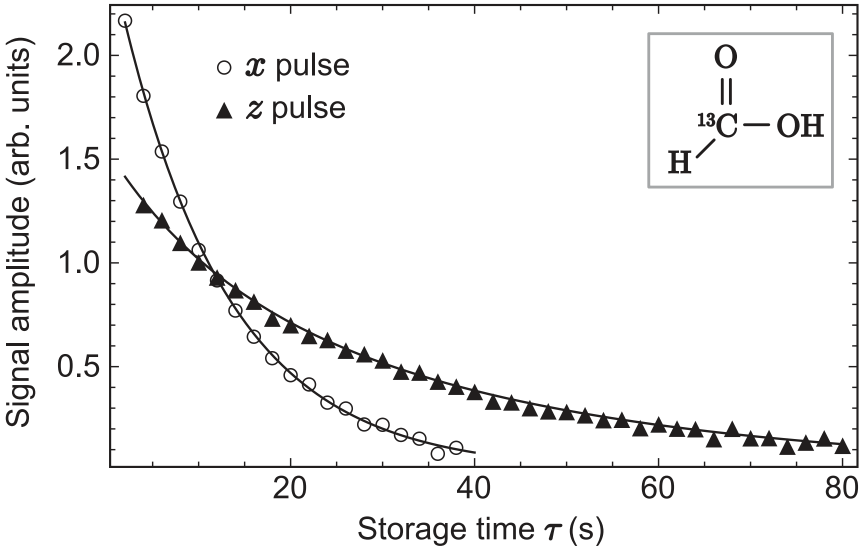

Figure 8.3: Decay of signal amplitude as a function of storage time for magnetic-field pulses applied in the indicated directions using sample FAIII. The solid lines overlaying the data are fits to single (double) exponentials for *x (z)* magnetic-field pulses. Adapted with permission from Ref. [67]. ©2014 American Physical Society.

states and reflects the lifetime of the singlet state T_s. The fast decay is a result of equilibration within the triplet states, which reduces the population imbalance between the $|T_0\rangle$ and $|S_0\rangle$ states. Single and biexponential decays for relaxation of dipole and singlet polarization are predicted by a phenomonological rate-equation model, described at the end of this Chapter.

Formic acid samples were mixtures of ^{13}C-labeled formic acid, acetonitrile, and H_2O. The samples were flame sealed in 5-mm NMR tubes after four or five cycles of freezing and thawing under vacuum in order to remove dissolved gases, in particular oxygen, which can cause additional relaxation.

Sample and content (FA,A,H_2O)	T_1 (s)	T_f (s)	T_s (s)	T_2 (s)
FAI (100,0,10)	5.8(1)	2.4(3)	18.4(3)	8.0(5)
FAII (50,100,10)	8.0(5)	8.84(7)	26.5(5)	10.3(3)
FAIII (5,50,5)	11.8(1)	10(3)	37(2)	16.2(4)

Table 8.1: Summary of contents (in μL) and decay times T_1, T_f, T_s and T_2 for several samples. FA = formic acid, A = acetonitrile.

The main results for three different samples (containing formic acid, acetonitrile and water) are presented in Table 8.1. Dilution of formic acid with acetonitrile/water mixtures was performed to reduce intermolecular interactions and to promote fast exchange of the carboxyl proton. As can be seen in Table 8.1, an increased fractional content of acetonitrile increases the singlet lifetime, likely due to a reduction in viscosity and decreased correlation times. It is interesting to note that the lifetime of the singlet-triplet coherence is longer than the T_1 relaxation time for all samples listed in Table 8.1. This is a situation rarely encountered in high-field NMR because T_1 relaxation in high field corresponds to exchange of populations between two Zeeman eigenstates, and T_2 relaxation corresponds to dephasing of a coherence between the Zeeman eigenstates. In the zero field case at hand, the T_1 relaxation of the dipole moment corresponds to relaxation of population differences between the states $|T_{\pm1}\rangle$, whereas the observed singlet-triplet coherence involves the states $|T_0\rangle$ and $|S_0\rangle$.

The theory of nuclear spin relaxation in two-spin systems has been studied extensively for the case of homonuclear spins in low magnetic field [155, 165, 159, 158] and can be found in Ref. [155]. These formulas can be adapted to heteronuclear systems. Rate expressions for relaxation due to dipole-dipole interactions or external fluctuating fields can be found in Ref. [155]. In the case of dipole-dipole relaxation, the ratio of T_2 to T_1 should be $T_2/T_1 = 9/5$. If externally fluctuating fields due to paramagnetic impurities or other nuclei (for example, the carboxyl proton) limit the lifetime, we expect a ratio $T_2/T_1 = 2$, assuming that the fields are uncorrelated at the two nuclei. We measure T_2/T_1 to be 1.28 – 1.37, which indicates that T_2 may be limited by temperature or magnetic-field inhomogeneities.

We suspect that exchange of the carboxyl proton, or possibly some paramagnetic impurity, ultimately limits the lifetime of the singlet state. This is supported by the observation that all lifetimes have a roughly linear dependence on temperature. In sample FAII, T_s decreases by about 10% as the temperature is increased in the range of 20 – 60 °C, while T_f, the fast component of the relaxation, increases by a similar fractional amount. We observe that T_1 increases by about 10% over this range, consistent with the expectation that dipole-dipole relaxation is suppressed by improved motional narrowing at elevated temperatures.

The increased lifetime of the singlet state is not strictly limited to the case of two-spin systems [166, 156, 167]. In systems where there are two strongly coupled spins and a series of weaker couplings, we also observe an extension in the lifetime of the manifolds where the strongly coupled system is in the spin-singlet state. Singly labeled ^{13}C-benzene is one such example, in which there is a strongly coupled $^{1}\mathrm{H}-^{13}\mathrm{C}$ system, weakly coupled to a set of distant spins, resulting in splitting of the single zero-field NMR line. A portion of the zero-field spectrum of singly labeled ^{13}C benzene in the neighborhood of the one-bond J-coupling frequency, acquired after application of an x directed pulse, is shown inset in Fig. 8.4. A complete discussion of the zero-field spectrum resulting from ^{13}C-labeled benzene is presented in Ref. [65]. Individual lines are typically about 10 mHz (HWHM). The signal is absorptive as expected from dipole polarization of the triplet manifolds. Application of a pulse in the z direction produces a signal with the same frequencies and with dispersive lineshape, as expected from polarization of the singlet state. The decay of the signal amplitude (for the peak indicated by the arrow in the inset) is given in the main panel for x pulses (corresponding to triplet polarization) and z pulses (corresponding to singlet polarization). While multiple decay rates are likely, our signal-to-noise ratio is not sufficient to cleanly differentiate between them, so we fit these data to single decaying exponentials, as indicated by the solid lines. The decay times extracted from the fit are $T_1 = 19(1)$ s and $T_s = 30(2)$ s, for pulses applied in the x and z directions, respectively. Decay curves for the other peaks yield similar lifetimes. These results confirm that the long lifetime of heteronuclear spin singlet states is not limited to the case of two isolated heteronuclear spins, but can be extended to systems consisting of two strongly

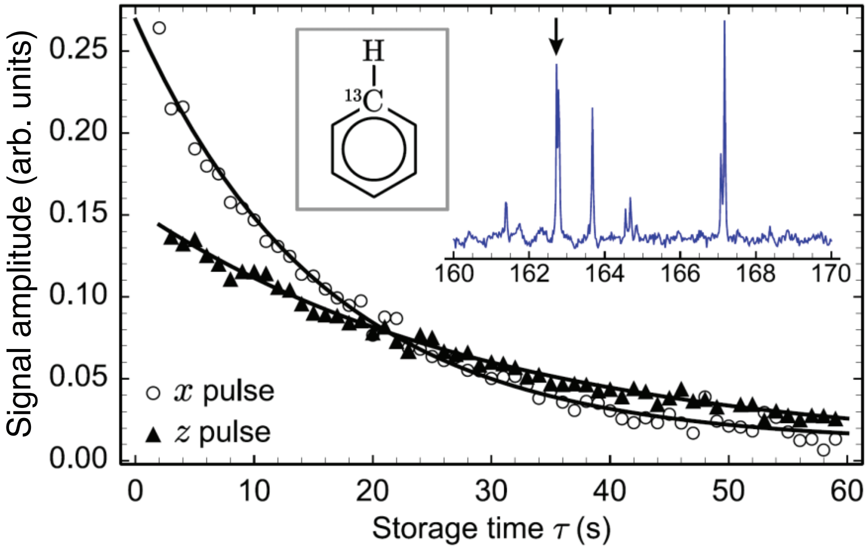

Figure 8.4: Decay of signal amplitude in benzene-$^{13}C_1$ for magnetic field pulses applied in the x (circles) and z (triangles) directions (this spectrum is the result of averaging five transients). The solid lines overlaying the data are fits to single decaying exponentials. The inset shows a portion of the zero-field spectrum, and the arrow indicates the peak from which these decay curves are extracted. Adapted with permission from Ref. [67]. ©2014 American Physical Society.

coupled heteronuclear spins with weakly coupled distant spins.

8.3 Significance and Future Directions

We have shown that the lifetime of heteronuclear spin-singlet states in zero magnetic field can be substantially longer than that of the dipole moment in the triplet state. In ^{13}C-labeled formic acid, we find that the singlet lifetime is a factor of three longer than the lifetime of the triplet dipole moment. The extended lifetime of singlet states in homonuclear spin pairs has been known for some time, but extended lifetime of heteronuclear spin singlets has not been observed before. One advantage of working with heteronuclear spin-singlets is that they can be manipulated by DC magnetic-field pulses to produce observable magnetization. The use of sensitive atomic magnetometers, as employed here, enables direct observation of this magnetization in zero field. Typically, singlet states are not eigenstates of the high-field Zeeman Hamiltonian, and if a high degree of symmetry is not present in the molecule of choice, RF spin locking has to be implemented in order to remove chemical shifts. At zero magnetic field, heteronuclear as well as homonuclear spin systems are naturally coupled into long-lived eigenstates. This vastly expands the range of chemical systems which can exhibit long-lived spin order, motivating further research in zero-field NMR as a valuable spectroscopic tool.

8.4 Relaxation Rate Equations

In describing the relaxation of the system after it arrives in zero field, we use rate equations that govern the populations of singlet and triplet states and neglect the possibility that off-diagonal elements develop between the degenerate states $|T_{-1,0,+1}\rangle$ of the triplet manifold. Let us denote the excess of populations in the $|T_{+1}\rangle$, $|T_0\rangle$, $|T_{-1}\rangle$, and $|S_0\rangle$ states by a_1, a_0, a_{-1}, and b_0, respectively. The polarized part of the density matrix following a delay τ after adiabatic transport to zero field and prior to application of a pulse of magnetic field is devoid of coherences and can be written

$$\rho(\tau) = a_1(\tau)T_1 + a_0(\tau)T_0 + a_{-1}(\tau)T_{-1} + b_0(\tau)S_0,$$

where τ is the delay between arrival of the sample in zero field and application of a pulse of magnetic field to excite coherences. Prepolarization with adiabatic transfer to zero field as described above gives the initial values $a_{\pm1}(0) = \pm\delta_0$, $a_0(0) = -\epsilon_0$, and $b(0) = \epsilon_0$. The rate equations governing the relaxation of populations in the eigenstates as a function of τ are

$$\begin{aligned}
\dot{a}_1 &= -\Gamma_3(a_1 - a_0) - \Gamma_{T2}(a_1 - a_{-1}) - \Gamma_2(a_1 - b_0), \\
\dot{a}_0 &= -\Gamma_3(a_0 - a_1) - \Gamma_3(a_0 - a_{-1}) - \Gamma_1(a_0 - b_0), \\
\dot{a}_{-1} &= -\Gamma_3(a_{-1} - a_0) - \Gamma_4(a_{-1} - a_1) - \Gamma_2(a_{-1} - b_0), \\
\dot{b}_0 &= -\Gamma_2(2b_0 - a_1 - a_{-1}) - \Gamma_1(b_0 - a_0). \qquad (8.2)
\end{aligned}$$

Here, Γ_1, Γ_2, Γ_3, and Γ_4 represent the rates of cross relaxation between the states $|S_0\rangle \leftrightarrow |T_0\rangle$, $|S_0\rangle \leftrightarrow |T_{\pm1}\rangle$, $|T_0\rangle \leftrightarrow |T_{\pm1}\rangle$, and $|T_{-1}\rangle \leftrightarrow |T_{+1}\rangle$, respectively.

As described in Section 4.2 the signal amplitude following a pulse of magnetic field in the z direction is proportional to the difference in population between the states $|T_0\rangle$ and $|S_0\rangle$, ϵ. Similarly, the signal amplitude following a pulse of magnetic field in the x direction is proportional to the difference in population between the states $|T_{\pm1}\rangle$, δ. Thus it will be useful to write the polarized part of the density matrix as

$$\rho(\tau) = \delta(\tau)(T_1 - T_{-1}) + \epsilon(\tau)(S_0 - T_0) + \eta(\tau)(T_0 + S_0) + \gamma(\tau)(T_1 + T_{-1}), \qquad (8.3)$$

where $\delta = (a_1 - a_{-1})/2$, $\epsilon = (a_0 - b_0)/2$, $\eta = (a_0 + b_0)/2$, and $\gamma = (a_1 + a_{-1})/2$. The rate equations (8.2) can now be rewritten

$$\begin{aligned}
\dot{\delta} &= -(\Gamma_2 + \Gamma_3 + 2\Gamma_4)\delta & (8.4) \\
\dot{\epsilon} &= -(2\Gamma_1 + \Gamma_2 + \Gamma_3)\epsilon + (\Gamma_2 - \Gamma_3)\eta - (\Gamma_2 - \Gamma_3)\gamma & (8.5) \\
\dot{\eta} &= (\Gamma_2 - \Gamma_3)\epsilon - (\Gamma_2 + \Gamma_3)\eta + (\Gamma_2 + \Gamma_3)\gamma & (8.6) \\
\dot{\gamma} &= -(\Gamma_2 - \Gamma_3)\epsilon + (\Gamma_2 + \Gamma_3)\eta - (\Gamma_2 + \Gamma_3)\gamma. & (8.7)
\end{aligned}$$

With the initial conditions $\delta(0) = \delta_0$, $\eta(0) = 0$, $\epsilon(0) = -\epsilon_0$, and $\gamma(0) = 0$, the solutions for $\delta(\tau)$ and $\epsilon(\tau)$ are

$$\begin{aligned}
\delta(\tau) = \quad & \delta_0 e^{-(\Gamma_2+\Gamma_3+2\Gamma_4)\tau} & (8.8) \\
\epsilon(\tau) = \quad & \epsilon_0/(2A)[-2\Gamma_1 + \Gamma_2 + \Gamma_3 - A]e^{-\{+\Gamma_1+3(\Gamma_2+\Gamma_3)/2+A/2\}\tau} + \\
& \epsilon_0/(2A)[-2\Gamma_1 + \Gamma_2 + \Gamma_3 + A]e^{-\{+\Gamma_1+3(\Gamma_2+\Gamma_3)/2-A/2\}\tau}. & (8.9)
\end{aligned}$$

Here, $A = \sqrt{9(\Gamma_2 - \Gamma_3)^2 + (2\Gamma_1 - 2\Gamma_2)(2\Gamma_1 - 2\Gamma_3)}$. We see that the dipole moment in the triplet state, proportional to δ, decays with a rate equal to $1/T_1 = \Gamma_2 + \Gamma_3 + 2\Gamma_4$. The population difference between states $|T_0\rangle$ and $|S_0\rangle$, proportional to ϵ, has a biexponential decay, with fast and slow time constants given by

$$
\begin{aligned}
1/T_f &= \Gamma_1 + 3(\Gamma_2 + \Gamma_3)/2 + A/2 && (8.10)\\
1/T_s &= \Gamma_1 + 3(\Gamma_2 + \Gamma_3)/2 - A/2. && (8.11)
\end{aligned}
$$

Fitting the decay of signal amplitude for the case of the x pulse (see Fig. 8.3) to Eq. (8.8) yields $1/T_1 = (\Gamma_2 + \Gamma_3 + 2\Gamma_4) = 0.0848(7)$ s^{-1}. Fitting the decay of signal amplitude for the z pulse to Eq. (8.9) yields $\Gamma_1 = 0.0042(36)$, $\Gamma_2 = 0.0081(27)$, and $\Gamma_3 = 0.0294(87)$ s^{-1}, corresponding to $1/T_f = 0.094$ s^{-1} and $1/T_s = 0.027$ s^{-1}.

Chapter 9

Summary and Outlook

Summarizing the results of this dissertation, we have addressed several recent advances in the study of zero- and ultra-low-field nuclear magnetic resonance (ZULF-NMR) spectroscopy using optical magnetometry. We have considered the spin dynamics of systems evolving primarily under the influence of electron-mediated indirect spin-spin couplings, with perturbations provided by weak external magnetic fields, residual dipolar couplings, and weak couplings to other spins. The resulting spectra yield detailed information about chemical identity, molecular spin topology, electronic structure, configuration/geometry, and mesoscale material structure. Long relaxation times give rise to high-resolution spectra, which allows high-precision measurement of local interactions. The symmetry of the zero-field Hamiltonians permits both the observation of interactions that are otherwise truncated in high-field NMR, and the formation of long-lived antisymmetric heteronuclear singlet-like states that cannot be formed in large external fields. These results point to a bright future for ZULF-NMR as a complimentary technique to high-field NMR, with a wide range of potential applications in chemical analysis, materials characterization, and precision measurement of fundamental physical symmetries.

We began by describing the basic principles of ZULF-NMR from the standpoint of quantum mechanics. Starting with the fundamental origins of nuclear spin, we then considered the density operator describing an arbitrary ensemble of coupled nuclear spin systems and how the interaction of the density operator with various spin Hamiltonians leads to spectra from which information about the spin system can be extracted. We have also summarized the operation of alkali vapor atomic magnetometers as sensitive detectors of low-frequency magnetic resonance signals. Operating in the spin-exchange relaxation-free regime, we are able to obtain magnetometer sensitivities on the order of $10 - 100\ \mathrm{fT}/\sqrt{\mathrm{Hz}}$, sufficient to yield high signal-to-noise ratios in ZULF-NMR spectra. We then detailed the means by which observable magnetization signals are produced in ZULF-NMR experiments, including the generation of non-equilibrium spin polarization and the transformation of spin order into oscillating magnetization using magnetic field pulses.

In order to extract chemically relevant information in the absence of chemical shifts, we have described the methods for the interpretation of zero-field J-spectra. A basic qualitative description of zero-field spectra may be understood in terms of XA_n systems, providing topological information about simple isotopically labeled functional groups. This was then expanded to $(\mathrm{XA}_n)\mathrm{B}_m$

systems, where the perturbation from additional weakly coupled spins leads to additional fine structure that may be calculated analytically from first and second-order perturbation theory. More complex molecules, such as benzene derivatives, are interpreted in terms of a larger perturbing spin space, where the topology of the weakly coupled space is revealed by consistent multiplet patterns. We have also presented a geometric picture of the perturbation theory calculations in terms of projections of perturbing spin operators onto the total angular momentum of the strongly coupled system.

We have also shown that additional information may be encoded in ZULF-NMR spectra by reintroducing Zeeman and dipole-dipole coupling Hamiltonians as perturbations on the J-coupling. Applying weak magnetic fields lifts the degeneracy within angular momentum manifolds, allowing us to resuscitate information about gyromagnetic ratios and spin topologies that were otherwise ambiguous. By preparing anisotropic stretched gel samples with varying degrees of alignment, we have shown the effects of dipole-dipole coupling as a perturbation on J-spectra, in strong agreement with theoretical predictions without any free parameters. We also revealed a dependence of the zero-field spectrum on the heteronuclear “flip-flop” term of the dipole-dipole Hamiltonian that is truncated at high-field and thus invisible to conventional NMR. This suggests that, in principle, zero-field NMR may be capable of measuring other so-called “non-secular” terms. Taking advantage of the symmetry of zero-field NMR, we have also demonstrated the formation of long-lived heteronuclear spin-singlet states, overturning the “conventional” viewpoint that singlet states can only be formed between homonuclear spins.

We will now consider some possible future directions for ZULF-NMR.

9.1 Near Future: Multiple Pulse Zero-Field NMR

9.1.1 Multidimensional Zero-Field Correlation Spectra

Figure 9.1 shows a prototypical two-dimensional zero-field NMR correlation spectrum of a mixture of ethanol-1-^{13}C and ethanol-2-^{13}C isotopomers, zoomed in on the complex region including the $K_A = 1$ peaks of ethanol-1-^{13}C and the $K_A = \frac{3}{2}$ peaks of ethanol-2-^{13}C. Cross-peaks are visible for correlated transitions within a given isotopomer, but no intermolecular cross-peaks appear, as would be expected due to the absence of intermolecular J-couplings.

The spectrum in Fig. 9.1 was obtained by applying a pulse sequence analogous to the high-field COSY experiment, varying the delay between two magnetic field pulses. Schematically, the pulse sequence, involving a sudden transfer to zero magnetic field achieved by quickly turning off the guiding field after shuttling, is

$$\text{polarize} \; - \; \text{shuttle} \; - \; \text{solenoid off} \; - (\pi_x)_{^{13}C-^{1}H} \; - \; \tau_1 \; - \; (\overline{\pi_x})_{^{13}C-^{1}H} \; - \; \text{acquire}\,(\tau_2)\,, \qquad (9.1)$$

where τ_1 is a variable delay time, $(\pi_x)_{^{13}C-^{1}H}$ is a magnetic field pulse equivalent to a relative rotation between ^{13}C and ^{1}H nuclear spins of π radians about the x axis, and $(\overline{\pi_x})_{^{13}C-^{1}H}$ is a magnetic field pulse equivalent of equivalent magnitude and opposite polarity (applied with the opposite polarity in order to account for pulse imperfections). Naively comparing to the two-spin case of Section

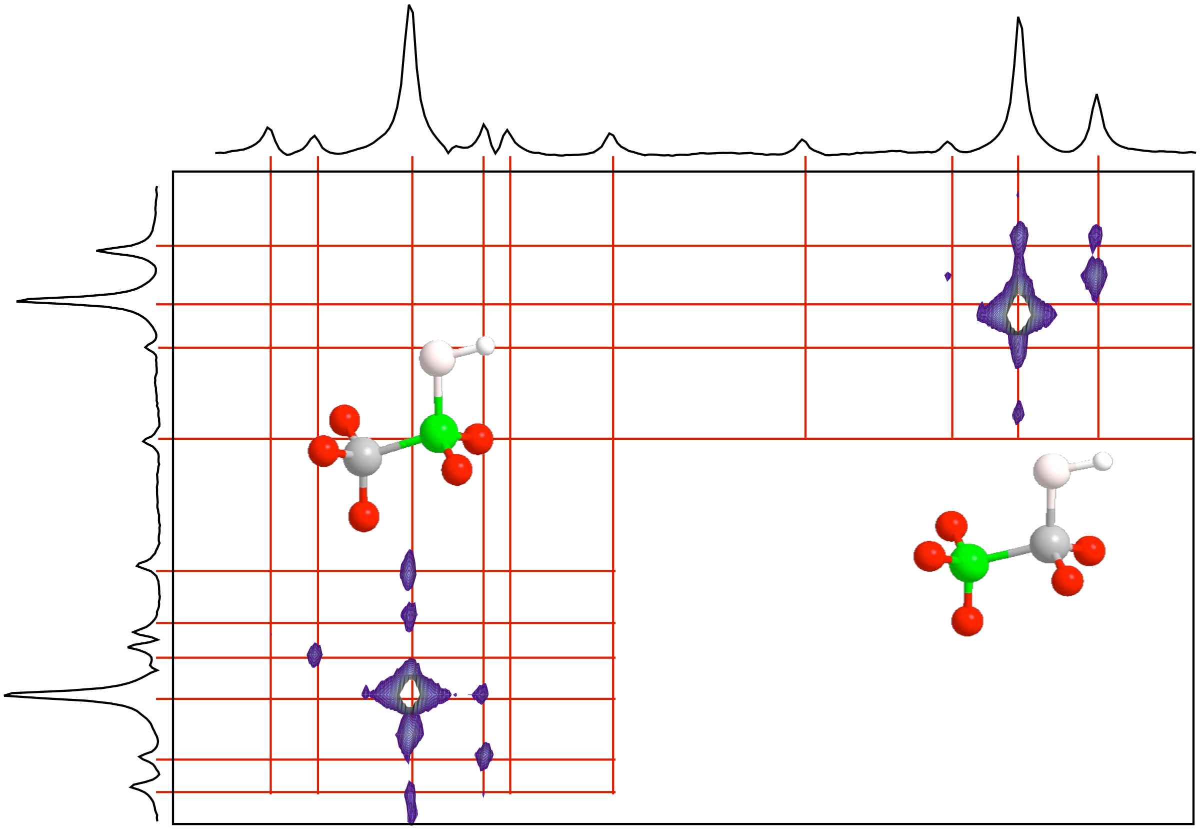

Figure 9.1: 2D Zero-field NMR correlation spectrum of a mixture of ethanol-1-^{13}C and ethanol-2-^{13}C, zoomed in to show cross-peaks in the area of greatest spectral complexity.

4.2.2, the $(\pi_x)_{^{13}C-^{1}H}$ would be expected to transform zero-quantum coherence to double-quantum coherence, which is then allowed to evolve for a time τ_1, after which it is converted back to observable zero-quantum coherence by the $(\overline{\pi_x})_{^{13}C-^{1}H}$ pulse. This would lead to cross-peaks appearing between peaks that are connected by double-quantum coherences. A more complete theory of coherence transfer in zero-field NMR is certainly necessary to fully describe the experiment, and to develop pulse sequences that provide more specific information, but the preliminary results of Fig. 9.1 indicate that current magnetometer sensitivity and pulse fidelity should be sufficient for future multidimensional experiments.

9.1.2 Decoupling in Zero-Field NMR

The cancellation of residual magnetic fields amounts to the decoupling of all remaining vector operators from the perspective of the ZULF-NMR density matrix. Symmetrized pulse sequences that achieve time-reversal of rank-1 spherical tensor operators can be used to generate an average Hamiltonian that does not contain a Zeeman term. This was demonstrated by some of the early pioneers of field-cycling zero-field NMR for homonuclear systems using coherent isotropic averaging [168] that was used to completely decouple first-rank tensors while scaling second-rank tensors by about 1/3.[1] It should be possible to extend the approach of Refs. [168, 169] to heteronuclear systems using composite isotropic trajectories

Sufficiently fast decoupling sequences for tensors of various rank could also be used to extend relaxation times of hyperpolarized systems at zero field by decoupling low-frequency contributions to the spectral density function, which may be the primary mechanism of relaxation at zero field if higher frequency components self-decouple. Increasing polarization lifetimes by such means could be extremely valuable for hyperpolarized spectral imaging techniques if relaxation mechanisms can indeed be efficiently decoupled.

Spectral editing employing selective heteronuclear or homonuclear decoupling would also permit the study of larger complex systems which might otherwise yield overly complex, overlapping spectra, making interpretation difficult or impossible.

9.2 Possible Future: Molecular Parity Non-Conservation

ZULF-NMR is particularly well-suited to the measurement of interactions that do not commute with the high-field Zeeman Hamiltonian. One example of such an interaction is the antisymmetric J-coupling[2], which has not been observed in high-field NMR, but may be observable in ZULF-NMR. Because J^{anti} transforms as a bivector (or pseudovector), it encodes a sense of rotation, as well as an orientation, such that it may be treated as a “chiral” interaction. Observing the effects of J^{anti} in ZULF-NMR experiments could lead to novel techniques for the measurement and quantification of chirality.

---

[1] This essentially amounts to a zero-field spin-echo.

[2] More specifically, the irreducible rank-1 components of the J-coupling tensor.

Furthermore, when considering the full molecular Hamiltonian including the parity non-conservation (PNC) terms due to the weak nuclear force,[3], the only first-order PNC contribution to NMR observables corresponds to an antisymmetric J-coupling [143]. Because J^{anti} has no effect on high-field NMR spectra, the authors of Ref. [143] did not treat this first-order effect any further beyond writing the term:

$$\begin{aligned}\mathbf{I}_N \cdot \mathbf{J}^{(1)}_{\mathrm{PNC}} \cdot \mathbf{I}_{N'} = \frac{-G_{\mathrm{F}}}{\sqrt{2}mc}\frac{\mu_0}{4\pi}e\hbar\left(1 - 4\sin^2\theta\right)(\mathbf{I}_N \times \mathbf{I}_{N'})\,\frac{\mathbf{r}_{N'N}}{\mathbf{r}^3_{N'N}} \\ \times\left[\lambda_N\gamma_{N'}\langle 0|\sum_k \delta\left(\mathbf{r}_{Nk}\right)|0\rangle + \lambda_{N'}\gamma_N\langle 0|\sum_k \delta\left(\mathbf{r}_{N'k}\right)|0\rangle\right], \quad (9.2)\end{aligned}$$

where G_{F} is the Fermi constant, θ is the Weinberg-Salam angle ($\sin^2\theta = 0.2236$), and λ_N is a nucleus-dependent factor that is near to unity. $\mathbf{r}_{N'N}$ is the vector connecting the two nuclei N and N', and $\mathbf{r}_{Nk}$ is the vector connecting the nucleus N to a given electron k. It is particularly worth noting that the weak charge $Q_N = \left[Z\left(1 - 4\sin^2\theta\right) - N\right]$ does not appear in Eq. (9.2), so unlike many other proposed PNC measurements, there is no requirement for nuclei with high atomic numbers.

9.3 Towards Science Fiction: FUNdamental Physics

Precision measurements of anomalous spin couplings might lead to new limits on fundamental physical constants, such as nuclear electric dipole moments or relative couplings between matter and antimatter. Such measurements could further constrain the parameters for possible theoretical particles predicted by new physics beyond the Standard Model, including – for example – QCD axions or axion-like-particles, potential dark matter candidates.

9.3.1 Polarized Nuclear Targets Based on ZULF PHIP

It has also been proposed that ZULF-NMR techniques for the manipulation of polarized nuclear spin states prepared via PHIP[4] may be used to prepare polarized nuclear targets. High density nuclear targets with high spin polarization are desirable for a range of nuclear and particle physics experiments, particularly those aimed at studying nucleon structure. Additionally, the fast and robust reversal of polarization is necessary in order to control for systematic effects in sensitive measurements of fundamental symmetries. It should be possible develop a polarized nuclear target utilizing parahydrogen-induced polarization that satisfies these parameters and furthermore does not require cryogenic temperatures or large magnetic fields. The proposed technique is based on previous zero-field NMR work with parahydrogen [71, 72, 69, 121] as well as the target concept discussed in Ref. [170].

---

[3] Specifically, the neutral current, which involves the exchange of Z_0 bosons.

[4] Parahydrogen-induced polarization – see Section 4.3.

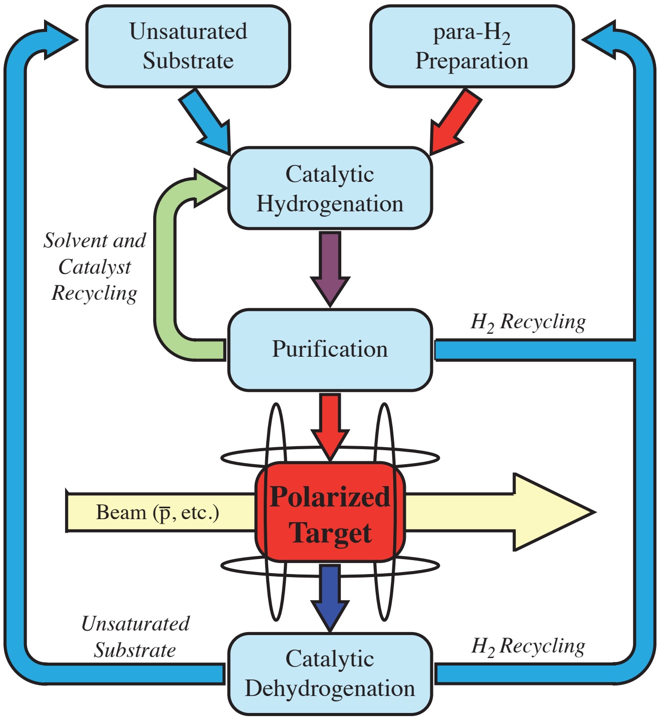

Figure 9.2: Block diagram of proposed experimental arrangement for the production of a polarized nuclear target using ZULF-NMR techniques and parahydrogen-induced polarization.

The general concept of the proposed target, polarized via hydrogenative PHIP, is depicted in Fig. 9.2. First, pure parahydrogen is prepared by cryogenically cooling hydrogen in the presence of a magnetic symmetry-breaking catalyst. Depending on overall desired flow rates, this may be achieved either in a batch or continuous flow mode. The parahydrogen is then mixed with an unsaturated substrate (containing a double bond), for example, ^{13}C-enriched acetylene ($^{13}C_2H_2$). Because acetylene, along with many other small unsaturated molecules, is extremely reactive, appropriate measures must be taken to avoid explosion hazards, as acetylene can undergo an explosive decomposition reaction even in the absence of oxygen.

Following the mixing of the substrate with parahydrogen, a catalytic hydrogenation (e.g. using dissolved or supported Wilkinson's catalyst) occurs within a reaction vessel. The product of this reaction will initially be in a state such that the two proton spins from the parahydrogen molecule are in a singlet state, and all other spins are thermally polarized. Once the product is formed, the total spin state (obtained by the coupling of all spin angular momenta in the molecule) will evolve under the electron-mediated spin-spin coupling (J-coupling), thus spreading the "singlet order" of the parahydrogen spins throughout the coupled system. Because the hydrogenation reaction is not instantaneous, and, further, occurs at a distribution of times throughout the sample, the relevant situation is the incoherently averaged steady state produced by the spread of singlet order. Subsequently, a DC magnetic field pulse is applied to convert the singlet order into oscillating magnetization, equivalent to time-dependent reversible nuclear polarization in the pulse direction.

The choice of appropriate substrate, catalyst, and reaction conditions is essential for the design and optimization of the proposed nuclear target. Because the non-equilibrium spin order is spread throughout all spins in the molecule, it is preferable to minimize the number of magnetic nuclei in order to maximize the degree of polarization. However, the high vapor pressure and reactivity of small unsaturated molecules pose additional challenges in the handling of the materials, and the choice of reaction mechanisms. It is also necessary that the chosen system possesses a long polarization relaxation time to maximize the time during which data can be collected using this target.

Alternatively, polarization may be achieved using non-hydrogenative PHIP, which builds up polarization in molecules that act as labile ligands with polarization-transfer catalysts. The mechanism is similar to that utilized in the signal amplification by reversible exchange (SABRE) technique, where the spin order of parahydrogen is transferred to target molecules during the formation of transient complexes with metal catalysts [73]. This method has the advantage of minimizing the need for chemical regeneration of the target, and the formation of steady-state polarization has been demonstrated [171].

This project has been proposed to be carried out within the Matter–Antimatter Asymmetry division at the Helmholtz-Institut Mainz, to interface with the Facility for (Low-Energy) Antiproton and Ion Research (FAIR/FLAIR).

Bibliography

[1] Zermelo, E. (1930) über grenzzahlen und mengenbereiche: Neue untersuchungen über die grundlagen der mengenlehre. *Fundamenta Mathematicæ* **16**, 29–47.

[2] Jech, T. J. (1997) *Set Theory*. (Springer-Verlag, New York, NY), 2nd edition.

[3] Gödel, K & Brown, G. W. (1940) *The consistency of the axiom of choice and of the generalized continuum-hypothesis with the axioms of set theory*. (Princeton University Press, Princeton, NJ) No. 3.

[4] Camus, A. (1955) *The Myth of Sisyphus, and Other Essays*. (Vintage International, New York). Translated from the original French by Justin O'Brien.

[5] Sartre, J.-P. (1956) *Being and Nothingness*. (Philosophical Library, New York, NY). Translated from the original French by Hazel E. Barnes.

[6] Pauli, W. (1940) The Connection Between Spin and Statistics. *Phys. Rev.* **58**, 716.

[7] Weinberg, S. (1964) Feynman Rules for Any Spin. *Phys. Rev.* **133**, B1318–B1332.

[8] Wigner, E. (1931) *Gruppentheorie und ihre Anwendung auf die Quantenmechanik der Atomspektren*. (Springer, Wiesbaden).

[9] Gell-Mann, M. (1956) The Interpretation of the New Particles as Displaced Charge Multiplets. *Il Nuovo Cimento* **4**, 848–866.

[10] White, T. H. (1938) *The Sword in the Stone*. (Collins, UK).

[11] Misner, C. W, Thorne, K. S, & Wheeler, J. A. (1973) *Gravitation*. (Freeman, New York).

[12] Nakahara, M. (2003) *Geometry, Topology and Physics*. (Taylor & Francis, Boca Raton, FL).

[13] Nash, C & Sen, S. (1983) *Topology and Geometry for Physicists*. (Academic Press, London).

[14] Frankel, T. (2012) *The Geometry of Physics: An Introduction*. (Cambridge University Press, Cambridge, UK), 3rd edition.

[15] Poincaré, H. (1885) Sur les courbes définies par les équations différentielles. *J. Math. Pures Appl.* **4**, 167–244.

[16] Minkowski, H. (1910) Die Grundgleichungen für die elektromagnetischen Vorgänge in bewegten Körpern. *Mathematische Annalen* **68**, 472–525.

[17] Poincaré, M. H. (1906) Sur la dynamique de lélectron. *Rendiconti del Circolo Matematico di Palermo* **21**, 129–175.

[18] Schur, I. (1905) *Neue Begründung der Theorie der Gruppencharaktere*, Sitzungsberichte der Königlich-Preussischen Akademie der Wissenschaften zu Berlin. (Königlich-Preussische Akademie der Wissenschaften, Berlin).

[19] Sakurai, J. J & Napolitano, J. (2011) *Modern Quantum Mechanics*. (Addison-Wesley, San Francisco).

[20] Hall, B. (2003) *Lie Groups, Lie Algebras, and Representations: An Elementary Introduction*. (Springer, New York).

[21] Weinberg, S. (1995) *The Quantum Theory of Fields: Volume 1, Foundations*. (Cambridge University Press, Cambridge, UK).

[22] Dirac, P. A. M. (1928) The Quantum Theory of the Electron. *Proc. R. Soc. Lond. A* **117**, 610–624.

[23] Lee, T. D & Yang, C. N. (1956) Question of Parity Conservation in Weak Interactions. *Phys. Rev.* **104**, 254–258.

[24] Wu, C. S, Ambler, E, Hayward, R. W, Hoppes, D. D, & Hudson, R. P. (1957) Experimental Test of Parity Conservation in Beta Decay. *Phys. Rev.* **105**, 1413–1415.

[25] Garwin, R. L, Lederman, L. M, & Weinrich, M. (1957) Observations of the Failure of Conservation of Parity and Charge Conjugation in Meson Decays: the Magnetic Moment of the Free Muon. *Phys. Rev.* **105**, 1415–1417.

[26] Ageev, E, Alexakhin, V. Y, Alexandrov, Y, Alexeev, G, Amoroso, A, Badełek, B, Balestra, F, Ball, J, Baum, G, Bedfer, Y, et al. (2005) Measurement of the spin structure of the deuteron in the DIS region. *Physics Letters B* **612**, 154–164.

[27] Myhrer, F & Thomas, A. (2008) A possible resolution of the proton spin problem. *Physics Letters B* **663**, 302 – 305.

[28] Londergan, J. (2009) Nucleon resonances and quark structure. *Int. J. Mod. Phys. E* **18**, 1135–1165.

[29] Mayer, M. G & Jensen, J. H. D. (1955) *Elementary Theory of Nuclear Shell Structure*. (Wiley, New York).

[30] Paschen, F & Back, E. (1912) Normale und anomale Zeemaneffekte. *Annalen der Physik* **344**, 897–932.

[31] Helgaker, T, Jaszuński, M, & Pecul, M. (2008) The quantum-chemical calculation of NMR indirect spin-spin coupling constants. *Prog. Nucl. Mag. Res. Sp.* **53**, 249–268.

[32] Ramsey, N. F. (1953) Electron Coupled Interactions between Nuclear Spins in Molecules. *Phys. Rev.* **91**, 303.

[33] Helgaker, T & Pecul, M. (2004) *Spin–Spin Coupling Constants with HF and DFT Methods*. (Wiley-VCH Verlag GmbH & Co. KGaA, Weinheim, FRG), pp. 101–121.

[34] Levitt, M. H. (2008) *Spin Dynamics: Basics of Nuclear Magnetic Resonance*. (John Wiley & Sons, West Sussex, England).

[35] Feynman, R. P. (1948) Space-Time Approach to Non-Relativistic Quantum Mechanics. *Rev. Mod. Phys.* **20**, 367–387.

[36] Bernstein, H. J, Pople, J. A, & Schneider, W. G. (1957) The Analysis of Nuclear Magnetic Resonance Spectra. 1. Systems of 2 and 3 Nuclei. *Can. J. Chem.* **35**, 65–81.

[37] Pople, J. A, Schneider, W. G, & Bernstein, H. J. (1957) The Analysis of Nuclear Magnetic Resonance Spectra II: Two Pairs of Two Equivalent Nuclei. *Can. J. Chem.* **35**, 1060–1072.

[38] Pople, J. A & Schaefer, T. (1960) The Analysis of Complex Nuclear Magnetic Resonance Spectra: I. Systems with One Pair of Strongly Coupled Nuclei. *Mol. Phys.* **3**, 547–556.

[39] Weitekamp, D. P, Bielecki, A, Zax, D, Zilm, K, & Pines, A. (1983) Zero-Field Nuclear Magnetic Resonance. *Phys. Rev. Lett.* **50**, 1807–1810.

[40] Zax, D. B, Bielecki, A, Zilm, K. W, Pines, A, & Weitekamp, D. P. (1985) Zero-Field NMR and NQR. *J. Chem. Phys.* **83**, 4877–4905.

[41] Clarke, J & Braginski, A. I. (2006) *The SQUID Handbook*. (Wiley-VCH, Weinheim).

[42] Trabesinger, A. H, McDermott, R, Lee, S. K, Muck, M, Clarke, J, & Pines, A. (2004) SQUID-detected liquid state NMR in microtesla fields. *J. Phys. Chem. A* **108**, 957–963.

[43] Hartwig, S, Albrecht, H, Scheer, H, Burghoff, M, & Trahms, L. (2013) A Superconducting Quantum Interference Device Measurement System for Ultra Low-Field Nuclear Magnetic Resonance. *Appl. Magn. Reson.* **44**, 9–22.

[44] Shim, J. H, Lee, S.-J, Yu, K.-K, Hwang, S.-M, & Kim, K. (2014) Strong Pulsed Excitations Using Circularly Polarized Fields for Ultra-Low Field NMR. *J. Magn. Reson.* **239**, 87–90.

[45] Kraus Jr, R. H, Kraus Jr, R, Espy, M, Magnelind, P, Volegov, P, et al. (2014) *Ultra-Low Field Nuclear Magnetic Resonance: A New MRI Regime*. (Oxford University Press, Oxford, UK).

[46] Inglis, B, Buckenmaier, K, SanGiorgio, P, Pedersen, A. F, Nichols, M. A, & Clarke, J. (2013) MRI of the Human Brain at 130 Microtesla. *Proc. Nat. Acad. Sci.* **110**, 19194–19201.

[47] Espy, M, Matlashov, A, & Volegov, P. (2013) SQUID-Detected Ultra-Low Field MRI. *J. Magn. Reson.* **229**, 127–141.

[48] Kelso, N, Lee, S.-K, Bouchard, L.-S, Demas, V, Mueck, M, Pines, A, & Clarke, J. (2009) Distortion-free magnetic resonance imaging in the zero-field limit. *J. Magn. Reson.* **200**, 285–290.

[49] Cohen-Tannoudji, C, DuPont-Roc, J, Haroche, S, & Laloë, F. (1969) Detection of the Static Magnetic Field Produced by the Oriented Nuclei of Optically Pumped He3 Gas. *Phys. Rev. Lett.* **22**, 758–760.

[50] Allred, J. C, Lyman, R. N, Kornack, T. W, & Romalis, M. V. (2002) High-sensitivity atomic magnetometer unaffected by spin-exchange relaxation. *Phys. Rev. Lett.* **89**, 130801.

[51] Seltzer, S. J. (2008) Ph.D. thesis (Princeton University).

[52] Happer, W & Mathur, B. S. (1967) Effective Operator Formalism in Optical Pumping. *Phys. Rev.* **163**, 12–25.

[53] Budker, D & Romalis, M. (2007) Optical Magnetometry. *Nature Phys.* **3**, 227–234.

[54] Happer, W & Tang, H. (1973) Spin-Exchange Shift and Narrowing of Magnetic Resonance Lines in Optically Pumped Alkali Vapors. *Phys. Rev. Lett.* **31**, 273–276.

[55] Happer, W & Tam, A. C. (1977) Effect of rapid spin exchange on the magnetic-resonance spectrum of alkali vapors. *Phys. Rev. A* **16**, 1877–1891.

[56] Kominis, I. K, Kornack, T. W, Allred, J. C, & Romalis, M. V. (2003) A subfemtotesla multichannel atomic magnetometer. *Nature* **422**, 596–599.

[57] Dang, H. B, Maloof, A. C, & Romalis, M. V. (2010) Ultrahigh sensitivity magnetic field and magnetization measurements with an atomic magnetometer. *Appl. Phys. Lett.* **97**, 151110.

[58] Shah, V, Knappe, S, Schwindt, P. D. D, & Kitching, J. (2007) Subpicotesla atomic magnetometry with a microfabricated vapour cell. *Nature Photon.* **1**, 649–652.

[59] Mhaskar, R, Knappe, S, & Kitching, J. (2012) A low-power, high-sensitivity micromachined optical magnetometer. *Applied Physics Letters* **101**, 241105.

[60] Griffith, W. C, Knappe, S, & Kitching, J. (2010) Femtotesla atomic magnetometry in a microfabricated vapor cell. *Optics Express* **18**, 27167–27172.

[61] Theis, T. (2012) Ph.D. thesis (University of California, Berkeley).

[62] Ganssle, P. J. (2014) Ph.D. thesis (University of California, Berkeley).

[63] Seltzer, S & Romalis, M. (2004) Unshielded three-axis vector operation of a spin-exchange-relaxation-free atomic magnetometer. *Appl. Phys. Lett.* **85**, 4804–4806.

[64] Ledbetter, M. P, Theis, T, Blanchard, J. W, Ring, H, Ganssle, P, Appelt, S, Blümich, B, Pines, A, & Budker, D. (2011) Near-Zero-Field Nuclear Magnetic Resonance. *Phys. Rev. Lett.* **107**, 107601.

[65] Blanchard, J. W, Ledbetter, M. P, Theis, T, Butler, M. C, Budker, D, & Pines, A. (2013) High-Resolution Zero-Field NMR J-Spectroscopy of Aromatic Compounds. *J. Am. Chem. Soc.* **135**, 3607–3612.

[66] Theis, T, Blanchard, J. W, Butler, M. C, Ledbetter, M. P, Budker, D, & Pines, A. (2013) Chemical Analysis Using J-Coupling Multiplets in Zero-Field NMR. *Chemical Physics Letters* **580**, 160–165.

[67] Emondts, M, Ledbetter, M. P, Pustelny, S, Theis, T, Patton, B, Blanchard, J. W, Butler, M. C, Budker, D, & Pines, A. (2014) Long-Lived Heteronuclear Spin-Singlet States in Liquids at a Zero Magnetic field. *Phys. Rev. Lett.* **112**, 077601.

[68] Budker, D & Kimball, D. F. J. (2013) *Optical Magnetometry*. (Cambridge University Press, Cambridge, UK).

[69] Butler, M. C, Kervern, G, Theis, T, Ganssle, P. J, Blanchard, J. W, Budker, D, & Pines, A. (2013) Parahydrogen-Induced Polarization at Zero Magnetic Field. *J. Chem. Phys.* **138**, 234201.

[70] Dennison, D. M. (1927) A note on the specific heat of the hydrogen molecule. *Proceedings of the Royal Society of London. Series A* **115**, 483–486.

[71] Theis, T, Ganssle, P, Kervern, G, Knappe, S, Kitching, J, Ledbetter, M. P, Budker, D, & Pines, A. (2011) Parahydrogen-Enhanced Zero-Field Nuclear Magnetic Resonance. *Nature Phys.* **7**, 571–575.

[72] Theis, T, Ledbetter, M. P, Kervern, G, Blanchard, J. W, Ganssle, P. J, Butler, M. C, Shin, H. D, Budker, D, & Pines, A. (2012) Zero-Field NMR Enhanced by Parahydrogen in Reversible Exchange. *J. Am. Chem. Soc.* **134**, 3987–3990.

[73] Adams, R. W, Aguilar, J. A, Atkinson, K. D, Cowley, M. J, Elliott, P. I, Duckett, S. B, Green, G. G, Khazal, I. G, López-Serrano, J, & Williamson, D. C. (2009) Reversible interactions with para-hydrogen enhance NMR sensitivity by polarization transfer. *Science* **323**, 1708–1711.

[74] Wind, R. A. (2007) Dynamic Nuclear Polarization and High-Resolution NMR of Solids. *eMagRes*.

[75] Walker, T. G & Happer, W. (1997) Spin-exchange optical pumping of noble-gas nuclei. *Rev. Mod. Phys.* **69**, 629.

[76] King, J. P, Coles, P. J, & Reimer, J. A. (2010) Optical Polarization of C-13 Nuclei in Diamond Through Nitrogen Vacancy Centers. *Phys. Rev. B* **81**, 073201.

[77] Wang, H.-J, Shin, C. S, Avalos, C. E, Seltzer, S. J, Budker, D, Pines, A, & Bajaj, V. S. (2013) Sensitive Magnetic Control of Ensemble Nuclear Spin Hyperpolarization in Diamond. *Nat. Commun.* **4**.

[78] Fischer, R, Bretschneider, C. O, London, P, Budker, D, Gershoni, D, & Frydman, L. (2013) Bulk Nuclear Polarization Enhanced at Room Temperature by Optical Pumping. *Phys. Rev. Lett.* **111**, 057601.

[79] Navon, G, Song, Y, Room, T, Appelt, S, Taylor, R, & Pines, A. (1996) Enhancement of solution NMR and MRI with laser-polarized xenon. *Science* **271**, 1848–1850.

[80] Rõõm, T, Appelt, S, Seydoux, R, Hahn, E. L, & Pines, A. (1997) Enhancement of surface NMR by laser-polarized noble gases. *Phys. Rev. B* **55**, 11604–11610.

[81] Abragam, A & Proctor, W. (1958) Spin temperature. *Phys. Rev.* **109**, 1441.

[82] Goldman, M & Landesman, A. (1963) Dynamic polarization by thermal mixing between two spin systems. *Phys. Rev.* **132**, 610.

[83] Cherubini, A, Payne, G, Leach, M, & Bifone, A. (2003) Hyperpolarising 13C for NMR Studies Using Laser-Polarised129Xe: SPINOE vs Thermal Mixing. *Chem. Phys. Lett.* **371**, 640–644.

[84] Jiménez-Martínez, R, Kennedy, D. J, Rosenbluh, M, Donley, E. A, Knappe, S, Seltzer, S. J, Ring, H. L, Bajaj, V. S, & Kitching, J. (2014) Optical Hyperpolarization and NMR Detection of 129Xe on a Microfluidic Chip. *Nat Commun.* **5**.

[85] Ward, H. R, Lawler, R. G, Loken, H. Y, & Cooper, R. A. (1969) Nuclear polarization in the products of chemical reactions occurring in the absence of a magnetic field. *J. Am. Chem. Soc.* **91**, 4928–4929.

[86] Roth, H. D. (1996) Chemically Induced Dynamic Nuclear Polarization. *eMagRes*.

[87] Till, U, Timmel, C, Brocklehurst, B, & Hore, P. (1998) The Influence of Very Small Magnetic Fields on Radical Recombination Reactions in the Limit of Slow Recombination. *Chem. Phys. Lett.* **298**, 7–14.

[88] Kiryutin, A. S, Korchak, S. E, Ivanov, K. L, Yurkovskaya, A. V, & Vieth, H.-M. (2012) Creating Long-Lived Spin States at Variable Magnetic Field by Means of Photochemically Induced Dynamic Nuclear Polarization. *J. Phys. Chem. Lett.* **3**, 1814–1819.

[89] Mamin, H, Kim, M, Sherwood, M, Rettner, C, Ohno, K, Awschalom, D, & Rugar, D. (2013) Nanoscale Nuclear Magnetic Resonance With a Nitrogen-Vacancy Spin Sensor. *Science* **339**, 557–560.

[90] Meriles, C. A, Jiang, L, Goldstein, G, Hodges, J. S, Maze, J, Lukin, M. D, & Cappellaro, P. (2010) Imaging Mesoscopic Nuclear Spin Noise With a Diamond Magnetometer. *J. Chem. Phys.* **133**, 124105.

[91] Degen, C, Poggio, M, Mamin, H, & Rugar, D. (2007) Role of Spin Noise in the Detection of Nanoscale Ensembles of Nuclear Spins. *Phys. Rev. Lett.* **99**, 250601.

[92] Vaara, J, Jokisaari, J, Wasylishen, R. E, & Bryce, D. L. (2002) Spin–spin coupling tensors as determined by experiment and computational chemistry. *Prog. Nucl. Mag. Res. Sp.* **41**, 233–304.

[93] Harris, R. K. (1986) *Nuclear Magnetic Resonance Spectroscopy: A Physicochemical View*. (Longman, Burnt Mill).

[94] Karplus, M. (1959) Contact Electron-Spin Coupling of Nuclear Magnetic Moments. *J. Chem. Phys.* **30**, 11.

[95] Soncini, A & Lazzeretti, P. (2003) Nuclear spin-spin coupling density in molecules. *J. Chem. Phys.* **118**, 7165.

[96] Soncini, A & Lazzeretti, P. (2003) Nuclear spin–spin coupling density functions and the Fermi hole. *J. Chem. Phys.* **119**, 1343.

[97] Malkina, O. L & Malkin, V. G. (2003) Visualization of nuclear spin-spin coupling pathways by real-space functions. *Angew. Chem. Int. Ed. Engl.* **42**, 4335–8.

[98] Cremer, D & Gräfenstein, J. (2007) Calculation and analysis of NMR spin-spin coupling constants. *Phys. Chem. Chem. Phys.* **9**, 2791–816.

[99] Wu, A & Cremer, D. (2003) Analysis of multipath transmission of spin–spin coupling constants in cyclic compounds with the help of partially spin-polarized orbital contributions. *Phys. Chem. Chem. Phys.* **5**, 4541.

[100] Bifulco, G, Dambruoso, P, Gomez-Paloma, L, & Riccio, R. (2007) Determination of relative configuration in organic compounds by NMR spectroscopy and computational methods. *Chem. Rev.* **107**, 3744–79.

[101] Krivdin, L. B. (2007) Recent advances in theoretical calculations of indirect spin–spin coupling constants. *Annu. R. NMR. S.* **61**, 133–245.

[102] Chernyshev, K. A, Krivdin, L. B, Larina, L. I, Konkova, T. V, Demina, M. M, & Medvedeva, A. S. (2007) Configurational Assignment of Carbon, Silicon and Germanium Containing Propynal Oximes by Means of C–1H, 13 C–13C and 15N–1H spin–spin coupling constants. *Magn. Reson. Chem.* **45**, 661–666.

[103] Krivdin, L. B, Khutsishvili, S. S, Shemyakina, O. A, Contreras, H, Mal, A. G, & Trofimov, B. A. (2007) Stereochemical study of iminodihydrofurans based on experimental measurements and SOPPA calculations of 13C–13C spin–spin coupling constants. *Magn. Reson. Chem.* **45**, 758–765.

[104] Sutter, K & Autschbach, J. (2012) Computational Study and Molecular Orbital Analysis of NMR Shielding, Spin-Spin Coupling, and Electric Field Gradients of Azido Platinum Complexes. *J. Am. Chem. Soc.* **134**, 13374–13385.

[105] Pietrzak, M, Benedict, C, Gehring, H, Daltrozzo, E, & Limbach, H.-H. (2007) NMR studies and DFT calculations of the symmetric intramolecular NHN-hydrogen bond of bis-(2-pyridyl)-acetonitrile: Isotope labeling strategy for the indirect 13C-detection of 15N15N couplings. *J. Mol* **844-845**, 222–231.

[106] de la Lande, A, Fressigné, C, Gérard, H, Maddaluno, J, & Parisel, O. (2007) First-principles molecular dynamics evaluation of thermal effects on the NMR (1)J(Li,C) spin-spin coupling. *Chem. Eur. J.* **13**, 3459–69.

[107] Grzesiek, S, Cordier, F, Jaravine, V, & Barfield, M. (2004) Insights into biomolecular hydrogen bonds from hydrogen bond scalar couplings. *Prog. Nucl. Mag. Res. Sp.* **45**, 275–300.

[108] Pecul, M, Sadlej, J, & Helgaker, T. (2003) Calculations of hydrogen-bond-transmitted indirect nuclear spin–spin couplings: a comparison of density-functional and ab initio methods. *Chem. Phys. Lett.* **372**, 476–484.

[109] Ledbetter, M. P, Crawford, C. W, Pines, A, Wemmer, D. E, Knappe, S, Kitching, J, & Budker, D. (2009) Optical detection of NMR J-spectra at zero magnetic field. *J. Magn. Reson.* **199**, 25–29.

[110] Butler, M. C, Ledbetter, M. P, Theis, T, Blanchard, J. W, Budker, D, & Pines, A. (2013) Multiplets at Zero Magnetic Field : The Geometry of Zero-Field NMR. *J. Chem. Phys.* **138**, 184202.

[111] Chertkov, V. A & Sergeyev, N. M. (1983) 13C isotope effects on the parameters of proton magnetic resonance spectra of benzene. *J. Magn. Reson.* **52**, 400–406.

[112] Ledbetter, M, Pustelny, S, Budker, D, Romalis, M, Blanchard, J, & Pines, A. (2012) Liquid-State Nuclear Spin Comagnetometers. *Phys. Rev. Lett.* **108**, 1–5.

[113] Schaefer, T, Sebastian, R, & Penner, G. H. (1985) 1h nuclear magnetic resonance spectral parameters of toluene. implications for conformational analysis and isotope shifts. *Can. J. Chem.* **63**, 2597–2600.

[114] Barfield, M, Fallick, C, Hata, K, Sternhell, S, & Westerman, P. (1983) Conformational, bond-order, and substituent dependencies of ortho-benzylic coupling constants. *J. Am. Chem. Soc.* **105**, 2178–2186.

[115] Laatikainen, R. (1986) An application of nJ (CH2, H) and 5J (OH, H) long-range couplings in the conformational analysis of 2-hydroxybenzyl methyl ether in various solvents. Computational strategies for spectral analysis and determination of association thermodynamic parameters. *Magn. Reson. Chem.* **24**, 588–594.

[116] Kolehmainen, E, Laatikainen, R, & Kral, V. (1986) Long-range proton–proton spin–spin coupling constants in some aryl-substituted methylenemalonaldehydes. conformational dependence of meta-and ortho-benzylic couplings in styrenoic systems. *Magn. Reson. Chem.* **24**, 498–502.

[117] Schaefer, T. E. D & Takeuchi, S. (1989) A positive 6J(H,CH0) in some meta derivatives of benzaldehyde. A simple model. *Can. J. Chem.* **67**, 827–830.

[118] Appelt, S, Haesing, F. W, Sieling, U, Gordji-Nejad, A, Glöggler, S, & Blümich, B. (2010) Paths from weak to strong coupling in NMR. *Phys. Rev. A* **81**, 23420.

[119] Slichter, C. P. (1990) *Principles of Magnetic Resonance*. (Springer, Berlin Heidelberg), 3rd edition.

[120] Appelt, S, Haesing, F. W, Kuehn, H, Sieling, U, & Blümich, B. (2007) Analysis of molecular structures by homo- and hetero-nuclear J-coupled NMR in ultra-low field. *Chem. Phys. Lett.* **440**, 308–312.

[121] Collel, J, Turschmann, P, Glöggler, S, Schleker, P, Theis, T, Ledbetter, M, Budker, D, Pines, A, Blümich, B, & Appelt, S. (2013) Fundamental Aspects of Parahydrogen Enhanced Low-Field Nuclear Magnetic Resonance. *Phys. Rev. Lett.* **110**, 137602.

[122] Halse, M. E & Callaghan, P. T. (2008) A dynamic nuclear polarization strategy for multi-dimensional Earth's field NMR spectroscopy. *J. Magn. Reson.* **195**, 162–168.

[123] Glöggler, S, Muller, R, Colell, J, Emondts, M, Dabrowski, M, Blümich, B, & Appelt, S. (2011) Para-hydrogen induced polarization of amino acids, peptides and deuterium–hydrogen gas. *Phys. Chem. Chem. Phys.* **13**, 13759–13764.

[124] Greenberg, Y. S. (1998) Application of superconducting quantum interference devices to nuclear magnetic resonance. *Rev. Mod. Phys.* **70**, 175–222.

[125] McDermott, R, Trabesinger, A. H, Muck, M, Hahn, E. L, Pines, A, & Clarke, J. (2002) Liquid-state NMR and scalar couplings in microtesla magnetic fields. *Science* **295**, 2247–2249.

[126] Schwindt, P. D. D, Knappe, S, Shah, V, Hollberg, L, Kitching, J, Liew, L. A, & Moreland, J. (2004) Chip-scale atomic magnetometer. *Appl. Phys. Lett.* **85**, 6409–6411.

[127] Diehl, P & Khetrapal, C. (1969) in *NMR Basic Principles and Progress / Grundlagen und Fortschritte*, NMR Basic Principles and Progress / Grundlagen und Fortschritte, eds. Diehl, P, Fluck, E, & Kosfeld, R. (Springer, Berlin Heidelberg) Vol. 1, pp. 1–95.

[128] Emsley, J & Lindon, J. (1975) *NMR Spectroscopy Using Liquid Crystal Solvents*. (Pergamon Press, Oxford).

[129] Tjandra, N & Bax, A. (1997) Direct Measurement of Distances and Angles in Biomolecules by NMR in a Dilute Liquid Crystalline Medium. *Science* **278**, 1111–1114.

[130] Tycko, R, Blanco, F. J, & Ishii, Y. (2000) Alignment of Biopolymers in Strained Gels: A New Way To Create Detectable Dipole–Dipole Couplings in High-Resolution Biomolecular NMR. *J. Am. Chem. Soc.* **122**, 9340–9341.

[131] Chou, J. J, Gaemers, S, Howder, B, Louis, J. M, & Bax, A. (2001) A simple apparatus for generating stretched polyacrylamide gels, yielding uniform alignment of proteins and detergent micelles*. *Journal of Biomolecular NMR* **21**, 377–382.

[132] Tjandra, N, Omichinski, J. G, Gronenborn, A. M, Clore, G. M, & Bax, A. (1997) Use of dipolar 1H–15N and 1H–13C couplings in the structure determination of magnetically oriented macromolecules in solution. *Nature Structural & Molecular Biology* **4**, 732–738.

[133] Clore, G. M, Gronenborn, A. M, & Tjandra, N. (1998) Direct structure refinement against residual dipolar couplings in the presence of rhombicity of unknown magnitude. *J. Magn. Reson.* **131**, 159–162.

[134] Prestegard, J. H, Al-Hashimi, H. M. l, & Tolman, J. R. (2000) NMR structures of biomolecules using field oriented media and residual dipolar couplings. *Quarterly Reviews of Biophysics* **33**, 371–424.

[135] Trigo-Mourino, P, Sifuentes, R, Navarro-Vazquez, A, Gayathri, C, Maruenda, H, & Gil, R. R. (2012) Determination of the absolute configuration of 19-OH-(-)-eburnamonine using a combination of residual dipolar couplings, DFT chemical shift predictions, and chiroptics. *Nat. Prod. Commun.* **7**, 735–738.

[136] Saupe, A. (1964) Kernresonanzen in kristallinen flüssigkeiten und in kristallinflüssigen lösungen. teil i. *Zeitschrift Naturforschung Teil A* **19**, 161.

[137] Saupe, A. (1965) Das protonenresonanzspektrum von orientiertem benzol in nematisch-kristallinflüssiger lösung. *Zeitschrift Naturforschung Teil A* **20**, 572.

[138] Caspary, W. J, Millett, F, Reichbach, M, & Dailey, B. P. (1969) Nmr determination of deuterium quadrupole coupling constants in nematic solutions. *J. Chem. Phys.* **51**, 623–627.

[139] Kessler, M, Ring, H, Trambarulo, R, & Gordy, W. (1950) Microwave spectra and molecular structures of methyl cyanide and methyl isocyanide. *Phys. Rev.* **79**, 54–56.

[140] Zax, D. B, Bielecki, A, Zilm, K. W, & Pines, A. (1984) Heteronuclear Zero-Field NMR. *Chem. Phys. Lett.* **106**, 550–553.

[141] Thayer, A. M, Luzar, M, & Pines, A. (1987) Zero-Field NMR Study of the Biaxial Smectic-E Phase. *Liq. Cryst.* **2**, 241–244.

[142] Harris, K. J, Bryce, D. L, & Wasylishen, R. E. (2009) NMR line shapes from AB spin systems in solids – The role of antisymmetric spin–spin coupling. *Can. J. Chem.* **87**, 1338–1351.

[143] Barra, A. L & Robert, J. B. (1996) Parity Non-Conservation and NMR Parameters. *Mol. Phys.* **88**, 875–886.

[144] Carravetta, M, Johannessen, O. G, & Levitt, M. H. (2004) Beyond the T_1 Limit: Singlet Nuclear Spin States in Low Magnetic Fields. *Phys. Rev. Lett.* **92**, 153003.

[145] Pileio, G, Carravetta, M, & Levitt, M. H. (2010) Storage of nuclear magnetization as long-lived singlet order in low magnetic field. *Proc. Nat. Acad. Sci.* **107**, 17135–17139.

[146] Sarkar, R, Ahuja, P, Moskau, D, Vasos, P. R, & Bodenhausen, G. (2007) Extending the scope of singlet-state spectroscopy. *ChemPhysChem* **8**, 2652–2656.

[147] Sarkar, R, Ahuja, P, Vasos, P. R, & Bodenhausen, G. (2008) Measurement of slow diffusion coefficients of molecules with arbitrary scalar couplings via long-lived spin states. *ChemPhysChem* **9**, 2414–2419.

[148] Cavadini, S, Dittmer, J, Antonijevic, S, & Bodenhausen, G. (2005) Slow diffusion by singlet state NMR spectroscopy. *J. Am. Chem. Soc.* **127**, 15744–15748.

[149] DeVience, S. J, Walsworth, R. L, & Rosen, M. S. (2012) Dependence of nuclear spin singlet lifetimes on RF spin-locking power. *J. Magn. Reson.* **218**, 5–10.

[150] Ghosh, R, Kadlecek, S, Ardenkjaer-Larsen, J. H, Pullinger, B, Pileio, G, Levitt, M, Kuzma, N, & Rizi, R. (2011) Measurements of the persistent singlet state of N2O in blood and other solventsPotential as a magnetic tracer. *Magn. Reson. Med.* **66**, 1177–1180.

[151] Pileio, G, Carravetta, M, Hughes, E, & Levitt, M. H. (2008) The long-lived nuclear singlet state of 15N-nitrous oxide in solution. *J. Am. Chem. Soc.* **130**, 12582–12583.

[152] Warren, W. S, Jenista, E, Branca, R. T, & Chen, X. (2009) Increasing hyperpolarized spin lifetimes through true singlet eigenstates. *Science* **323**, 1711–1714.

[153] Vasos, P, Comment, A, Sarkar, R, Ahuja, P, Jannin, S, Ansermet, J.-P, Konter, J, Hautle, P, Van Den Brandt, B, & Bodenhausen, G. (2009) Long-lived states to sustain hyperpolarized magnetization. *Proc. Nat. Acad. Sci.* **106**, 18469–18473.

[154] Feng, Y, Davis, R. M, & Warren, W. S. (2012) Accessing long-lived nuclear singlet states between chemically equivalent spins without breaking symmetry. *Nat. Phys.* **8**, 831–837.

[155] Carravetta, M & Levitt, M. H. (2005) Theory of long-lived nuclear spin states in solution nuclear magnetic resonance. I. Singlet states in low magnetic field. *J. Chem. Phys.* **122**, 214505.

[156] Pileio, G & Levitt, M. H. (2007) J-Stabilization of singlet states in the solution NMR of multiple-spin systems. *J. Magn. Reson.* **187**, 141–145.

[157] Pileio, G & Levitt, M. H. (2009) Theory of long-lived nuclear spin states in solution nuclear magnetic resonance. II. Singlet spin locking. *J. Chem. Phys.* **130**, 214501.

[158] Pileio, G. (2010) Relaxation theory of nuclear singlet states in two spin-1/2 systems. *Prog. Nuc. Magn. Reson. Spect.* **56**, 217–231.

[159] Tayler, M. C & Levitt, M. H. (2011) Singlet nuclear magnetic resonance of nearly-equivalent spins. *Phys. Chem. Chem. Phys.* **13**, 5556–5560.

[160] DeVience, S. J, Walsworth, R. L, & Rosen, M. S. (2013) Nuclear spin singlet states as a contrast mechanism for NMR spectroscopy. *NMR in Biomedicine* **26**, 1204–1212.

[161] Bornet, A, Ahuja, P, Sarkar, R, Fernandes, L, Hadji, S, Lee, S. Y, Haririnia, A, Fushman, D, Bodenhausen, G, & Vasos, P. R. (2011) Long-Lived States to Monitor Protein Unfolding by Proton NMR. *ChemPhysChem* **12**, 2729–2734.

[162] Ahuja, P, Sarkar, R, Vasos, P. R, & Bodenhausen, G. (2009) Diffusion coefficients of biomolecules using long-lived spin states. *J. Am. Chem. Soc.* **131**, 7498–7499.

[163] Levitt, M. H. (2012) Singlet nuclear magnetic resonance. *Annual review of physical chemistry* **63**, 89–105.

[164] Kohler, S, Yen, Y, Wolber, J, Chen, A, Albers, M, Bok, R, Zhang, V, Tropp, J, Nelson, S, Vigneron, D, et al. (2007) In vivo 13carbon metabolic imaging at 3T with hyperpolarized 13C-1-pyruvate. *Magnetic Resonance in Medicine* **58**, 65–69.

[165] Pileio, G, Carravetta, M, & Levitt, M. H. (2009) Extremely Low-Frequency Spectroscopy in Low-Field Nuclear Magnetic Resonance. *Phys. Rev. Lett.* **103**, 083002.

[166] Pileio, G, Concistrè, M, Carravetta, M, & Levitt, M. H. (2006) Long-lived nuclear spin states in the solution NMR of four-spin systems. *J. Magn. Reson.* **182**, 353–357.

[167] Ahuja, P, Sarkar, R, Vasos, P. R, & Bodenhausen, G. (2009) Long-lived States in Multiple-Spin Systems. *ChemPhysChem* **10**, 2217–2220.

[168] Llor, A, Olejniczak, Z, & Pines, A. (1995) Coherent Isotropic Averaging in Zero-Field Nuclear Magnetic Resonance. 1. General Theory and Icosahedral Sequences. *J. Chem. Phys.* **103**, 3966–3981.

[169] Llor, A, Olejniczak, Z, & Pines, A. (1995) Coherent Isotropic Averaging in Zero-Field Nuclear Magnetic Resonance. 2. Cubic Sequences and Time-Reversal of Spin Couplings. *J. Chem. Phys.* **103**, 3982–3997.

[170] Budker, D, Ledbetter, M, Appelt, S, Bouchard, L, & Wojtsekhowski, B. (2012) Polarized nuclear target based on parahydrogen induced polarization. *Nucl. Instrum. Meth. A* **694**, 246 – 250.

[171] Hövener, J.-B, Schwaderlapp, N, Lickert, T, Duckett, S. B, Mewis, R. E, Highton, L. A. R, Kenny, S. M, Green, G. G. R, Leibfritz, D, Korvink, J. G, Hennig, J, & von Elverfeldt, D. (2013) A Hyperpolarized Equilibrium for Magnetic Resonance. *Nat. Commun.* **4**, 2946.

[172] Blanchard, J. W, Belieres, J.-P, Alam, T. M, Yarger, J. L, & Holland, G. P. (2011) NMR Determination of the Diffusion Mechanisms in Triethylamine-Based Protic Ionic Liquids. *J. Phys. Chem. Lett.* **2**, 1077–1081.

[173] Blanchard, J. W, Groy, T. L, Yarger, J. L, & Holland, G. P. (2012) Investigating Hydrogen-Bonded Phosphonic Acids with Proton Ultrafast MAS NMR and DFT Calculations. *J. Phys. Chem. C* **116**, 18824–18830.

[174] Greenberg, Y. S. (1998) Application of Superconducting Quantum Interference Devices. *Rev. Mod. Phys.* **70**, 175.

[175] McDermott, R, Trabesinger, A, Muck, M, Hahn, E, Pines, A, & Clarke, J. (2002) Liquid-State NMR and Scalar Couplings in Microtesla. *Science* **295**, 2247.

[176] Ledbetter, M. P, Saielli, G, Bagno, A, Tran, N, & Romalis, M. V. (2012) Observation of Scalar Nuclear Spin-Spin Coupling in van der Waals Complexes. *Proc. Nat. Acad. Sci.* **109**, 12393.

[177] Budker, D & Romalis, M. (2009) Atomic Magnetometer. *Nat. Phys.* **3**, 227.

[178] Theis, T, Ganssle, P, Kervern, G, Knappe, S, Kitching, J, Ledbetter, M. P, Budker, D, & Pines, A. (2011) Parahydrogen-Enhanced Zero-Field Nuclear Magnetic Resonance. *Nature. Phys.* **7**, 571.

[179] Ernst, R. R, Bodenhausen, G, & Wokaun, A. (1987) *Principles of Nuclear Magnetic Resonance in One and Two Dimensions*. (Clarendon Press, Oxford, UK).

[180] Becker, E. D. (2000) *High Resolution NMR*. (Academic Press, New York), 3rd edition.

[181] Hahn, E & Maxwell, D. (1951) Chemical Shift and Field Independent Frequency Modulation of the Spin Echo Envelope. *Phys. Rev.* **84**, 1246.

[182] McNeil, E. B, Slichter, C. P, & Gutowsky, H. S. (1951) ”Slow Beats” in F19 Nuclear Spin Echoes. *Phys. Rev.* **84**, 1245.

[183] Ramsey, N. F & Purcel, E. M. (1952) Interaction Between Nuclear Spins in Molecules. *Phys. Rev.* **85**, 143.

[184] Bloembergen, N, Purcell, E, & Pound, R. (1947) Nuclear Magnetic Relaxation. *Nature* **160**, 475.

[185] Kruk, D, Herrmann, A, & Rossler, E. (2012) Field-cycling NMR Relaxometry of Viscous Liquids and Polymers. *Prog. Nucl. Magn. Reson. Spectrosc.* **63**, 33–64.

[186] Connor, T. M & McLauchlan, K. A. (1965) High Resolution Nuclear Resonance Studies of the Chain Conformation of Polyethylene Oxide. *J. Phys. Chem.* **69**, 1888.

[187] Pachler, K & Wessels, P. (1972) Nuclear Magnetic Resonance Study of 2-Fluoroethanol and Ethylene Glycol. *J. Mol. Struct.* **6**, 471.

[188] D.Y. Han, A.J. Woo, I. N & Hong, S. (2002) Molecular Conformation of Hydrogen-Bonded Ethylene Glycol in Sodalite: A 1H CRAMPS NMR, IR, and 2H NMR Study. *J. Phys. Chem. B* **106**, 6206.

[189] Salman, S. R, Farrant, R. D, Sanderson, P. N, & Lindon, J. C. (1993) Conformation of Ethane-1,2-diol from Analysis of Gradient-Enhanced Inverse Detection. *Magn. Reson. Chem.* **31**, 585–589.

[190] Chidichimo, G, Imbardelli, D, Longeri, M, & Saupe, A. (1988) Conformation of Ethylene Glycol Dissolved in a Nematic-Lyotropic Solution: an N.M.R. Analysis. *Mol. Phys.* **65**, 1143.

[191] Pearce, C & Sanders, J. (1994) Improving the Use of Hydroxyl Proton Resonances in Structure Determination and NMR Spectral Assignment: Inhibition of Exchange by Dilution. *J. Chem. Soc. Perkin Trans. 1* **1994**, 1119.

[192] Petterson, K, Stein, R, Drake, M, & Roberts, J. (2005) An NMR Investigation of the Importance of Intramolecular Hydrogen Bonding in Determining the Conformational Equilibrium of Ethylene Glycol. *Magn. Reson. Chem.* **43**, 225.

[193] Lomas, J. S. (2013) 1H NMR Spectra of Ethane-1,2-diol and Other Vicinal Diols in Benzene: GIAO/DFT Shift Calculations. *Magn. Reson. Chem.* **51**, 32–41.

[194] Cabral, B. C, Albuquerque, L, & Fernandes, F. S. (1991) Ab Initio Study of the Conformational Equilibrium of Ethylene Glycol. *Theor. Chim. Acta* **78**, 271.

[195] Nagy, P, Dunn-III, W, Alagona, G, & Ghio, C. (1991) Theoretical Calculations on 1,2-Ethanediol. Gauche-Trans Equilibrium in Gas-Phase and Aqueous Solution. *J. Am. Chem. Soc.* **113**, 6719.

[196] Cramer, C & Thuhlar, D. (1994) Quantum Chemical Conformational Analysis of 1,2-Ethanediol: Correlation and Solvation Effects on the Tendency To Form Internal Hydrogen Bonds in the Gas Phase and in Aqueous Solution. *J. Am. Chem. Soc.* **116**, 3892.

[197] Saiz, L, Padro, J, & Guardia, E. (2001) Structure of Liquid Ethylene Glycol: A Molecular Dynamics Simulation Study with Different Force Fields. *J. Chem. Phys.* **114**, 3187.

[198] Maiti, N. C, Zhu, Y, Carmichael, I, Serianni, A. S, & Anderson, V. E. (2006) 1JCH Correlates with Alcohol Hydrogen Bond. *J. Org. Chem.* **71**, 2878–2880.

[199] Crittenden, D. L, Thompson, K. C, & Jordan, M. J. T. (2005) On the Extent of Intramolecular Hydrogen Bonding in Gas-Phase and Hydrated EG. *J. Phys. Chem. A* **109**, 2971–2977.

[200] Chopra, D, Rowa, T. N. G, Arunan, E, & Klein, R. A. (2010) Crystalline Ethane-1,2-diol Does Not Have Intra-Molecular Hydrogen Bonding:Experimental and Theoretical Charge Density Studies. *J. Mol. Struct.* **964**, 126–133.

[201] Murli, C, Lu, N, Dong, Z, & Song, Y. (2012) Hydrogen Bonds and Conformations in Ethylene Glycol Under Pressure. *J. Phys. Chem. B* **116**, 12574.

[202] Zhang, N, Li, W, Chen, C, Zuo, J, & Weng, L. (2013) Molecular Dynamics Study on Water Self-Diffusion in Aqueous Mixtures of Methanol, Ethylene Glycol and Glycerol: Investigations from the Point of View of Hydrogen Bonding. *Molecular Physics* **10**, 1080.

[203] Møller, C & Plesset, M. S. (1934) Note on an Approximation Treatment for Many-Electron Systems . *Phys. Rev.* **46**, 0618 – 22.

[204] Tomasi, J, Mennucci, B, & Cammi, R. (2005) Quantum Mechanical Continuum Solvation Models. *Chem. Rev.* **105**, 2999–3094.

[205] Frisch, M. J, Trucks, G. W, Schlegel, H. B, Scuseria, G. E, Robb, M. A, Cheeseman, J. R, Scalmani, G, Barone, V, Mennucci, B, Petersson, G. A, Nakatsuji, H, Caricato, M, Li, X, Hratchian, H. P, Izmaylov, A. F, Bloino, J, Zheng, G, Sonnenberg, J. L, Hada, M, Ehara, M, Toyota, K, Fukuda, R, Hasegawa, J, Ishida, M, Nakajima, T, Honda, Y, Kitao, O, Nakai, H, Vreven, T, Montgomery, Jr., J. A, Peralta, J. E, Ogliaro, F, Bearpark, M, Heyd, J. J, Brothers, E, Kudin, K. N, Staroverov, V. N, Kobayashi, R, Normand, J, Raghavachari, K, Rendell, A, Burant, J. C, Iyengar, S. S, Tomasi, J, Cossi, M, Rega, N, Millam, J. M, Klene, M, Knox, J. E, Cross, J. B, Bakken, V, Adamo, C, Jaramillo, J, Gomperts, R, Stratmann, R. E, Yazyev, O, Austin, A. J, Cammi, R, Pomelli, C, Ochterski, J. W, Martin, R. L, Morokuma, K, Zakrzewski, V. G, Voth, G. A, Salvador, P, Dannenberg, J. J, Dapprich, S, Daniels, A. D, Farkas, , Foresman, J. B, Ortiz, J. V, Cioslowski, J, & Fox, D. J. (2009) Gaussian 09 Revision B.01. Gaussian Inc. Wallingford CT 2009.

[206] Jensen, F. (2010) The Optimum Contraction of Basis Sets for Calculating SpinSpin Coupling Constants. *Theor. Chem. Acc.* **126**, 371–382.

[207] Lomas, J. S. (2013) 1H NMR Spectra of Ethane-1,2-diol and Other Vicinal Diols in Benzene: GIAO/DFT Shift Calculations. *Magn. Reson. Chem.* **51**, 32–41.

[208] MonoEthyleneGlycol Global Company. (2008) *Ethylene glycol product guide* (MonoEthyleneGlycol Global Company).

[209] Geerke, D. P & van Gunsteren, W. F. (2007) The Performance of Non-Polarizable and Polarizable Force-Field Parameter Sets for Ethylene Glycol in Molecular Dynamics Simulations of the Pure Liquid and its Aqueous Mixtures. *Mol. Phys.* **105**, 1861–1881.

[210] Kaiser, A, Ismailova, O, Koskela, A, Huber, S. E, Ritter, M, Cosenza, B, Benger, W, Nazmutdinov, R, & Probst, M. (2014) Ethylene Glycol Revisited: Molecular Dynamics Simulations and Visualization of the Liquid and its Hydrogen-Bond Network . *J. Mol. Liq.* **189**, 20 – 29. Fluid phase associations.

[211] Car, R & Parrinello, M. (1985) Unified Approach for Molecular Dynamics and Density-Functional Theory. *Phys. Rev. Lett.* **55**, 2471–2474.

[212] Cheng, Y.-L, Chen, H.-Y, & Takahashi, K. (2011) Theoretical Calculation of the OH Vibrational Overtone Spectra of 1-n Alkane Diols (n = 24): Origin of Disappearing Hydrogen-Bonded OH Peak. *J. Phys. Chem. A* **115**, 5641–5653.

Appendix A

Appendix: Ethylene Glycol

Appendix haiku
Measuring viscous liquid:
Ethylene glycol

We have also applied ZULF-NMR techniques to the study of a model viscous liquid, ethylene glycol. These results have been submitted to the Journal of Magnetic Resonance as

- Shimizu, Y., Blanchard, J.W., Pustelny, S., Saielli, G., Bagno, A., Ledbetter, M.P., Budker, D., and Pines, A. Zero-Field Nuclear Magnetic Resonance Spectroscopy of Viscous Liquids. Submitted.

The results of this paper are presented as an Appendix to this dissertation because they are by comparison peripheral to the general narrative, and may perhaps be considered more as a bridge connecting the current work to my undergraduate work on non-standard liquids [172] and quantum chemistry calculations of NMR parameters [173].

A.1 Introduction

Recent developments in zero- and ultra-low-field (ZULF) NMR with superconducting quantum interference devices (SQUIDs) [174, 175, 176] and atomic magnetometers [177, 109, 178, 64] open new possibilities for imaging and spectroscopy. In conventional NMR spectroscopy, chemical shifts and spin-spin couplings are utilized to distinguish molecular structures [179, 180], where spin-spin couplings are treated as a first-order perturbation to the Zeeman energy. To obtain high sensitivity and resolution of chemical shifts, high magnetic fields are conventionally used, requiring expensive radio-frequency spectrometers and bulky superconducting magnets with cryogenic cooling. ZULF-NMR with atomic magnetometers utilizing alkali-atom vapor cells has enabled non-cryogenic, desktop spectroscopy [109, 178, 64]. While chemical shifts vanish at zero field, ZULF-NMR spectra are governed by indirect nuclear spin-spin couplings called scalar or J-couplings that depend on the electronic structure and geometry of the molecule [109, 120]. In contrast to the chemical shift due to diamagnetic current of the occupied orbitals, the J-coupling is an indirect interaction between nuclear spins through second-order hyperfine effects [181, 182, 183, 179, 180], and thus serves as a sensitive local probe of molecular geometry and electronic structure.

Until now, investigations of ZULF NMR with atomic magnetometers have focused on low-viscosity liquids with simple molecular structures and weak intermolecular interactions [109, 178, 64], achieving half width at half maximum as low as ≈ 0.01 Hz [65, 67, 112] comparable to that of advanced high-field (HF) NMR. Many materials of practical interest – polymers or proteins, for example, feature significant van der Waals interactions and hydrogen bonds. Therefore, the ability to detect such interactions through their J-coupling spectra in ZULF NMR is of significant importance. Compared to HF-NMR, ZULF NMR may have advantages in resolution because of the absence of the static and dynamic broadening mechanisms inherent in the spectroscopy of chemical shifts. For a liquid sample, the linewidth of ZULF NMR is governed by the dynamical width due to nuclear dipole fields and J-coupling [180]. However, the magnitude of J-couplings sensitively depends on the molecular conformation and interactions in a way that is not always straightforward to predict.

Here we use a model system, $^{13}C_2$-labeled ethylene glycol (EG, HO-$^{13}CH_2$-$^{13}CH_2$-OH), featuring strong intermolecular hydrogen bonds. NMR has been utilized to investigate molecular dynamics [184, 180, 185] and conformational equilibria of polyalcohols [186, 187, 188, 189, 190, 191, 192, 193]. Among ten non-equivalent isomers of EG with different dihedral angles in one C-C and two C-O torsion angles, theoretical calculations have shown that two *gauche* conformers with a C-C torsion angle at possible potential minima, 60° and 300°, are favorable rather than *trans* conformers with a torsion angle of 180° [194, 195, 196, 197, 198, 199, 200, 201, 202]. The two-bond J-couplings in ^{1}H NMR measurements support the predominant *gauche* state [186, 187, 188, 189, 190, 191, 192, 193]. However, NMR studies of EG have been usually made in solution states [186, 187, 188, 189, 190, 191, 192, 193] possibly due to the broadening of NMR spectra in neat EG, and the effect of intermolecular hydrogen bonding between EG molecules for the conformations remains insufficiently explored.

In this paper, we study the effect of viscosity on ZULF- and HF-NMR spectra by controlling the viscosity through varying temperature and water content of EG solutions. We observe changes in ZULF-NMR spectra that are due to minute changes in J-couplings that can be attributed to intermolecular hydrogen bonding and molecular dynamics in bulk EG.

A.2 Experimental Details

The ZULF-NMR apparatus has been described previously in Ref. [64] and references therein. An EG sample pre-polarized in a permanent 2.0 T magnet situated outside the magnetic shield was shuttled to the zero-field region through a guiding coil. Because the low frequencies of ZULF-NMR preclude the use of inductive detection, NMR signals were detected with an atomic magnetometer incorporating a Rb vapor cell (^{87}Rb and 1300 torr N_2) operating at 180°C. The alkali vapor was optically polarized with circularly polarized light tuned to the D1 transition. Magnetic field measurements were performed by continuously monitoring optical rotation of linearly polarized light, propagating in a direction perpendicular to the pump beam, tuned about 100 GHz away from the center of the pressure broadened D1 transition. Optical rotation of the probe beam was monitored by using a balanced polarimeter or by using a polarimetry scheme involving a quarter-wave plate/photoelastic modulator and a crossed polarizer. In the latter case, phase sensitive detection was used. ZULF NMR transient signals were collected for 4-12 s following application of a $\sim$1 ms duration magnetic-field pulse to excite nuclear spin coherences. For the measurements presented here, 256 or fewer transients were averaged prior to Fourier transformation. The sample temperature was controlled by flowing hot air and monitored with a thermocouple.

NMR measurements were performed with bulk EG (1,2-^{13}C ethanediol from Sigma Aldrich with 1-2% water content as measured by Karl-Fischer titration) and dilutions with distilled water in a 5 mm diameter pyrex tube. The materials were used without further purification. The volume of EG was 100 μL for the undiluted sample and 50 μL for aqueous solutions. NMR tubes were sealed with parafilm to reduce evaporation and absorption of water. The spectra were obtained by Fourier transformation of the free-decay signals after cancellation of phase independent external noise (e.g., that from power lines) and subtraction of thermal-drift signals of the magnetometer. To obtain the linewidth and shift of spectral peaks, the ZULF spectra were fitted to a sum of Lorentzians.

A.3 Computational Method

The optimized structure of each of the ten conformers was obtained via energy minimization including second-order Møller-Plesset correlation energy corrections [203] and using a triple-ζ quality correlation-consistent basis set augmented with diffuse functions (MP2/aug-cc-pVTZ). Solvent reaction field of chloroform (dielectric constant ε = 4.7) and ethylene glycol (ε = 37.7) was included by means of the polarisable continuum model [204]. Electronic energies were corrected with the addition of enthalpy and entropy corrections at 298 K to obtain the Gibbs free energies. Subsequent calculations of J-couplings, also in the presence of the solvent reaction field, were run using density functional theory with the BHandH functional [205] and the pcJ-2 basis set [206], which is specifically tailored for the calculation of spin-spin couplings. All contributions to J were included: the Fermi-contact, diamagnetic and paramagnetic spin-orbit and spin-dipole terms. All calculations were run with the Gaussian09 software package [205]. Following Ref. [207], we label each structure with three letters representing the HOCC, OCCO and CCOH dihedral angles. Lower case g, g′, t indicate values around +60°, −60° and 180°, respectively, while uppercase G and T refer to the gauche or trans OCCO conformation, respectively. Figures are shown in Supporting Information. Degeneracy of the conformers was taken into account in the calculation of the population distribution and weighted average J-couplings.

A.4 Results and Discussion

The thermal variations of internuclear interactions were studied by ZULF NMR spectra of bulk ethylene glycol. Figure 1 shows ZULF NMR spectra at temperatures from 30 to 108 °C. To understand these spectra, we first note that an isolated $^{13}CH_2$ group produces a signal at $(3/2)^1J_{CH}$ [109], corresponding to ≈210 Hz. In EG, two such groups are coupled together via one-bond carbon-carbon coupling $^1J_{CC}$, a two-bond proton-carbon coupling $^2J_{CH}$, and two inequivalent three-bond proton-proton couplings $^3J_{HH,1} = J(H_1, H_3) = J(H_2, H_4)$ and $^3J_{HH,2} = J(H_1, H_4) = J(H_2, H_3)$. These additional couplings produce the rich splitting patterns shown in Fig. A.1.

The profile is in qualitative agreement with the simulation obtained from the time-evolution of the density matrix for six spin-$\frac{1}{2}$ nuclei [109] evaluated with the values of the coupling constants obtained from HF NMR [192]. The simulated J-coupling spectra at 76 °C, as shown in Fig. A.1 (b-c), were obtained using the following values: $^1J_{CH} = 141.2$ Hz, $^1J_{CC} = 40.0$ Hz, $^2J_{CH} = -2.0$ Hz, $^3J_{HH,1} = 4.0$ Hz, and $^3J_{HH,2} = 5.9$ Hz. To simulate the potential effects of slow hydroxyl proton exchange, additional simulations were performed, as shown in Fig. A.1 (d-e), using the calculated values: $^3J_{HOH} = 5.40$ Hz, $^2J_{COH} = -3.45$ Hz, $^3J_{COH} = 5.03$ Hz, $^4J_{HOH} = 0.02$ Hz, and $^5J_{(OH)(OH)} = 0.12$ Hz, with these couplings scaled by a dimensionless parameter λ ($\lambda = 0$ implies no coupling to the hydroxyl protons due to fast exchange and $\lambda = 1$ implies full coupling, as would be the case in the absence of hydroxyl exchange). Comparison between the simulations and the experimental spectra in Fig. A.1 suggests that all couplings to hydroxyl protons are averaged to zero by chemical exchange. The vicinal proton coupling,$^2J_{HH}$, has no observable effect on the spectrum [192].

As the temperature is increased beyond 90 °C, an additional doublet structure becomes apparent for each line with a splitting of 0.7 Hz. We attribute this splitting to an external magnetic field that appears due to imperfect residual-field shimming at elevated temperatures, consistent with Fig. A.1(c). Note that the linewidth of the ZULF spectra decreases with increased temperature (Fig.A.2). While the linewidth exceeds 2 Hz full width at half-maximum at room temperature, we have $\delta\nu = 0.30$ Hz at 108°C. As seen in Fig. A.2(b), $\delta\nu$ follows the viscosity [208] as a function of temperature. The narrowing with increasing temperature is likely due to enhanced molecular tumbling [184]. The linewidth may also be affected by hydroxyl proton exchange, which leads to relaxation via modulation of J-coupling frequencies, as discussed in Ref. [120]. Together with the line narrowing, the spectral intensity increases due to reduced relaxation during shuttling, reflecting an increase of the spin-lattice relaxation time.

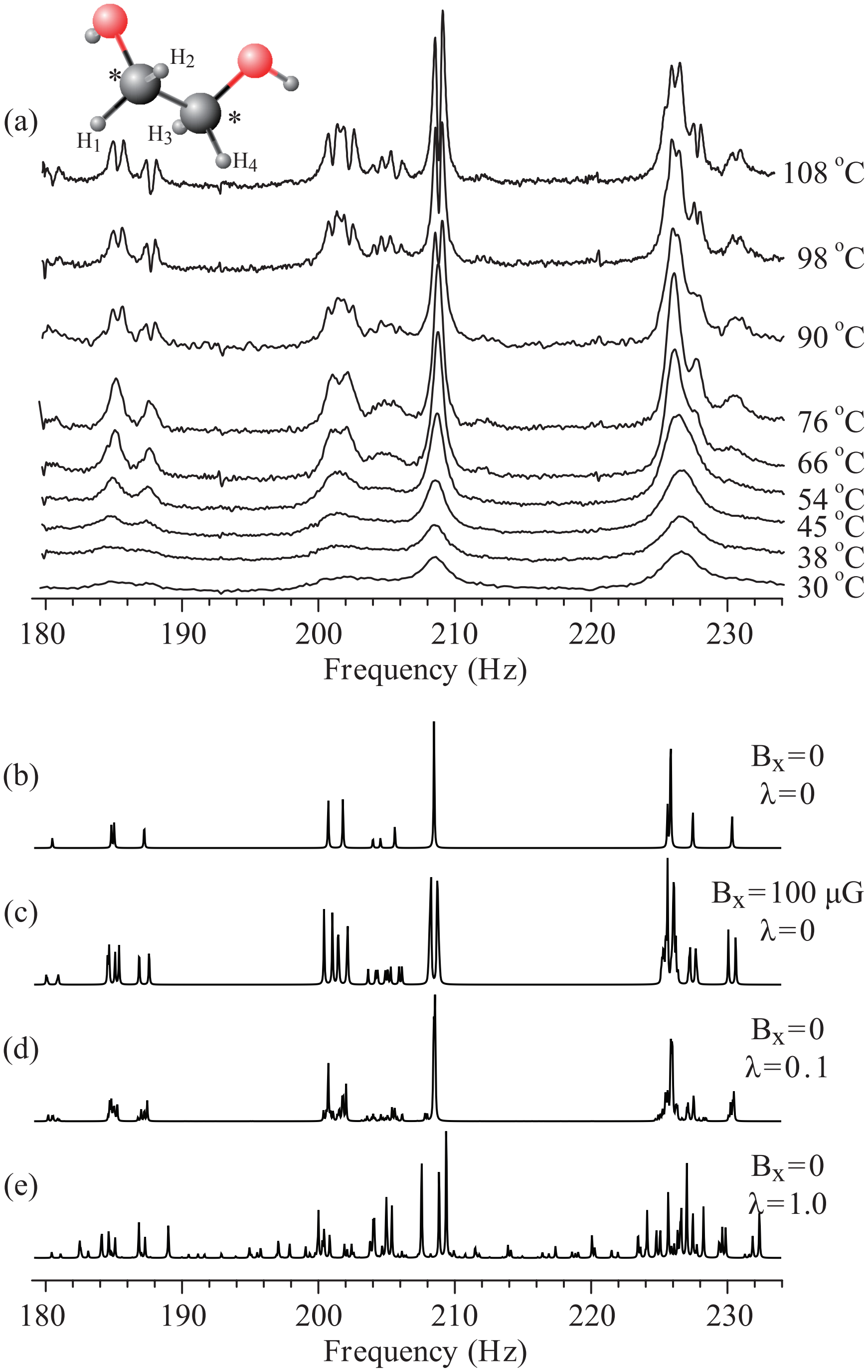

Figure A.1: (a) Temperature dependence of the ZULF-NMR spectrum of bulk $^{13}C_2$-ethylene glycol. The vertical axis is the Fourier transformed lock-in signal. The inset figure shows molecular structure of ethylene glycol (gauche conformer) where $*$ denotes ^{13}C, small spheres: H atoms; intermediate spheres: O. (b) Simulation of 76°C spectrum without couplings to hydroxyl protons at zero magnetic field. (c) Spectral simulation without couplings to hydroxyl protons in the presence of a 100 μG field. (d) Spectral simulation with couplings to hydroxyl protons scaled by $\lambda = 0.1$ at zero magnetic field. (e) Spectral simulation including full couplings to hydroxyl protons ($\lambda = 1$) at zero magnetic field. Simulated spectra are shown with narrow linewidth (extended relaxation time) in order to reveal fine structure.

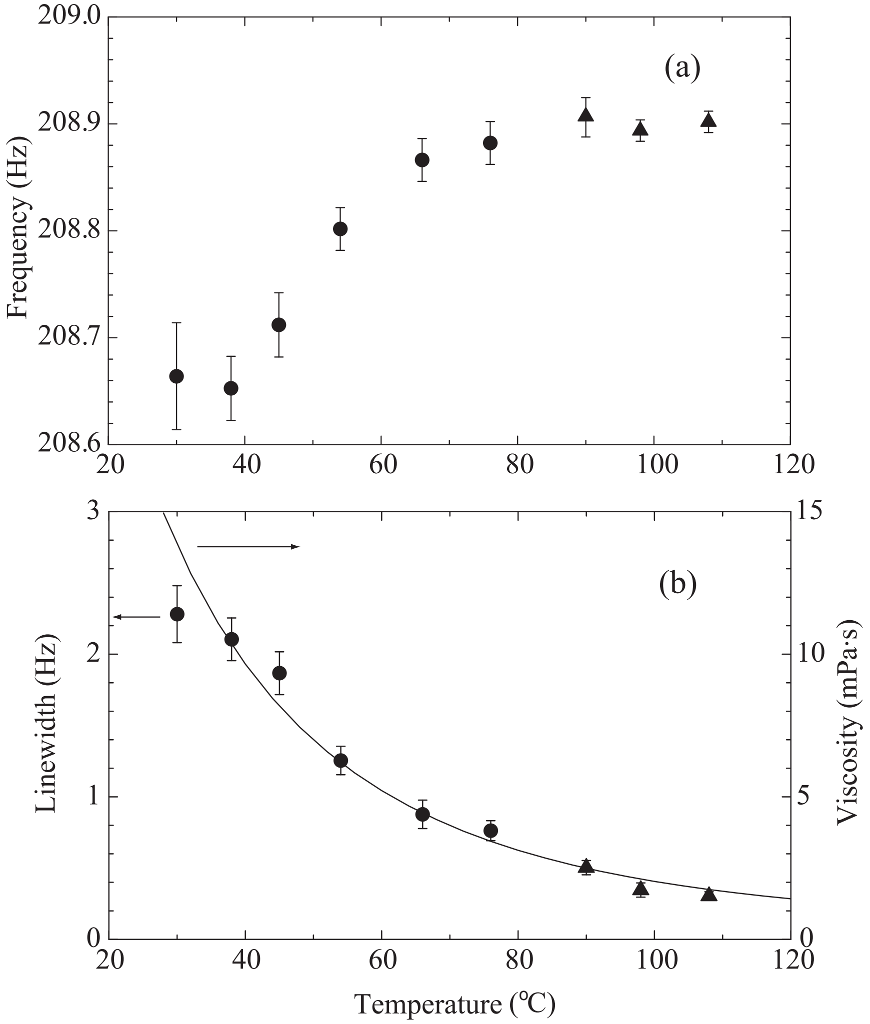

Figure A.2: (a) Central resonance frequency and (b) its linewidth plotted against temperature for bulk $^{13}C_2$-ethylene glycol. The data shown by closed triangles are obtained from fitting with two Lorentzians with the same fixed intensities for a doublet; the averaged frequency of a doublet is plotted for 90 °C and above. The solid line in (b) shows temperature dependence of viscosity, and is not a fit.

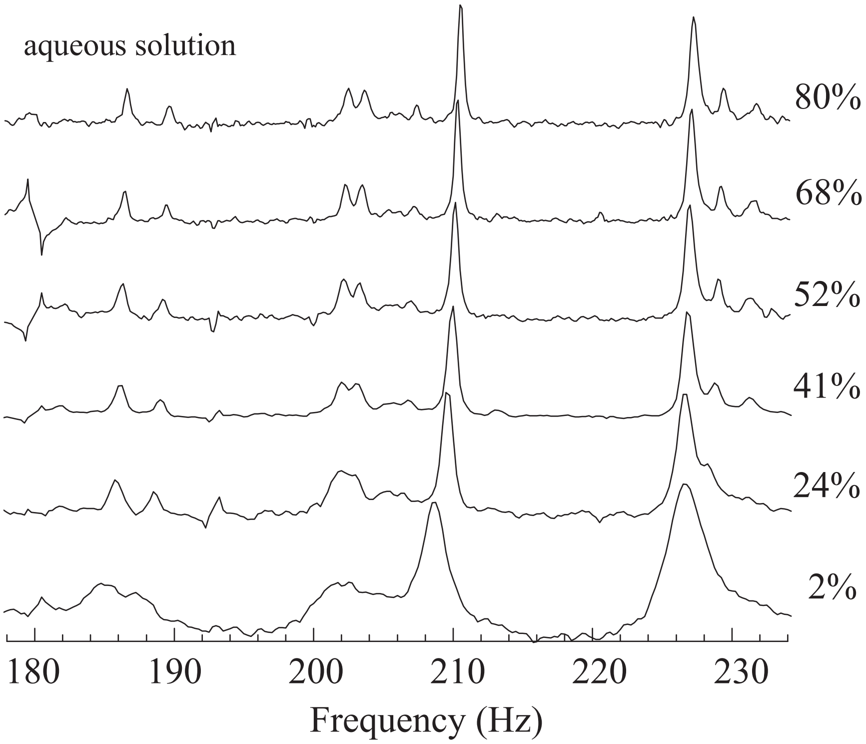

Figure A.3: ZULF NMR spectra for aqueous solutions of $^{13}C_2$-ethylene glycol as a function of water content (wt %) measured at 36°C. The intensity is normalized by the maximum intensity at each concentration.

In addition to the appearance of extra structures with increasing temperature, the spectra exhibit a slight positive shift, e.g. from 208.65(5) at 38 °C to 208.92(1) Hz at 108 °C for the central intense peak, as shown in Fig. A.2(a). The position of this peak is primarily determined by the sum of $^1J_{\mathrm{CH}}$ and $^2J_{\mathrm{CH}}$, which may provide information about the conformational equilibrium, though a rigorous means of extracting all coupling constants from the ZULF spectrum would provide stronger support.

To examine the effect of solution concentration on molecular conformation, we measured ZULF NMR for aqueous EG solutions with different concentrations, as shown in Fig. A.3. We find narrowing of ZULF NMR spectral features, similar to what is observed in the thermal variation for the bulk sample. Presumably, this reflects the reduction of the correlation time of molecular rotations with both increasing temperature and dilution, improving the averaging of the dipole-dipole interactions that broaden the lines.

Each line shows an approximately parallel shift to higher frequency with increasing water content, keeping the interval between the lines approximately constant. A parallel shift of the spectrum would indicate that the effect is due to $^1J_{\mathrm{CH}}$, though deviations from a perfectly parallel shift would indicate that effects are due to changes in $^2J_{\mathrm{CH}}$. The much larger shift [1.8 Hz between 2% and 80%, Fig. A.4(a)] compared to the thermal shift in neat EG [≈ 0.3 Hz between 40 and 110°C, Fig. A.2(a)] highlights the importance of the solvent effects.

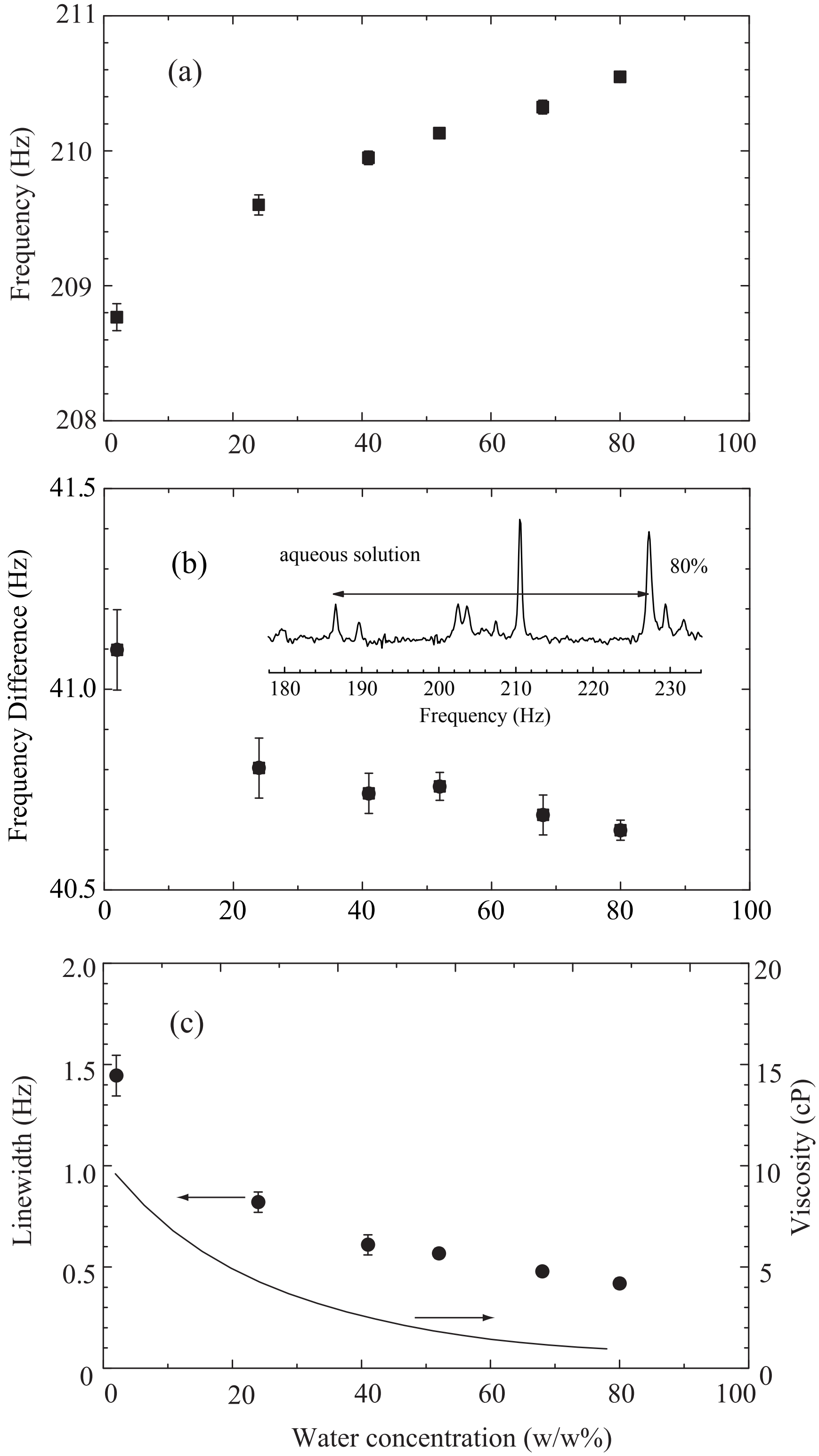

Figure A.4: (a) Central-resonance frequency, (b) multiplet width proportional to $^1J_{\mathrm{CC}}$, and (c) the central-resonance linewidth vs. the concentration of aqueous $^{13}\mathrm{C}_2$-ethylene glycol solution. The solid curve in (c) shows viscosity data for the aqueous solution [208].

Dilution with water exponentially suppresses the viscosity [Fig. A.4(c)] and also tends to replace hydrogen bonds among EG molecules with those to water. The linewidth also scales as viscosity, as observed in the temperature dependence, indicating the correlation time of molecular tumbling governs the linewidth. In contrast to the thermal variation, an offset linewidth of 0.3 Hz (the left vertical axis) remains in the scaling relation, presumably due to the effect of water protons in the infinite-dilution limit. This linewidth is substantially greater than would be attributed to magnetic field inhomogeneity or temperature gradients (approximately 0.01 Hz) [65, 67, 112], and should be primarily representative of the intrinsic spin-spin relaxation time.

A detailed understanding of the shifts towards higher frequencies observed both with increasing temperature and dilution with water would require an accurate description of the conformers' populations. Molecular-dynamics simulations would be able, in principle, to provide the full distribution of dihedral angles of EG. However, currently available classical force fields are not sufficiently accurate to describe hydrogen bonds and the associated key dihedral angles involving the OH groups (indeed, there is no generally accepted parameterization even of the OCCO angle [197, 209, 210]). On the other hand, Car-Parrinello simulations [211] are too demanding for the slow dynamics of a viscous fluid. Thus here we only attempt to provide a qualitative description.

To this end it is convenient first to examine the simpler case of EG in chloroform ($CHCl_3$), where intermolecular interactions, especially H bonds, are expected to play a negligible role. The experimental data from the literature are compared with the results of DFT calculations where the EG molecule is embedded in a continuous medium with the dielectric constant of $CHCl_3$ (see Computational Method). This case serves as a test of the performance of the theoretical level selected. We then compare the experimental data here reported with the results of DFT calculations where the dielectric constant has been set to the value in EG in order to model long range solvent effects in the neat liquid. However, explicit intermolecular H bonds cannot be fully described by this method.

The results of the calculations in chloroform are summarized in Table A.1. For each conformer there are 28 couplings which are reduced to 10 independent values because of fast rotation and/or molecular symmetry. In Table A.1, we only report the averaged values; for example $^1J_{\mathrm{CH}}$ is the average of four calculated couplings of each ^{13}C with its two protons.

In agreement with previous theoretical investigations, [207, 212] the most stable conformer is tGg′ followed by gGg′ and g′Gg′, which account for about 90% of the total. Most G conformers exhibit some intramolecular hydrogen bonding (HB), as expected for an essentially isolated molecule. The Boltzmann-averaged J values can be directly compared with those reported in [192] measured in $CDCl_3$, because this solvent is expected to have negligible HB with the solute EG. The agreement is good, especially for the couplings involving ^{13}C: the average absolute error is just 0.37 Hz, which gives us confidence on the calculated population distribution in $CHCl_3$.

Calculated couplings using the solvent reaction field of EG differ only slightly from those in $CHCl_3$; this is not unexpected because, even though the calculations include the long-range dielectric response of the environment, no explicit solvent molecules account for intermolecular HB. However, in EG, solvent intermolecular hydrogen bonds are not negligible and may change the relative conformer stability, although the experimental results in Table A.2 do not show striking differences compared with the experimental values of Table A.1.

	$^1J_{CH}$ (Hz)	$^1J_{CC}$ (Hz)	$^2J_{CH}$ (Hz)	$^3J_{HH,1}$ (Hz)	$^3J_{HH,2}$ (Hz)	Dgn.	ΔG (kcal/mol)	%Pop
g′Gg′	140.4	39.9	-1.0	3.0	6.5	2	0.28	14.8
gGg′	141.2	38.0	-1.3	3.2	6.8	4	0.36	25.9
gGg	139.4	38.0	-0.8	2.8	7.1	2	1.59	1.6
gTg′	141.5	41.1	-3.8	12.6	6.2	2	1.82	1.1
gTg	141.6	41.1	-3.8	12.6	6.1	2	1.96	0.9
tGg′	141.5	39.8	-2.0	2.9	6.7	4	0.00	47.9
tGg	139.5	40.8	-1.7	2.1	7.0	4	1.72	2.6
tGt	139.8	43.2	-2.6	1.7	6.9	2	1.45	2.1
tTg	141.9	43.6	-4.6	12.3	6.3	4	1.79	2.3
tTt	142.1	46.1	-5.3	12.0	6.3	1	1.65	0.7
$\langle J\rangle_{298K}$	141.2	39.6	-1.8	3.4	6.7			
J_{exp}	141.6	39.3	-1.6	2.6	6.4			

Table A.1: Calculated J-coupling constants for ethylene glycol conformers in chloroform. The expectation values for each coupling constant at 298K are weighted by fractional conformer populations, obtained in terms of the relative energies and degeneracies. Experimental values taken from Ref. [192]. Coupling constants involving hydroxyl protons are included in the Supporting Information.

	$^1J_{CH}$ (Hz)	$^1J_{CC}$ (Hz)	$^2J_{CH}$ (Hz)	$^3J_{HH,1}$ (Hz)	$^3J_{HH,2}$ (Hz)	Dgn.	ΔG (kcal/mol)	%Pop
g′Gg′	140.8	39.9	-1.1	2.9	6.6	2	0.30	12.2
gGg′	141.7	38.1	-1.3	3.2	6.8	4	0.20	28.6
gGg	140.0	38.6	-0.8	2.4	7.0	2	1.12	3.1
gTg′	141.9	41.2	-3.8	12.6	6.2	2	1.59	1.4
gTg	141.9	41.2	-3.8	12.5	6.1	2	1.62	1.3
tGg′	142.0	39.7	-2.0	3.0	6.7	4	0.00	40.4
tGg	140.3	40.8	-1.7	2.2	6.9	4	1.09	6.4
tGt	140.6	43.0	-2.6	1.9	6.9	2	1.06	3.4
tTg	142.1	43.5	-4.6	12.3	6.3	4	1.64	2.6
tTt	142.2	46.0	-5.3	12.1	6.3	1	1.60	0.7
$\langle J\rangle_{298K}$	141.6	39.6	-1.8	3.7	6.7			
J_{exp}	141.2	40.0	-2.0	4.0	5.9			

Table A.2: Calculated J-coupling constants for ethylene glycol conformers in ethylene glycol. The expectation values for each coupling constant at 298K are weighted by fractional conformer populations, obtained in terms of the relative energies and degeneracies. Experimental values are taken from this work. Coupling constants involving hydroxyl protons are included in the Supporting Information.

The experimental value of $^1J_{\mathrm{CH}}$ in neat EG at room temperature ($\approx$141.2 Hz) is slightly lower than in CDCl$_3$. This suggests that the population distribution in bulk EG is different from what we have calculated using EG as a solvent, and, because of intermolecular interactions, likely enriched in some conformers with low values of $^1J_{\mathrm{CH}}$, such as gGg, tGg or tGt, to remain within G conformers. The magnitude of $^2J_{\mathrm{CH}}$ is also slightly larger in neat EG than in CDCl$_3$, also likely due to stabilization of conformers with more negative values of $^2J_{\mathrm{CH}}$ due to intermolecular interactions. The variations in these values may explain the small shift towards higher frequencies as the temperature is increased because the frequency of the central resonance is, to first order, $\frac{3}{2}(^1J_{\mathrm{CH}} +^2 J_{\mathrm{CH}})$. If the conformers with smaller values of $^1J_{\mathrm{CH}}+^2J_{\mathrm{CH}}$ are more stabilized by intermolecular interactions in bulk EG, an increase in temperature would produce an increase in the average value and therefore a shift of the central resonance of the ZULF spectrum. A similar rationale may explain the even larger shift observed when EG is diluted in water, even though a precise determination of the various conformers population in EG and the exact values of their couplings, is not possible.

It is noteworthy that the C-C coupling constant is also strongly dependent on the EG conformation. As a general rule, and similarly to the $^1J_{\mathrm{CH}}$ case, we note that G conformers exhibit smaller $^1J_{\mathrm{CC}}$ couplings (38-41 Hz) while T conformers exhibit larger $^1J_{\mathrm{CC}}$ (41-45 Hz) couplings. A rough measure of the strength of this coupling is given by the width of the “multiplet” centered around $\frac{3}{2}(^1J_{\mathrm{CH}}+^2J_{\mathrm{CH}})$. As shown in Fig. A.4(b), the spectral features move slightly together with increasing dilution, indicating a decrease in $^1J_{\mathrm{CC}}$.

A.5 Conclusions and Outlook

In this work, intermolecular interactions were studied with ZULF-NMR in ethylene glycol, a prototypical viscous liquid. For a bulk sample we observed relatively broad J-coupling spectra with reduced intensity compared to low-viscosity liquids. The linewidh of the ZULF spectral features varies in the same way as viscosity does in the thermal and the aqueous concentration dependences. We observed small changes in the J-coupling constants while controlling the influence of intermolecular interactions with heating and dilution. The results are consistent with high-field NMR studies.

Overall, density functional theory calculations successfully model the conformer distribution and J-couplings in EG, provided that they are experimentally determined under conditions where intermolecular interactions are weak (i.e., in chloroform). When such interactions are strong (bulk EG or aqueous solution), we expect the population of conformer to be altered. Nevertheless, the agreement between calculations and experiment is still quite good. Therefore, the capability of accurately measuring J-couplings by ZULF-NMR, coupled with their computational predictions, can provide information on the conformer distribution.

Our results illustrate the capability of ZULF-NMR for determining molecular structures and conformations in viscous liquids with significant intermolecular interactions and fast relaxation. The linewidth of ZULF-NMR can be free from inhomogeneous fields and chemical shift anisotropy, and is thus a straightforward method for the measurement of intrinsic relaxation times.

Application of ZULF-NMR to non-liquid samples such as gels and polymers is an interesting direction for further investigation. ZULF-NMR may be particularly useful for the study of anisotropic materials, as the spin-spin interaction tensors are not truncated by large magnetic fields, allowing for the measurement of so-called "non-secular" terms. In combination with multi-dimensional and decoupling techniques, applications to more complex biologically relevant molecules are also the goals of ZULF-NMR. However, for materials with relaxation times shorter than 0.5 s, prepolarized nuclear spins become unpolarized during the shuttling process to the zero-field region. Further technical improvements (e.g., faster shuttling) will be necessary for application to solid systems with fast relaxation rates.

Appendix B

Mathematica Notebooks

B.1 Data Processing Code (Mathematica)

An early version of this notebook was developed by Micah Ledbetter, to whom the author is thoroughly indebted.

It should be noted that the command “//Rasterize” is used in several places in order to reduce the file size and to prevent PDF viewers from crashing while attempting to render the vector images. In general, these commands are not used, as vector images are preferable when preparing figures.

The data presented are for a particularly nice-looking sample of acetonitrile-2-^{13}C in a stretched polyvinyl acetate gel that did not appear in Chapter 7 because it was the only sample of its series (series 13 – sample C; the condensed label being, somewhat poetically, 13-C) to yield useful data.

ZULF NMR Data Processing

Functions (Initialize First)

```
In[1]:=
     fourpos[data_, dt_] := Module[{nerp},
       ft = 2 / Sqrt[Length[data]] Fourier[data];
       ft = Drop[ft, -Length[data] / 2];
       nuvals = Table[ 1 / (Length[data] * dt) * (j - 1), {j, 1, Length[data] / 2}];
       ft = Transpose[{nuvals, ft}]
      ]
```

```
In[2]:= cullkeepx[data_, xr_] := Module[{jmin, jmax, dx, dum, xrange},
       xrange = {Max[{xr[[1]], data[[1, 1]]}], Min[{xr[[2]], data[[Length[data], 1]]}]};
       dx = data[[2, 1]] - data[[1, 1]];
       dum = Drop[data, -Floor[(data[[Length[data], 1]] - xrange[[2]]) / dx]];
       Drop[dum, Floor[(xrange[[1]] - data[[1, 1]]) / dx]]]
```

```
In[3]:= culldelx[data_, xrange_] := Module[{jmin, jmax, dx, dum},
       dx = data[[2, 1]] - data[[1, 1]];
       jmin = Floor[(xrange[[1]] - data[[1, 1]]) / dx];
       jmax = Floor[(xrange[[2]] - data[[1, 1]]) / dx];
       dum = Drop[data, {jmin, jmax}]
      ]
```

```
In[4]:= readave[basedir_, basefname_, start_, ntrans_, dt_] := Module[{ner},
          SetDirectory[basedir <> basefname];
          fname = basefname <> "-FIDTransient";

          zeroes = "";
          Do[zeroes = zeroes <> "0", {j, 4 - StringLength[ToString[start]]}];
          name = fname <> zeroes <> ToString[start] <> ".txt";
          filenamesread = {name};
          dat = Import[name, "Table"];
          nhead = 1;
          While[nhead += 1; dat[[nhead]] ≠ {"[TransientData]"}];
          dat = Drop[dat, nhead];
          dat = Flatten[ Drop[dat, -2]];
          avedat = dat;
          If[ntrans > 1,
           Do[
            zeroes = "";
            Do[zeroes = zeroes <> "0", {j, 4 - StringLength[ToString[ind]]}];
            name = fname <> zeroes <> ToString[ind] <> ".txt";
            filenamesread = Join[filenamesread, {name}];
            dat = Import[name, "Table"];
            nhead = 1;
            While[nhead += 1; dat[[nhead]] ≠ {"[TransientData]"}];
            dat = Drop[dat, nhead];
            dat = Flatten[ Drop[dat, -2]];
            avedat = avedat + dat;
            , {ind, start + 1, start + ntrans - 1}], 0];


          avedat = avedat / ntrans;
          tvals = Table[dt * i, {i, 1, Length[dat]}];
           Transpose[{tvals, avedat}]
         ]
```

```
In[5]:= readaveND[basedir_, basefname_] := Module[{ner},

           fname = basedir <> basefname <> "\\" <> basefname <> ".txt";
           header = Import[fname, "Table"];
           nD = 0;
           np = 0;
           sr  = 0.0;
           dimpoints = {};
           For[i = 1, i <= Length[header], i++,
            If[Length[header[[i]]] < 1, Continue[]];
             If[header[[i, 1]] == "nDimensions=",
              nD = header[[i, 2]]; dimpoints = Table[0, {j, 1, nD - 1}]];
            If[header[[i, 1]] == "SamplingRate=", sr = header[[i, 2]]];
            If[header[[i, 1]] == "NPoints=", np = header[[i, 2]]];
            If[header[[i, 1]] == "IndirectDim" && nD > 0,
             dimpoints [[header[[i, 2]]]] = header[[i, 4]], Return];];

           ndData = {};
           done = True;
           step = Table[1, {j, 1, nD - 1}];
           k = 0;
           While[done,
            k += 1;
            fname  = basedir <> basefname <> "\\";
            fnamestring = "";
            For[j = 1, j < nD, j++,
             fnamestring = fnamestring <> "D" <>
                IntegerString[j, 10, 2] <> "-" <> IntegerString[step[[j]], 10, 4] <> "\\";];

            newfname = fname <> fnamestring <> "AverageFID.txt";
            dat = Import[newfname, "Table"];

            nhead = 1;
            While[dat[[nhead]] ≠ {"[FID]"}, nhead += 1];
            dat = Drop[dat, nhead];
            dat = Flatten[ Drop[dat, -2]];
            ndData = Append[ndData, dat];
            For[i = 1, i < nD, i++,
             If[step[[i]] < dimpoints[[i]],
                   step[[i]]++;
                   For[j = 1, j < i, j++, step[[j]] = 1];
               Goto["notdone"]];
                 ];
            done = False;
            Label["notdone"];
           ];

           (*This will return an array containing arrays of data. The first
            dimension is incremented first, then the next, etc. So for a 2-dimensional
             array, it goes {1, 1}, {2, 1}, {3, 1}, {4, 1}, {1, 2}, {2, 2}, {3, 2}...*)
           Return[ndData];];
```

```
In[6]:=
    average2D[arraydata_, points_] := Module[{ner},
       (*Give this an array points and it will average the second dimension*)
       np = Length[arraydata[[1]]];
       output = Table[Table[0, {i, 1, np}], {j, 1, points[[1]]}];
       For[i = 1, i <= points[[2]], i++,
                For[k = 1, k <= points[[2]], k++,
                     output[[i]] += arraydata[i + (k - 1) * points[[2]]];];
        output[[i]] /= points[[2]]; ];
       Return[output];];
```

```
In[7]:= readave2D[basedir_, basefname_, start_, ntrans_, dt_] := Module[{ner},
      fname = basedir <> basefname <> "FIDTransient";

      zeroes = "";
      Do[zeroes = zeroes <> "0", {j, 4 - StringLength[ToString[start]]}];
      name = fname <> zeroes <> ToString[start] <> ".txt";
      filenamesread = {name};
      dat = Import[name, "Table"];
      nhead = 1;
      While[nhead += 1; dat[[nhead]] ≠ {"[TransientData]"}];
      dat = Drop[dat, nhead];
      dat = Flatten[ Drop[dat, -2]];
      avedat = dat;
      If[ntrans > 1,
       Do[
        zeroes = "";
        Do[zeroes = zeroes <> "0", {j, 4 - StringLength[ToString[ind]]}];
        name = fname <> zeroes <> ToString[ind] <> ".txt";
        filenamesread = Join[filenamesread, {name}];
        dat = Import[name, "Table"];
        nhead = 1;
        While[nhead += 1; dat[[nhead]] ≠ {"[TransientData]"}];
        dat = Drop[dat, nhead];
        dat = Flatten[ Drop[dat, -2]];
        avedat = avedat + dat;
        , {ind, start + 1, start + ntrans - 1}], 0];


      avedat = avedat / ntrans;
      tvals = Table[dt * i, {i, 1, Length[dat]}];
       Transpose[{tvals, avedat}]
     ]
```

```
In[8]:= read[basedir_, basefname_, ind_, dt_] := Module[{ner},
          SetDirectory[basedir <> basefname];
          fname = basefname <> "-FIDTransient";

          zeroes = "";
          Do[zeroes = zeroes <> "0", {j, 4 - StringLength[ToString[ind]]}];
          dat = Import[fname <> zeroes <> ToString[ind] <> ".txt", "Table"];
          nhead = 1;
          While[nhead += 1; dat[[nhead]] ≠ {"[TransientData]"}];
          dat = Drop[dat, nhead];
          dat = Flatten[ Drop[dat, -2]];

          tvals = Table[dt * i, {i, 1, Length[dat]}];
           Transpose[{tvals, dat}]
         ]

In[9]:= func[a_, nu_, phi_, t_]  := a * Sin[2 * Pi * nu * t + phi]

In[10]:= submodule[data_, freq_] := Module[{dat},
          dat = data;
          pars = FindFit[dat, func[a, freq, phi, t], {{a, 0.01}, {phi, 0}}, t];
          dat[[All, 2]] = dat[[All, 2]] - func[a, freq, phi, dat[[All, 1]]] /. pars;
          dat]


In[11]:= hannwindow[j_, jmax_] = Sin[π j / (jmax)]^2
         poly[a0_, a1_, a2_, a3_, t_] = a0 + a1 * t + a2 * t^2 + a3 * t^3;
```

Out[11]= $$\mathrm{Sin}\left[\frac{\mathrm{j}\,\pi}{\mathrm{jmax}}\right]^2$$

```
In[13]:= Options[PlotAndFit] = {DoFit → True, ShowPlot → True, FitParameters → All};
         PlotAndFit[FitData_, FitFunction_, InitialParameters_, opts___] := Module[{nerp},
           If[DoFit /. {opts} /. Options[PlotAndFit],
            FP = FitParameters /. {opts} /. Options[PlotAndFit];
            If[FP === All, FP = Table[True, {Length[InitialParameters]}]];
            DummyFitVariables = Table[
              If[FP⟦i⟧, DummyVariable[i], InitialParameters⟦i⟧], {i, Length[InitialParameters]}];
            FittedParameters = DummyFitVariables /. FindFit[FitData, phasemix2[DummyFitVariables,
                x], Flatten[Table[If[FP⟦i⟧, {{DummyVariable[i], InitialParameters⟦i⟧}}, {}],
                 {i, Length[InitialParameters]}], 1], x, MaxIterations → 150],
            FittedParameters = InitialParameters
           ];
           fitpics =
            {ListPlot[FitData, Joined → True, PlotRange → All, Axes → False, Frame → True],
             Plot[FitFunction[FittedParameters, x], {x, First[FitData]⟦1⟧, Last[FitData]⟦1⟧},
              PlotStyle → RGBColor[1, 0, 0], PlotRange → All]};
           FittedParameters]


In[15]:= rotatedata[th_] := Module[{nerp},
           rotift = ift;
           rotrft = rft;
           rotift[[All, 2]] = ift[[All, 2]] * Cos[th] + rft[[All, 2]] * Sin[th];
           rotrft[[All, 2]] = -ift[[All, 2]] * Sin[th] + rft[[All, 2]] Cos[th];
          ]
```

```
In[16]:= complexLor[a_, ν0_, dν_, ϕ_, ν_] = a (I (ν - ν0) dν + dν^2) / ((ν - ν0) ^ 2 + dν^2) * Exp[I ϕ];
         Lor[a_, ν0_, dν_, ν_] = (a (ν - ν0) dν) / ((ν - ν0) ^ 2 + dν^2);
         minfunc[dat_, a_, ν0_, dν_, ϕ_, a2_, ν02_, dν2_, ϕ2_] :=
          Sum[Abs[dat[[i, 2]] - complexLor[a, ν0, dν, ϕ, dat[[i, 1]]] -
              complexLor[a2, ν02, dν2, ϕ2, dat[[i, 1]]]] ^ 2, {i, 1, Length[dat]}]
         decayfunc[a_, T1_, b_, c_, t_] = a * Exp[-t / T1] + b + c * t;
```

Calibrate Magnetometer (Requires Path to Calibration File)

```
In[20]:= (*Set directory and file name for calibration file*)

         dir = "/Users/jwblanch/Desktop/Research/ZF_Data/Birge_Calibration/";
         calfile = "calibration_3-14-14_y-xpulse.txt";


         (*Define parameters of the calibration*)

         Vtest = 1.4; (* Test signal voltage *)
         Res = 10^6; (* Test resistance *)
         αy = 0.33; (* Conversion factor (Gauss/Amp) for the test coil *)


In[23]:= SetDirectory[dir];
         (caldat = Import[dir <> calfile, "Table"]) // MatrixForm;
         (caldat = Drop[caldat, 2]) // MatrixForm;
         caldat = Drop[caldat, {18}];
         caldat = Drop[caldat, 2];
         caldat[[All, 2]] = caldat[[All, 2]] * Sqrt[2];
         caldat[[All, 3]] = caldat[[All, 3]] * Sqrt[2];
         p1 = ListPlot[caldat[[All, {1, 2}]],
            PlotStyle → RGBColor[1, 0, 0], PlotRange → All, Joined → False];
         p2 = ListPlot[caldat[[All, {1, 3}]], PlotStyle → RGBColor[0, 1, 0],
            PlotRange → All, Joined → False];
         Show[p1, p2, PlotRange → All] // Rasterize

         compcaldat = caldat[[All, {1, 2}]];
         compcaldat[[All, 2]] = compcaldat[[All, 2]] + I * caldat[[All, 3]];
```

Out[32]=

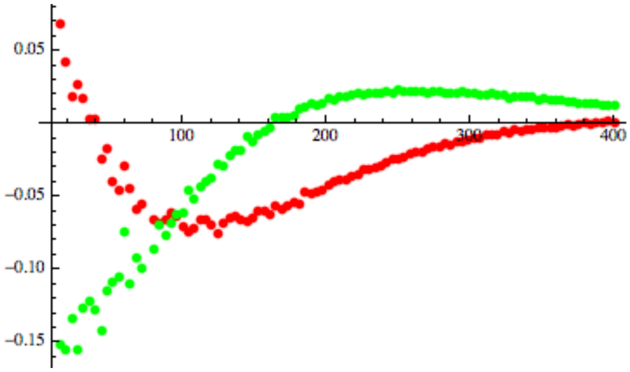

```
In[35]:= (*Now we fit the phase and magnitude of the calibration data*)

         gpars = {a → 0.08, dν → 100, ϕ → Pi, ν0 → 0, a2 → 0.08, dν2 → 100, ϕ2 → Pi, ν02 → 50};
         prange = All;
         pars = FindMinimum[minfunc[compcaldat, a, ν0, dν, ϕ, a2, ν02, dν2, ϕ2],
              {{a, a /. gpars}, {ν0, ν0 /. gpars}, {dν, dν /. gpars}, {ϕ, ϕ /. gpars}, {a2, a2 /. gpars},
               {ν02, ν02 /. gpars}, {dν2, dν2 /. gpars}, {ϕ2, ϕ2 /. gpars}}, MaxIterations → 200][[2]];
         pdr = ListPlot[Re[compcaldat], PlotStyle → RGBColor[1, 0, 0],
             PlotRange → All, Axes → False, Frame → True];
         pdi = ListPlot[Transpose[{compcaldat[[All, 1]], Im[compcaldat[[All, 2]]]}],
             PlotStyle → RGBColor[0, 0, 1], PlotRange → All];
         p = pars;
         pfr = Plot[Re[complexLor[a, ν0, dν, ϕ, ν] + complexLor[a2, ν02, dν2, ϕ2, ν] /. p],
             {ν, Min[compcaldat[[All, 1]]], Max[compcaldat[[All, 1]]]},
             PlotRange → All, PlotStyle → {RGBColor[1, 0, 0], Dashed}];
         pfi = Plot[Im[complexLor[a, ν0, dν, ϕ, ν] + complexLor[a2, ν02, dν2, ϕ2, ν] /. p],
             {ν, Min[compcaldat[[All, 1]]], Max[compcaldat[[All, 1]]]},
             PlotRange → All, PlotStyle → {RGBColor[0, 0, 1], Dashed}];
         Show[pdr, pfr, pdi, pfi] // Rasterize
         phase[ν_] = ArcTan[Re[complexLor[a, ν0, dν, ϕ, ν] + complexLor[a2, ν02, dν2, ϕ2, ν]],
              Im[complexLor[a, ν0, dν, ϕ, ν] + complexLor[a2, ν02, dν2, ϕ2, ν]]] /. pars;
         phasecor[ν_] = Exp[-I phase[ν]] /. pars;
         mag[ν_] = Abs[complexLor[a, ν0, dν, ϕ, ν] + complexLor[a2, ν02, dν2, ϕ2, ν] /. pars];

         magcal[nu_] = 10^6 * Vtest / Res * αy / mag[nu];
```

```
FindMinimum ::cvmit : Failed to converge to the requested accuracy or precision within 200 iterations . >>
```

Out[43]=

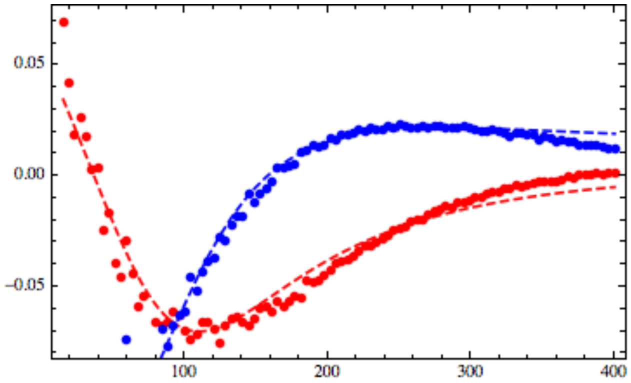

```
In[48]:= Plot[magcal[nu], {nu, 0, 400}, Frame → True,
           Axes → False, FrameLabel → {"Frequency (Hz)", "μG/Volt"}] // Rasterize
```

Out[48]=

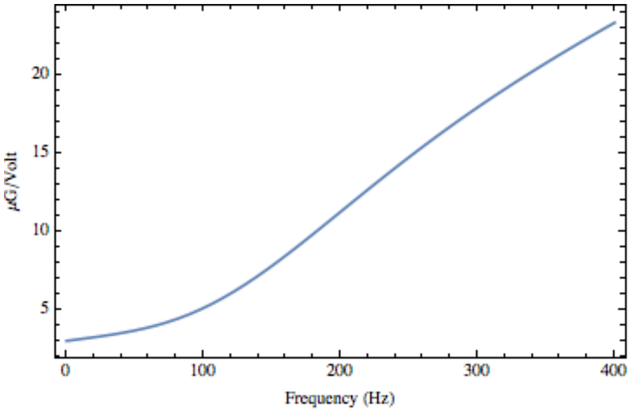

```
In[49]:=
         (*This polynomial fit doesn't usually work,
         but may be useful if the normal calibration approach fails*)


         (*
         poly[a0_,a1_,a2_,a3_,a4_,a5_,nu_] =a0+a1*nu+a2*nu^2+a3 nu^3+a4 nu^4+a5 nu^5;

           phasedat = Transpose[{caldat[[All,1]],ArcTan[caldat[[All,2]],caldat[[All,3]]]}];
           phasedat[[All,2]] = Mod[phasedat[[All,2]]-1*Pi,2Pi];
           polypars = FindFit[phasedat,
             poly[a0,a1,a2,a3,a4,a5,nu],{{a0,5},{a1,1},{a2,1},{a3,1},{a4,1},{a5,1}},nu]
           phasepoly[nu_] = poly[a0,a1,a2,a3,a4,a5,nu]/.polypars;

           magdat = Transpose[{caldat[[All,1]],Sqrt[caldat[[All,2]]^2+caldat[[All,3]]^2]}];
           pplot=ListPlot[phasedat,PlotRange→All,Axes→False,
           Frame→True,FrameLabel→{"Frequency (Hz)","Phase (rad)"}];
         mplot = ListPlot[magdat,PlotRange→All,Axes→False,Frame→True,
           FrameLabel→{"Frequency (Hz)","Signal (V)"}];

         pfit = Plot[phase[ν],{ν,0,400},Axes→False,Frame→True,PlotStyle→Red];
         mfit = Plot[mag[ν],{ν,0,400},Axes→False,Frame→True,PlotStyle→Red];
         polyplot =
          Plot[phasepoly[ν],{ν,0,400},Axes→False,Frame→True,PlotStyle→Green,PlotRange→All];

         GraphicsArray[{Show[pplot,pfit,polyplot],Show[mplot,mfit]}]*)
```

Importing Non-Averaged Data From Paul’s Code

```
fitparshigh = {};
fitparslow = {};
datsum = {};

basedir = "/Users/jwblanch/Desktop/Research/ZF_DATA/2014Mar26/";

SetDirectory[basedir]

/Users/jwblanch/Desktop/Research/ZF_Data/2014Mar06
```

```
start = 1;
naves = 1024;
basefname = "AcCN_in_PvAc_17E_xPulse_0000";
data = readave[basedir, basefname, start, naves, 1 / 2000.];

(* And for future convenience, let's just export the
  averaged data as a table that can be read by the next section... *)

Export[
  "/Users/jwblanch/Desktop/Research/ZF_DATA/2014Mar26/AcCN_in_PvAc_17E_xPulse_1024scans.
    txt", data, "Table"];
```

Importing Data as a Table

```
In[50]:= (*Note that the data must be in the form of a two-
          column table with the time value in the first column and the voltage reading in the
           second column. Other data formats must first be converted into this format.*)

         data = Import[
            "/Users/jwblanch/Desktop/Research/ZF_DATA/2013Oct15/acetonitrile_PVAc-13C_014uA_128
              scans.txt", "Table"];
```

Processing

```
In[51]:= (*Plot the raw data to make sure there are no major issues*)
         ListLinePlot[data, PlotRange → All] // Rasterize
```

Out[51]=

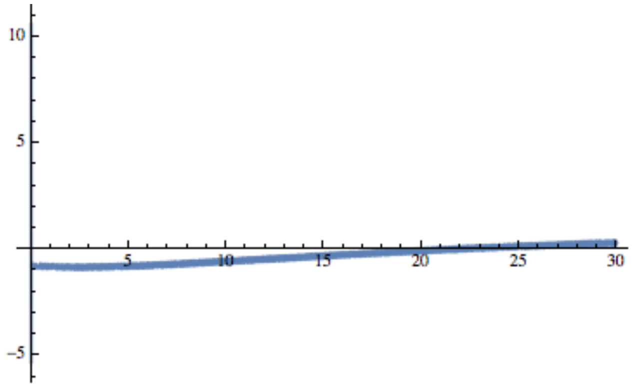

```
In[52]:= (* Backwards Prediction *)


         (*Use this to drop garbage data points from the
          beginning of your data set. Not generally necessary. *)
         dat = Drop[data, 000];


         (*Set the number of points to remove and replace by backwards prediction*)
         replace = 40;

         (*Set the number of points upon which to base the backwards predictin*)
         samplepoints = 500;
```

```
dat1 = Drop[dat, -(Length[dat] - samplepoints)];
ddat = Drop[dat1, replace];
p1 = ListLinePlot[ddat];

(*Big fitting function*)
func[a0_, a1_, a2_, b0_, b1_, b2_, b3_, b4_, b5_, b6_, b7_, b8_, b9_, b10_,
   nu0_, nu1_, nu2_, nu3_, nu4_, nu5_, nu6_, nu7_, nu8_, nu9_, nu10_, phi0_,
   phi1_, phi2_, phi3_, phi4_, phi5_, phi6_, phi7_, phi8_, phi9_, phi10_, t_] =
  a0 + a1 * t + a2 * t^2 + b0 Sin[2 * Pi * nu0 t + phi0] + b1 * Sin[2 * Pi * nu1 * t + phi1] +
   b2 * Sin[2 * Pi * nu2 * t + phi2] + b3 * Sin[2 * Pi * nu3 * t + phi3] +
   b4 * Sin[2 * Pi * nu4 * t + phi4] + b5 * Sin[2 * Pi * nu5 * t + phi5] + b6 *
    Sin[2 * Pi * nu6 * t + phi6] + b7 * Sin[2 * Pi * nu7 * t + phi7] + b8 * Sin[2 * Pi * nu8 * t + phi8] +
   b9 * Sin[2 * Pi * nu9 * t + phi9] + b10 * Sin[2 * Pi * nu10 * t + phi10];

(*Here we store the fit as the variable "pars". It may be
 necessary to vary the initial guesses for frequenies, phases, etc.*)
pars = FindFit[ddat, func[a0, a1, a2, b0, b1, b2, b3, b4, b5, b6,
    b7, b8, b9, b10, nu0, nu1, nu2, nu3, nu4, nu5, nu6, nu7, nu8, nu9, nu10,
    phi0, phi1, phi2, phi3, phi4, phi5, phi6, phi7, phi8, phi9, phi10, t],
   {
    (*********Here is where we set the intitial guesses for fitting***********)
    {a0, -1},
    {a1, 0},
    {a2, 0},
    {b0, 0.0},
    {b1, 0.0},
    {b2, 0.0},
    {b3, 0.0},
    {b4, 0.0},
    {b5, 0.0},
    {b6, 0.0},
    {b7, 0.0},
    {b8, 0.0},
    {b9, 0.0},
    {b10, 0.0},
    {nu0, 8},
    {nu1, 12},
    {nu2, 60},
    {nu3, 180},
    {nu4, 134},
    {nu5, 136},
    {nu6, 240},
    {nu7, 267},
    {nu8, 269},
    {nu9, 273},
    {nu10, 300},
    {phi0, 4},
    {phi1, 4},
    {phi2, 4},
    {phi3, 04},
    {phi4, 04},
    {phi5, 04},
    {phi6, 04},
    {phi7, 04},
    {phi8, 01},
    {phi9, 4},
    {phi10, 4}},
```

```
   t, MaxIterations → 3000];
p2 =
  Plot[func[a0, a1, a2, b0, b1, b2, b3, b4, b5, b6, b7, b8, b9, b10, nu0, nu1, nu2, nu3, nu4,
     nu5, nu6, nu7, nu8, nu9, nu10, phi0, phi1, phi2, phi3, phi4, phi5, phi6, phi7, phi8, phi9,
     phi10, t] /. pars, {t, 0, Max[ddat[[All, 1]]]}, PlotStyle → Red];


(*Now we plot a comparison of the data and the backwards prediction fit*)
Show[p1, p2, PlotRange → All] // Rasterize


(*Now we replace the removed points with the backwards predicted points,
forming a new data set, "extdat"*)
extdat = dat;
extdat[[1 ;; replace, 2]] =
  func[a0, a1, a2, b0, b1, b2, b3, b4, b5, b6, b7, b8, b9, b10, nu0, nu1, nu2,
    nu3, nu4, nu5, nu6, nu7, nu8, nu9, nu10, phi0, phi1, phi2, phi3, phi4, phi5,
    phi6, phi7, phi8, phi9, phi10, extdat[[1 ;; replace, 1]]] /. pars;
```

```
FindFit ::sszero :
 The step size in the search has become less than the tolerance prescribed by the PrecisionGoal option , but
     the gradient is larger than the tolerance specified by the AccuracyGoal option . There
     is a possibility that the method has stalled at a point that is not a local minimum . >>
```

Out[61]=

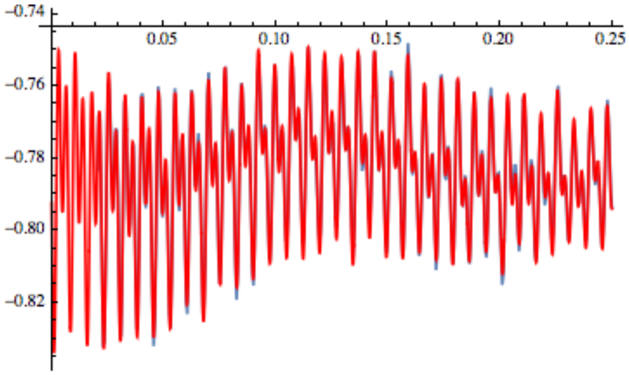

```
In[64]:= (*Background/Drift Correction*)


         Clear[T2]
         dat30 = extdat;


         (*This is a ridiculous fitting function that seems to work most of the time. Better
          fits can sometimes be obtained by altering the order of the polynomial terms.*)
         polyn[a0_, a1_, a2_, a3_, a4_, a5_, a6_, a7_, a8_, ν_, ϕ_, T2_, b0_, t_] =
           a0 + a1 * t + a2 * t^2 + a3 * t^3 + a4 * t^4 + a5 * t^5 +
            (a6 + a7 * t + a8 * t^2 + 0 * t^3 + 0 * t^4 + 0 * t^5 + 0 * t^6) * Exp[-t / T2] * b0 * Sin[2 Pi * ν * t + ϕ] +
            0 * Sin[2 Pi * 180 * t + ϕ];
         cpars = FindFit[dat30, polyn[a0, a1, a2, a3, a4, a5, a6, a7, a8, ν, ϕ, T2, b0, t],
           {{a0, 1}, {a1, 1}, {a2, 1}, {a3, 1}, {a4, 1}, {a5, 1}, {a6, 1}, {a7, 1},
            {a8, 1}, {ν, .1}, {ϕ, 4}, {T2, 8}, {b0, 1}}, t, MaxIterations → 50]
         p1 = ListPlot[dat30, Joined → True, PlotRange → All, Frame → True,
            FrameLabel → {"Time (s)", "Signal (V)"}, Axes → False];
         p2 = Plot[polyn[a0, a1, a2, a3, a4, a5, a6, a7, a8, ν, ϕ, T2, b0, t] /. cpars,
            {t, 0.01, Length[dat30] / 2000.}, PlotStyle → RGBColor[1, 0, 0], PlotRange → All];
         Show[p1, p2] // Rasterize


         (*We now perform the background/drift correction,
         producing a new data set called "subdat"*)
         subdat = extdat;
         subdat[[All, 2]] = subdat[[All, 2]] -
             polyn[a0, a1, a2, a3, a4, a5, a6, a7, a8, ν, ϕ, T2, b0, extdat[[All, 1]]] /. cpars;
         ListLinePlot[subdat[[1 ;; Length[subdat]]], PlotRange → All] // Rasterize

         subdat2 = subdat;

         FindFit ::cvmit : Failed to converge to the requested accuracy or precision within 50 iterations . ≫

Out[67]= {a0 → -0.775376, a1 → -0.05067, a2 → 0.0128537, a3 → -0.000758237,
          a4 → 0.0000212406, a5 → -2.35235 × 10^-7, a6 → -0.000533617, a7 → 0.0000197298,
          a8 → 5.47645 × 10^-8, ν → 0.185743, ϕ → 7.83355, T2 → -4.74446, b0 → -0.271567}
```

Out[70]=

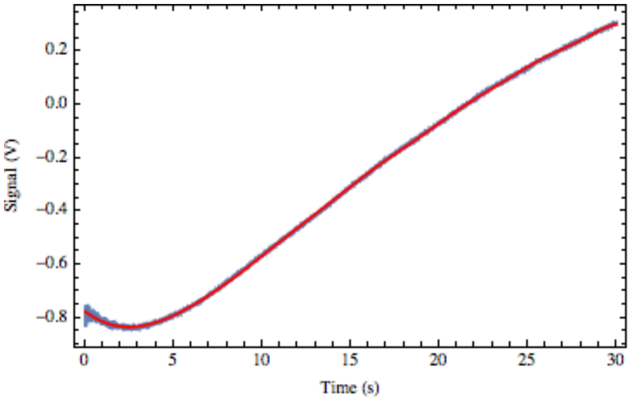

Out[73]=

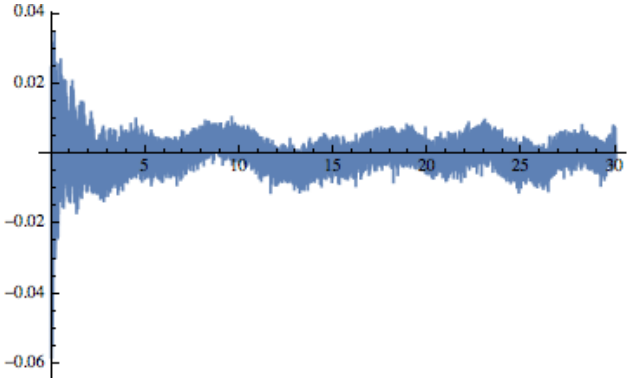

In[75]:=

```
(* Exponential Apodization *)

(*Line-broadening is achieved by multiplying by a
  decaying exponential. May be varied by varying the value of "lb"*)
lb = 0.1;

subdat2[[All, 2]] = subdat[[All, 2]] * Exp[-subdat[[All, 1]] * lb];
ListLinePlot[subdat2, PlotRange → All] // Rasterize
```

Out[77]=

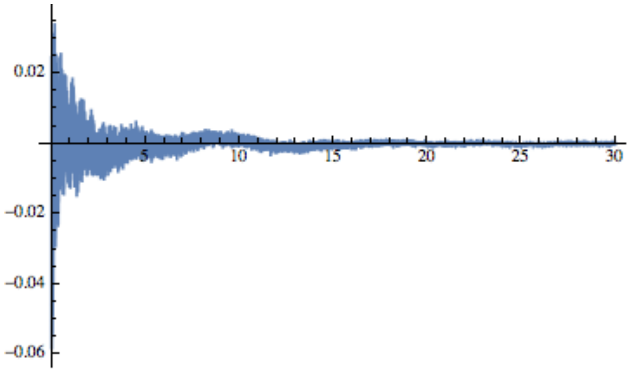

In[78]:=

```
(* Zero-Filling *)
zeros = Table[{Length[subdat2] / 2000. + j * 1 / 2000., 0}, {j, 1, Length[extdat] * 4}];
subdat = Join[subdat2, zeros];
```

```
In[80]:= (* Fourier Transform *)
         prange = All;
         tstart = (1 / 2000.) * 00;


         (*Plot window is defined in Hz, between "leftlimit" and "rightlimit"*)
         leftlimit = 1;
         rightlimit = 300;


         (*Overall phase may be adjusted by varying "th"*)
         th = -0.5;



         ft = fourpos[subdat[[All, 2]], subdat[[2, 1]] - subdat[[1, 1]]];
         ftcor = cullkeepx[ft, {leftlimit, rightlimit}];
         Do[ftcor [[i, 2]] =
             ftcor[[i, 2]] * Exp[I th] * magcal[ftcor[[i, 1]]] * Exp[I 2 * Pi * tstart ftcor[[i, 1]]] *
              Exp[I * phase[ftcor[[i, 1]]]] * 100 000, {i, 1, Length[ftcor]}];
         SetOptions[ListPlot, Joined → True, PlotRange → All, Frame → True, Axes → False,
           FrameLabel → {"Frequency (Hz)", "Signal (fT)"}, PlotRange → prange];


         (*The real spectrum, pdr, is plotted by default. Imaginary and absolute
          value spectra are also available as "pdi" and "pda", respectively.*)

         pdr = ListPlot[Re[ftcor], PlotStyle → RGBColor[1, 0, 0],
             PlotRange → prange, AspectRatio → .4, ImageSize → 625] // Rasterize
         pdi = ListPlot[Transpose[{ftcor[[All, 1]], Im[ftcor[[All, 2]]]}],
             PlotStyle → RGBColor[0, .5, 1], PlotRange → prange, AspectRatio → 0.4, ImageSize → 625];
         pda = ListPlot[Abs[ftcor], PlotStyle → RGBColor[0, 0, 0],
             PlotRange → prange, AspectRatio → 0.4, ImageSize → 625];
```

Out[89]=

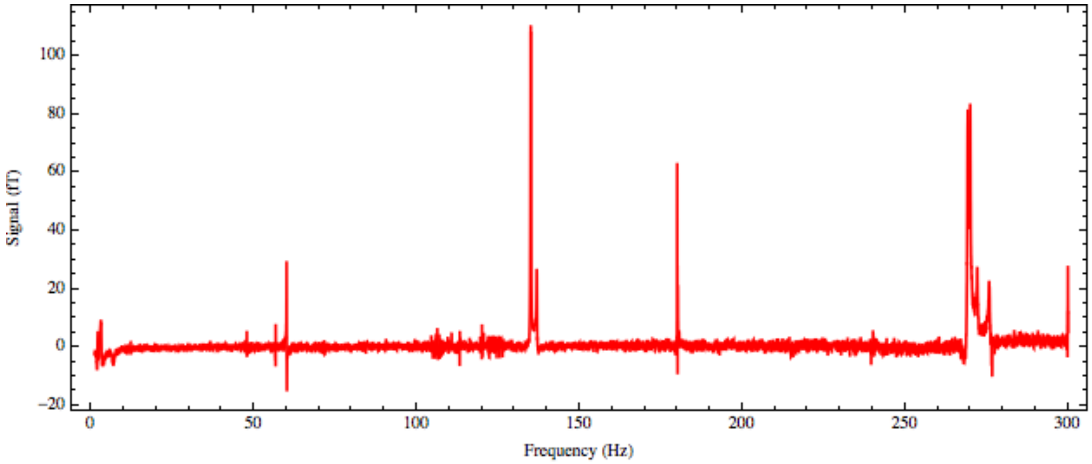

Fitting to 2 Complex Lorentzians

```
In[92]:= (*We begin by reinitializing the full spectrum
          (or at least a sufficiently large portion of it...)*)
```

```
th = -0.5;
ft = fourpos[subdat[[All, 2]], subdat[[2, 1]] - subdat[[1, 1]]];
ftcor = cullkeepx[ft, {0, 300}];

Do[ftcor [[i, 2]] =
   ftcor[[i, 2]] * Exp[I th] * magcal[ftcor[[i, 1]]] * Exp[I 2 * Pi * tstart ftcor[[i, 1]]] *
     Exp[I * phase[ftcor[[i, 1]]]] * 100 000 + 0.00, {i, 1, Length[ftcor]}];



(*The fitting window is defined in Hz between "fitleft" and "fitright"*)
fitleft = 132;
fitright = 140;


ft1j = cullkeepx[ftcor, {fitleft, fitright}];

(*To fit to a sum of two complex Lorentzians, we use the function "minfunc2"*)
minfunc2[dat_, a_, ν0_, dν_, ϕ_, a2_, nu2_, dν2_, ϕ2_] :=
 Sum[Abs[dat[[i, 2]] - complexLor[a, ν0, dν, ϕ, dat[[i, 1]]] -
     complexLor[a2, nu2, dν2, ϕ2, dat[[i, 1]]] - 0.0000]^2, {i, 1, Length[dat]}]



(*As before, we store the fit values to "pars" -
 careful selection of starting parameters is often essential here! *)

dum = ft1j;
pars = FindMinimum[minfunc2[dum, a, ν0, dν, ϕ, a2, nu2, dν2, ϕ2],
    {
     (******* Here we define the starting guesses for the fitting function *********)
     {a, 5}, {ν0, 134.75}, {dν, 0.1}, {ϕ, 0},
     {a2, 1}, {nu2, 136.9}, {dν2, .1}, {ϕ2, 0.6}},
    MaxIterations → 500][[2]];




(*Now we plot the fits along with the data for comparison*)
SetOptions[ListPlot, Joined → True, PlotRange → All, Frame → True,
  Axes → False, FrameLabel → {"Frequency (Hz)", "Signal (fT)"}, ImageSize → 300];

pdr = ListPlot[Re[dum], PlotStyle → RGBColor[0, 0, 0]];
pdi =
  ListPlot[Transpose[{dum[[All, 1]], Im[dum[[All, 2]]]}], PlotStyle → RGBColor[0, 0, 0]];
pfr = Plot[Re[complexLor[a, ν0, dν, ϕ, ν] + complexLor[a2, nu2, dν2, ϕ2, ν] + 0.0000 /. pars],
   {ν, Min[dum[[All, 1]]], Max[dum[[All, 1]]]},
   PlotRange → All, PlotStyle → RGBColor[1, 0, 0]];
pfi = Plot[Im[complexLor[a, ν0, dν, ϕ, ν] + complexLor[a2, nu2, dν2, ϕ2, ν] + 0.0000 /. pars],
   {ν, Min[dum[[All, 1]]], Max[dum[[All, 1]]]},
   PlotRange → All, PlotStyle → RGBColor[1, 0, 0]];


GraphicsGrid[{{Show[pdr, pfr], Show[pdi, pfi]}}] // Rasterize

( "a₁="  a   {}  "ν₁="  ν0   "Δν₁="  dν   {}  "ϕ₁="  ϕ  )
( "a₂="  a2  {}  "ν₂="  nu2  "Δν₂="  dν2  {}  "ϕ₂="  ϕ2 ) /. pars // TableForm
```

```
FindMinimum ::sszero :
  The step size in the search has become less than the tolerance prescribed by the PrecisionGoal option ,
      but the gradient is larger than the tolerance specified by the AccuracyGoal option . There
      is a possibility that the method has stalled at a point that is not a local minimum . ≫
```

Out[107]=

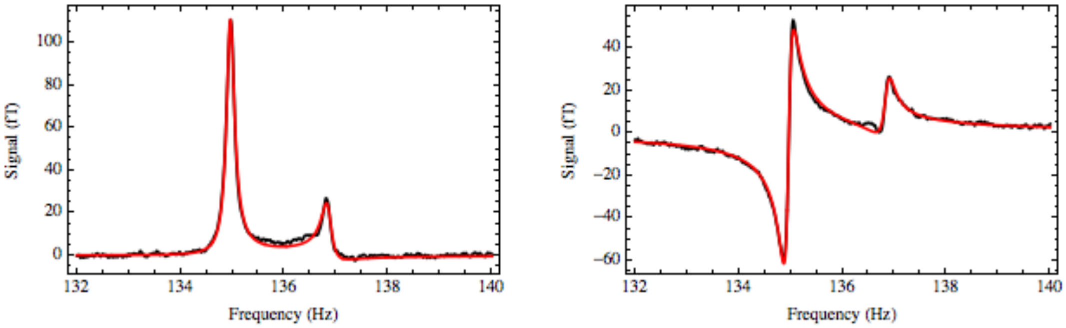

```
Out[108]//TableForm=
     a₁=    -110.01       ν₁=    134.953    Δν₁=    0.0949723       ϕ₁=    -15.7991
     a₂=    26.1688       ν₂=    136.846    Δν₂=    0.119616        ϕ₂=    13.174
```

Fitting to 3 Complex Lorentzians

```
In[439]:= (*We begin by reinitializing the full spectrum
           (or at least a sufficiently large portion of it...)*)

          th = -0.5;
          ft = fourpos[subdat[[All, 2]], subdat[[2, 1]] - subdat[[1, 1]]];
          ftcor = cullkeepx[ft, {0, 300}];

          Do[ftcor [[i, 2]] =
             ftcor[[i, 2]] * Exp[I th] * magcal[ftcor[[i, 1]]] * Exp[I 2 * Pi * tstart ftcor[[i, 1]]] *
               Exp[I * phase[ftcor[[i, 1]]]] * 100 000 + 0.00, {i, 1, Length[ftcor]}];



          (*The fitting window is defined in Hz between "fitleft" and "fitright"*)
          fitleft = 132;
          fitright = 140;


          ft1j = cullkeepx[ftcor, {fitleft, fitright}];

          (*To fit to a sum of three complex Lorentzians, we use the function "minfunc3"*)
          minfunc3[dat_, a_, ν0_, dν_, ϕ_, a2_, nu2_, dν2_, ϕ2_, a3_, nu3_, dν3_, ϕ3_] :=
           Sum[Abs[dat[[i, 2]] -
               complexLor[a, ν0, dν, ϕ, dat[[i, 1]]] - complexLor[a2, nu2, dν2, ϕ2, dat[[i, 1]]] -
               complexLor[a3, nu3, dν3, ϕ3, dat[[i, 1]]] - 0.0000]^2, {i, 1, Length[dat]}]



          (*As before, we store the fit values to "pars" -
           careful selection of starting parameters is often essential here! *)

          dum = ft1j;
          pars = FindMinimum[minfunc3[dum, a, ν0, dν, ϕ, a2, nu2, dν2, ϕ2, a3, nu3, dν3, ϕ3],
```

```
        {
         (******* Here we define the starting guesses for the fitting function *********)
         {a, 5}, {ν0, 134.75}, {dν, 0.1}, {ϕ, 0},
         {a2, 1}, {nu2, 136.25}, {dν2, .1}, {ϕ2, 3.4},
         {a3, 2}, {nu3, 136.9}, {dν3, 0.3}, {ϕ3, 1.7}},
        MaxIterations → 500][[2]];
```

```
(*Now we plot the fits along with the data for comparison*)
SetOptions[ListPlot, Joined → True, PlotRange → All, Frame → True,
  Axes → False, FrameLabel → {"Frequency (Hz)", "Signal (fT)"}, ImageSize → 300];

pdr = ListPlot[Re[dum], PlotStyle → RGBColor[0, 0, 0]];
pdi =
  ListPlot[Transpose[{dum[[All, 1]], Im[dum[[All, 2]]]}], PlotStyle → RGBColor[0, 0, 0]];
pfr = Plot[Re[complexLor[a, ν0, dν, ϕ, ν] + complexLor[a2, nu2, dν2, ϕ2, ν] +
      complexLor[a3, nu3, dν3, ϕ3, ν] + 0.0000 /. pars],
   {ν, Min[dum[[All, 1]]], Max[dum[[All, 1]]]}, PlotRange → All,
   PlotStyle → RGBColor[1, 0, 0]];
pfi = Plot[Im[complexLor[a, ν0, dν, ϕ, ν] + complexLor[a2, nu2, dν2, ϕ2, ν] +
      complexLor[a3, nu3, dν3, ϕ3, ν] + 0.0000 /. pars],
   {ν, Min[dum[[All, 1]]], Max[dum[[All, 1]]]}, PlotRange → All,
   PlotStyle → RGBColor[1, 0, 0]];


GraphicsGrid[{{Show[pdr, pfr], Show[pdi, pfi]}}] // Rasterize

⎛"a₁="  a  {} "ν₁=" ν0  "Δν₁=" dν  {} "ϕ₁=" ϕ ⎞
⎜"a₂=" a2  {} "ν₂=" nu2 "Δν₂=" dν2 {} "ϕ₂=" ϕ2⎟ /. pars // TableForm
⎝"a₃=" a3  {} "ν₃=" nu3 "Δν₃=" dν3 {} "ϕ₃=" ϕ3⎠
```

```
FindMinimum ::cvmit : Failed to converge to the requested accuracy or precision within 500 iterations . ≫
```

Out[454]=

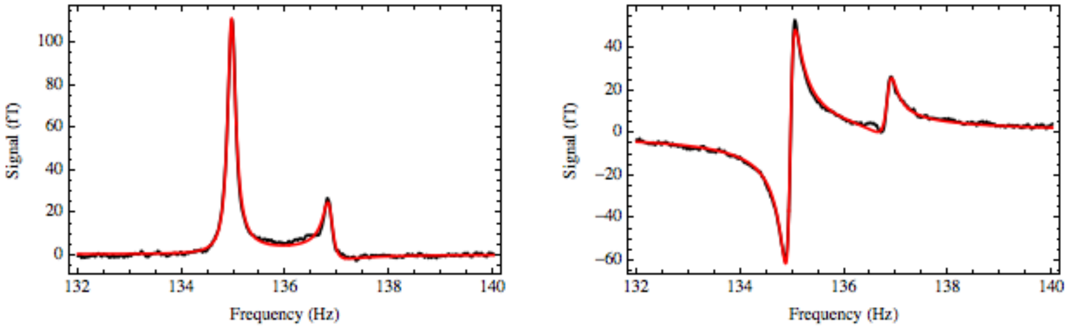

Out[455]//TableForm=

```
a₁=   109.988       ν₁=   134.953   Δν₁=   0.094107     ϕ₁=   -6.37323
a₂=   -0.610759     ν₂=   142.677   Δν₂=   -22.3736     ϕ₂=   2.63154
a₃=   26.2292       ν₃=   136.849   Δν₃=   0.116145     ϕ₃=   0.636766
```

B.2 Simulation Code (Mathematica)

Micah Ledbetter was the author of an early version of this notebook, as well.

ZULF NMR J-Spectrum Simulation

Define Spin System

```
In[1]:= (* Number of spins in calculation *)
        hbar = 6.5 × 10^-16 (* eV s *);
        kT = 1 / 40 / (6.5 × 10^-16);
        γh = 2 Pi * 4257.7;
        γc = 2 Pi * 1070.8;

        Nspins = 7;
```

```
In[6]:= (* Jnetwork for benzaldehyde

         Schaefer, T.
         Can. J. Chem. Vol. 67, 1989
          "A Positive 6J(H,CHO)in some meta derivatives of benzaldehyde. A simple model"

          nJCH for n=3,4,5 unknown

        *)

        jnet = Table[0, {i, 1, Nspins}, {j, 1, Nspins}];

        J1CH := 174.85 * 2 * Pi
        J3CH := 4.92 * 2 * Pi
        J4CH := 0.72 * 2 * Pi
        J5CH := 0.69 * 2 * Pi
        J23  := 7.695 * 2 Pi
        J24  := 1.333 * 2 * Pi
        J25  := 0.624 * 2 * Pi
        J26  := 1.738 * 2 * Pi
        J34 := 7.443 * 2 * Pi
        J35 := 1.236 * 2 * Pi
        J4H := -0.152 * 2 * Pi
        J5H := 0.431 * 2 * Pi
        J6H := -0.018 * 2 * Pi

        jnet[[1, 2]] = J3CH;
        jnet[[1, 3]] = J4CH;
        jnet[[1, 4]] = J5CH;
        jnet[[1, 5]] = J4CH;
        jnet[[1, 6]] = J3CH;
        jnet[[1, 7]] = J1CH;

        jnet[[2, 3]] = J23;
        jnet[[2, 4]] = J24;
        jnet[[2, 5]] = J25;
        jnet[[2, 6]] = J26;
        jnet[[2, 7]] = J4H;
```

```
jnet[[3, 4]] = J34;
jnet[[3, 5]] = J35;
jnet[[3, 6]] = J25;
jnet[[3, 7]] = J5H;

jnet[[4, 5]] = J34;
jnet[[4, 6]] = J24;
jnet[[4, 7]] = J6H;

jnet[[5, 6]] = J23;
jnet[[5, 7]] = J5H;

jnet[[6, 7]] = J4H;

jnet // MatrixForm

(* Set up J-coupling and gamma networks *)

gamma := {γc, γh, γh, γh, γh, γh, γh}
(Jnet := jnet)
γ1 = γh;
γ2 = γc;
```

```
Out[41]//MatrixForm=
 0  30.9133  4.52389  4.3354   4.52389  30.9133   1098.61
 0    0      48.3491  8.37549  3.92071  10.9202  -0.955044
 0    0        0      46.7657  7.76602  3.92071   2.70805
 0    0        0        0      46.7657  8.37549  -0.113097
 0    0        0        0        0      48.3491   2.70805
 0    0        0        0        0        0      -0.955044
 0    0        0        0        0        0         0
```

Initializes functions to generate spin-matrices, Hamiltonians, Rotation matrices.

```
In[46]:= imax = 2^Nspins;

In[47]:= σ = {1 / 2 {{0, 1}, {1, 0}}, 1 / 2 {{0, -I}, {I, 0}}, 1 / 2 {{1, 0}, {0, -1}}};
         MatrixForm /@ σ
```

Out[48]=

$$\left\{\begin{pmatrix} 0 & \frac{1}{2} \\ \frac{1}{2} & 0 \end{pmatrix}, \begin{pmatrix} 0 & -\frac{i}{2} \\ \frac{i}{2} & 0 \end{pmatrix}, \begin{pmatrix} \frac{1}{2} & 0 \\ 0 & -\frac{1}{2} \end{pmatrix}\right\}$$

```
In[49]:= ZeemanBasis := Module[{ner},
           stretch = Table[1 / 2, {k, 1, Nspins}];
           (* Stretched state where all spins point along Z *)
           basis = Table[stretch, {i, 1, 2^(Nspins)}];
           Do[Do[basis[[i + 1, k]] = basis[[i + 1, k]] * (-1)^(Quotient[i, 2^(k - 1)]),
              {i, 0, 2^(Nspins) - 1}], {k, 1, Nspins}];
           basis]
         (* basis is the uncoupled Zeeman basis *)
         ZeemanBasis;
```

```
In[51]:= (* a,bth matrix element of the qth component of the jth spin *)
         IMatrixElement[j_, q_, a_, b_] := Module[{ner},
           plist = Table[dum, {dum, 1, Nspins}];
           plist = Drop[plist, {j}];
           Product[
              KroneckerDelta[ basis[[a, plist[[dum]]]], basis[[b, plist[[dum]]]] ],
             {dum, 1, Length[plist]}] σ[[q]][[-1 * basis[[a, j]] + 3 / 2, -1 * basis[[b, j]] + 3 / 2]]
          ]

In[52]:= IOperators := Module[{ner},
           IOps = Table[{Table[IMatrixElement[j, 1, a, b], {a, 1, imax}, {b, 1, imax}],
               Table[IMatrixElement[j, 2, a, b], {a, 1, imax}, {b, 1, imax}],
               Table[IMatrixElement[j, 3, a, b], {a, 1, imax}, {b, 1, imax}]}, {j, 1, Nspins}];
           IOps]

         IOperators;

In[54]:= Hj := Sum[ Jnet[[i, j]]
             (IOps[[i, 1]].IOps[[j, 1]] + IOps[[i, 2]].IOps[[j, 2]] + IOps[[i, 3]].IOps[[j, 3]]),
           {i, 1, Nspins}, {j, 1, Nspins}]

In[55]:= Hz := - (Bx * Sum[gamma[[i]] IOps[[i, 1]], {i, 1, Nspins}] +
              By * Sum[gamma[[i]] IOps[[i, 2]], {i, 1, Nspins}] +
              Bz * Sum[gamma[[i]] IOps[[i, 3]], {i, 1, Nspins}])

In[56]:= Mutotx = Sum[gamma[[j]] IOps[[j, 1]], {j, 1, Nspins}];
         Mutoty = Sum[gamma[[j]] IOps[[j, 2]], {j, 1, Nspins}];
         Mutotz = Sum[gamma[[j]] IOps[[j, 3]], {j, 1, Nspins}];

In[59]:= Mutot[q_] := Sum[gamma[[j]] IOps[[j, q]], {j, 1, Nspins}];

In[60]:= Ixtot := Sum[IOps[[j, 1]], {j, 1, Nspins}];
         Iytot := Sum[IOps[[j, 2]], {j, 1, Nspins}];
         Iztot := Sum[IOps[[j, 3]], {j, 1, Nspins}];

In[63]:= (* y pulse of area B1t = Pi/2/(γh-γc) *)
         (Rx[B1t_] := MatrixExp[I B1t Sum[IOps[[i, 1]] * gamma[[i]], {i, 1, Nspins}]]) //
           MatrixForm;
         (Ry[B1t_] := MatrixExp[I B1t Sum[IOps[[i, 2]] * gamma[[i]], {i, 1, Nspins}]]) // MatrixForm;
         (Rz[B1t_] := MatrixExp[I B1t Sum[IOps[[i, 3]] * gamma[[i]], {i, 1, Nspins}]]) // MatrixForm;

In[66]:= (* J-coupling time evolution operator *)
         (* (U[t_] = MatrixExp[-I (Hj+Hz) t])//MatrixForm;*)

In[67]:= (* initial density matrix I1 dot I2 *)
         (*(rho0 =MatrixExp[1.(IOps[[1,1]].IOps[[2,1]]+IOps[[1,2]].IOps[[2,2]]+
                  IOps[[1,3]].IOps[[2,3]])]/Tr[MatrixExp[IOps[[1,1]].IOps[[2,1]]+
                 IOps[[1,2]].IOps[[2,2]]+IOps[[1,3]].IOps[[2,3]]]])//MatrixForm*)

In[68]:= (* density matrix elements in the basis of eigenstates of the hamiltonian *)
         Rho[ρ_, eigensystem_, a_, b_] := Conjugate[eigensystem[[2, a]]].ρ.eigensystem[[2, b]];
```

```
In[69]:= (* Time dependent magnetization given initial density matrix ρ and eigensystem *)
         Magnetization[ρ_, eigensystem_, q_, t_] :=
          Sum[Exp[- I (Chop[eigensystem[[1, a]] - eigensystem[[1, b]]]) t]
              Chop[Rho[ρ, eigensystem, a, b] * Conjugate[eigensystem[[2, b]]].Mutot[q].
                 eigensystem[[2, a]]], {a, 1, imax}, {b, 1, imax}] // ExpToTrig // Chop

         (* Time dependent magnetization given initial density matrix ρ and eigensystem *)
         Magxt[ρ_, eigensystem_, t_] :=
          Sum[Exp[- I (Chop[eigensystem[[1, a]] - eigensystem[[1, b]]]) t]
              Chop[Rho[ρ, eigensystem, a, b] * Conjugate[eigensystem[[2, b]]].Mutotx.
                 eigensystem[[2, a]]], {a, 1, imax}, {b, 1, imax}] // ExpToTrig // Chop
         Magyt[ρ_, eigensystem_, t_] := Sum[Exp[- I (Chop[eigensystem[[1, a]] - eigensystem[[1, b]]])
                t] Chop[Rho[ρ, eigensystem, a, b] * Conjugate[eigensystem[[2, b]]].Mutoty.
                 eigensystem[[2, a]]], {a, 1, imax}, {b, 1, imax}] // ExpToTrig // Chop
         Magzt[ρ_, eigensystem_, t_] := Sum[Exp[- I (Chop[eigensystem[[1, a]] - eigensystem[[1, b]]])
                t] Chop[Rho[ρ, eigensystem, a, b] * Conjugate[eigensystem[[2, b]]].Mutotz.
                 eigensystem[[2, a]]], {a, 1, imax}, {b, 1, imax}] // ExpToTrig // Chop


In[73]:= SingletOrder[ρ_, eigensystem_, t_, j_, k_] :=
          Sum[Exp[- I (Chop[eigensystem[[1, a]] - eigensystem[[1, b]]]) t]
              Chop[Rho[ρ, eigensystem, a, b] * Conjugate[eigensystem[[2, b]]].Mutoty.
                 eigensystem[[2, a]]], {a, 1, imax}, {b, 1, imax}] // ExpToTrig // Chop

In[74]:= AL[ω_, ω0_, Γ_] = Γ / ((ω - ω0)^2 + Γ^2);
         DL[ω_, ω0_, Γ_] = (ω - ω0) / ((ω - ω0)^2 + Γ^2);

In[76]:= (* Fourier transform of magnetization given initial density matrix ρ and eigensystem *)
         Magxω[ρ_, eigensystem_, Γ_, ω_] :=
          Sum[(AL[ω, (Chop[eigensystem[[1, a]] - eigensystem[[1, b]]]), Γ] +
              I DL[ω, (Chop[eigensystem[[1, a]] - eigensystem[[1, b]]]), Γ])
            Chop[Rho[ρ, eigensystem, a, b] * Conjugate[eigensystem[[2, b]]].
               Mutotx.eigensystem[[2, a]]], {a, 1, imax}, {b, 1, imax}]
         Magyω[ρ_, eigensystem_, Γ_, ω_] := Sum[
            (AL[ω, (Chop[eigensystem[[1, a]] - eigensystem[[1, b]]]), Γ] +
              I DL[ω, (Chop[eigensystem[[1, a]] - eigensystem[[1, b]]]), Γ])
            Chop[Rho[ρ, eigensystem, a, b] * Conjugate[eigensystem[[2, b]]].
               Mutoty.eigensystem[[2, a]]], {a, 1, imax}, {b, 1, imax}]
         Magzω[ρ_, eigensystem_, Γ_, ω_] := Sum[
            (AL[ω, (Chop[eigensystem[[1, a]] - eigensystem[[1, b]]]), Γ] +
              I DL[ω, (Chop[eigensystem[[1, a]] - eigensystem[[1, b]]]), Γ])
            Chop[Rho[ρ, eigensystem, a, b] * Conjugate[eigensystem[[2, b]]].
               Mutotz.eigensystem[[2, a]]], {a, 1, imax}, {b, 1, imax}]

In[79]:= (* Check Orthogonality *)
         CheckOrthog[sys_] := Table[Conjugate[sys[[2, i]]].sys[[2, j]],
              {i, 1, Length[sys[[1]]]}, {j, 1, Length[sys[[1]]]}] // Chop // MatrixForm


In[80]:= (* Function for orthogonalizing two eigenvectors  using Gram-Schmidt *)
         OrthoNormalize[system_, g_, h_] := Module[{sys},
           sys = system;
           sys[[2, g]] = sys[[2, g]] / Sqrt[Conjugate[sys[[2, g]]].sys[[2, g]]];
           sys[[2, h]] = sys[[2, h]] - (Conjugate[sys[[2, h]]].sys[[2, g]]) sys[[2, g]];
           sys[[2, h]] = sys[[2, h]] / Sqrt[Conjugate[sys[[2, h]]].sys[[2, h]]];
           sys]
```

Also initialize some numerical functions

```
In[81]:= fourpos[data_, dt_] := Module[{nerp},
           ft = 2 / Sqrt[Length[data]] Fourier[data];
           ft = Drop[ft, -Length[data] / 2];
           nuvals = Table[ 1 / (Length[data] * dt) * (j - 1), {j, 1, Length[data] / 2}];
           ft = Transpose[{nuvals, ft}]
          ]

In[82]:= cullkeepx[data_, xrange_] := Module[{jmin, jmax, dx, dum},
           dx = data[[2, 1]] - data[[1, 1]];
           dum = Drop[data, -(Length[data] - Floor[xrange[[2]] / dx])];
           Drop[dum, Floor[xrange[[1]] / dx]]]

In[83]:= culldelx[data_, xrange_] := Module[{jmin, jmax, dx, dum},
           dx = data[[2, 1]] - data[[1, 1]];
           jmin = Floor[(xrange[[1]] - data[[1, 1]]) / dx];
           jmax = Floor[(xrange[[2]] - data[[1, 1]]) / dx];
           dum = Drop[data, {jmin, jmax}]
          ]

In[84]:=
         singlecomplexLor[ν0_, a_, ϕ_, dν_, br_, bi_, ν_] =
           a ( (ν - ν0) dν - I dν^2) / ((ν - ν0) ^2 + dν^2) * Exp[I ϕ] + br + bi * I;

In[85]:= singleminfunc[dat_, ν0_, a_, ϕ_, dν_, br_, bi_] :=
          Sum[Abs[dat[[i, 2]] - singlecomplexLor[ν0, a, ϕ, dν, br, bi, dat[[i, 1]]]]^2,
           {i, 1, Length[dat]}]
```

Etc

```
In[86]:= (*  Magnetic field *)
         Bx := 0.00;
         By := 0.00;
         Bz := 0.00;
         (* Eigenstates,values *)
         esys = Eigensystem[Chop[Hj + Hz]];
         Do[esys[[2, i]] = esys[[2, i]] / Norm[esys[[2, i]]], {i, 1, Length[esys[[2]]]}]

In[91]:= (U[t_] := MatrixExp[-I (Hj + Hz) t]) // MatrixForm;

         rhot[rho_, t_] := Module[{Ut},
           Ut = U[t];
           Ut.rho.Inverse[Ut]]
```

Thermal polarization

```
In[93]:=
      (* For thermal polarization *)
      (* initial density matrix in spin-temp distribution *)
      (* Apply a pulse with product of B1 t, in y direction *)

      Bp = 18000;
      beta = Bp gamma / kT;
      Clear[beta];
      beta = Table[γh Bp / kT, {j, 1, Nspins}];
      Z = Sum[beta[[i]] * IOps[[i, 3]], {i, 1, Nspins}];
      (rho0 = MatrixExp[Z] / Tr[MatrixExp[Z]]) // MatrixForm;
      (* Density matrix after rotating about uncoupled spins about y *)
      b1t = 4 Pi / (γh);
      (rho1 = Ry[b1t].rho0.Inverse[Ry[b1t]]) // MatrixForm;


In[101]:= Clear[mz]

In[102]:= (* Generate observable *)
          mz[t_] = Magzt[rho1, esys, t];

In[103]:= (* conversion to moles *)
          molespercc = 2 * 1.0415 / 106.12 * 6.02 * 10^23 (* molecules per cc *)
          hbarcgs = 1.05 × 10^-27;

Out[103]= 1.18165 × 10^22

In[105]:= dt = 0.001;
          T2 = 4;
          acq = 20;
          ts = 0 × 10 dt;
          mzvals =
            Chop[Table[mz[t] Exp[-t / T2], {t, ts, acq - dt, dt}]] molespercc hbarcgs 10^-4 * 10^12;
          tvals = Table[t, {t, ts, acq - dt, dt}];

In[111]:= Length[tvals]

Out[111]= 20000

In[112]:= Length[mzvals]

Out[112]= 20000

In[113]:= mzvals[[1]]

Out[113]= 597.216

In[114]:= pars = FindFit[Transpose[{tvals, Chop[mzvals]}], A * Exp[-t / T2], {{A, -1}}, t];
           mzvals = mzvals - A * Exp[-tvals / T2] /. pars;
          ListLinePlot[Transpose[{tvals, mzvals}],
            PlotRange → All, FrameLabel → {"Time (s)", "Signal (μG)"}];
```

```
In[127]:= dum = Drop[mzvals, 000];
          ListLinePlot[dum, PlotRange → All] // Rasterize
```

Out[128]=

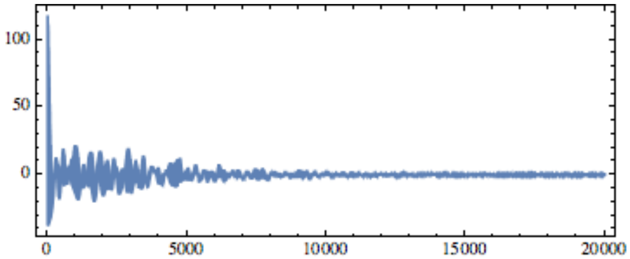

```
In[123]:= ftsim = fourpos[dum, dt];
          ftsim = cullkeepx[ftsim, {167.35, 182.35}];
          SetOptions[ListLinePlot, Axes → False,
            Frame → True, PlotRange → All, AspectRatio → 0.4, BaseStyle → 13];
          pdrsim = ListLinePlot[Re[ftsim], PlotStyle → RGBColor[0, 0, 0],
             ImageSize → 625, FrameLabel → {"Frequency (Hz)", "Re M_z (pT)"}] // Rasterize
```

Out[126]=

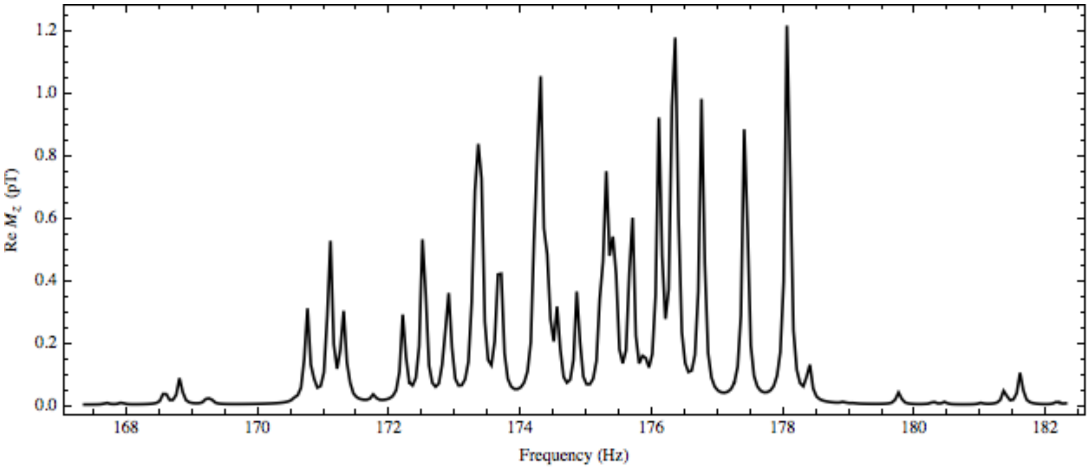

```
In[137]:= ftsimlow = fourpos[dum, dt];
          ftsimlow = cullkeepx[ftsimlow, {0, 20}];
          SetOptions[ListLinePlot, Axes → False,
            Frame → True, PlotRange → All, AspectRatio → 0.4, BaseStyle → 13];
          pdrsimlow = ListLinePlot[Re[ftsimlow], PlotStyle → RGBColor[0, 0, 0],
             ImageSize → 625, FrameLabel → {"Frequency (Hz)", "Re Mz (pT)"}] // Rasterize
```

Out[140]=

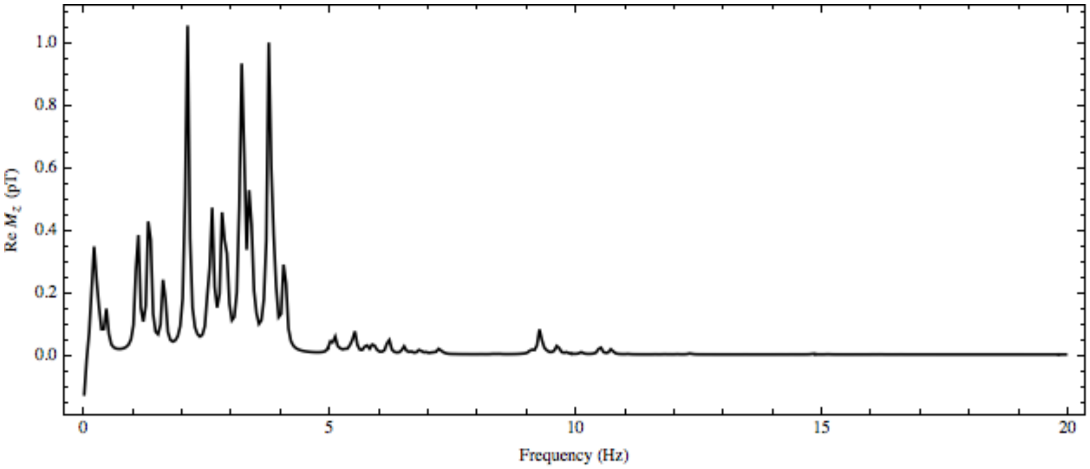

```
In[133]:= ftsimfull = fourpos[dum, dt];
          ftsimfull = cullkeepx[ftsimfull, {0, 200}];
          SetOptions[ListLinePlot, Axes → False,
            Frame → True, PlotRange → All, AspectRatio → 0.4, BaseStyle → 13];
          pdrsimfull = ListLinePlot[Re[ftsimfull], PlotStyle → RGBColor[0, 0, 0],
             ImageSize → 625, FrameLabel → {"Frequency (Hz)", "Re Mz (pT)"}] // Rasterize
```

Out[136]=

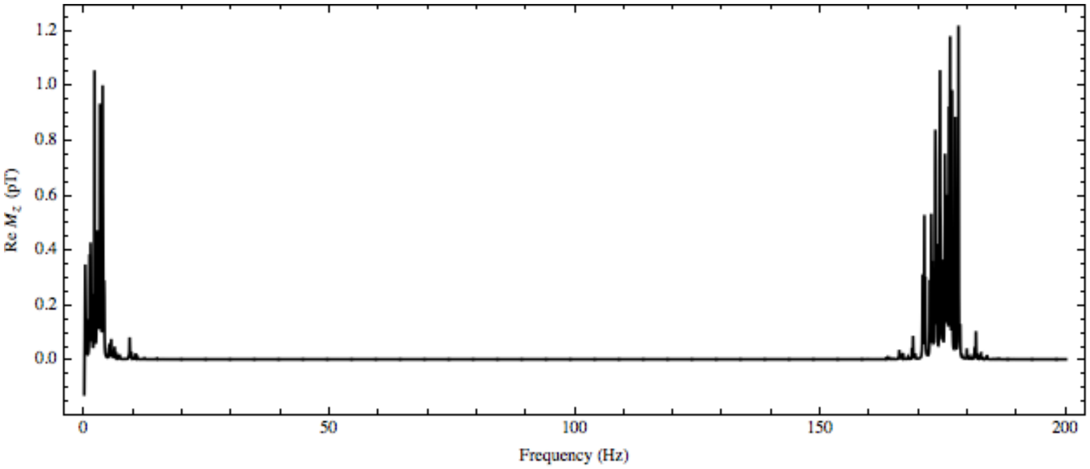

Comparison with Experiment

```
Show[{pdrsim, pdrexp}]
```

Out[142]=